

Stony Brook University



OFFICIAL COPY

The official electronic file of this thesis or dissertation is maintained by the University Libraries on behalf of The Graduate School at Stony Brook University.

© All Rights Reserved by Author.

**A Critical Assessment of In-Flight Particle State During
Plasma Spraying of YSZ and its Implications on
Coating Properties and Process Reliability**

A Dissertation Presented

by

Vasudevan Srinivasan

to

The Graduate School

In Partial Fulfillment of the

Requirements

for the Degree of

Doctor of Philosophy

in

Materials Science and Engineering

Stony Brook University

August 2007

Stony Brook University

The Graduate School

Vasudevan Srinivasan

We, the dissertation committee for the above candidate for the
Doctor of Philosophy degree, hereby recommend
acceptance of this dissertation.

Dr. Sanjay Sampath – Dissertation Advisor
Professor, Materials Science and Engineering

Dr. Andrew Gouldstone – Chairperson of Defense
Assistant Professor, Materials Science and Engineering

Dr. Herbert Herman
Distinguished Professor Emeritus, Materials Science and Engineering

Dr. Jon P. Longtin
Associate Professor, Mechanical Engineering
Stony Brook University

This dissertation is accepted by the Graduate School

Lawrence Martin
Dean of the Graduate School

Abstract of the Dissertation

A Critical Assessment of the In-Flight Particle State During Plasma Spraying of YSZ and Its Implications on Coating Properties and Process Reliability

by

Vasudevan Srinivasan

Doctor of Philosophy
in
Materials Science and Engineering

Stony Brook University
2007

Air plasma spray is inherently complex due to the deviation from equilibrium conditions, three dimensional nature, multitude of interrelated (controllable) parameters and (uncontrollable) variables involved, and stochastic variability at different stages. The resultant coatings are complex due to the layered high defect density microstructure. Despite the widespread use and commercial success for decades in earthmoving, automotive, aerospace and power generation industries, plasma spray has not been completely understood and prime reliance for critical applications such as thermal barrier coatings on gas turbines are yet to be accomplished.

This dissertation is aimed at understanding the in-flight particle state of the plasma spray process towards designing coatings and achieving coating reliability with the aid of non-contact in-flight particle and spray stream sensors. Key issues such as the phenomena of optimum particle injection and the definition of spray stream using particle state are investigated. Few strategies to modify the microstructure and properties of Yttria Stabilized Zirconia coatings are examined systematically using the framework of process maps. An approach to design process window based on design relevant coating properties is presented. Options to control the process for enhanced reproducibility and reliability are examined and the resultant variability is evaluated systematically at the different stages in the process. The 3D variability due to the difference in plasma characteristics has been critically examined by investigating splats collected from the entire spray footprint.

Dedicated To
My Parents, Sister, Nephew and Late Grand Father

Table of Contents

List of Figures	ix
List of Tables	xxiii
1 Introduction.....	1
1.1 Thermal Barrier Coatings	1
1.2 Plasma Spray Processing of YSZ	3
1.3 Prime Reliance and Coating Design.....	4
1.3.1 Knowledge of the Behavior in Service of Plasma Sprayed TBCs.....	5
1.3.2 Knowledge of the Coating Microstructure and Properties	7
1.3.3 Process Considerations for APS YSZ.....	10
1.4 Focus of this Dissertation	17
2 Statement of the Problem.....	18
2.1 Radial Injection of Particles into Plasma Jet	19
2.2 Torch Parameters – Particle State – Coating Relation	19
2.3 Coating Reliability via Process Reliability.....	21
3 Experimental Techniques.....	22
3.1 Process and Equipments	22
3.1.1 Plasma Spray System.....	22
3.1.2 Splat Collection.....	22
3.1.3 Procedure	24
3.2 Materials	25
3.2.1 Feedstock	25
3.2.2 Substrates	29
3.3 In-situ Measurements.....	30
3.3.1 In-flight Diagnostics	30
3.3.2 In-situ Coating Sensor.....	36
3.4 Post Processing Analysis	39
3.4.1 Characterization	39
3.4.2 Property Measurements	40
3.4.3 Analysis.....	40
4 External Radial Injection of Particles: Salient Observations and Optimization Strategies	42
4.1 Introduction.....	42
4.2 Experimental Methods.....	43
4.2.1 Materials and Process	43

4.2.2	Sensors and Diagnostics	44
4.2.3	Procedure and Methodology	44
4.3	Results and Discussion	45
4.3.1	Role of Carrier Gas on Particle Trajectory	45
4.3.2	Implications of Particle Trajectory on Particle State	46
4.3.3	Carrier Gas Flow Vs Plume Position	47
4.3.4	Examining Validity of the Phenomena for a Range of Process Conditions	49
4.3.5	Implications of the Observed Phenomena	54
4.4	Summary and Conclusion	57
5	A Critical Examination of Particle State and Spray Stream.....	59
5.1	Process-Particle State Relation	59
5.1.1	Introduction.....	59
5.1.2	Background.....	59
5.1.3	Implications of First Order Process Maps	63
5.1.4	Comparison of Feedstock Morphologies	65
5.1.5	Summary and Conclusion	69
5.2	Process Control Using In-flight Particle State: Observations and Considerations.....	70
5.2.1	Introduction.....	70
5.2.2	Experimental Details.....	70
5.2.3	Results and Discussion	73
5.2.4	Summary and Conclusion	83
5.3	Examining Temperature Distributions and Particle Melting	84
5.3.1	Introduction.....	84
5.3.2	Particle Melting Index.....	84
5.3.3	Spray Stream Melting Index	88
5.3.4	Summary and Conclusion	96
6	Synthesis of Process Maps and Strategies to Alter Microstructure: Integrating Process Science and Material Properties.....	98
6.1	Introduction.....	98
6.1.1	Plasma Spray Conditions	98
6.1.2	Deposition conditions	100
6.1.3	Feedstock Characteristics.....	100
6.2	Synthesis of Second Order Process Maps	101
6.2.1	Influence of Particle State	101
6.2.2	Influence of Deposition Conditions	112
6.3	Approaches to Significantly Modify the Microstructure and Properties	119
6.3.1	Introduction.....	119
6.3.2	Experimental Details.....	119

6.3.3	Results and Discussion	120
6.3.4	Summary and Conclusion	130
7	Assessment of Process Variability	132
7.1	Variability at Different Stages in the Process.....	132
7.1.1	Introduction.....	132
7.1.2	Experimental Details.....	133
7.1.3	Results and Discussion	136
7.1.4	Summary and Conclusion.....	144
7.2	Examining the Variation in Splat Characteristics within the Spray Footprint	145
7.2.1	Introduction.....	145
7.2.2	Experimental Details.....	146
7.2.3	Results and Discussion	148
7.2.4	Summary and Conclusion.....	153
8	Discussion of Salient Observations.....	155
8.1	Particle Injection.....	155
8.2	Examining Particle State and Spray Stream.....	157
8.2.1	Validity of the Measured Particle Temperatures	158
8.2.2	Difference between Ensemble Temperature and Average Particle Temperature	158
8.2.3	Source of the Variation.....	159
8.3	Investigating Temperature Distributions	162
8.3.1	Difference in Shift of T-V Space between PD and AS Morphology Feedstock	162
8.3.2	Difference in Behavior of Hollow Spherical Particles	163
8.4	Examining the Possibility to Assess Melting States from Measured Particle Temperature.....	165
8.5	Process Control Based on Voltage/Power.....	167
8.6	High Variability in Coating Properties.....	169
9	Synthesis.....	171
9.1	Integration of Results.....	171
9.2	Conclusions.....	172
10	Suggestions for Future Work	175
10.1	Improvements to Definition of Particle.....	175
10.1.1	Powder Morphology	175
10.1.2	Thermal History of Particles.....	175
10.2	Definition of Spray Stream and Process Control	176
10.2.1	Single Particle Sensor Vs Ensemble Sensor	176
10.2.2	Choice of In-Flight Parameters to Completely Describe the Spray Stream for True In-flight Process Control	176

10.3	Shift in In-Flight Particle State With Time	178
10.4	Determining Adhesion and Cohesion Behavior of Coatings via In-Situ Curvature Monitoring	179
10.5	Splat Map	179
10.6	DVC Threshold in Deposition Rate.....	180
11	Bibliography	183

List of Figures

Figure 1: A sketch of an aircraft gas turbine engine. The combustor and turbine structural components are heat shielded using TBCs (Picture courtesy of Sulzer Metco Inc, Westbury, NY)	1
Figure 2: Schematic of a typical (four layer) TBC system. Temperature profile shown across the layers demonstrating the thermal barrier effect of the top coat.....	2
Figure 3: Microstructure along length scales in air plasma sprayed YSZ (micrographs courtesy of Dr. Kulkarni, Stony Brook University) [60].....	4
Figure 4: Requirements for prime reliance (Figure adapted from [61])	5
Figure 5: A schematic sketch of some of the prevalent failure mechanisms in TBC systems (figure from Evans et al. [6]).....	6
Figure 6: Capability, benefits and limitations of some commonly used and some advanced microstructural characterization techniques (courtesy of Dr. Kulkarni, Stony Brook University).....	9
Figure 7: A schematic of the different stages in the plasma spray process. The red color arrows represent a First Order Process Map and the blue color arrows represent a Second Order Process Map.....	11
Figure 8: Schematic identifying the different states in the process, the variable clusters and the different variables that influence the processing of TBCs by APS.....	12
Figure 9: Process maps and identifying process windows based on particle state and porosity of coatings (figure from Dr. Friis [143]).....	13
Figure 10: A second order process map identifying trend in microstructure, property and particle state. The two data points not along the trend are from hollow spherical feedstock, indicating the difference in behavior of this morphology (figure courtesy of Dr. Vaidya).....	13
Figure 11: Drift in the process in the hour time scale (figure from Leblanc [166])	15
Figure 12: Control strategy based on controlling two in-flight particle properties while limiting the key plasma forming and injection related hardware parameters proposed by Vardelle and Fauchais [35].....	16
Figure 13: Substrates placed on a heated substrate holder. In the swipe method of splat collection, the torch passes over the substrates once.....	23
Figure 14: A schematic of the snapshot method of splat collection	23

Figure 15: Experimental set up to collect snapshot of spray footprint in the form of splats	24
Figure 16: Typical experimental sequence	24
Figure 17: Normalized volume of particles at the different sizes for the different morphology feedstock.....	25
Figure 18: Normalized number of particles at the different sizes for the different morphology feedstock.....	27
Figure 19: Normalized volume of particles at the different sizes for the different size feedstock	27
Figure 20: Normalized volume of particles at the different sizes for the different size feedstock	28
Figure 21: Components of the DPV 2000 sensor	31
Figure 22: Principle of measurement of DPV 2000.....	31
Figure 23: Measurement volume of DPV 2000.....	32
Figure 24: A schematic of the types of measurements made with DPV 2000	32
Figure 25: Limits of detection of DPV 2000	33
Figure 26: Measurement volume, location of measurement and setup of SPT and IPP	34
Figure 27: Integrated sensor setup	34
Figure 28: Picture of the actual integrated sensor setup	35
Figure 29: Calibration assembly used for the coordinate calibration of sensors with respect to the torch.....	35
Figure 30: In-situ coating property sensor (ICP-4) with an aluminum sample mounted.....	36
Figure 31: Knife-edge holder. The sample is held using screw-hook system and spring.....	36
Figure 32: Front-end of curvature data acquisition. The graph inside the figure shows the distance measured by the laser and the temperature measured behind the substrate as a function of time	37
Figure 33: Theory behind the calculation of curvature using three points in space. Figure from [146].....	38
Figure 34: Curvature and temperature as a function of time during preheating, deposition and subsequent cooling to room temperature.....	38

Figure 35: Curvature as a function of temperature during heat cycling (after the deposit has cooled down to room temperature). Heating data is noisy; cooling data is smooth.....	39
Figure 36: Laser Strobe Control Vision TM image of orthogonal external injection of particles into a DC thermal plasma jet.....	42
Figure 37: Change in particle trajectory as a function of carrier gas flow observed via xenon strobe imaging.....	45
Figure 38: Change in plume position as a function of carrier gas flow for different primary gas flows.....	46
Figure 39: Mean particle temperature and velocity (from 10,000 particles measured using DPV 2000) for various carrier gas flows. Maximum could be observed in both T and V	46
Figure 40: Time averaged ensemble temperature (from IPP) for various carrier gas flows. Maximum is observed.....	47
Figure 41: Preferred plume position observed for the different process parameter combinations in a statistical design of experiments including carrier gas as one of the primary parameters. All parameters remaining the same, change in carrier gas flow can result in identifiable under and over injected states.....	48
Figure 42: Mean particle temperature and velocity (from 10,000 particles measured using DPV 2000) as a function of plume position. Maximum could be observed in both T and V	49
Figure 43: Mean particle temperature and velocity (from 10,000 particles measured using DPV 2000) as a function of carrier gas flow for different primary gas (Ar) flows. Maxima could be observed in both T and V in each case	50
Figure 44: Mean particle temperature and velocity (from 10,000 particles measured using DPV 2000) as a function of plume position for different primary gas (Ar) flows. Maxima could be observed in both T and V in each case. The plume position of the maximum is the same in each case. Compare to Figure 43.....	50
Figure 45: Mean particle temperature and velocity (from 10,000 particles measured using DPV 2000) as a function of plume position for different primary gas (N ₂) flows for N ₂ -H ₂ plasma gas mixture. Maximum could be observed in both T and V in each case. The plume position of the maximum is the same in each case. Compare Figure 44 for Ar-H ₂	51
Figure 46: Mean particle temperature and velocity (from 10,000 particles measured using DPV 2000) as a function of plume position for	

	different feedstock morphologies. Maximum could be observed in both T and V in each case at similar plume position	52
Figure 47:	Mean particle temperature and velocity (from 10,000 particles measured using DPV 2000) as a function of plume position for different angles of particle injection. Inset shows a schematic of the injection angles. Maximum could be observed in both T and V in each case	53
Figure 48:	Mean particle temperature and velocity (from 10,000 particles measured using DPV 2000) as a function of plume position for different feed rates (left – low feed rate; right – high feed rate). Maximum could be observed in both T and V in each case at similar plume position.....	54
Figure 49:	Controlling particle injection via plume position results in enhanced reproducibility in measured particle state (IO) as compared to intentional variation of plume position on either side of the optimum (w/o IO). w/o IO depicts the extreme case where carrier gas flow is maintained constant with time resulting in different plume positions due to change in the DC plasma jet	55
Figure 50:	Temperature distributions for different particle injection shown with the underlying peaks [158]. Optimizing injection shifts the distribution to higher temperatures resulting in better melting and higher deposition efficiency. (Top - optimized injection; Bottom - under injected)	56
Figure 51:	Variation (maximum range normalized over the average of that parameter) in properties from few repeated experiments. Controlling plume position results in reduced variability in thickness per pass with no significant improvement in the variability in particle state, indicating controlled coating build-up [192]	57
Figure 52:	Extended central composite design of experiment using three significant plasma-forming torch parameters [146].....	60
Figure 53:	Torch parameter vectors in T-V space	61
Figure 54:	First order process maps from a variety of feedstock, hardware and torch parameters [146].....	62
Figure 55:	An illustration of the tuning-in procedure.....	64
Figure 56:	Process boundary in T-V space for FC feedstock.....	65
Figure 57:	Process instabilities and errors	65
Figure 58:	Time dependence of average particle temperature from repeated DoE center point condition (same process parameters) for the different morphological feedstock.....	66

Figure 59: Time dependent behavior of voltage for hollow spherical morphology	66
Figure 60: Comparison of process parameter vectors in T-V space. Fig (a) shows the behavior of each of the three morphology feedstock to change in mass flow. Fig (b) and (c) show similar behavior of each of the three morphology feedstock to change in hydrogen ratio and amperage (or current) respectively.....	67
Figure 61: Behavior of all the three morphology feedstock overlaid in the T-V space.....	68
Figure 62: Procedure followed to achieve same average temperature and velocity. Solid line represents the solution path. Dotted lines represent the fundamental source of the issue/solution and the bold dotted lines represent the immediate source of solution	72
Figure 63: Visualization of the many possible solutions possible for the torch parameters to achieve the same target temperature and velocity.....	72
Figure 64: Variability in in-flight particle properties, ensemble plume properties, coating attributes, microstructure and properties of coatings in experiment set A (PD morphology).....	74
Figure 65: Velocity distribution of particles measured at the flow center using DPV. The distributions are Gaussian and quite comparable	74
Figure 66: Particle temperature distribution arranged by increasing total input power from bottom to top. The distributions are multi-modal and are different from each other	75
Figure 67: Melting Index distributions for the different experiments resulting in same average temperature and velocity arranged by increasing total input power from bottom to top. One can observe the multi-modal nature of the distribution and the relative differences	76
Figure 68: Through thickness elastic modulus from instrumented indentation showing significant variation for the five experiments which resulted in same average temperature and velocity	76
Figure 69: Achieving similar average temperature and velocity - comparison between using wide range of torch parameters Vs small range of parameters. Narrow parameter space results in lesser variability.....	77
Figure 70: Assessment of variability within experiment set B – FC morphology.....	79
Figure 71: Assessment of variability within experiment set C – AS morphology	79
Figure 72: Ensemble temperature dependence on total mass flow, hydrogen ratio and current	81
Figure 73: Ensemble temperature as a function of input power	81

Figure 74: Plume width as a function of total mass flow	81
Figure 75: Deposition efficiency varying as a function of plume width	82
Figure 76: Deposition efficiency as a function of temperature.....	82
Figure 77: Temperature distribution fitted with the underlying peaks. Red color represents the melting peak consisting of partially molten particles	86
Figure 78: Particle temperature distribution against normalized particle count for the different process conditions exploring the extremes of the process space. Shift in temperature distribution from left to the right (low temperature to high temperature) can be observed with increasing average temperature (bottom to top)	87
Figure 79: Melting index distribution with the melting status regions identified. Red peak – melting peak (partially molten particles); Blue peak and Green Peak and either completely molten or completely unmolten depending on whether are located in the positive or negative side respectively	88
Figure 80: Particle temperature distribution for two different process conditions with same mean temperature but different mean velocities. One can observe the shift in the sub-distributions, which forms the basis for Spray Stream Melting Index	89
Figure 81: Correlating Spray Stream Melting Index to relative deposition efficiency for the coatings obtained from (i) Second Order Process Map – red square (refer section 6.2.1), (ii) Feedstock size distribution – blue circle (refer section 6.3.3.1.1) and (iii) Same T-V PD – green triangle (<i>Set A exp</i> ; refer section 5.2.3.1).....	90
Figure 82: Comparison of volume percentage of molten particles obtained from the distribution and the deposition efficiency. Volume percentage of molten particles obtained from particle Melting Index of individual particles classified using the approach in Figure 79	91
Figure 83: Particle temperature distributions for Ferrite system. Melting peak (in red) can be observed as well as the shift in distribution	93
Figure 84: Particle temperature distribution for Mo under different process conditions. Shift in distribution could be observed	93
Figure 85: Particle temperature distribution for widely different process conditions for YSZ sprayed under Ar-H ₂ plasma with a swirl flow. Shift in distributions can be observed with some distributions comprising only of completely molten particles.....	94
Figure 86: A plot of relative deposition efficiency Vs Spray Stream Melting Index (SSMI) for three process conditions. SSMI has been evaluated from experimental data using two different methods and from simulation	

data and compared. Both the experimental methods result in a good fit in the expected direction, whereas the simulation results show opposite trend with a poor fit.....	95
Figure 87: Schematic representation of the progressive knowledge in terms of exploring the process space using in-flight particle sensors.....	99
Figure 88: In-flight process space resulting from the extreme torch parameters. (a) Measured particle state - temperature and velocity and (b) calculated particle state – Melting Index and Reynolds Number	101
Figure 89: Splat micrographs superimposed on a plot of Melting Index Vs Reynolds Number. All images are at 200X. All splats are fairly disc shaped due to high substrate temperature (280°C). At very high MI and Re splashing can be observed (orange color). Low MI and high Re (green and brown color) results in poor melting, which is reflected in the area covered by the splats and by the smaller size of splats implying melting of fine particles.....	102
Figure 90: Splat Flattening Ratio (FR) as a function of Reynolds Number (Re). Red data points represent FR calculated from Madejski model and black data points represent measured FR from splats obtained on polished high temperature substrate. Good trend observed between measured and calculated vales except at high Re	103
Figure 91: Contour plot of Flattening Ratio (FR) as a function of Melting Index (MI) and Reynolds Number (Re). Re has the most influence on FR.....	103
Figure 92: Relative deposition efficiency (DE) contour in Melting Index (MI) - Reynolds Number (Re) space. DE increases as MI increases and Re decreases due to improved melting resulting from longer dwell time of particles in the plume.....	104
Figure 93: Through thickness thermal conductivity (k) measured by laser flash technique in the Melting Index (MI) – Reynolds Number (Re) space. MI contributes to k by better melting and hence better contact, wetting and spreading behavior of splats and Re contributes by better adhesion between splats during coating build-up	105
Figure 94: Through thickness modulus from instrumented indentation in the Melting Index (MI) – Reynolds Number space (Re). Modulus increases with both MI and Re. The jump in modulus from 44 to 53 is due to enhanced melting (44 is at the melting point whereas 53 is on the molten side).....	105
Figure 95: In-plane modulus from in-situ curvature shown in the Melting Index (MI) – Reynolds Number space (Re). Modulus increases primarily with Re though MI also has an influence.....	106

Figure 96: Microstructural (left) and property (right) regimes identified in the Melting Index (MI) – Reynolds Number (Re) space. Arrows indicate approximate direction of increase of property	106
Figure 97: Particle state space designed and controlled to identify process windows for design.....	107
Figure 98: Contour plot of through thickness thermal conductivity in the Melting Index-Reynolds Number space	108
Figure 99: Contour plot of in-plane curvature modulus in the Melting Index-Reynolds Number space	109
Figure 100: Contour plot of through thickness indentation modulus in the Melting Index-Reynolds Number space	109
Figure 101: Identifying process window in the Melting Index – Reynolds Number space taking into account the thermal conductivity, in-plane modulus and through thickness modulus of coatings.....	110
Figure 102: A schematic representation of the role of the different variables classified as deposition conditions on the coating microstructure and properties.....	112
Figure 103: Schematic of design of experiment and the parameters used.....	113
Figure 104: Contour plot of the response of thickness per pass of the coating to the feed rate and pass rate. No clear trend could be established and the contours do not follow the iso-Deposition Rate lines	114
Figure 105: Relation between Deposition Rate and Thickness Per Pass.....	114
Figure 106: Contour plot of the response of through thickness thermal conductivity of the coating to the feed rate and pass rate. Though no clear trend could be established, higher Deposition Rates appear to increase the thermal conductivity	115
Figure 107: Contour plot of the response of in-plane modulus (from curvature) of the coating to the feed rate and pass rate. Though no clear trend could be established in comparison with the iso-Deposition Rate lines.....	115
Figure 108: Contour plots of cross-section DPV scan showing particle flux or spray stream shape. A 20% increase in plume width in the Y direction is observed for a 70° angle of impact in comparison with the standard or 90° for the same torch conditions due to the orientation of the spray stream to the diagnostics.....	116
Figure 109: Variation in properties for a small change in the angle of impact	117

Figure 110: Different feedstock size distributions represented in the T-V space (left) and in the MI-Re space (right)	121
Figure 111: Particle temperature distribution obtained from 10,000 particles at the flow center for the three different feedstock size distributions. The melting point is shown by the vertical line. One can observe the shift in distributions implying different extents of melting	122
Figure 112: Splat flattening ratio for the different feedstock size distributions. The coarse distribution shows moderately higher flattening ratio due to very high Reynolds Number	122
Figure 113: Thickness per pass and deposition efficiency (DE) for the different feedstock size distributions. Fine distribution shows highest DE while coarse particles show the lowest. Since the ensemble is a mixture of the coarse and the fine distributions, it is in between. This correlates well with the melting assessed from the temperature and Melting Index distributions.....	123
Figure 114: In-plane elastic modulus from curvature and through thickness modulus from indentation for the different feedstock size distributions. In both orientations ensemble feedstock shows the highest modulus closely followed by the other two size distributions	123
Figure 115: Through thickness thermal conductivity for the different feedstock size distributions. Coarse feedstock shows the highest thermal conductivity, fine shows the lowest and ensemble is in between	124
Figure 116: The temperature-velocity space for the two different nozzles used. The data point in bold represents the temperature and velocity at which the splats and deposits were made	125
Figure 117: Distributions of particle Melting Index (left) and Reynolds Number (right) are shown with an inset figure showing of the average MI and Re for the different nozzle diameters used. 6mm nozzle results in marginally lower melting while drastically increasing the Reynolds Number	125
Figure 118: Spray Stream Melting Index calculated from the temperature distributions of 6mm and 8mm nozzle. No significant difference is observed.....	126
Figure 119: Splat flattening ratio measured (circle) and calculated (square) as a function of Reynolds Number for 6mm and 8mm nozzles. Higher Re results in higher flattening ratio for the 6 mm nozzle.....	126
Figure 120: Properties of deposits made with 6 mm and 8 mm nozzles	127
Figure 121: T-V space for the different morphology feedstock. All three morphologies share a large common T-V space. Same average	

particle T and V (2661 °C and 125 m/s) were achieved within a narrow tolerance limit of ± 10 °C in T and ± 2 m/s in V (schematically represented by the box in the center of the T-V space)	128
Figure 122: Average Melting Index and Reynolds Number for the different morphology feedstock. The values appear to be very different due to the scale. In comparison to the overall range possible from the first order process map, the MI values are similar while the Re values are moderately different for PD	128
Figure 123: Melting Index distributions for the different morphology feedstock. The distributions appear similar except for a small difference at high temperature for hollow spherical (PD) morphology	129
Figure 124: Properties obtained for the different morphology feedstock.....	130
Figure 125: Process understanding from a design perspective. Significant variables have been identified and clustered for better focus	132
Figure 126: Illustration of the procedure used to adjust the temperature and velocity. Target and the allowed range are marked in the figure.....	135
Figure 127: Variability in average particle properties from single particle measurements at the flow center as measured by DPV2000 for the different process control methods. Variability in temperature and velocity is shown in fig a (left) and fig b (right) respectively. Temperature does not show any significant difference whereas velocity shows difference	137
Figure 128: Ensemble plume properties. Plume ensemble temperature measured by IPP 2000 (fig a) shows less than half the variability of other methods for the OT method. Plume width measured by SPT (fig b) shows least variability for FV method.....	138
Figure 129: Plume position subtracted from the optimum plume position. FV and OI method show the least variability while FP method shows the highest variability.....	138
Figure 130: Particle temperature distributions overlaid from individual experiments for each process control method. No clear distinction could be observed amongst the different methods.....	139
Figure 131: Detailed comparison of particle temperature distributions in the FV method. (i) Low H ₂ (ii) High H ₂ . The distributions have been fitted with three underlying peaks. Completely molten content in (ii) is higher than in (i) and ratio of area under P3 to P1 is clearly much higher for (ii).....	140

Figure 132: Variability in thickness per pass of the coatings produced by the different methods. Controlling the in-flight state results in better control of thickness per pass/deposition efficiency	141
Figure 133: Variability in total porosity for the four different methods. Controlling the in-flight state (OI and OT) shows the least variability	142
Figure 134: Variability in elastic modulus of coatings (a) via instrumented indentation along the thickness direction and (b) via curvature method in the plane of the coating.....	143
Figure 135: Variability in thermal conductivity for the different methods. Clearly, fixed voltage method shows the least variability and optimized T-V method shows highest variability (~4 times of FV and ~1.5 times that of traditional approach or FP).....	143
Figure 136: Temperature and velocity distributions representing the range of variability possible.....	145
Figure 137: Splat Map – Schematic (fig a) and Actual (fig b)	147
Figure 138: Correlation between particles in the plume as captured by a cross-section scan by DPV 2000 and the splats. The pictures on the top are photographed splat maps and are not shown to scale. The bottom pictures are contour maps of the particle flow at the standoff. In fig b, the entire plume has not been captured in particle diagnostics due to the plume being wider than the scanning grid (as revealed by the contour maps in the post-processing). The flow contours appear to capture the shape of the splat map for both the ceramic system (fig a) and metallic system (fig b).....	148
Figure 139: Splat map with coordinates from DPV contour map superimposed for Abracor amorphous alloy. ‘a’ corresponds to the nozzle axis, ‘b’ to the flow center measured from DPV and ‘c’ to the ‘visual’ flow center from the splat map. There exists discrepancy between flow centers detected using DPV (point ‘b’) and splat map (point ‘c’).....	149
Figure 140: Flow contours of particles measured using DPV scan across the spray stream for YSZ. Straight flow shows circular contours while swirl flow results in elliptical contours.....	149
Figure 141: Optical micrographs of representative splats from the different regions in the splat map for Abracor. Splat morphology can be observed to vary from disc shaped to splashed to splashed with missing core in the different regions.....	150
Figure 142: Flattening ratio measured at different regions in the splat map	151
Figure 143: Flattening ratio (Madejski model) distribution across the spray stream for YSZ	151

Figure 144: Integrated powder XRD profile of amorphous alloy. Different extents of amorphous content could be observed in regions 1 and 2.....	152
Figure 145: Integrated powder XRD profile of alpha alumina. Gamma phase is present in region 1 but is not present significantly in region 2.....	153
Figure 146: Schematic of particle injection and spray stream trajectory.....	156
Figure 147: Simulation results showing plasma temperature profiles and the interaction of the injected particles (at two different carrier gas flows – top: under injected and bottom: optimum injection) resulting in different trajectories. Different extent of penetration in the hot zone can be observed as well as the spread of the trajectory consisting of different particle sizes.....	156
Figure 148: Tan of plume angle and ratio of initial vertical velocity to the horizontal velocity at the spray distance as a function of carrier gas flow for different primary gas flows. The vertical black lines correspond to the optimum injection. Blue horizontal line intersecting the velocity ratio axis shows that optimum injection occurs at the same value of velocity ratio. The red horizontal line intersecting the tan (θ) axis shows that the optimum occurs at the same plume angle.....	157
Figure 149: Relative deposition efficiency as a function of Melting Index for experiment <i>set A</i> . Deposition efficiency decreases with increasing Melting Index.....	159
Figure 150: Contour maps of particle flux across the spray stream at the spray distance for the 5 experiments (section 5.2.3.1) where average temperature and velocity were same but the deposits were different. Difference in overall shape and location of the flux center could be observed.....	160
Figure 151: Contour maps of particle temperature across the spray stream at the spray distance for the 5 experiments (section 5.2.3.1) where average temperature and velocity were same but the deposits were different. Difference in shape does not appear to be very significant. There is a large ‘flat’ region at the flow center	161
Figure 152: Particle temperature distribution from particles measured (a) at the flow center and (b) across the spray stream. The difference in distribution is clear.....	161
Figure 153: Shift in T-V space for solid spherical and hollow spherical morphologies.....	162
Figure 154: Temperature distributions for hollow spherical morphology and solid spherical morphology at the two extreme process conditions. Melting	

and shift in temperature distributions is the reason for the observed shift in T-V space in Figure 153	163
Figure 155: Distributions of particle size (D), temperature (T) and velocity (V) for hollow spherical morphology feedstock at one process condition. Different particle sizes have been selected (in darker color) to understand which part of the temperature and velocity distribution they contribute. The vertical line in T is the melting point. Particles less than 20 microns and greater than 60 microns both contribute to the second of the three peaks in T distribution, while particles between 20 and 40 microns contribute to the third of the three peaks	164
Figure 156: A schematic of the possible particle states with respect to particle behavior in-flight taking into account melting, re-solidification and vaporization (Figure adapted from reference [186]).....	165
Figure 157: Particle state space for the two process conditions that were controlled to have similar voltage and power. Both conditions also resulted in similar average particle states (shown in the scale of the process maps).....	167
Figure 158: Plot correlating Spray Stream Melting Index (SSMI) to deposition efficiency (DE). The two data points pertaining to the discussion in this section are marked. Since two data points will always give a 100% fit, additional data covering the entire operational space (altering the SSMI from possible minimum to maximum) is shown to provide perspective of the goodness of fit.....	168
Figure 159: Spray steam contour plots for particle flow/flux, temperature and velocity for the two different process conditions that resulted in comparable average particle characteristics. Difference can be observed in flow pattern as well as the temperature contour.....	168
Figure 160: Variability observed at the different stages for repeated experiments with no process control (data from FP method discussed in section 7.1.2.3.1)	169
Figure 161: Fidelity of laser flash technique to measure thermal conductivity for plasma sprayed YSZ coating. Only in figure ‘b’ coefficient of variation is used (in the whole section).....	170
Figure 162: A schematic of the critical issues studied and their integration to coating design	171
Figure 163: A schematic of different slopes of particle surface temperatures due to difference in plasma characteristics merging at the spray distance to result in same temperature	177
Figure 164: A plot of distance of the sample from the laser Vs time during preheating, spraying and cooling, and thermal cycling (left) and	

during thermal cycling (right). At the end of the coating cooling, stress relaxation/balance is still happening even after reaching room temperature (point A) although no visible delamination was observed at the end of coating cooling. In the inset plot on the right, onset of delamination (point B) as well as delamination failure (point C) (full spallation - adhesive failure) could be detected in the distance (or displacement profile) even at relatively low temperatures..... 179

Figure 165: Elimination of splat from the periphery that contribute to coating build-up to reduce variability..... 180

Figure 166: Stiffening of the coatings at higher temperatures (strains)..... 181

Figure 167: Large area enclosed between heating and cooling curves. No hysteresis observed 181

Figure 168: Schematic probing the existence of a threshold value of Deposition Rate resulting in transition from layered coatings to dense vertically cracked (or segmented crack) coatings 182

List of Tables

Table 1: Different morphology feedstock of YSZ used in this study.....	26
Table 2: Feedstock used in the splat studies	28
Table 3: Sensors at CTSR – type, principle of operation, measurement details and typical data output.....	30
Table 4: Process parameters used in the study of injection. Shown in italics is the parameter used in that particular study	44
Table 5: Contribution to average particle temperature (measured by DPV at flow center) from significant torch parameters and their combinations [146].....	61
Table 6: Contribution to average particle velocity (measured by DPV at flow center) from significant torch parameters and their combinations [146].....	61
Table 7: Process conditions and feedstock details.....	71
Table 8: Summary of torch parameters used in the different process control methods for the angular morphology YSZ feedstock. Sensor based process control is italicized in table.....	135
Table 9: Feedstock and process parameters used in the study.....	146
Table 10: Possible combinations of relations between flame temperature, particle surface temperature and particle melting temperature involved in the calculation in ‘A’	166

Acknowledgements

Not so long ago, I was in elementary school curious to know about everything I saw and everything that happened around me. Successful transition from that curious worry-free school kid to a Doctor of Philosophy was made possible by the unconditional love, care and continuing support of my parents Mrs. Bhooma and Mr. Srinivasan, my sister Mrs. Gayathri Devi, and my late grand father Mr. Rengarajan.

I derived inspiration to pursue research and do Ph.D. from my interactions with Dr. Varadhan (chemistry teacher in high school), Mrs. Anuradha (lecturer in undergraduate), Dr. Bala Srinivasan (then lecturer, advisor and mentor in undergraduate) and Dr. Shaju (guide/advisor for a small but life altering research project).

During graduate school at Stony Brook University, I had a good learning experience in the Center for Thermal Spray Research guided by my advisor Prof. Sanjay Sampath. Interactions with Prof. Andrew Gouldstone, Prof. Herbert Herman, Prof. Jon Longtin and Prof. Hui Zhang have enriched my experience.

In this segment of my learning curve I had the opportunity to work with and learn from numerous colleagues. Discussions and interactions with Anirudha Vaidya, Tilo Streibl, Martin Friis, Anand Kulkarni, Glenn Bancke, Joshua Margolies, Shaun Kubik, Li Li, Swarnima Deshpande, Wanhuk 'Brian' Choi, Wesley Francillon, Weiguang Chi, Alfredo Valarezo, Yajie Liu, Antonio Caccavale, Jose Colmenares, Atin Sharma, Yuhong Wu, Wei Zhang, Meng Qu, Shanshan Liang, Justin and Chris Morck have helped me professionally.

My stay here in Stony Brook has been a pleasure, partly due to the many friends I made. Interactions with and support from Lysa Russo, Andrew Gouldstone, Eileen Zappia and Anirudha Vaidya have beaconed my sail through the at-times rough sea.

As my life continues past the graduate school, I would like to place on records my sincere gratitude to God for making me who I am and always lighting up the path ahead just enough.

Chapter I

1 Introduction

1.1 Thermal Barrier Coatings

The need for higher operating efficiencies, output power and reliability while concurrently lowering cost, enhancing safety and being environment friendly has necessitated system level enhancements in the design of propulsion and power generation turbines. Careful consideration has been given to each of the key sub-systems (Figure 1) for improvement in component design, cooling technology, overall efficiency of compressor and achieving higher turbine inlet temperatures. Of these, higher operating temperature is considered to have a high potential for increased efficiency as well as output power. To achieve higher operating temperatures, the structural components (exposed to heat such as the combustor and turbine) need to withstand higher temperature. This can be accomplished through improved cooling concepts and/or a thermal barrier coating (TBC) put in place to reduce the temperature experienced by the metallic structural component. TBCs offer a more attractive and efficient solution to the above problem and is the primary reason for the widespread use of TBCs, especially in the aerospace and power generation industries [1-5].

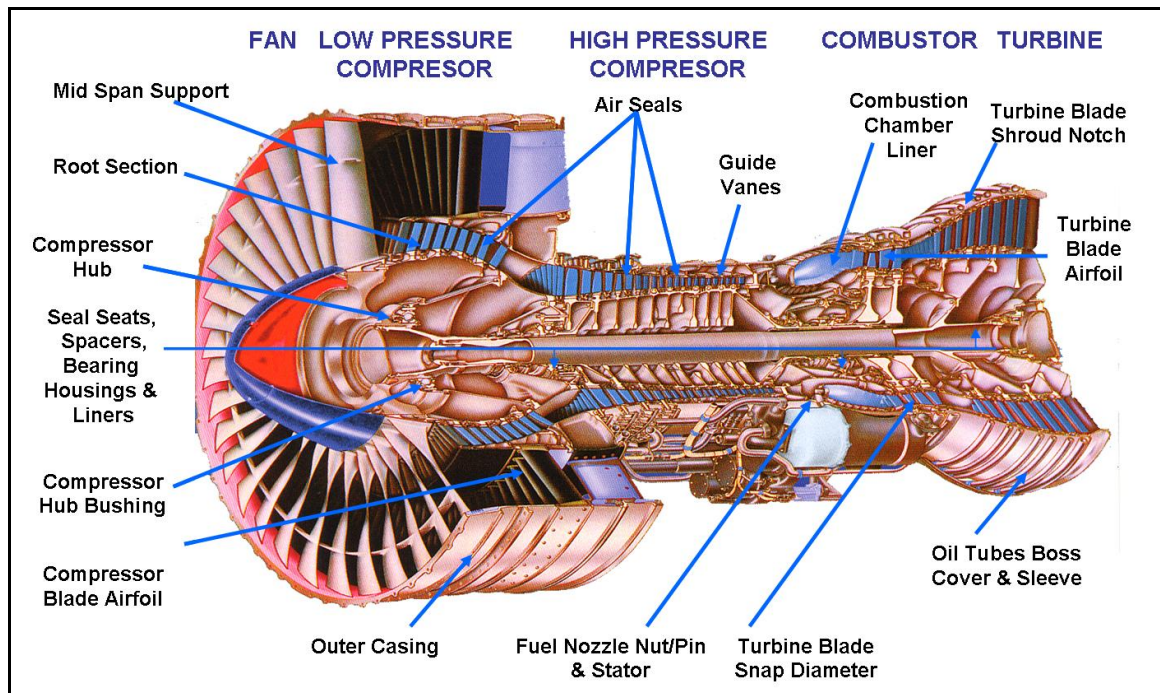


Figure 1: A sketch of an aircraft gas turbine engine. The combustor and turbine structural components are heat shielded using TBCs (Picture courtesy of Sulzer Metco Inc, Westbury, NY)

A thermal barrier system typically consists of four sections (Figure 2); (i) the structural super alloy component, (ii) aluminum containing metallic alloy bond coat, (iii) thin, thermally grown oxide (TGO) primarily of aluminum oxide (dynamically evolving in service), and (iv) top coat or the TBC itself. Each of these sections have distinctly different thermo-physical properties and serve well defined functions; (a) top coat – thermal insulation, (b) TGO – oxidation protection to the underlying super alloy, (c) bond coat – sacrificial oxidation to form TGO and (d) super alloy – structural load bearing component [4, 6, 7].

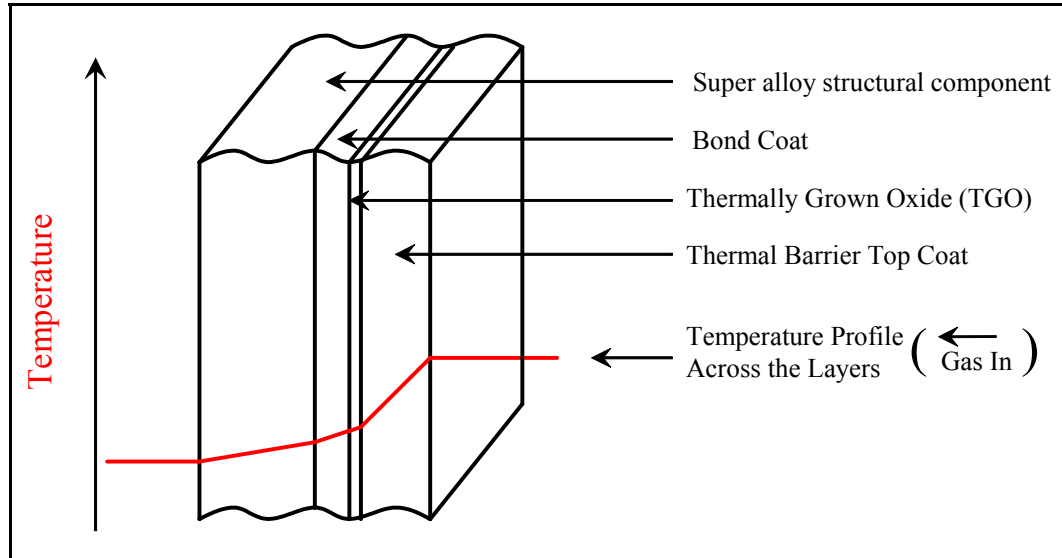


Figure 2: Schematic of a typical (four layer) TBC system. Temperature profile shown across the layers demonstrating the thermal barrier effect of the top coat

The fundamental requirements for TBC materials are (i) high melting point, (ii) low thermal conductivity, (iii) phase and structural stability at the high operational temperatures, (iv) minimal mismatch (thermal and hence strain) between the coating and the underlying structural component, (v) strain tolerance, and (vi) chemical inertness. Different material systems were considered for this purpose including Alumina, Mullite, Titania, Zircon, Lanthanum Zirconate, and Zirconia stabilized with a host of dopants and codopants such as Ytria, Calcia, Lanthana, Ceria-Ytria. Each material system has its own benefits and limitations [1, 8-10].

Due to the high coefficient of thermal expansion, low thermal conductivity and higher thermal shock resistance, 7-8% Ytria partially stabilized Zirconia (YSZ) has been the material of choice for the top coat despite the associated limitations such as transparency to oxygen transport, sintering at elevated temperatures (>1473K) and phase instability (>1443K) [1, 8-11].

YSZ top coats have been predominantly fabricated by Electron Beam Physical Vapor Deposition (EBPVD) and Air Plasma Spray (APS) though other techniques such as D-gun, solution precursor plasma spray (SPPS) and hybrid arc and magnetron sputtering

have been explored with limited success [12-17]. The EB-PVD based system has been found to be attractive system for smaller hot section components such as those used in aero engines while plasma spray has been the method of application for larger components. Plasma sprayed TBC is considered in this study.

1.2 Plasma Spray Processing of YSZ

Plasma sprayed Yttria Stabilized Zirconia (YSZ) coatings are among the most widely used materials in aerospace and power generation gas turbines. They have been the workhorse of the industry for some three decades now, but the last decade has seen explosive growth in their utilization both in the propulsion and land based turbine industry. Key attributes for this growth is not only performance but also the ease of applicability and overall benefits in terms of life cycle costs.

The thermo mechanical properties of YSZ guided by their unique microstructure are the key features that make these materials useful in their application as thermal barrier coatings (Figure 3). Notably, the porous, defected, layered microstructure of the plasma sprayed coatings can substantially reduce the already low intrinsic thermal conductivity of YSZ by as much as 60% (Typical thermal conductivities of plasma sprayed YSZ is about 1 W/mK compared to bulk value of 2.5 W/mK) [9]. Furthermore the porosity, cracks and myriad array of interfaces also offer mechanical compliance to this system enabling their thermo-mechanical compatibility during cyclic thermal exposure between room temperature and over 1000°C operating temperature [18-20]. YSZ has a high coefficient of thermal expansion, close to the super alloy structural components. Finally, the YSZ system has also been noted to have superior fracture toughness thermo-chemical compatibility with the underlying bond coats and the dynamically evolving alumina scale at the interface [6, 9, 10, 21-23].

The evolution of the complex microstructure of plasma sprayed coatings is related to a number of processing variables. Despite scientific and technological progress in many fronts, the extraordinary complexity of the process and materials variables has stymied both scientific understanding of the process-structure-property relationships as well as industry/application related attributes such as coating design, property characterization and perhaps most important reliability. This has impeded the full utilization of TBCs into the “prime reliant” domain and continues to operate in the realm of life extension.

The situation is however changing. Driven both by scientific/technological interest and the availability of sophisticated measurement and modeling tools, there has been a sea change in our understanding of processing-microstructure-property triad as well as their performance linkages [24]. Notably, significant progress has been achieved over the last decade in our ability to characterize the plasma spray process, through the availability of a range of non-invasive diagnostic tools to monitor both plume and particles in the spray stream [25-36]. Furthermore, significant progress has been achieved in our ability to characterize the microstructural complexity through use of sophisticated techniques such as small angle x-ray and neutron scattering, high resolution microstructural

characterization and image analysis and image based modeling concepts [37-46]. Finally, quantification of thermal transport in the defected coatings and ability to clarify the unique non-linear thermo-mechanical properties and response has been achieved through recourse to combined experiments and modeling [47-59].

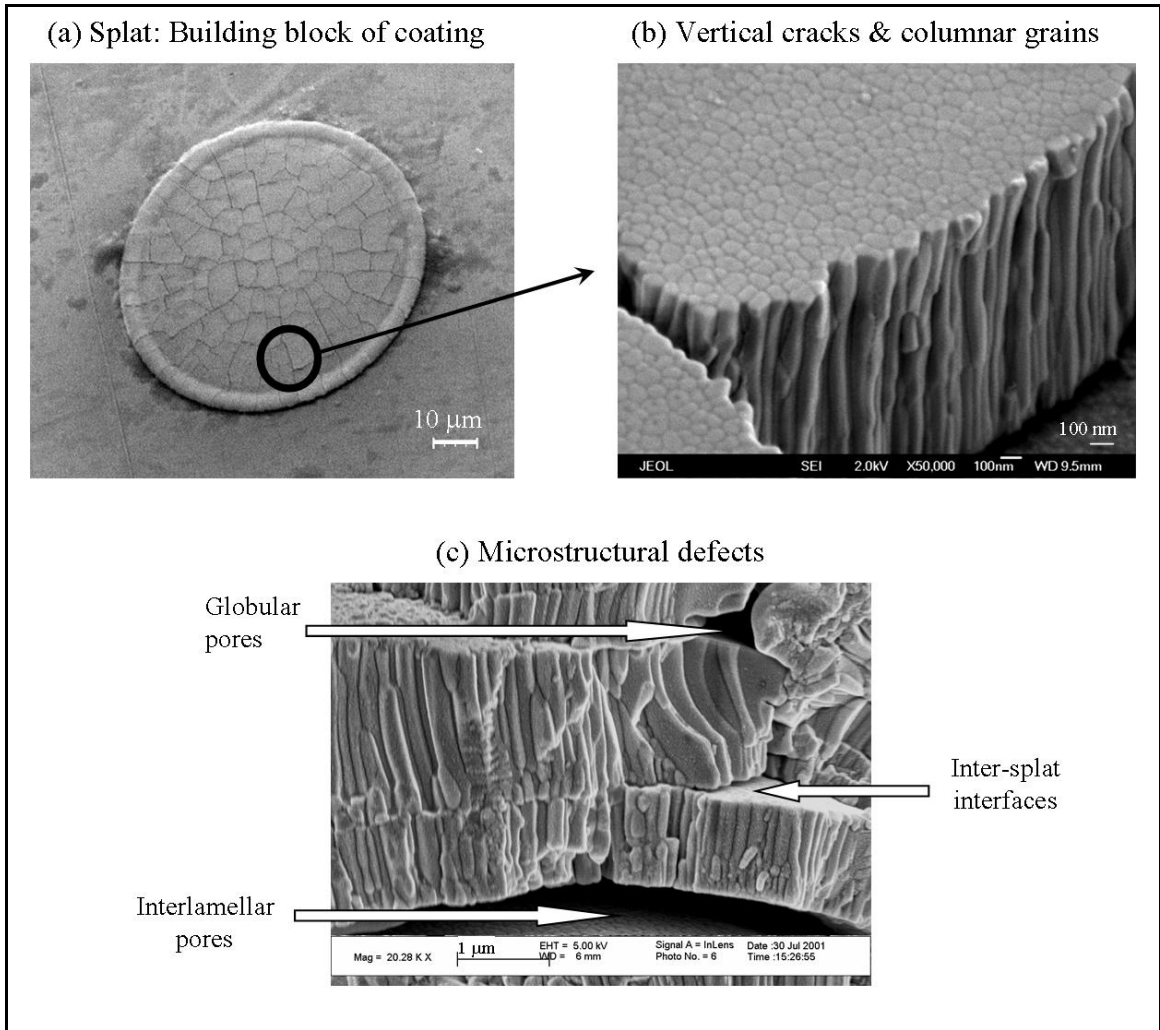


Figure 3: Microstructure along length scales in air plasma sprayed YSZ (micrographs courtesy of Dr. Kulkarni, Stony Brook University) [60]

1.3 Prime Reliance and Coating Design

Currently plasma sprayed TBCs are used as life extension coatings and not as prime reliant coatings. In other words failure of the TBC (top coat) does not constitute a system failure. Prime reliance requires reliable performance and predictable life of the coatings at the operating conditions. Prime reliance calls for fundamental understanding and thorough knowledge of the following [61] (Figure 4)

- Behaviour of the system (multi-layer coating + the component it is applied to) in service and performance
- Coating characteristics and properties
- Process variables, parameters and states

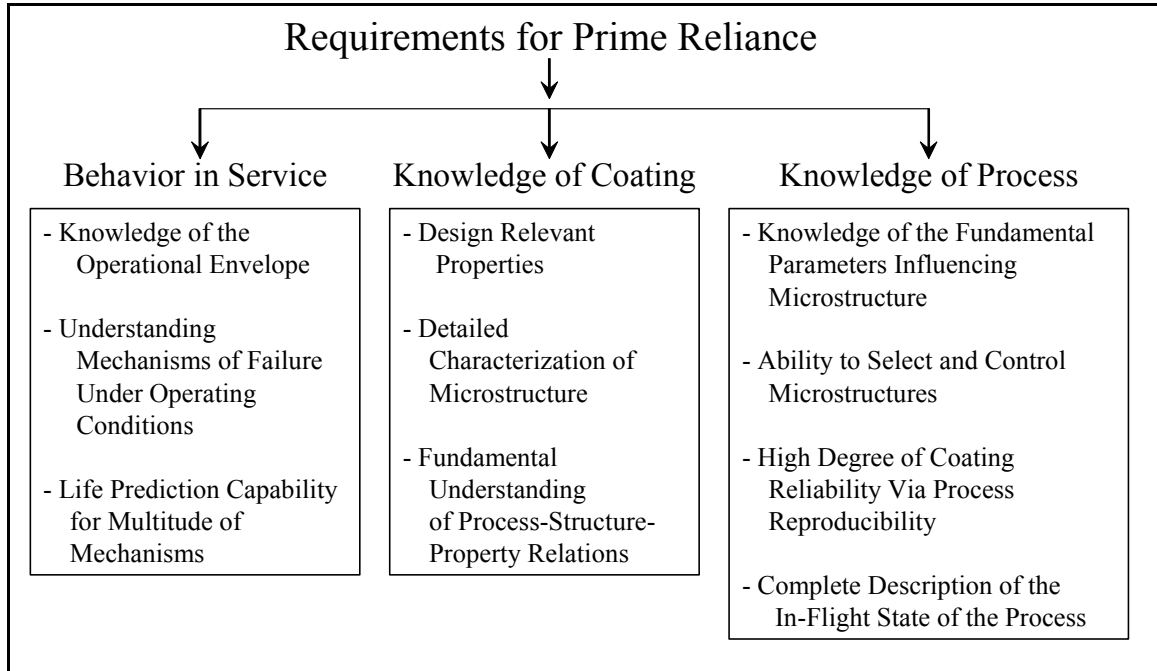


Figure 4: Requirements for prime reliance (Figure adapted from [61])

1.3.1 Knowledge of the Behavior in Service of Plasma Sprayed TBCs

In the recent years, there have been a number of studies on failure of TBCs. Some studies have focused on the TBC system as a whole (top coat-TGO-bond coat-super alloy) taking into account the synergistic effect of these layers, while some others have studied the individual components of the system. Some studies have evaluated the differences in life and performance of the TBC system produced under a wide variety of conditions (top coat: EBPVD Vs APS, bond coat: Pt-Al Vs MCrAlY; super alloy: different compositions) and exposed to different simulated operational environments (furnace Vs flame rig) and operational cycles (isothermal, short cycles and long cycles). Duplex coatings (bond coat + top coat) as well as functionally graded coatings have been studied. [4, 6, 19, 20, 22, 23, 58, 62-86]

Other studies have focused on understanding the fundamentals of failure such as the fracture mechanics and high temperature metallurgy involved [2, 6, 19, 23, 24, 65, 66, 68, 82, 87-91]. Though different materials combinations and processing methods fail different, some of the most prevalent mechanisms of TBC failure summarized by Evans

et al. [6] include formation of spinel between the top coat and TGO or between the TGO and bond coat, imperfections and undulations along the TGO interface and compaction of top coat assisted by foreign object damage [6]. The same is schematically shown in Figure 5. High temperature exposure related dynamic evolution of the TGO appears to be one of the critical elements in the failure of TBCs [6, 19].

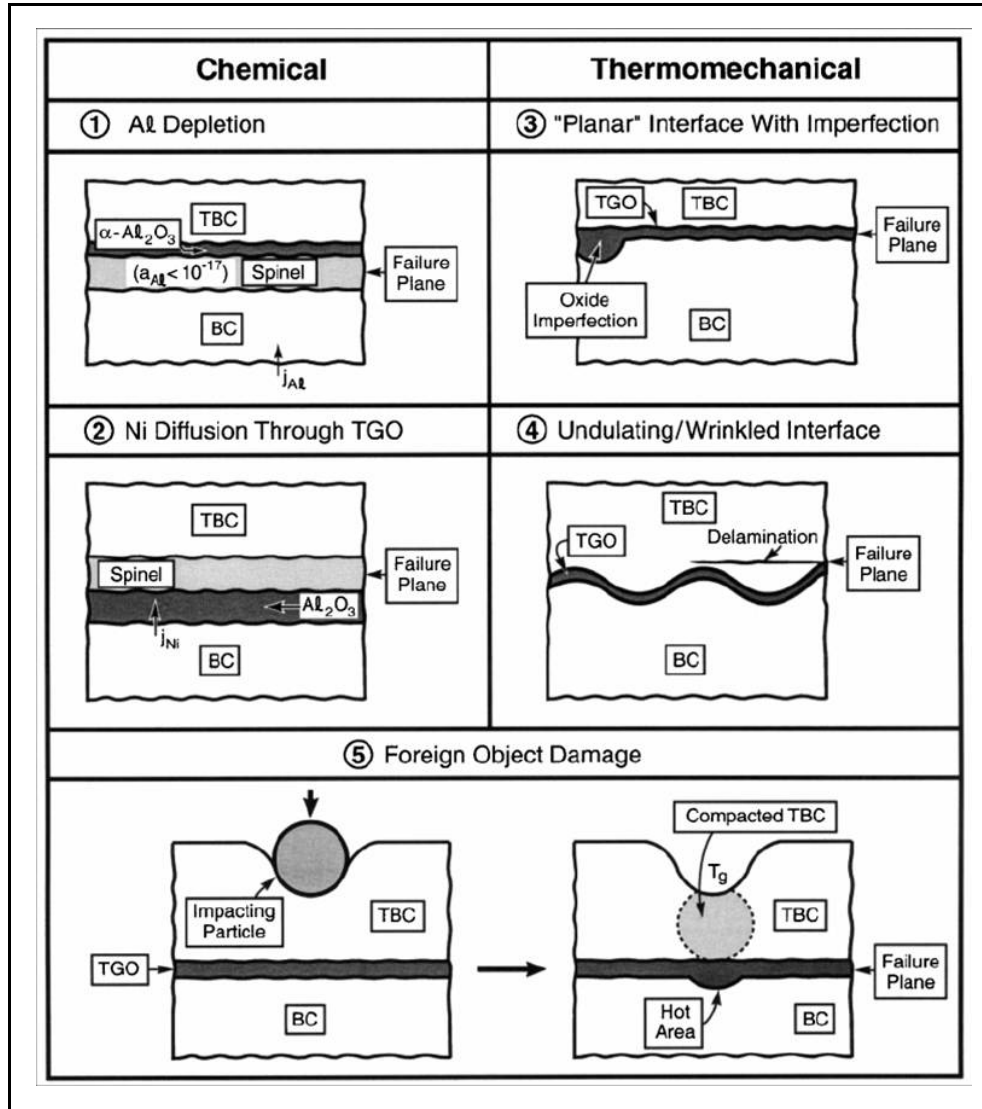


Figure 5: A schematic sketch of some of the prevalent failure mechanisms in TBC systems (figure from Evans et al. [6])

With respect to the TBC top coat, high temperature operating conditions result in two important detrimental aspects – increase in stiffness and thermal conductivity – both primarily due to sintering of coatings. Increased stiffness results in less strain tolerance. The formation of TGO and the resultant volume increase gives rise to stress at the TGO-top coat interface. Though these stresses are relatively small (~ 1 GPa [6]), they cannot be ignored. Further, the temperature excursion of these components results in mismatch

stresses between the predominantly γ -alumina TGO and the MCrAlY bond coat as well as between the TGO and the top coat. These stresses are quite high (~ 3 to 6 GPa [6]) due to the large temperature excursions between the operational cycles. Also with the number of cycles/duration of exposure, the TGO grows in thickness resulting in larger stresses [6, 19].

Increased thermal conductivity of the top coat results in the structural components being exposed to higher temperatures resulting in complex events and phenomenon due to creep, diffusion based dynamic depletion of species in the different layers and phase transformations. These contribute to the propensity for coating failure due to mismatch and stress [6, 19].

The bond coats are typically vacuum heat treated before the deposition of the top coat hence the issues arising from different processing scenarios are neutralized to some extent. The ceramic (YSZ) top coats typically do not undergo any post processing treatment before deployment in service. Hence understanding the top coat is of importance. Along these lines, studies have explored the possibility to alter/improve the top coat microstructure and properties by post processing using laser or the plasma itself [92, 93]. But fundamental understanding of the microstructure and properties of the top coats are essential.

1.3.2 Knowledge of the Coating Microstructure and Properties

Though all the failure mechanisms influencing the life and performance of plasma sprayed thermal barrier coatings have not been understood completely, it is appreciated that the composition, microstructure and properties of these coatings play an important role [6, 23, 24, 68, 70, 72, 94-98]. The chemical composition and microstructure of the top coat are important since they influence the sintering behavior, which in turn influences the evolution of properties in service [77]. Their properties are relevant because they directly influence the survival and performance of the TBC system.

Plasma sprayed YSZ coatings have a complex microstructure. There are primarily two kinds of microstructures, layered lamellar structure and segmented vertical cracked structure. Each has specific types of defect. Coatings with lamellar structure have inter-splat interfaces and inter-lamellar porosity (almost parallel to the plane of the coating). They also have globular porosity, usually interconnected, consisting of nano scale and micro scale pores (few hundred nanometers to few tens of microns). These coatings exhibit crack networks consisting of nano, micro and millimeter scale cracks oriented at different angles, predominantly along the direction of spray. The segmented coating has millimeter scale cracks oriented parallel to the spray direction and micro scale cracks and nano scale to micro scale globular pores. Each plays a significant role in influencing the properties at room temperature, ability to sinter and the high temperature property evolution [39, 40, 44, 45, 60, 99-106].

The defect structure is unique to plasma sprayed TBCs (YSZ) due to the nature of the process involving simultaneous melting, propulsion and deposition of millions of particles/droplets. Each particle spreads upon impact on the substrate to form pancake shaped splats, which are the fundamental building blocks of the coating. These rapid-solidified small-volume structures have been known to have defects ranging from crystalline imperfections to microscopic defects such as cracks. Directional solidification results in preferred orientation of grains with columnar structure, normal to the substrate. Upon solidification, the splat cracks to relieve the quenching stresses, which gives rise to the micro crack network in the microstructure. The interaction of the splat with the substrate or previously deposited splats (coatings) such as wetting, spreading, splashing and fragmentation determines the extent of bonding of splat and the interlamellar porosity, nano/micro pores and the number of interfaces per unit length through thickness. The stochastics of the process along with the splat characteristics results in globular pores of different sizes. Stochastics enabled trapping of unmolten particles can be observed in the microstructure [100, 101, 103, 107-110].

Studies on single splats have gained a lot of interest in the past couple of decades. Morphology of splats has been studied using optical and electron microscopy, scanning white light interferometry and atomic force microscopy. The wetting, spreading and fragmentation characteristics of splats have been studied and group parameters such as the flattening ratio and fragmentation degree have been proposed and validated to describe some of the characteristics. Factors affecting the splat formation and morphology such as the substrate temperature, roughness, adsorbed impurities and in-flight particle characteristics have been studied by many, both experimentally and theoretically. Detailed examination and characterization of the micro and nano scaled features have been made possible by high resolution and focused ion beam assisted electron microscopy. Traditional as well as micro scale x-ray diffraction and neutron diffraction have enabled studies on crystalline structure and residual stress. Crystalline structure and grain growth in splats have been studied. Defects have been characterized and advancements made in the understanding of their nature and source [111-126].

Comprehensive microstructural characterization of these high defect density structures is now possible due to the numerous advancements in this field. Quantitative image analysis of 2D [45] and 3D reconstructed [38] micrographs have been developed and honed. Pycnometry [127] and mercury intrusion porosimetry (MIP) [42] have been used to measure the porosity of coatings. To overcome some of the drawbacks of these techniques, more detailed methods like x-ray computed micro tomography (XCMT) [46], small angle neutron scattering (SANS) and a family of techniques based on scattering have been successfully demonstrated and used [40, 43, 128, 129]. Figure 6 outlines the capabilities and limitations of some of these characterization techniques. The various studies on microstructure-property relationships have suggested that the microstructural definition itself is quite complex, with strong anisotropic features such as interlamellar pores and splat interfaces being the key features that drive the observed properties and that porosity alone is not a sufficient descriptor of the microstructure. More information can be found elsewhere [60].

With respect to the properties of coatings, there are a few that are considered design-relevant. From the basic compatibility standpoint, the coefficient of thermal expansion and thermal shock resistance are necessary properties in any material considered for TBCs. From the functional standpoint, low thermal conductivity and good compliance and strain tolerance are preferred [1, 8]. Knowledge of basic mechanical properties such as yield strength and fracture toughness is important.

It is known that plasma sprayed YSZ coatings are anisotropic with two directions of significance – through thickness and in-plane – with respect to the coating [44]. Measurement/assessment of the design relevant properties of these high defect density systems is difficult, especially along both the anisotropic directions. Of the many techniques that exist to assess the aforementioned properties, a few are being used widely for their significance, ease and in-situ capabilities. Thermal conductivity of these coatings are typically measured based on flash techniques using either a laser or xenon flash source [53]. This can be measured in both orientations of the coating. In-situ high temperature measurements are now possible [53, 130-134].

Traditional techniques		
Technique	Benefits	Limitations
Image analysis	<ul style="list-style-type: none"> • Selective detection of features • Quantification of morphological aspects • Quantitative determination of feature size 	<ul style="list-style-type: none"> • Measures two-dimensional quantities • No compositional information obtained • Poor contrast images give rise to errors
Helium pycnometry	<ul style="list-style-type: none"> • Measures total porosity • Fast and reliable 	<ul style="list-style-type: none"> • Cannot distinguish between open and closed porosity • No pore size distribution information
Mercury intrusion porosimetry	<ul style="list-style-type: none"> • 3nm – 360μm • Measures surface connected porosity • Variety of porosity parameters obtained 	<ul style="list-style-type: none"> • Blind to closed porosity

Advanced characterization techniques		
Technique	Benefits	Limitations
SANS	<ul style="list-style-type: none"> • Nanometer resolution • Independent of pore morphology 	<ul style="list-style-type: none"> • Model based results • Extensive data analysis • Neutron source
CMT, USAXS, HE SAXS	<ul style="list-style-type: none"> • Pore shape, orientation, position and size distribution 	<ul style="list-style-type: none"> • Limited camera resolution • Expensive setup • Synchrotron x-ray source

Figure 6: Capability, benefits and limitations of some commonly used and some advanced microstructural characterization techniques (courtesy of Dr. Kulkarni, Stony Brook University)

Characterizing the mechanical behavior of coatings has come a long way from pull tests to classify the adhesion strength to determining the through thickness and in-plane elastic modulus using instrumented indentation [135-138]. Typically these indentation-

based techniques use load-depth relation to assess the elastic modulus based on Oliver-Pharr method [136]. For ceramics, the sampling depth is in microns and spherical indenters are used to minimize damage propagation during testing. Bend tests have been used to extract the elastic modulus (in compression and tension) and residual stress in the coatings [139]. In-situ sample curvature monitoring techniques have been used to obtain the quenching stress, thermal mismatch stress and hence the residual stress as well as elastic modulus of coatings based on theory established by Tsui and Clyne [52, 55, 56, 140]. More recently, a novel in-situ curvature monitoring has been developed at Stony Brook University using non-contact lasers for which hold the promise for potential applications in the spray booth for design relevant property measurements as well as for process control based on in-situ measurements of coating properties. A prototype sensor system based on the concept is now available for applications in spray booth environments. (In-situ coating property sensor ICP-4; Integrated Coating Solutions, Huntington Beach, California) [48, 49]. Theories have been proposed taking into account the non-linear mechanics of plasma sprayed TBCs, and stress-strain profiles have been obtained from curvature-temperature relation using the in-situ curvature technique [57].

In addition to all these room temperature studies, efforts are underway to understand the property evolution in-situ using embedded sensors, at different temperatures in simulated operational environments and otherwise exposing the coatings/components to simulated operational condition followed by periodical testing (at room temperature). Foreign object damage as well as erosion behavior of these coatings are also being studied.

1.3.3 Process Considerations for APS YSZ

It is widely accepted that the life and performance of plasma sprayed TBCs depend primarily on the operational environment, application conditions, choice of materials and the defect structure of the coatings. For a given material and type of application, the performance is influenced by the coating properties, which is in turn influenced primarily by the microstructure of the coatings. The various sub-processes and significant variables that influence the plasma spray process in general are shown in Figure 7.

There are two fundamental requirements when it comes to tailoring performance and life. One is to engineer the coating microstructure and properties to achieve the required performance and the other is to control the process to achieve the engineered microstructure reliably and repeatedly. There is considerable activity around the world to address the above two attributes both from scientific as well as engineering points of view.

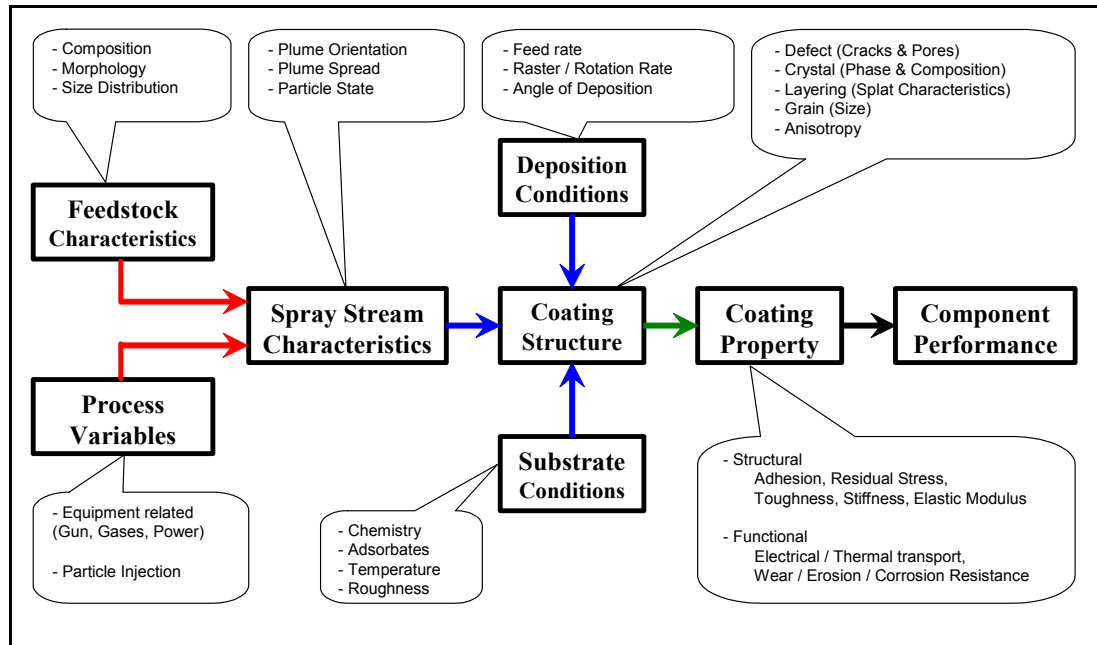


Figure 7: A schematic of the different stages in the plasma spray process. The red color arrows represent a First Order Process Map and the blue color arrows represent a Second Order Process Map

1.3.3.1 Engineering Coating Microstructure and Properties: Understanding the Process

Figure 8 is a schematic for plasma spray processing of TBCs showing the overall process link and the different stages in the process, variable clusters that represent the different stages in the process and the multitude of variables and features that comprises/characterizes the variable cluster. Coating design taking into account all these variables is a demanding task. Hence the most significant variables from these clusters of variables have to be identified and group parameters need to be established to describe the influence of these variables effectively based on scientific understanding of the process. Furthermore, the significant individual variables and group parameters have to be measured/calculated and then systematically altered for successful coating design.

Studies have addressed the different aspects that influence the coating microstructure and properties. Different properties and microstructures, from layered to dense segmented, have been obtained by altering the multitude of process parameters. Correlations have been established different process parameters and the coating microstructure and properties [24, 102, 140-147].

Studies have long suggested the importance of particle temperature and velocity and the need for those two parameters to be controlled [25, 28, 35, 148]. Some studies have suggested the need for the molten content of the spray stream to be controlled along with the temperature and velocity [28]. Numerous studies have assessed the influence of particle state on coating microstructure and properties of YSZ. These past studies have

been limited by the particle state space explored, the extent of control exercised on the process (especially on particle injection) [149-151].

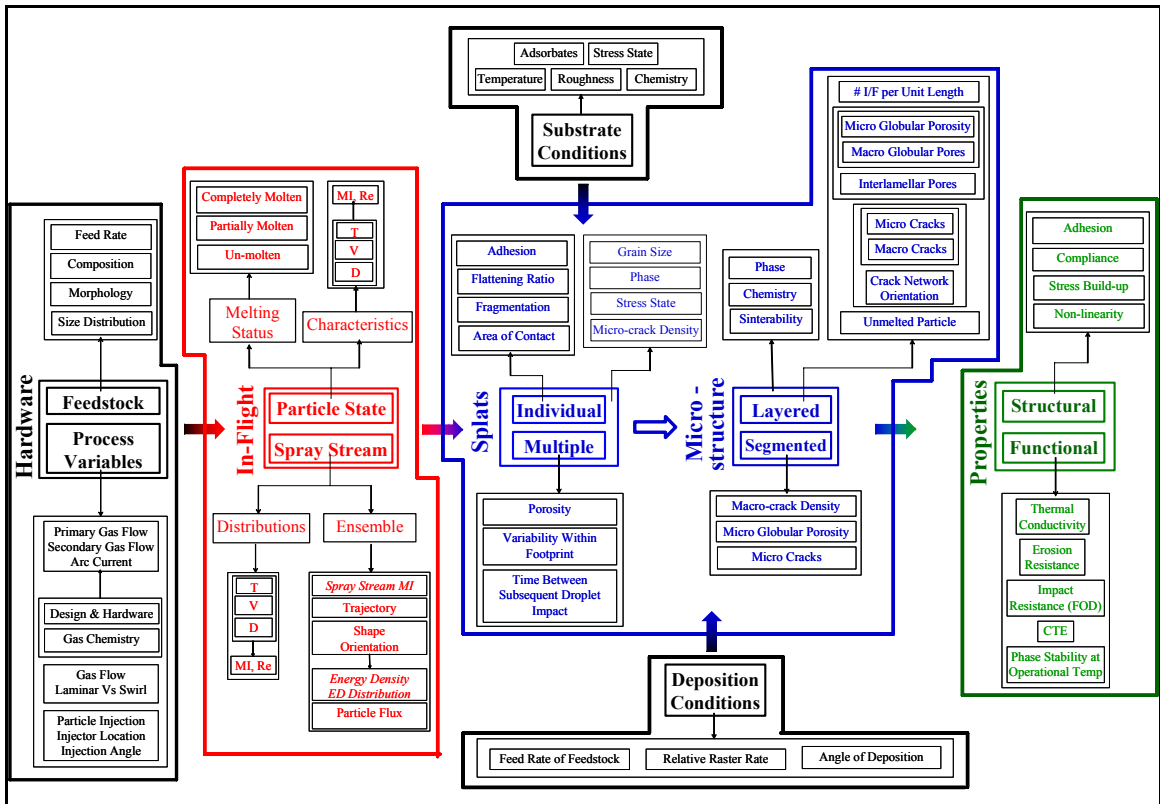


Figure 8: Schematic identifying the different states in the process, the variable clusters and the different variables that influence the processing of TBCs by APS

Figure 9 shows a second order process map where an approach has been suggested for designing process windows based only on microstructural features. Also the process range explored is not comprehensive [143]. In another version of the process map, porosity-property plot has been made for a few different feedstock morphologies under cold and hot substrate conditions and one particle state parameter has been superimposed on the porosity-thermal conductivity space (Figure 10) [146]. It is widely appreciated that porosity alone cannot explain the properties due to the complexities in describing the defect features in the coatings.

These studies have been made possible due to the availability of particle and spray stream sensors. Process sensors found their way into thermal spray actively in the middle of the previous decade. Sensors have been developed that can measure ensemble properties of the spray plume such as the temperature and trajectory [26]. DPV 2000 is an in-flight particle sensor that can isolate the particles based on selection and rejection criteria and measure the temperature, velocity and size of individual particles [32, 152]. Real-time imaging systems to monitor the injection [153, 154] as well as detect irregularities in the spray stream are available [155]. Sensors that can image the shape of

the particles in-flight, which could potentially help understand the melting state of the particles, are available [33]. Others sensors that provide similar details to the ones mentioned above using different measurement principles and/or techniques are available [156, 157].

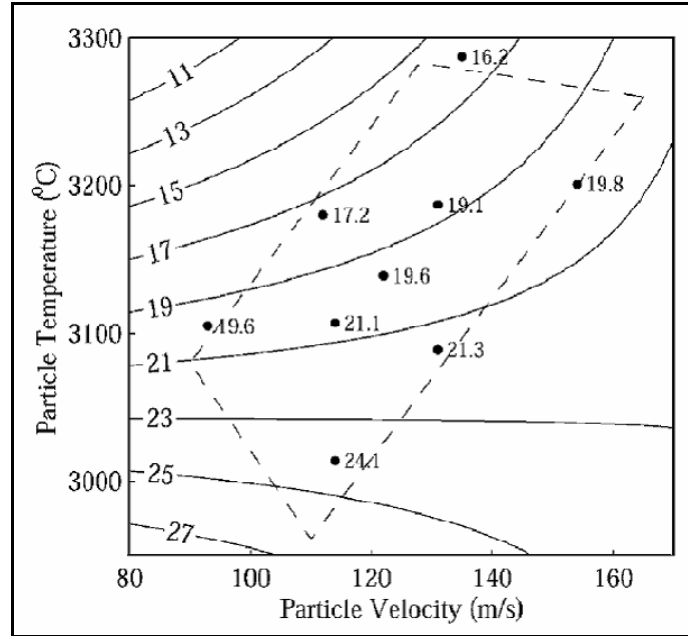


Figure 9: Process maps and identifying process windows based on particle state and porosity of coatings (figure from Dr. Friis [143])

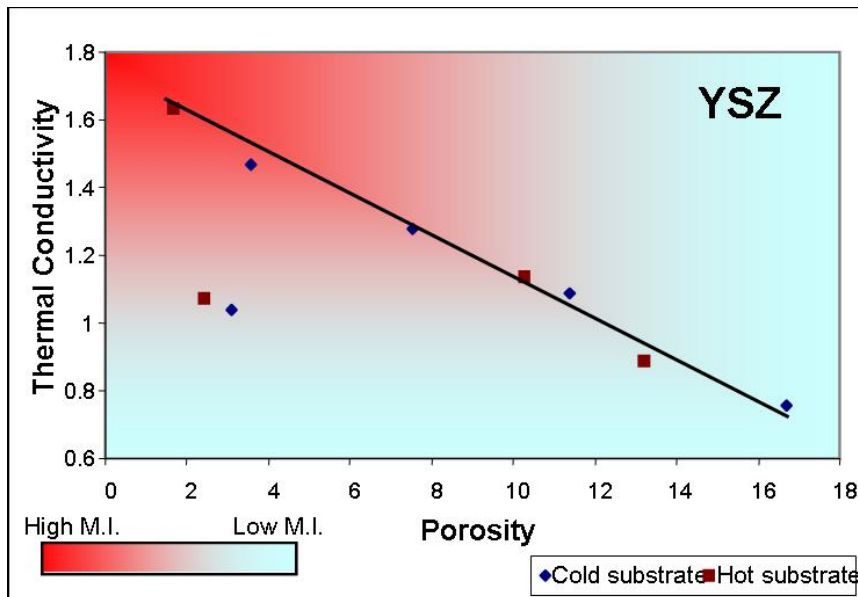


Figure 10: A second order process map identifying trend in microstructure, property and particle state. The two data points not along the trend are from hollow spherical feedstock, indicating the difference in behavior of this morphology (figure courtesy of Dr. Vaidya)

An integrated multi-sensor approach (such as the one at CTSR) can not only enable closer look at the process but also facilitate cross-correlation of sensor data [146, 158] and enhance the understanding of the sensors themselves as well as the process. Thorough understanding of the data from these different sensors combined with fundamental understanding of the process would lead to strategies to control the process using these sensors in real-time or near-real-time.

Numerous past studies have examined the effects of particle states on coating properties, principally based on particle temperature and velocities. These studies have included both ensemble measurements of particles states as well using individual particle measurements. The results clearly suggest that the particles states influence the splat formation dynamics and therefore associated microstructure development notably in the form of deposit porosity and associated properties such as thermal conductivity and elastic modulus [101-103, 111, 116, 119, 121, 122, 131, 134, 141, 142, 147, 151, 159-161]. In order to explain the particle states better to understand the splat and coating formation, group parameters such as Melting Index [147, 161], Reynolds Number and Kinetic Energy have been proposed.

Apart from these studies on the influence of particle state on coating properties there have been numerous studies on the influence other category of variables such as the deposition conditions and substrate conditions. From the deposition conditions, pass rate and feed rate has been varied to achieve dense vertically cracked coatings [140, 144, 162]. Deposition angles have also been studied [163, 164]. The substrate temperature and adsorbate effect has been explored and their influence on splat formation and coating build-up has been studied [111, 114, 165].

For tailoring coatings towards prime reliance the possible range of microstructures and properties needs to be established in an appropriately controlled process (control exercised at every stage in the process) in an integrated manner.

1.3.3.2 Coating Reliability via Process Reliability

Tailoring the microstructure of coatings enables achieving the required properties and performance. Achieving the tailored microstructure time and again on different components ensures predictable performance and life on all components, which is one of the requirements of prime reliance. This is possible by achieving coating reliability by understanding the process as a whole and controlling the significant scientific parameters on all key aspects of the process.

Process reproducibility is affected by the multitude of variables involved in the process. It is appreciated that some variables have profound influence on the reproducibility compared to the others [100]. Process and coating variability are of paramount importance to industry particularly in their efforts towards implementation of prime reliant thermal barrier coatings. In fact the rapid insertion of sensors for plasma

spray is based on the recent requirements in process and microstructural “stability” for YSZ based advanced thermal barrier coatings.

Of all the factors that influence reliability of coating microstructure and properties, deposition conditions (feed rate, pass rate, angle of deposition etc) and the substrate conditions (temperature, roughness etc) are relatively simple to control owing to their non-in-situ nature [100]. Controlling in-flight particle state is complicated since plasma spray process exhibits time dependent behavior at different time scales; Arc attachment-detachment in millisecond scale, powder feeding issues in second time scale, and more importantly the nozzle wear and degradation assisted drift in the process in hour time scale [35, 100, 166-171].

The variability in the in-flight state of the process due to the millisecond and second time scale variations account for the complexities in the coatings and are part of the stochastics of the coating build-up. But the variability or the drift in the process in the hour time scale influences the part-to-part variability and reliability. In a recent work by Leblanc and Moreau [166], this (relatively) long term unsteady nature of the process has been addressed (Figure 11). There appears to be three different stages for the unsteady nature of the process. Similar effects have been predicted by computational work aimed at understanding the behavior of arc dynamics [172-174].

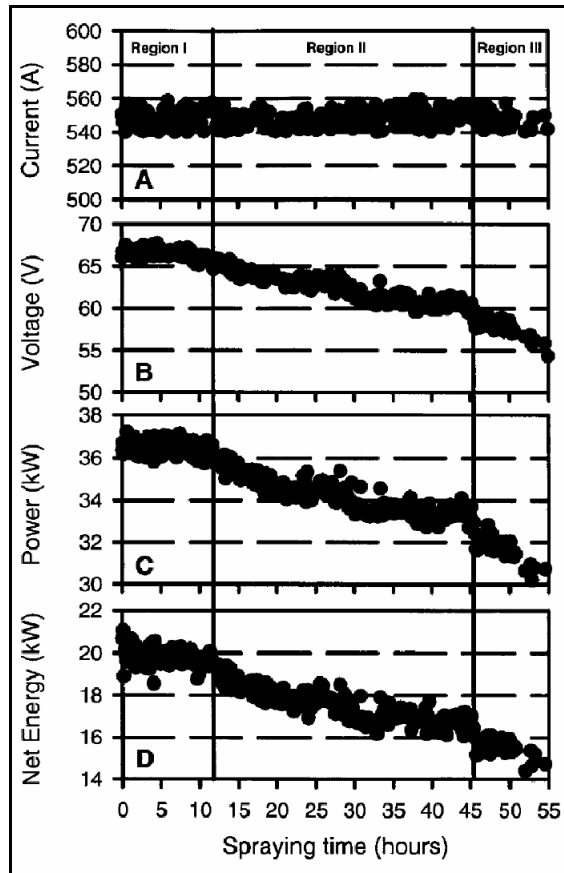


Figure 11: Drift in the process in the hour time scale (figure from Leblanc [166])

Effort has been directed towards identifying the inception of the different regions in the drift of the process, based on various measurable aspects of the process such as the plasma characteristics and arc dynamics and signature voltage behavior [166, 174-176]. Studies have also identified means to compensate for the decrease in voltage and the change in plasma characteristics based on process parameter selection and improved hardware design. Changing hydrogen flow (or volume ratio) to compensate for the degradation appears to influence the process drastically and further hasten the degradation process [177]. Alternately, process control by adjusting the current to compensate for the decreasing voltage was proposed.

As mentioned earlier, (average or ensemble) particle temperature and velocity have been considered for this purpose. Studies have identified methodologies for process control based on a combination of hardware and in-flight particle parameters (Figure 12) [35]. But science-based process monitoring and control has to consider the in-flight state of the process by identifying parameters (either simple or complex group parameters) since it is the in-flight state of the particles at the individual level and as spray stream as a whole that influences the coating characteristics. But recent studies (as will be shown in the subsequent sections of this dissertation) have identified the pitfalls in controlling just the particle state. Newer scientifically relevant in-flight parameters need to be identified for true in-flight process monitoring/control.

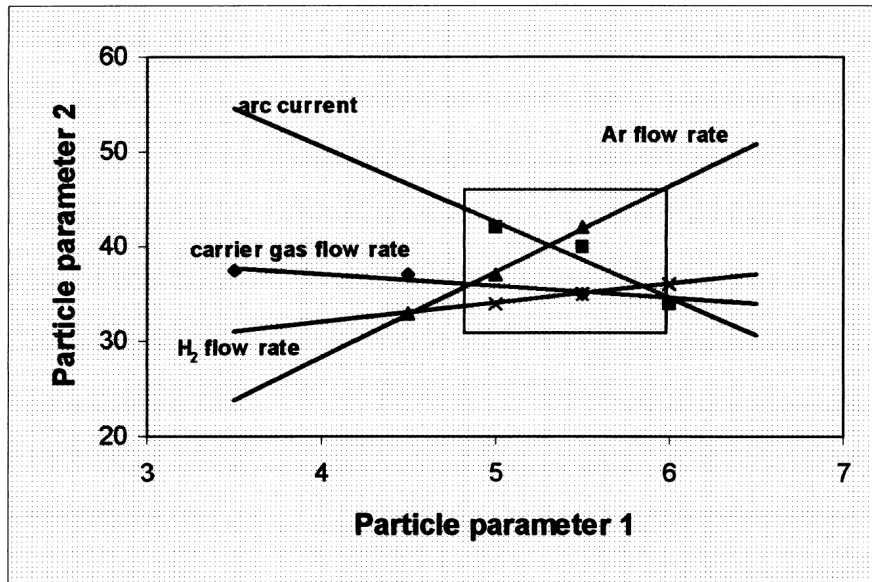


Figure 12: Control strategy based on controlling two in-flight particle properties while limiting the key plasma forming and injection related hardware parameters proposed by Vardelle and Fauchais [35]

Achievement of understanding of the process and its relationship to microstructure development would be incomplete without a detailed analysis of the process variability and measurement sensitivity of the various diagnostics and characterization methods.

1.4 Focus of this Dissertation

This dissertation will seek to develop an integrated understanding of the particle properties and their relation to deposit microstructure and properties. Major advances in process diagnostics and set-up (through a 3D arrangement), enhanced understanding of the role of feedstock injection and the availability of booth level coating property measurement tools (in-situ curvature sensors) have now enabled such an integrated strategy to relate processing related variables to particle spray stream response and therefore ultimately to coating properties. The goal here is to distill the interrelationships among the sub-processes through a carefully controlled experimental strategy.

Chapter II

2 Statement of the Problem

Plasma sprayed thermal barrier coatings are used extensively in advanced propulsion and power generation turbines. Currently these coatings are used as “life extensions” to the underlying super alloy structural components. Increasing performance and efficiency requirements are driving the concept of prime reliance, where the failure of coatings will lead to substantial degradation of the system performance.

Achieving prime reliance in plasma sprayed TBCs is a long term goal, necessitating consideration of the following issues

- Tailoring Coating Compliance and Thermal conductivity: Modify the microstructure and properties of coatings to achieve requisite performance via comprehensive understanding and exploration of the capabilities and limitations of the process
- Coating Dependability Through Process Reliability: Assess and control the variability in the process in order to consistently/reproducibly fabricate the coating microstructure and properties. This would enable achieving performance consistency in service and to minimize the propensity for premature failure (or any significant deviation from the expected performance)
- Failure Mechanisms: Comprehend the multitude of failure mechanisms during actual (or laboratory simulated) service conditions to enable system life prediction. Design relevant and performance affecting properties requires understanding and techniques to measure them needs to be established. This would guide the design of coatings

Pathway to understanding the various processes and sub-processes is considerably complex and requires a concerted, integrated interdisciplinary strategy. Understanding failure mechanisms is a major endeavor and numerous efforts are underway. However, synthesis and optimization of coatings is a critical first step to achieve predictable performance. Progress has been achieved in a number of areas including critical assessment of particle diagnostics, synthesis of process maps, splat and deposit formation dynamics and comprehensive assessment of the microstructure-property relationships. These developments in instrumentation, methodology and characterization have paved the way for a critical integrated assessment of the process-microstructure-property relationships. In light of these developments, opportunity exists to explore the process space systematically by dissecting the sub-processes to reveal its intricacies, and, understanding the interrelation among the various stages towards ultimately understanding coating build-up and property development for YSZ.

In an effort to achieve this overall goal, the following key issues are identified and addressed in this dissertation.

2.1 Radial Injection of Particles into Plasma Jet

The initial hot zone of the plasma represents significant density and temperature gradients. External radial injection of particles into the plasma jet is complex primarily due to the variability in in-flight particle state resulting from trajectory based interaction of particles with the plasma. Various process and material aspects influence particle injection. The plasma condition, injection location, angle of injection, carrier gas flow, powder feed rate are some of the process attributes that influence particle injection. Material density, conductivity, specific heat, particle shape and particle size distribution contribute to the material aspects influencing the injection of particles as well as the resulting particle state. Furthermore size segregation can occur in the spray stream impacted by the carrier gas flow [100, 105, 161, 178, 179].

The combined attributes of materials and process will ultimately determine the plasma-particle interaction and the particle state in-flight, which ultimately influences the spray process and associated deposition. Particle injection has been shown to influence the particle state as much as a large change in plasma-forming torch parameters [146]. Hence controlling particle injection becomes a necessary first step.

Previous studies have used visual diagnostic tools such as the Control Vision to qualitatively understand and identify proper injection [154]. Studies have also identified the existence of an optimum condition for injection based on the total spray stream intensity, which to a first approximation is an indication of the ensemble particle temperature [180]. The existence of this optimum condition has not been established across a wide range of process, injection and feedstock conditions that influence particle injection significantly. The basic criterion for the occurrence of the phenomena has not been completely explained. Whether the same injection condition results in simultaneously maximum heat and momentum transfer to particles remains to be understood. In-flight parameter to consistently identify optimum injection (based on achieving maximum in thermal and kinetic states of particle) that can be measured and controlled real-time has not been established. The influence of controlling injection based on the aforementioned optimum condition on the process downstream has not been studied systematically at every step in the process.

2.2 Torch Parameters – Particle State – Coating Relation

Successful use of materials depends on understanding their process-structure-property relations. It is especially true for YSZ coatings processed by APS, since the processing happens under non-equilibrium conditions resulting in layered high defect density microstructure. There exist primarily two non-equilibrium phenomena; (i) rapid heating and acceleration to melt and propel (respectively) the particles and (ii) rapid quenching of impacting molten particles. Both these phenomena are related to the *in-flight particle*

state, which forms a critical link between the hardware parameters and coating build-up. Hence the sustained interest in understanding the in-flight state of the particle [28, 32, 35, 100-102, 105, 146, 147, 181-184].

Advances in process diagnostics and set-up (through a 3D arrangement), enhanced understanding of the role of particle injection, improved description of particle state and the availability of booth level coating property measurement tools (in-situ curvature sensor) have now enabled an integrated strategy to relate processing related variables to particle spray stream response and therefore ultimately to coating properties. The primary goal here is to distill the interrelationships among the sub-processes through carefully controlled experiments. A few key issues remain to be understood towards this goal.

Studies have shown the insufficiency of particle temperature to describe the thermal component of particle state since it only represents the surface temperature. For low thermal conductivity ceramics such as YSZ, the surface temperature does not provide a complete understanding of the molten status since the core of the particle could be a different temperature and different molten status compared to the surface of the particle [27, 28, 32, 35, 152]. Grouped parameters such as Melting Index and Reynolds Numbers have been proposed to describe the particle state at individual particle level [147, 161]. On the other hand average particle temperature (and velocity) has been shown to influence the coating microstructure and properties with good correlation [25, 35, 143, 149-151, 160, 182, 185]. This raises the question whether average particle temperature and velocity are sufficient to completely describe the spray stream.

Importance of the amount of molten content of the spray stream in influencing the coating build-up and as an in-flight process control parameter is known [28]. So far calculating the molten content of the spray stream has been limited to simulations using models [186]. Calculating molten content of the spray stream from experimental data in near-real-time is yet to be accomplished. Recently, the temperature distributions have been analyzed and features not widely reported have been observed and have been related to melting [158]. This dissertation will seek to expand on this finding for a range of process conditions and feedstock characteristics towards addressing this issue. Based on the understanding of temperature and Melting Index distributions the melting behavior of different morphology feedstock is analyzed.

Numerous past studies have examined the effects of particle states on coating microstructure and properties. The results clearly suggest that the particles states influence the splat formation dynamics and therefore associated microstructure development [110-112, 114-116, 118-121, 125, 143, 149-151, 165, 177, 181, 186-191]. These past studies have been limited by the process space explored, extent of control exercised on the process (especially on particle injection) and the properties measured [143, 149]. To optimize coatings, the range of possible microstructures needs to be explored systematically, key functional and design-relevant properties have to be measured and the interrelations established. This study attempts to address this issue in an integrated manner using 3D arrangement of process sensors concurrently with the in-situ coating property sensor for a wide range of process, feedstock and deposition conditions.

A methodology for identifying process window based on the design relevant properties needs to be explored.

2.3 Coating Reliability via Process Reliability

Understanding the process and its relationship to microstructure development enables optimizing the coating properties for the required performance and life. But due to the unsteady, non-equilibrium and stochastic nature of the process, achieving the set properties repeatedly and reliably is not straight forward [166-169]. Efforts to optimize coating microstructure would be incomplete without a detailed analysis of the process variability and measurement sensitivity of the various diagnostics and characterization methods. Understanding the variability and methodologies to improve coating reliability through process reliability is important to achieve prime reliance. The rapid growth in the process sensor industry is primarily driven by this requirement to achieve process and microstructural “stability” for YSZ based TBCs.

In this regard, the dominant variables at each stage of the process and the associated variability needs to be examined and the implications of such variability understood. Process control methodologies to reduce variability at the different stages in the process to enhance coating reliability require careful consideration. This would necessitate understanding the hardware-particle state relation and their implications. Critical assessment of the in-flight state of the process and the associated 3D variability is a must for feedback based process control. This necessitates a thorough understanding of the implications of particle state variability on variability in microstructure and properties.

It is known that the coating buildup process is complex due to the various phenomena, some under non-equilibrium conditions, occurring in a very short period of time (micro to milli seconds). The particle state, wetting-spreading-flattening of particles/splats and the stochastics of buildup due to the flux of particles all play important roles in the resulting variability in the coating microstructure and properties [32, 35, 44, 71, 99-101, 103, 109, 112, 114, 118, 125, 143, 147, 149, 161, 164, 183, 185, 187, 192, 193]. The variability observed at the in-flight stage needs to be related to the variability in coating microstructure and properties and the source of variability understood in each step.

This dissertation contributes to the aforesaid aspects of plasma sprayed TBCs by

- Understanding and optimizing particle injection
- Developing comprehensive integrated relations between process and particle state (first order map), and particle state and coating microstructure and properties (second order map)
- Understanding the in-flight state of the process at the individual particle level and as a whole (spray stream)
- Systematically evaluating the variability at different stages in the process for different process control methodologies

Chapter III

3 Experimental Techniques

3.1 Process and Equipments

Conventional plasma spray processing can be accomplished using a variety of direct current (DC) torches, each with its own unique set of hardware resulting in innumerable configurations, which has been the key to the versatility and survival of the process. Some of the systems offer high flexibility in terms of swappable hardware, while some others are very robust even with the limited set of hardware. Each configuration has its own process boundaries, usually overlapping with other configurations of the same hardware. Processing of high melting temperature materials like YSZ narrows the operating process space, resulting in the use of a few torches with a limited array of hardware for each.

3.1.1 Plasma Spray System

The following equipments were used in this study

Torches: Sulzer Metco 7MB and Sulzer Metco F4-MB

Plasma Controls: Praxair 5000 and Sulzer Metco A 3000

Plasma Gases: N₂-H₂ and Ar-H₂

Gas Flows: Axial straight (N₂-H₂) and axial swirl (Ar-H₂)

Nozzles: 8mm exit dia, 6mm, 5mm, M2 (7.3 mm) with -5° injection, M2.5 and M3

Injectors: 1.8 mm exit diameter at 0° (radial, orthogonal to spray axis and vertically down into the plasma), +5° (outward) and +20°

Powder Feeders: Miller Thermal 1270 and Plasma Technik Twin-10

Robots: GMC Fanuk S400 and Staubli RX90

3.1.2 Splat Collection

3.1.2.1 Swipe Method

The “swipe method” of splat collection is the simplest and widely used method of splat collection. Usually a variety of substrates, either hot or cold, are mounted on a substrate holder as shown in Figure 13. The robot moves the torch linearly from one end of the substrate holder to the other. Typically robot speed range from 500 mm/s to 750 mm/s. Since only single splats are characterized to assess the flattening ratio,

fragmentation degree and other characteristics, the feed rate was maintained between 2 and 5 g/min allowing the area density of splats to be low.

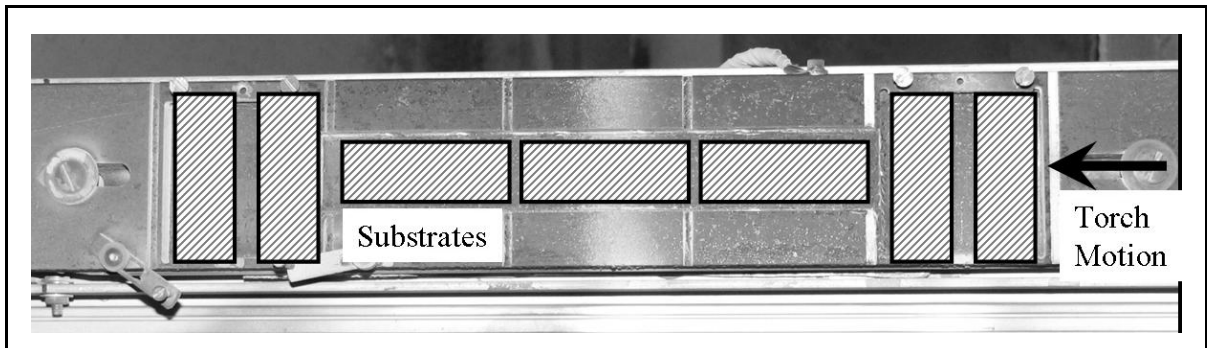


Figure 13: Substrates placed on a heated substrate holder. In the swipe method of sputter collection, the torch passes over the substrates once

3.1.2.2 Snapshot Method

Collecting the snapshot of the entire footprint provides the opportunity to characterize the splats with the approximate region in the plume known. With the aid of in-flight diagnostics data mapping, the splat characteristics could be correlated to the particle state. In order to collect a snapshot of the spray stream, a simple mechanical shutter mechanism was used. A rectangular sheet metal with a square aperture was triggered appropriately and let to fall vertically due to gravity. Figure 14 shows the schematic and Figure 15 shows the actual set up. The sample was held stationary behind the shutter in a heated substrate holder and the torch was parked right in front of the shutter. On triggering the shutter, the aperture exposes the substrate for about 50 ms and again protects it from being exposed to the spray stream.

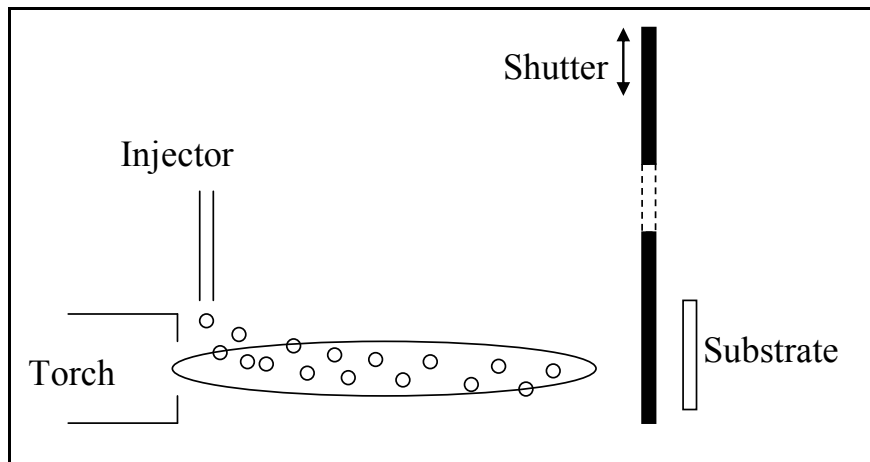


Figure 14: A schematic of the snapshot method of sputter collection

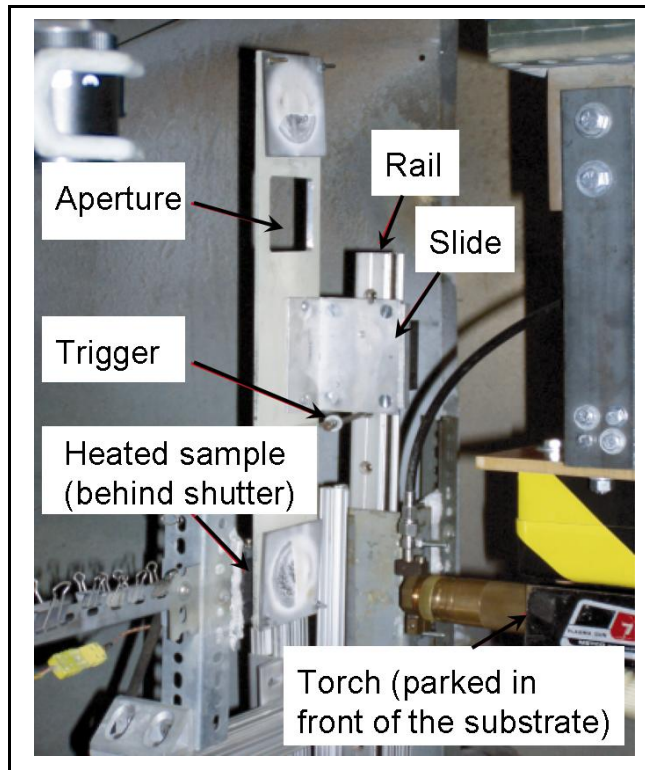


Figure 15: Experimental set up to collect snapshot of spray footprint in the form of splats

3.1.3 Procedure

Though one procedure was not followed for all the experiments, the typical experimental sequence or procedure followed is shown in Figure 16 in the form of a flowchart.

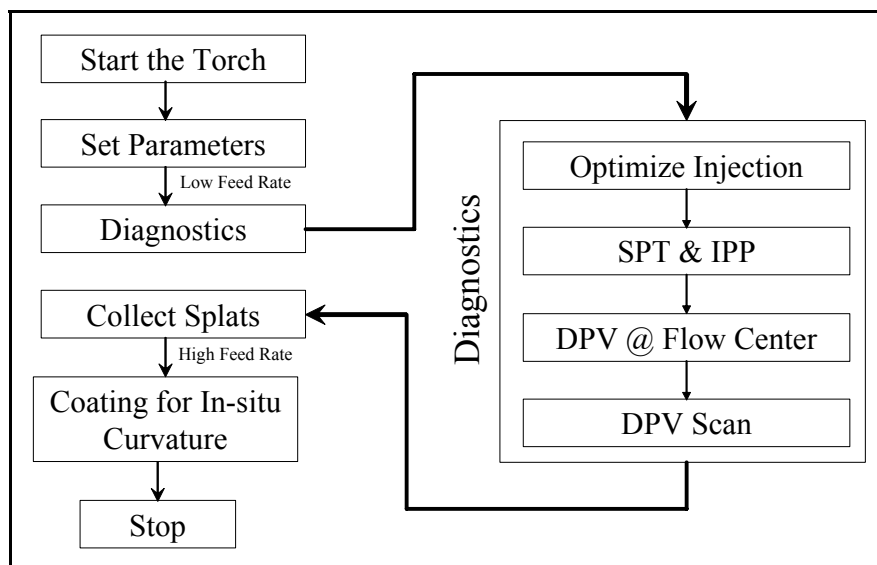


Figure 16: Typical experimental sequence

3.2 Materials

3.2.1 Feedstock

Yttria Stabilized Zirconia (YSZ) was used the most in this study. Other materials such as amorphous alloy, alpha and gamma alumina, titania, NiCr and NiCrAlY were also used to understand the evolution of splat characteristics and phases using splat maps.

3.2.1.1 Yttria Stabilized Zirconia

8% wt $Y_2O_3 - ZrO_2$ was used throughout this study. Carefully selected morphologies and size distributions of YSZ was used in the different studies to understand their role in influencing the particle state and to relate them to the coating structure and properties.

3.2.1.1.1 Different Morphologies

Three different morphology feedstock used in this study are shown in Table 1. All the morphologies mentioned in Table 1 except for the laboratory sample from LERMPS conform to the GE A50TF278 Class B specification for chemistry and size distribution. Their size distributions evaluated using Beckman Coulter LS 13 320 in the dry mode are shown in Figure 17 and Figure 18. One can observe the similarity in the volume distributions (Figure 17) of particles while their number distributions (Figure 18) are different. The laboratory sample from LERMPS is a much coarser feedstock with uniform thin shell with nominal size distribution $d_{10} = 30\mu m$, $d_{50} = 89\mu m$, $d_{90} = 154\mu m$.

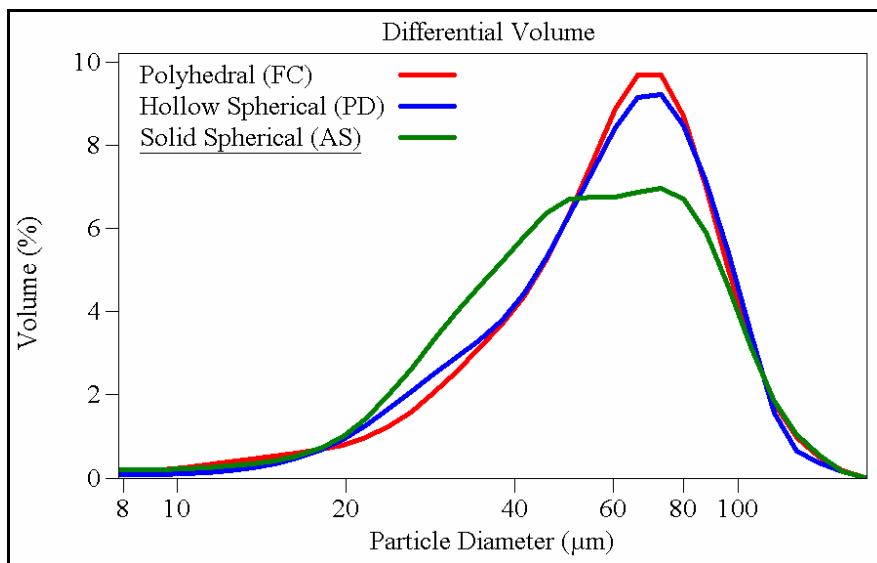
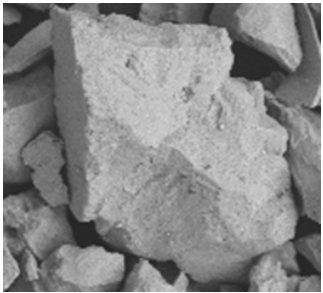
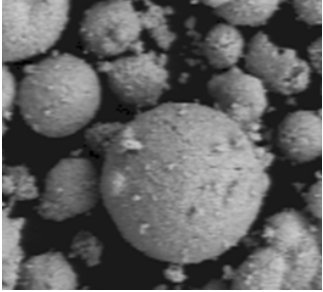
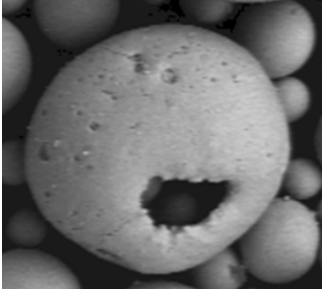
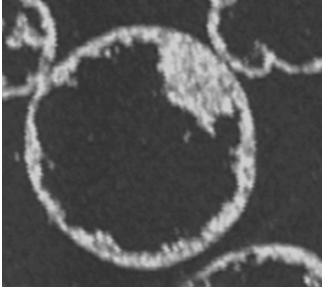


Figure 17: Normalized volume of particles at the different sizes for the different morphology feedstock

Table 1: Different morphology feedstock of YSZ used in this study

Morphology	Manufacturing Method	Manufacturer (Powder #)	Micrographs *
Polyhedral	Fused and Crushed	Saint-Gobain (HW 1532)	
Solid Spherical or Dense Spherical	Agglomerated and Sintered	H.C. Starck (Amperit 832.090)	
Hollow Spherical	Plasma Densified (Non uniform shell thickness)	Saint-Gobain (9204)	
		Sulzer Metco (204 NS)	
	Spray Dried and Sintered (Uniform shell thickness). Cross-section of powder particles mounted in epoxy shown	Laboratory Sample from LERMPS	

* Micrographs courtesy of Dr. Vaidya (first three from the top) and Dr. Bertrand (LERMPS) (bottom)

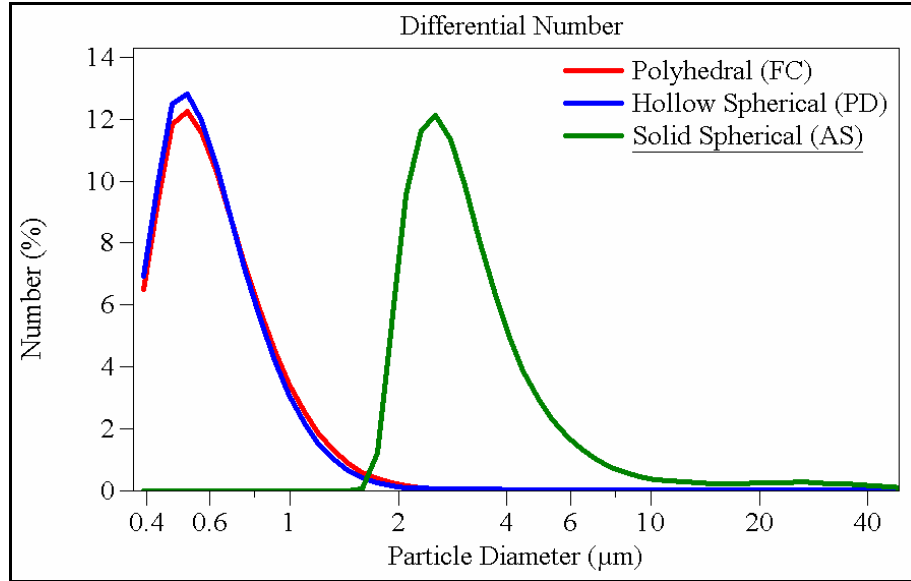


Figure 18: Normalized number of particles at the different sizes for the different morphology feedstock

3.2.1.1.2 Different Size Distributions

The different size distributions of polyhedral YSZ feedstock used in this study are shown in Figure 19 and Figure 20. The three different feedstock used are

- Ensemble: 10 – 75 μm (red color); Saint-Gobain; HW1532
- Fine 10 – 45 μm (blue color); Saint-Gobain; HW1622
- Coarse: 45 – 75 μm (green color); Saint-Gobain; HW1623

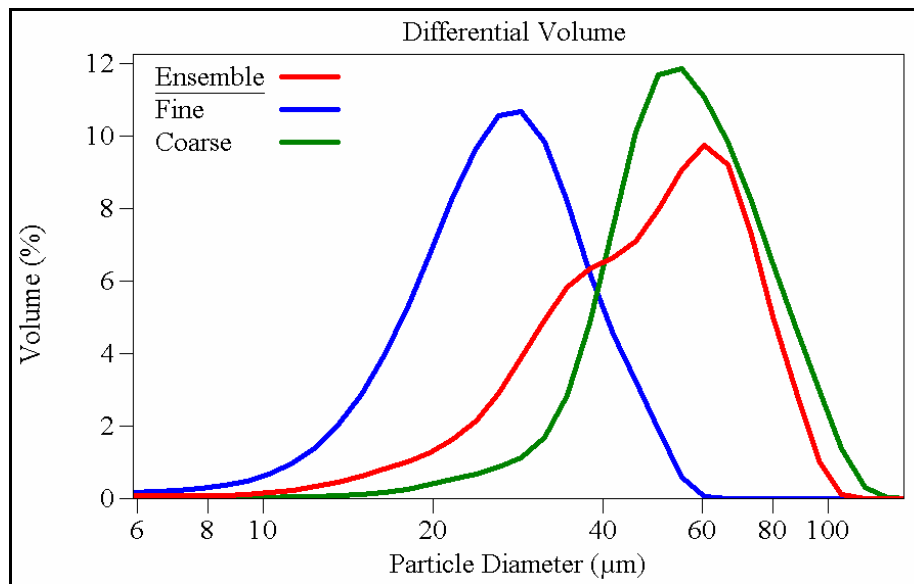


Figure 19: Normalized volume of particles at the different sizes for the different size feedstock

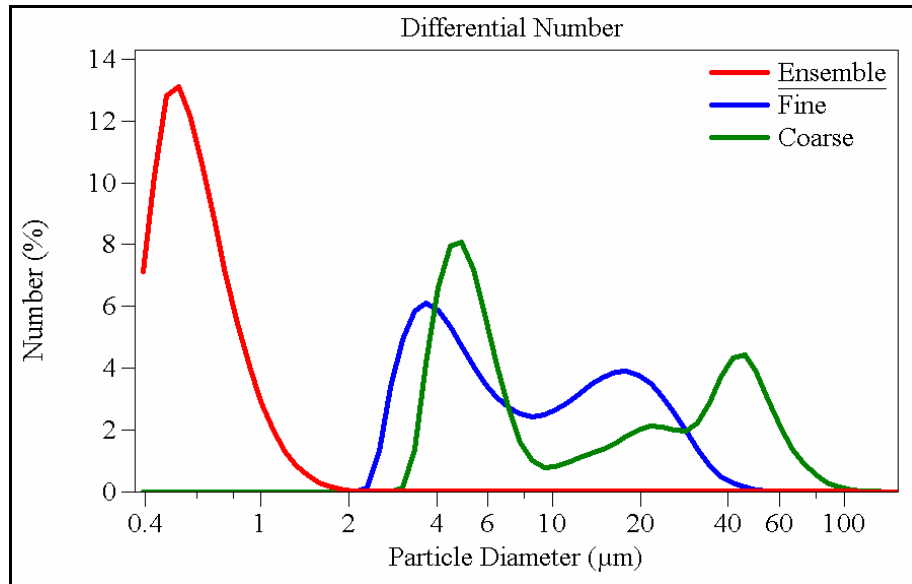


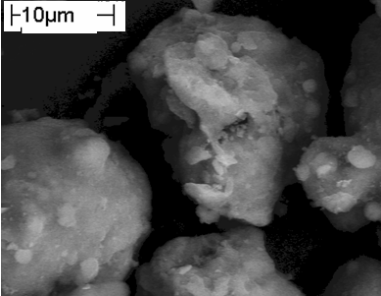
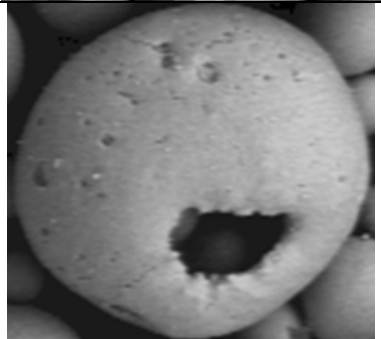
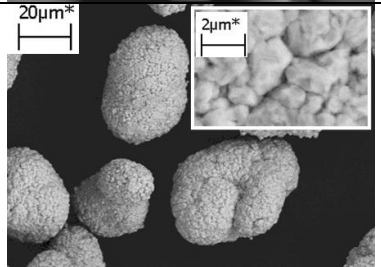
Figure 20: Normalized volume of particles at the different sizes for the different size feedstock

3.2.1.2 Other Materials

In the splat studies using the snapshot of the spray stream, few different feedstock materials were used. Table 2 provides the details.

Table 2: Feedstock used in the splat studies

Material	Powder Details	Size (μ)	Micrographs
Amorphous Alloy NiCrBSiMo	Abracor	20-180	
Alpha Alumina	Vista 340S	20-50	

Material	Powder Details	Size (μ)	Micrographs
Gamma Alumina	Vista 2901	10-70	
YSZ	Near-Mono-sized	63	
Ni	Sulzer Metco 56F-NS	20-60	

3.2.2 Substrates

Substrates were used primarily for collecting splats and for obtaining deposit for further characterization. Splats were usually collected on polished stainless steel and aluminum substrates maintained at about 270°C. In specific cases such as in understanding the 3D variability in the spray stream using splats from the snapshot of the footprint, other polished/smooth substrates such as silicon wafer and glass were used. To obtain deposits on in-situ curvature system (see section 3.3.2.1), aluminum alloy 6061 T6511 beam samples of dimensions 228 mm x 25 mm x 3 mm were used. This is primarily due to the better bonding of YSZ on aluminum and the larger deflections due to larger thermal mismatch (in order to facilitate reliable calculation of elastic modulus from curvature data). The choice of substrate is not critical since only relative comparison is made between the coatings made at different process conditions.

3.3 In-situ Measurements

3.3.1 In-flight Diagnostics

3.3.1.1 Sensors Used

Table 3 provides a brief summary of the sensors used in CTSR, their principle of operation, classification of the sensor based on their measurement type, measurement location and the typical data output.

Table 3: Sensors at CTSR – type, principle of operation, measurement details and typical data output

Sensor	Single Particle / Ensemble	Principle	Where in the plume is the data acquired	Information from data
DPV 2000 [32, 152]	Single particle	Two-wavelength pyrometry (TWP) and time of flight (ToF)	plume flow center @ SD (Single Point)	Distribution and Average of T, V and D
			grid of points across the plume @ SD (Scan)	T, V and D at each point on the scan
SPT	Ensemble	Line intensity imaging	1D section of the plume orthogonal to spray axis @ SD	Intensity profile, centroid (Z) and plume width (W)
IPP [26]	Ensemble	TWP	Cylindrical volume @ SD	Average ensemble T
PFI [155]	Ensemble	Filtered optical still imaging (FSI)	2D imaging orthogonal to spray axis	2D plume images parallel to spray axis and parameters from elliptical fit of the spray stream such as length, width and orientation
CV [154]	Ensemble	Filtered optical motion imaging	2D (motion) imaging orthogonal to the spray axis	Real-time visual monitoring and 2D images for post processing
Accuraspray G3 [156]	Ensemble	TWP and ToF. FSI	Cylindrical volume @ SD. 2D imaging orthogonal to spray	T, V, W, Z, Intensity (flux)
SprayWatch [157]	Ensemble	TWP and ToF; FSI	Cuboidal volume @ SD	T, V, W, Z, Intensity (flux)

3.3.1.1.1 DPV 2000

DPV 2000 (Tecnar Automation Ltd, Quebec, Canada) consists of a sensor head mounted on a Y-Z stage, fiber optic cable and the data acquisition computer (Figure 21). It is a non-contact individual particle measurement sensor capable of measuring up to 4000 particles per second at any point on a limited Y-Z plane that is aligned along the cross-section of the spray stream at the spray distance with its center coinciding with the torch axis. The incandescence of moving particles is detected by the sensor through the double slit mask, which is then processed to obtain the temperature of the particle through two-wavelength pyrometry, velocity by time of flight and size based on calibration from the total intensity, all from particles that qualify as ‘good particles’ (Figure 22). 1D CCD array in between the two slits detects the location of maximum intensity in the plume (called ‘autocenter’ position) following a preprogrammed algorithm involving multiple quick scans in the Y-Z plane.

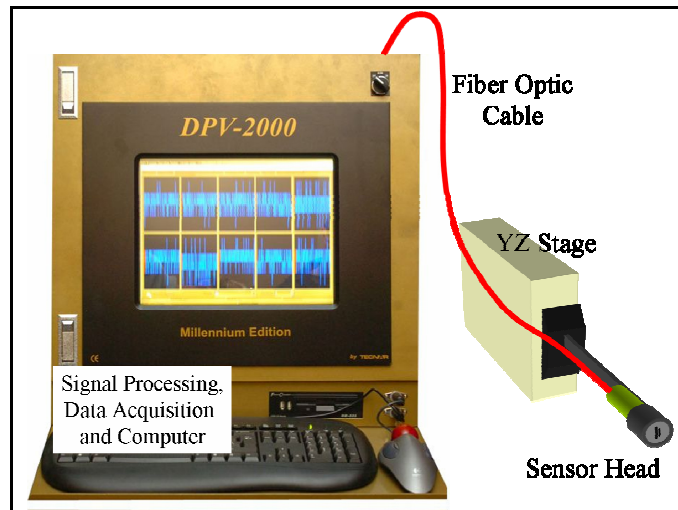


Figure 21: Components of the DPV 2000 sensor

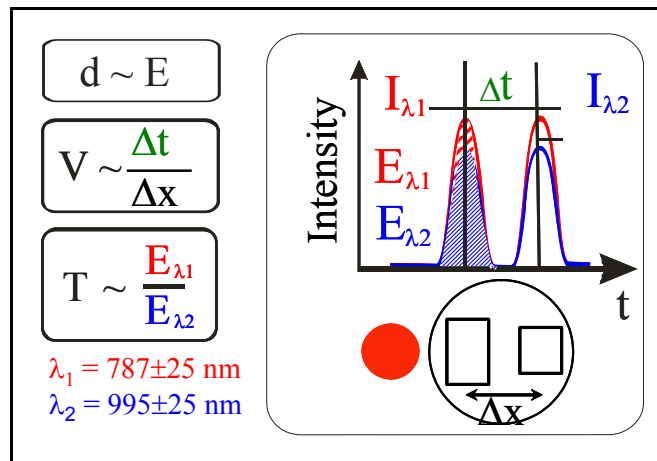


Figure 22: Principle of measurement of DPV 2000

The measurement volume or the volume within which particles are detected is governed by the system optics and the slit mask dimensions. The sensor used in this study is DPV-0016 with an 18 mm lens and P4590170 slit mask. The corresponding measurement volume is shown schematically in Figure 23.

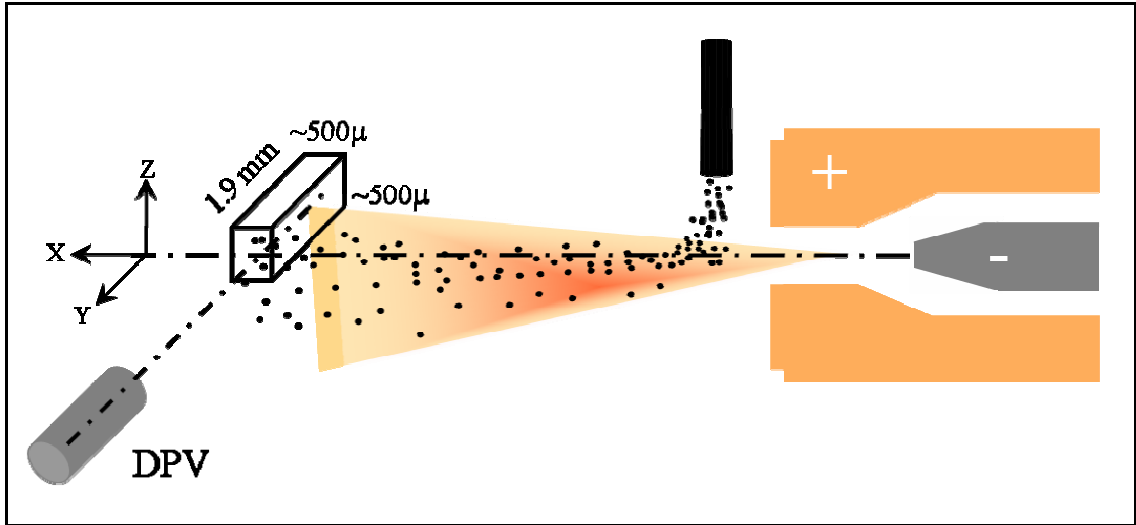


Figure 23: Measurement volume of DPV 2000

Usually two types of measurements are done – *single point measurement* at the ‘autocenter’ and *scan* in the form of a programmable grid superimposed on the limited Y-Z plane (Figure 24). The scan, preferably in the form of a square, can cover as much as 110 mm x 110 mm in the Y-Z plane symmetric to the torch axis. This distance depends on the Y-Z controller available and on the focus of the optics. Typically data is acquired from more than 10,000 particles in single point measurement (to reduce random error and improve statistical reliability) and about 300 particles at each location during scan.

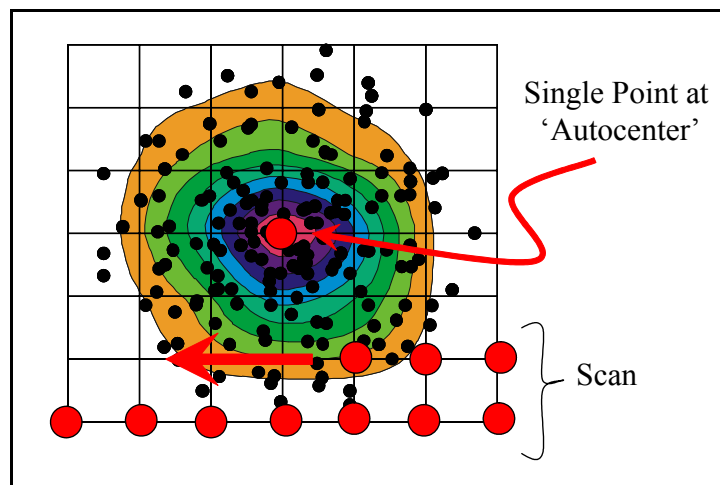


Figure 24: A schematic of the types of measurements made with DPV 2000

The detection resolution of the sensor and the sensitivity measurement depends on the size of the particle, the total intensity emitted by the particle apart from the system trigger level, which governs the delineation of particles from the background noise. The noise could be the digital amplification noise or due to the triggers from particles not within the measurement volume. Figure 25 shows the detection limits of the DPV sensor used in this study. This outlines the limits of detectable particle size and on the measurable particle temperature as a function of the emissivity of the material. Though the principle of measurement of temperature is independent of the emissivity due to the use of two-wavelength pyrometry, the total intensity emitted and measured is a function of the emissivity that is material and temperature dependent. More information on the sensor can be found in references [32, 152].

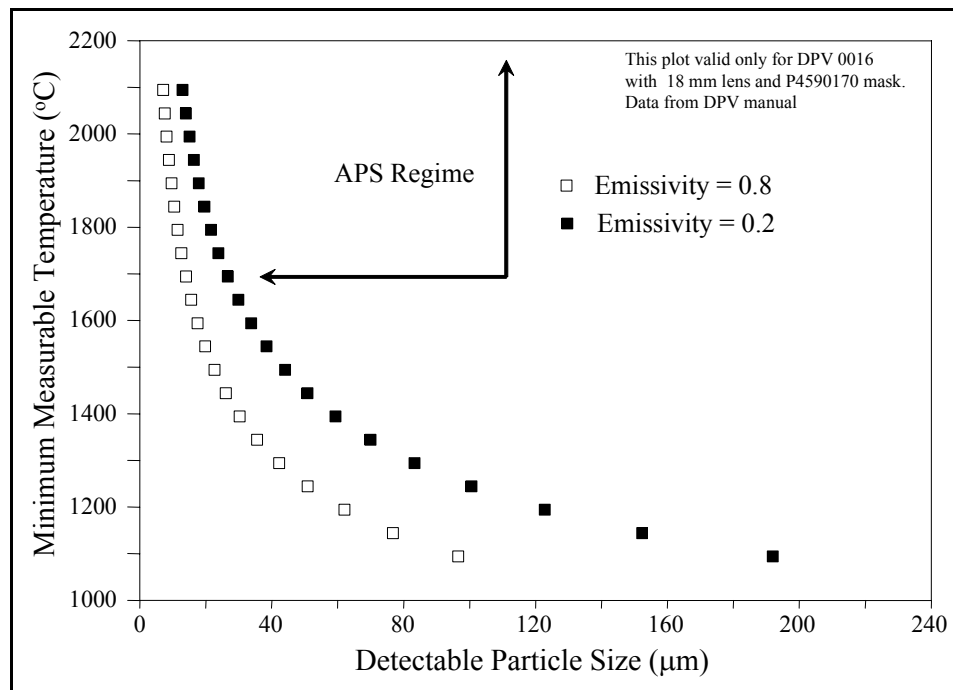


Figure 25: Limits of detection of DPV 2000

3.3.1.1.2 Torch Diagnostic System (TDS)

Torch Diagnostic System (TDS) (Inflight Ltd, Idaho Falls, ID, USA) comprises of Spray Pattern and Trajectory sensor (SPT) and Inflight Particle Pyrometer (IPP-2000). SPT is a 1D CCD camera placed perpendicular to the spray axis at the spray distance that records the intensity signal of the spray stream. This data can be processed to obtain maximum intensity, position of maximum intensity (Z) and plume width (W). IPP fiber optic based sensor which measures the temperature of the spray stream using two-wavelength pyrometry. The measurement volume is in the form of a cylinder of 5 mm diameter and 50 mm height (Figure 26). More information can be found in references [26, 28].

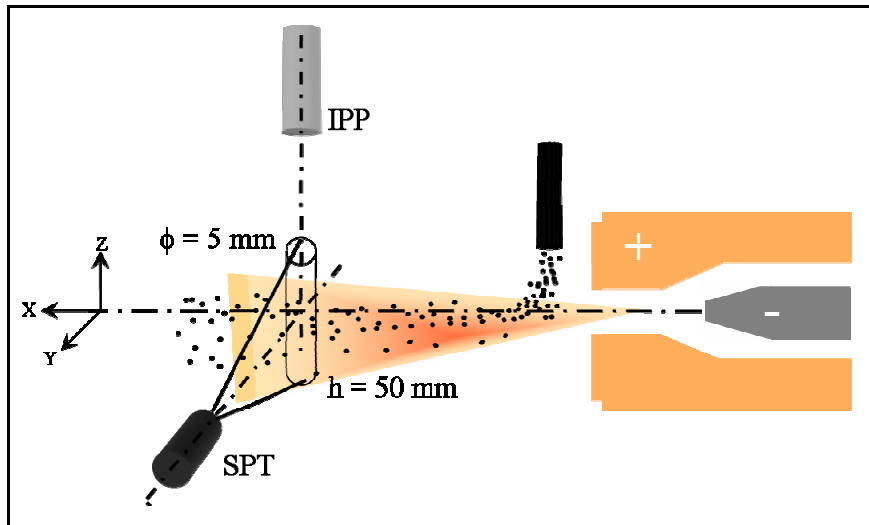


Figure 26: Measurement volume, location of measurement and setup of SPT and IPP

3.3.1.2 Integrated Set-up

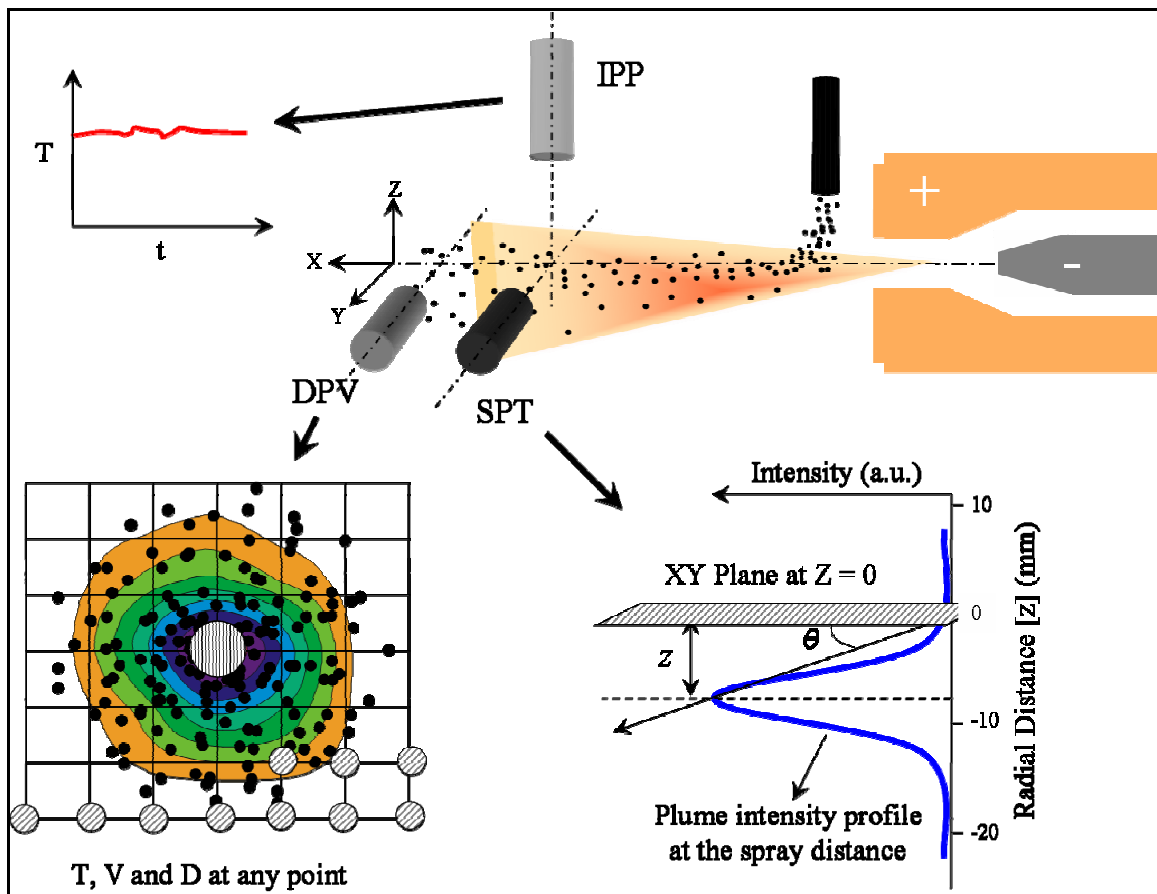


Figure 27: Integrated sensor setup

Figure 27 shows a schematic and Figure 28 the actual integrated sensor setup consisting of DPV 2000, SPT and IPP and the typical data acquired from these sensors. The coordinates of the measurement volume of these sensors should be aligned with reference to the torch that is mounted on the robot. Figure 29 shows the calibration assembly used. It is an iterative process that is repeated until the sensors are aligned such that the robot moves only in one axis (X) from one sensor to the other. So when a measurement is being made at a certain spray distance using DPV, SPT and IPP will be a lower spray distance and data can be recorded at the lower spray distance in addition to the spray distance corresponding to the measurement of DPV (by moving the torch to SPT).

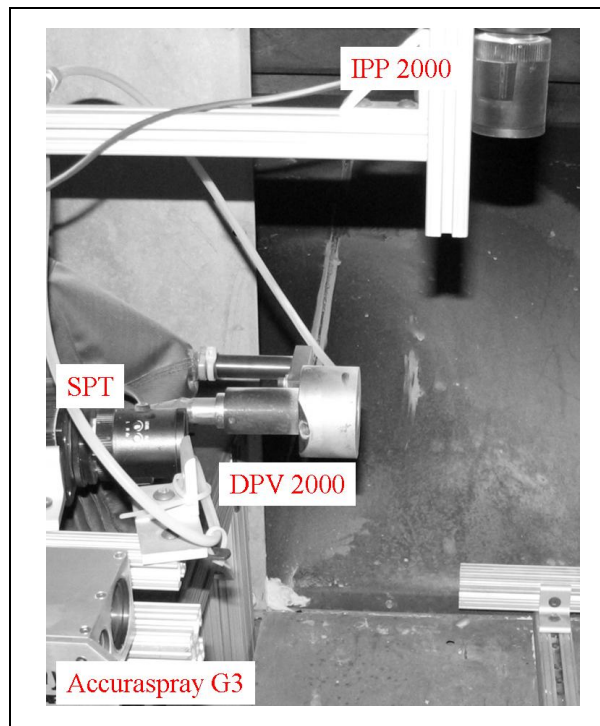


Figure 28: Picture of the actual integrated sensor setup

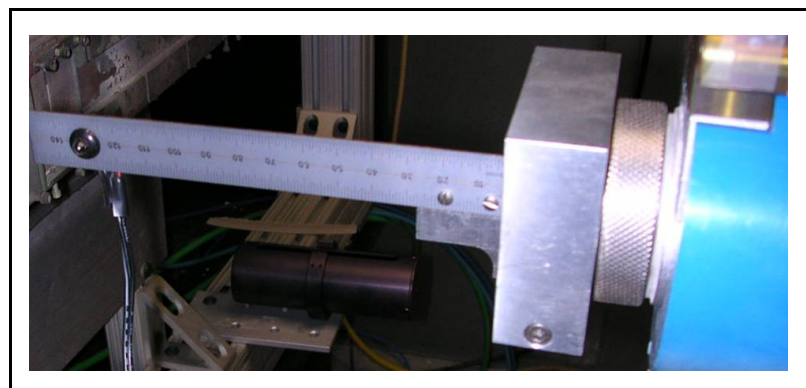


Figure 29: Calibration assembly used for the coordinate calibration of sensors with respect to the torch

3.3.2 In-situ Coating Sensor

3.3.2.1 In-situ Coating Property Sensor (ICP)

In-situ Coating Property sensor (ICP-4) (Integrated Coating Solutions, Huntington Beach, CA), houses three equi-spaced lasers for non-contact measurement of specimen deflection and two thermocouples for contact temperature measurement behind the substrate (Figure 30). The specimen is held in front of sensors on the knife-edge holder assembly using a spring holding mechanism. The knife-edge assembly consists of two contact thermocouples, two stainless steel rods with point contact and two dowel pins at the bottom to hold the sample against gravity (Figure 31).



Figure 30: In-situ coating property sensor (ICP-4) with an aluminum sample mounted



Figure 31: Knife-edge holder. The sample is held using screw-hook system and spring

The specimen is placed in front of the sensor during coating deposition and cooling and data is acquired. Figure 32 shows the front end software used for data acquisition. The specimen is then thermal cycled by a handheld gas torch moving across YSZ coating surface until the temperature reaches ~ 250 °C to 300 °C. After heating, the specimen is allowed to cool down to the room temperature under the forced air convection of the spray booth exhaust. Typically it takes 2 min to heat up and about 7 min to cool down.

Typical data acquired is in the form of distance of the specimen from three laser sensors, temperature from two thermocouples and time. The frequency of data acquisition is 10 Hz. The resolution of the sensor is inversely proportional to the data acquisition frequency; higher the frequency, poorer the resolution (~ 1 μm at 10 Hz and ~ 5 μm at 1 kHz). The distance data is then converted to curvature using 3 data points, typically using one laser in the middle (assuming symmetric curving of sample) and two fixed knife-edge points at the ends as shown in (Figure 33). Figure 34 shows a plot of curvature and temperature as a function of time.

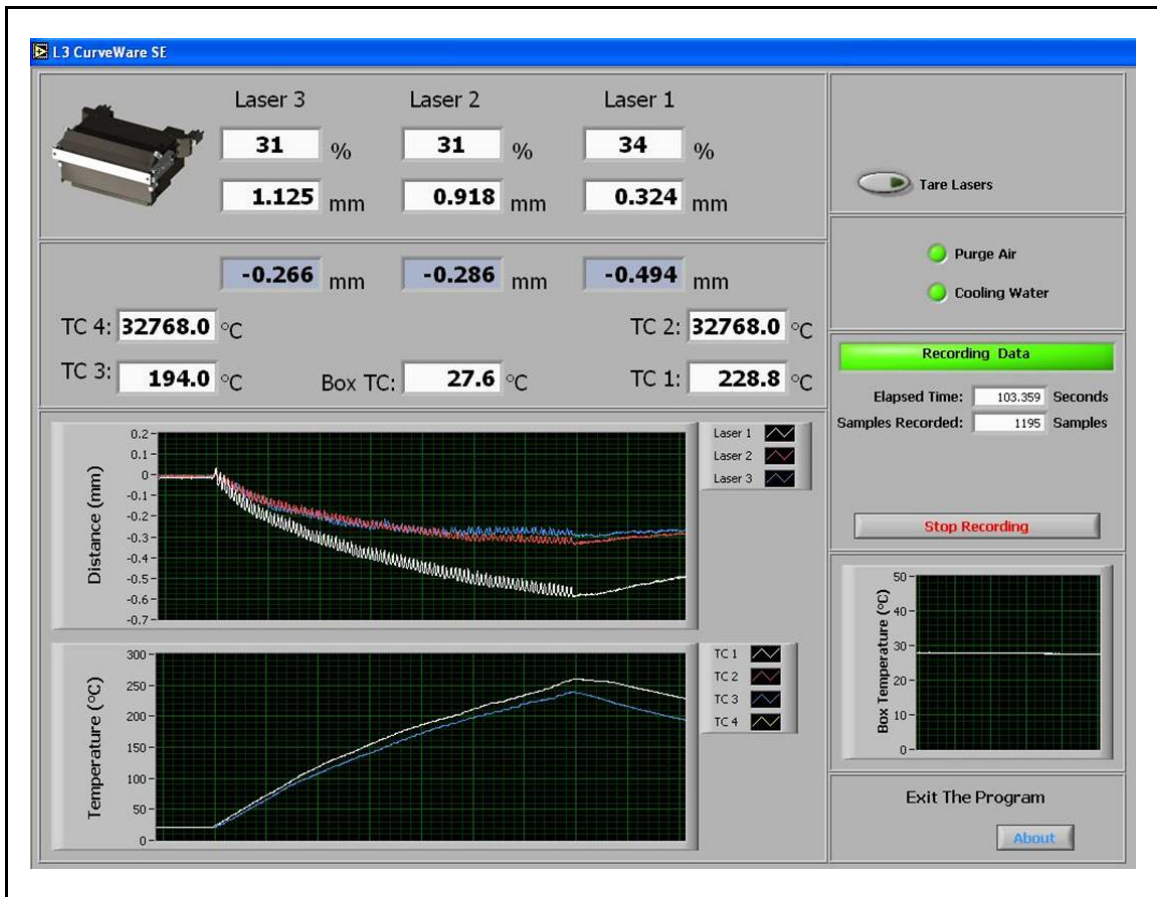


Figure 32: Front-end of curvature data acquisition. The graph inside the figure shows the distance measured by the laser and the temperature measured behind the substrate as a function of time

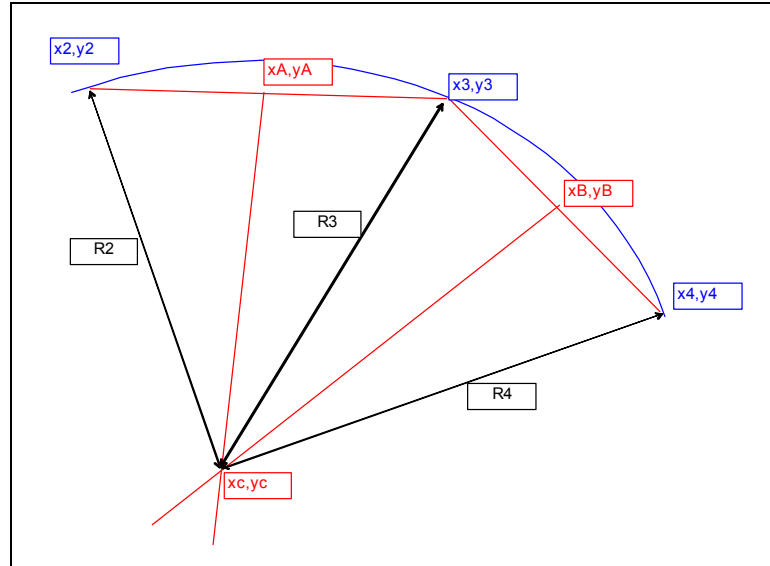


Figure 33: Theory behind the calculation of curvature using three points in space. Figure from [146]

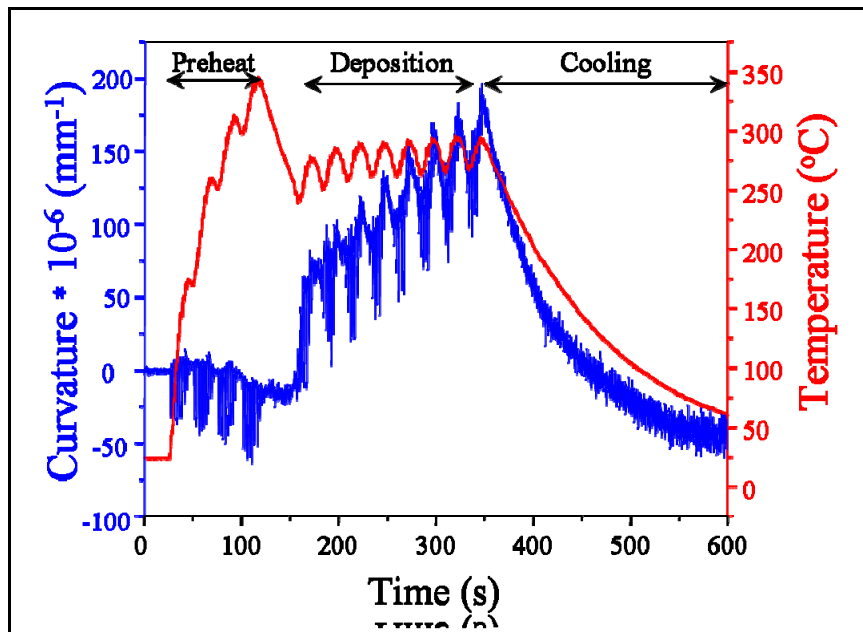


Figure 34: Curvature and temperature as a function of time during preheating, deposition and subsequent cooling to room temperature

There are fluctuations in curvature measurements when the specimen is heated with the hand torch due to the moving hand torch and the kinetic energy of flowing gas (Figure 35). Hence the data from the cooling of the sample is used for calculating in-plane elastic modulus and for further calculation of stress-strain profiles using computation. More information on the sensor and its application can be found in references [48, 49], while the theories used can be found in references [52, 57].

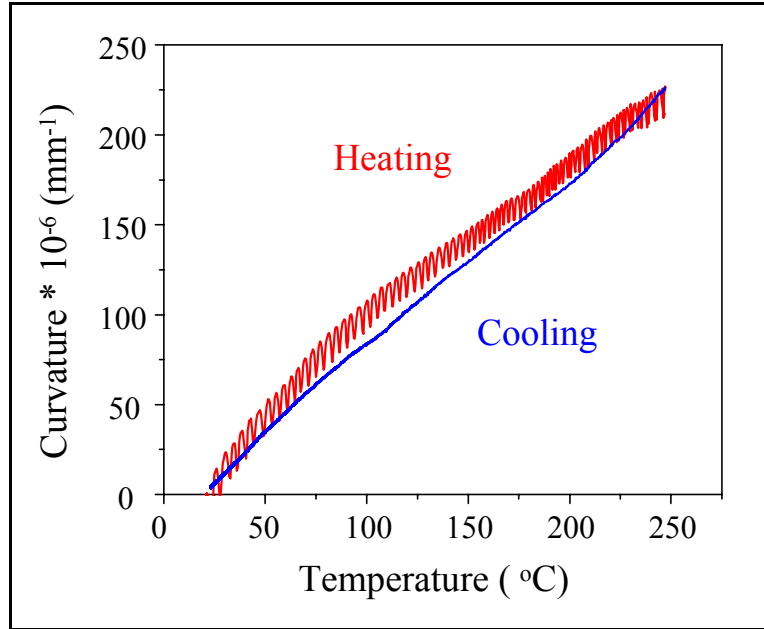


Figure 35: Curvature as a function of temperature during heat cycling (after the deposit has cooled down to room temperature). Heating data is noisy; cooling data is smooth

3.4 Post Processing Analysis

3.4.1 Characterization

3.4.1.1 Splats

The basic observation on splats was using optical microscopy to identify the different morphologies. Further observations were made under scanning white light interferometer from Zygo [194], to obtain the 3D profile of the splats. This data was further analyzed to obtain volume of splats from which the corresponding particle volume and size were calculated assuming no splashing/mass loss. Flattening ratios were calculated from experimental data (Equation 1) as well as using Madejski model (Equation 2) from the particle data from DPV.

$$\text{Flattening Ratio} = D / d$$

Equation 1

Where D is the splat diameter and d is the particle diameter

$$\xi = C \cdot Re^\alpha$$

Equation 2

Where $C = 1.18$, $\alpha = 0.2$ and $Re = \text{Reynolds Number}$. The values of C and α are for oxide ceramic splats [118, 121].

X-ray diffraction was done on a cluster of splats using General Area Detection Diffraction System (GADDS) for the phase content of the splats.

3.4.1.2 Coatings

The coatings were polished and observed under optical microscope. Image analysis was performed on twenty images for each sample based on the work by Friis [143].

3.4.2 Property Measurements

In-plane elastic modulus of coatings was calculated from curvature data from ICP based on the theory by Tsui and Clyne [52] as shown in Equation 3.

$$\Delta K = \frac{6 \cdot E'_c \cdot E'_s \cdot t_c \cdot t_s \cdot (t_s + t_c) \cdot \Delta T \cdot \Delta \alpha}{(E'_c)^2 \cdot t_c^4 + (4 \cdot E'_c \cdot E'_s \cdot t_c^3 \cdot t_s) + (6 \cdot E'_c \cdot E'_s \cdot t_c^2 \cdot t_s^2) + (4 \cdot E'_c \cdot E'_s \cdot t_c \cdot t_s^3) + (E'_s)^2 \cdot t_s^4}$$

Equation 3

Where ΔK is the difference in curvature, 'c' represents coating, 's' represents substrate, E' is the effective bi-axial modulus, ΔT is the different in temperature and $\Delta \alpha$ is the difference in coefficient of thermal expansion between the substrate and the coating.

Modulus in the through thickness direction was estimated using the Oliver-Pharr method [135, 136] from the load-depth relation obtained from Nanotest 600 (Micro Materials Ltd, Wrexham, UK) instrumented indentation. Spherical indenter with radius of 1/16" was used in most of the studies, while Berkovich indenter was also used in few studies.

Thermal conductivity was measured on free standing coatings using Holometrix laser flash thermal diffusivity instrument [53, 131].

3.4.3 Analysis

3.4.3.1 Temperature Distributions

The temperature distributions were observed to be multi-modal [158]. In order to understand the distributions, they were fitted with Gaussian profiles to represent the sub-distributions. Initially the overall distribution was fitted using three Gauss profiles using the least square fit method. One sub-distribution was observed to be occurring at about the same temperature. This was identified as the melting peak [158]. The temperature distributions from a variety of process conditions explored using the first order process

map were analyzed. The temperature at which the melting peak was observed (based on least square fit) was then averaged. This is used as the melting point (as observed from the analysis of DPV data) throughout the study. Subsequently, the distributions were again fitted with three Gauss profiles with one profile fixed at the melting point. The other temperatures at which the peak occurs in the remaining two sub-distributions were spaced out at least by 50 °C from the melting point since the average width of the melting peak at close to zero particle count was observed to be ± 50 °C.

Chapter IV

4 External Radial Injection of Particles: Salient Observations and Optimization Strategies

4.1 Introduction

Injection of powder particles into a DC plasma spray process is typically achieved through an injector orthogonal to the emanating plasma jet, usually top-down. Carrier gas carries the finely divided feedstock particles of the material of interest. Figure 36 illustrates this geometry through laser strobe imaging. The injection can be either internal within the nozzle or external to the torch (the latter being more popular in industry given its simplicity of operation) [100]. Injection angles as well as the distance of the injector tip from spray axis can be manipulated. Although significant experience base and applications have existed for this method, very limited scientific investigations have been conducted. The past limitations are associated with the lack of diagnostic and visualization tools, which has changed significantly in recent years.

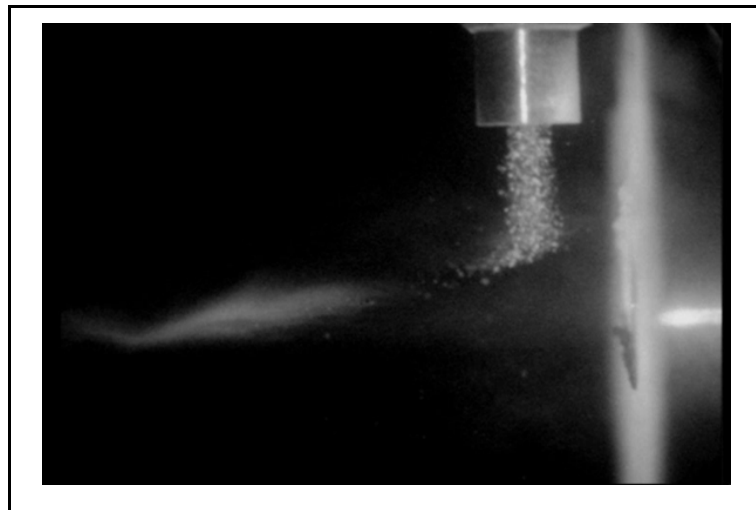


Figure 36: Laser Strobe Control Vision™ image of orthogonal external injection of particles into a DC thermal plasma jet

Ideal injection of particles would be axially through the torch. Novel variants in torch designs such as the three cathode design (Northwest Mettech Corp., North Vancouver, Canada), electromagnetically coalesced plasma using three cathodes (Flame Spray

Industries, Port Washington, NY) and stick type cathode with modifications (100 HE; Progressive Technologies Inc, Grand Rapids, MI) [195] have allowed for axial injection with some success. However, there are several design constraints and disadvantages that have prevented widespread implementation of this axial injection strategy. They include (a) arc instabilities introduced by the presence of solid particles within the plasma forming zone, (b) powder build-up and clogging of the nozzles during the spray, and (c) complexities in nozzle design and hardware assembly.

Radial injection into the plasma jet is dependent of various process and material characteristics. In the case of process, the plasma condition, the injector location, angle of injection, carrier gas flow, powder feed rate all influence the injection. Material density, conductivity, specific heat, particle shape and particle size distribution contribute to the material aspects influencing injection. Furthermore size segregation can occur in the spray stream impacted by the carrier gas flow. The combined attributes of materials and process will ultimately determine the plasma-particle interaction and the particle state in-flight.

During radial injection since the particles do not necessarily follow an axial flow path, the interaction of the trajectory with plasma jet becomes important. For a given material and feedstock attribute it is anticipated that an optimum exists for each torch design and parameter space. This study seeks to identify such a phenomenon for Yttria Stabilized Zirconia (YSZ) powder. Specifically, we seek to understand the role of radial injection on dynamics of plasma jet-particle interaction and the effectiveness of heat and momentum transfer to the particle within the plasma jet. Through this study we aim to address the carrier gas-particle-plasma interactions and offer a new approach for optimizing particle injection and achieving reproducible particle state.

4.2 Experimental Methods

4.2.1 Materials and Process

Particle injection was studied for the case of external injection into DC plasma generated by 7MB APS torch with an 8mm nozzle (Sulzer Metco). Key material of interest for this study is high melting low thermal conductivity Yttria Stabilized Zirconia (YSZ). Different morphologies of YSZ namely Polyhedral (FC), Solid Spherical (AS) and Hollow Spherical (PD) were investigated in this study (for more information on the morphologies refer [193]). Role of different plasma forming gas combinations (N_2-H_2 without swirl and $Ar-H_2$ with swirl flow), different primary gas flows (which is essentially similar to total mass flow) (for N_2-H_2 system) and different angles of injection (0° orthogonal to 20° forward) were also investigated. Sulzer Plasma Technik Twin 10 powder feeder was throughout this study. Hydrogen flow was 5 SLPM, current was 550 A, feed rate was 2 g/min and angle of injection is 0° (orthogonal) unless otherwise mentioned. Table 4 shows the process parameters used in this study.

Table 4: Process parameters used in the study of injection. Shown in *italics* is the parameter used in that particular study

Experiment	Plasma Gas	Primary Gas Flow (SLPM)	Carrier Gas Flow (SLPM)	Values Used
Carrier Gas Flows	Ar-H ₂	45	4.5 – 7	
Gas Chemistries	N ₂ -H ₂	30-60	1.6 – 5.4	
	Ar-H ₂		2.5 – 8	
Total Mass Flow	N ₂ -H ₂	30-60	1.6 – 5.4	
	Ar-H ₂		2.5 – 8	
Feedstock Morphology	N ₂ -H ₂	30-60	1.6 – 6.4	
Angle of Injection	Ar-H ₂	45	4.5 – 8	0°, 5°, 20°
Feed Rate	N ₂ -H ₂	30	1.6 – 4.6	2 – 30 g/min

4.2.2 Sensors and Diagnostics

Integrated sensor setup consisting of DPV 2000, Control Vision and SPT and IPP was used in this study Figure 27. DPV 2000 was used to measure temperature (T) and velocity (V) data from about 10,000 particles at the flow center, which was then averaged (called average particle T and V). Plume position was measured using SPT and ensemble temperature was measured using IPP. Control Vision was used for the visualization of the spray stream and post-processing analysis to observe the 2D trajectory.

4.2.3 Procedure and Methodology

All process parameters were kept constant except the carrier gas flow, which was changed systematically at regular intervals from a feasible minimum (below which feeding was interrupted) and maximum (above which the powder was over injected to cause unstable feeding and unreliable particle diagnostics). Torch, mounted on the robot, was parked at appropriately calibrated coordinates corresponding to each sensor to enable measurement of the in-flight data at the same spray distance of 130 mm. Particle and spray stream data was collected with each sensor at the same spray distance for each change in carrier gas flow. The same procedure was repeated for different primary gas flows, feedstock morphologies, gas chemistries and angles of injection and feed rates.

Repeated experiments were conducted with and without optimized injection in order to understand the role of particle injection in process variability. Coatings were made on beam samples 225 mm x 25 mm x 3.3 mm and their deflection was monitored using ICP. All relevant parameters were maintained constant between the different experiments.

4.3 Results and Discussion

4.3.1 Role of Carrier Gas on Particle Trajectory

It is widely appreciated that the carrier gas flow rate strongly influences the trajectory of the injected particles within the plasma jet and resultant effects on heat and momentum transfer from the plasma to the particle. Figure 37 illustrates this effect for a variety of carrier flow rates for laminar flow N_2-H_2 plasma spray system. These images were obtained through spray stream imaging using xenon strobe camera. Figure 38 provides a quantitative illustration of this effect (in 2D) indicating a linear relationship between centroid of the spray stream (referred to as plume position in this study) and carrier gas flow rates (data obtained from SPT sensor). Figure 38 further indicates that this linear behavior is independent of the primary plasma torch gas flow.

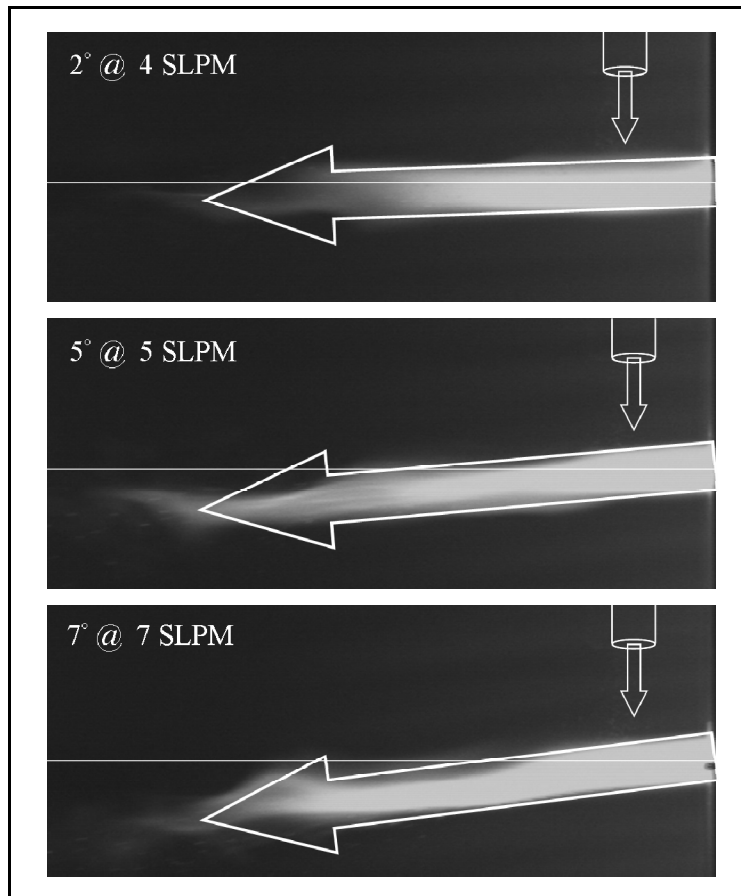


Figure 37: Change in particle trajectory as a function of carrier gas flow observed via xenon strobe imaging

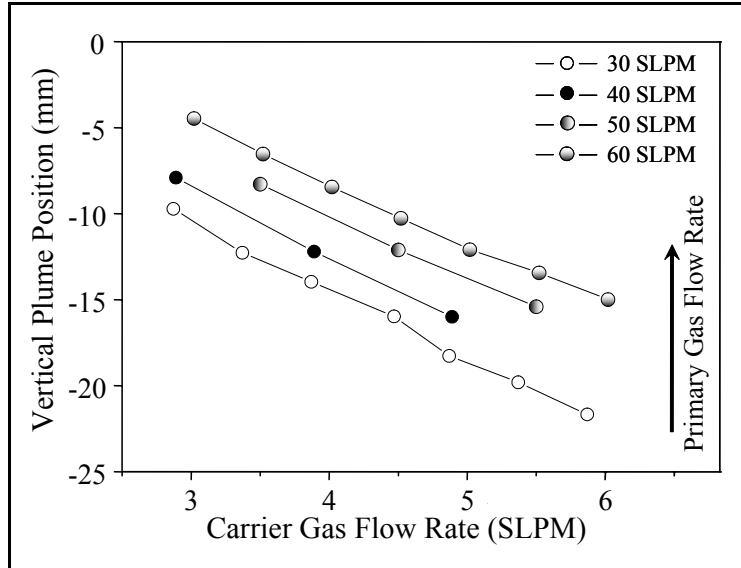


Figure 38: Change in plume position as a function of carrier gas flow for different primary gas flows

4.3.2 Implications of Particle Trajectory on Particle State

Clearly the location of the particles in the plasma jet will affect the thermal and momentum transfer from the plasma flame to the particles, especially given the strong thermal pinch in water cooled DC plasma torches. Simultaneous measurement of particle T and V was conducted during the injection studies and are plotted in Figure 39. It can be seen that both average particle T and V increases initially with increasing carrier flow, reaches a maximum and then reduces sharply with further increase in carrier flow.

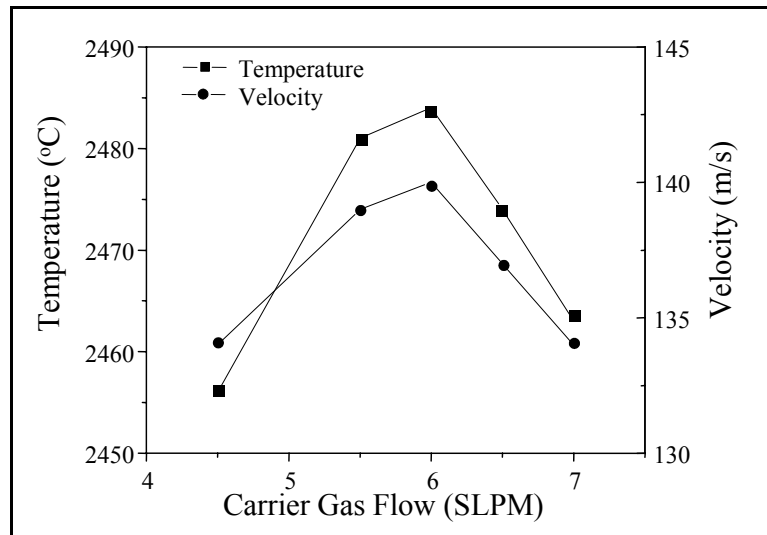


Figure 39: Mean particle temperature and velocity (from 10,000 particles measured using DPV 2000) for various carrier gas flows. Maximum could be observed in both T and V

It is clear that this maximum corresponds to the most efficient regime of plasma particle interaction in terms of thermal and momentum transfer. A notable feature is that both T and V reach a maximum at nominally the same carrier gas flow. These results of average T and V are based on measurement of 10,000 particles at the flow center using the DPV system. Simultaneous measurement of ensemble temperature using the IPP system also exhibits a similar maximum at identical carrier gas flows despite differences in measurement volumes and operation of the DPV and IPP sensors (Figure 40).

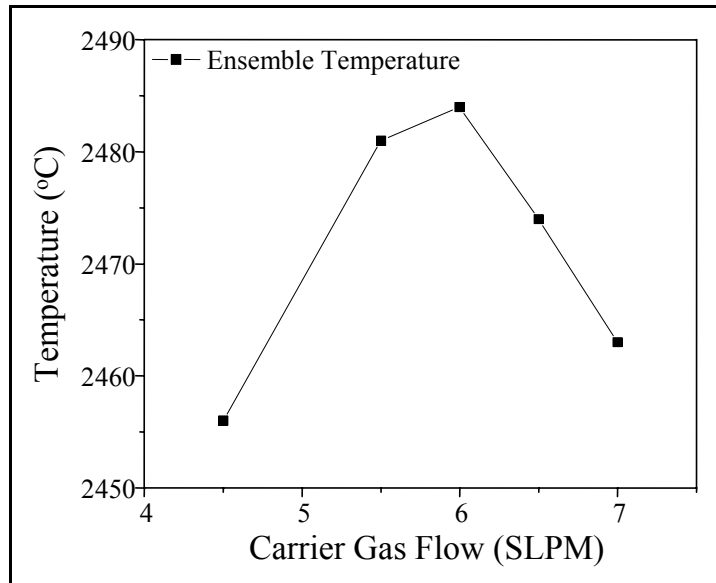


Figure 40: Time averaged ensemble temperature (from IPP) for various carrier gas flows. Maximum is observed

Similar observations have been made in the past by Vardelle et al. through radiated intensity measurements of the spray stream for alumina particles in an Ar-H₂ plasma and rationalized through computer simulations [180]. In their study, the total intensity of light radiated from the particles and the integral of the area under the intensity profile (at the spray distance) have been related to the temperature of the particles and heat transfer efficiency respectively and a maximum has been observed in both. However, direct correlation to individual particle T and V have not been reported in the earlier study. Furthermore, the above investigation examined primarily 2D effects.

4.3.3 Carrier Gas Flow Vs Plume Position

The presence of maximum in both particle T and V has been established as a function of carrier gas flow for a specific combination of plasma forming torch parameters. A key question arises whether the maximum in energy transfer between the plasma jet and the particles can be universally described based on carrier gas flow.

To critically assess this, a Design of Experiment (DoE) was constructed using the three significant plasma forming torch parameters (primary gas flow, secondary gas flow and arc current), along with carrier gas flow as the fourth parameter. Average particle temperature and the plume position for the different process conditions of this DoE are plotted in Figure 41. For most of the process conditions in the DoE the plume position was around -2 mm (marked by a vertical rectangle in the figure). For the same torch parameters, either over or under injection through non-optimum carrier gas flow rates results in reduced particle temperatures. This suggests the presence of a preferred plume position of about -2 mm (for this particular sensor set up) indicating an optimum plume position could be established independent of torch parameters.

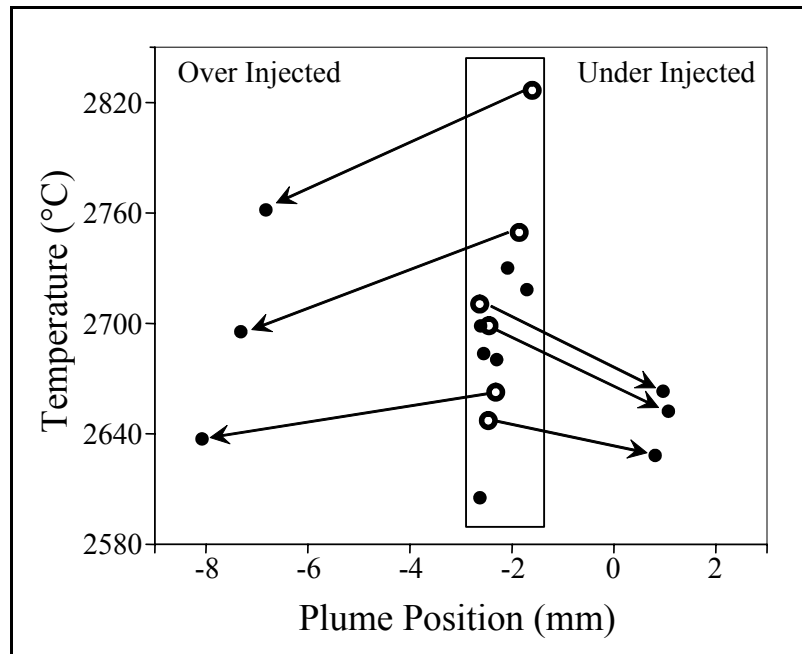


Figure 41: Preferred plume position observed for the different process parameter combinations in a statistical design of experiments including carrier gas as one of the primary parameters. All parameters remaining the same, change in carrier gas flow can result in identifiable under and over injected states

In light of this understanding, the T and V data plotted in Figure 39 as a function of carrier gas flow has been re-plotted as a function of plume position (Figure 42). Maximum in average particle T and V can be observed as a function of plume position. *This is a significant observation since the plume angle or position can now be used as a direct descriptor of an optimum rather than via hardware controls (carrier gas flow).*

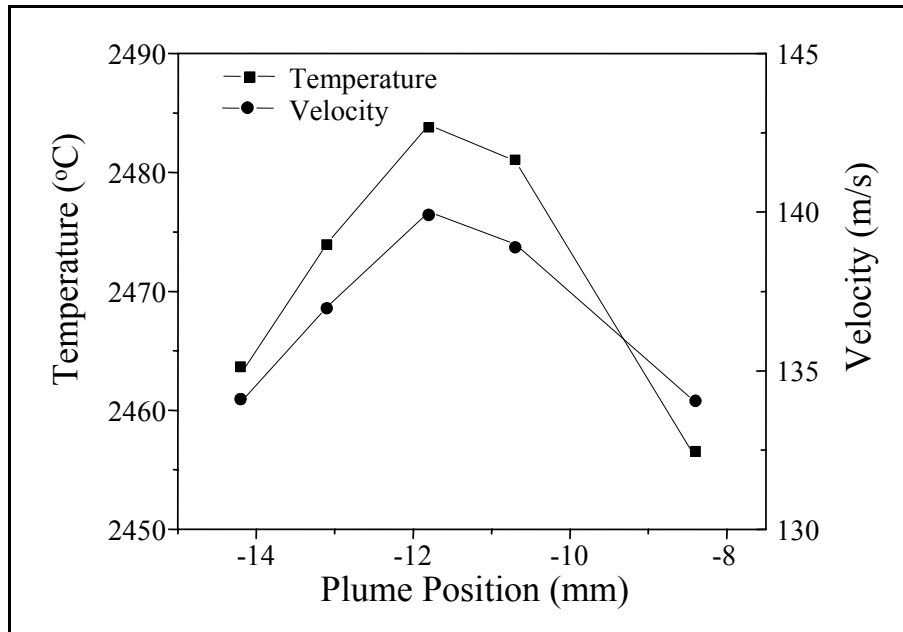


Figure 42: Mean particle temperature and velocity (from 10,000 particles measured using DPV 2000) as a function of plume position. Maximum could be observed in both T and V

4.3.4 Examining Validity of the Phenomena for a Range of Process Conditions

4.3.4.1 Total Mass Flow

Figure 43 shows a relationship of single particle averaged T and V (using DPV) by changing carrier gas flow for different primary gas flows. The presence of an optimum can again be observed. The results suggest that carrier gas flow rate required to achieve maximum T and V are different for the different primary gas flows. At the nominal operating parameters of 30 and 45 SLPM primary flows the trends are clear, however, at high primary flows such as 60 SLPM the effects saturate since particle penetration into the plasma jet becomes increasingly difficult.

In Figure 43 it can be noted that the maximum in average T and V occurs at different carrier gas flow rates for different primary gas flows. The results in Figure 43 are re-plotted in Figure 44 with respect to plume position rather than carrier gas flow. Figure 44 shows that the optimum plume position in terms of maximum T and V occurs at ~ 12 mm below the nozzle axis, for the current setup (sensor and hardware) at the nominal spray distance of 130 mm. *This confirms that plume position provides the most appropriate description of optimum particle injection (rather than carrier gas flow).*

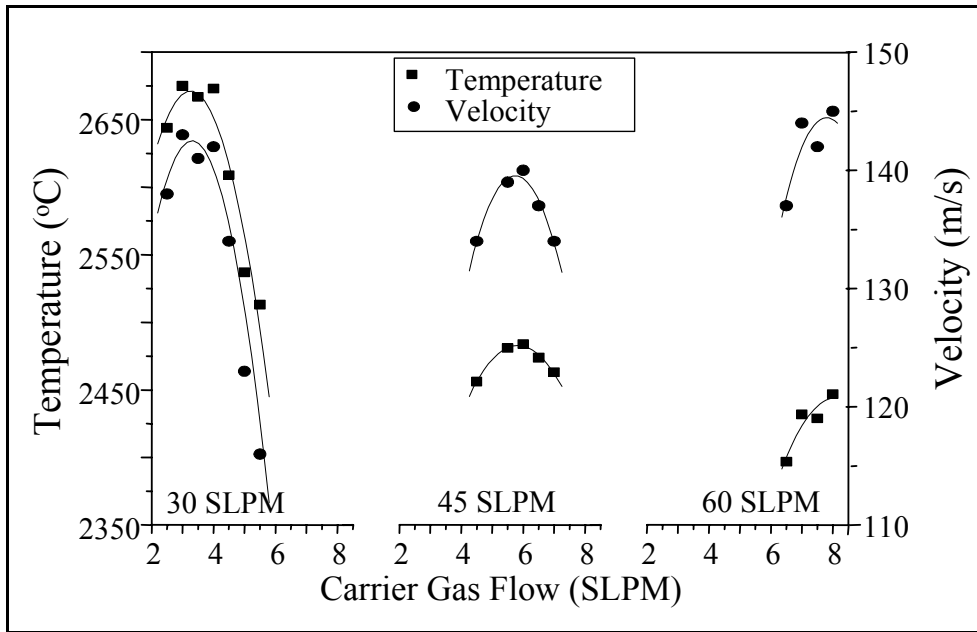


Figure 43: Mean particle temperature and velocity (from 10,000 particles measured using DPV 2000) as a function of carrier gas flow for different primary gas (Ar) flows. Maxima could be observed in both T and V in each case

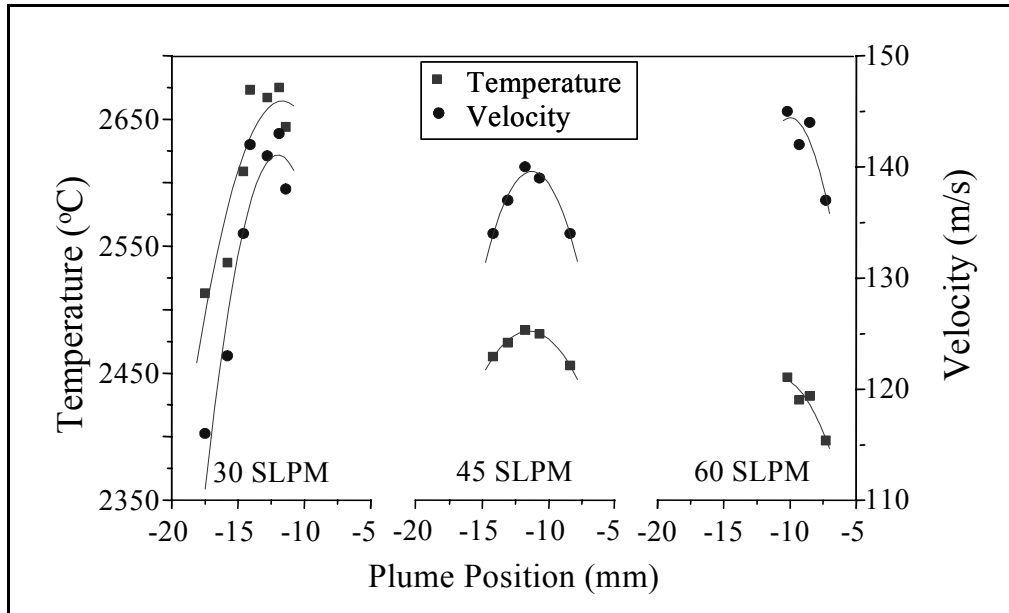


Figure 44: Mean particle temperature and velocity (from 10,000 particles measured using DPV 2000) as a function of plume position for different primary gas (Ar) flows. Maxima could be observed in both T and V in each case. The plume position of the maximum is the same in each case. Compare to Figure 43

4.3.4.2 Plasma Gas Chemistry (Ar-H₂ Vs N₂-H₂)

The results reported in Figure 43 and Figure 44 is from experiments conducted in Ar-H₂ plasma with swirl flow. In order to test the validity of the above observation, experiments were also conducted in N₂-H₂ plasma with laminar flow. Figure 45 compares the DPV averaged particle T and V with respect to plume position for a range of primary gas flows. Similar to the Ar-H₂ observation, existence of maxima in both T and V can be observed for various primary gas flows. Here again, the plume position at which the maximum occurs is invariant with respect to different primary gas flow rates and occurs at ~ 14 mm below nozzle axis (somewhat different compared to ~12 mm observed for Ar-H₂ system, nevertheless the same observed phenomena).

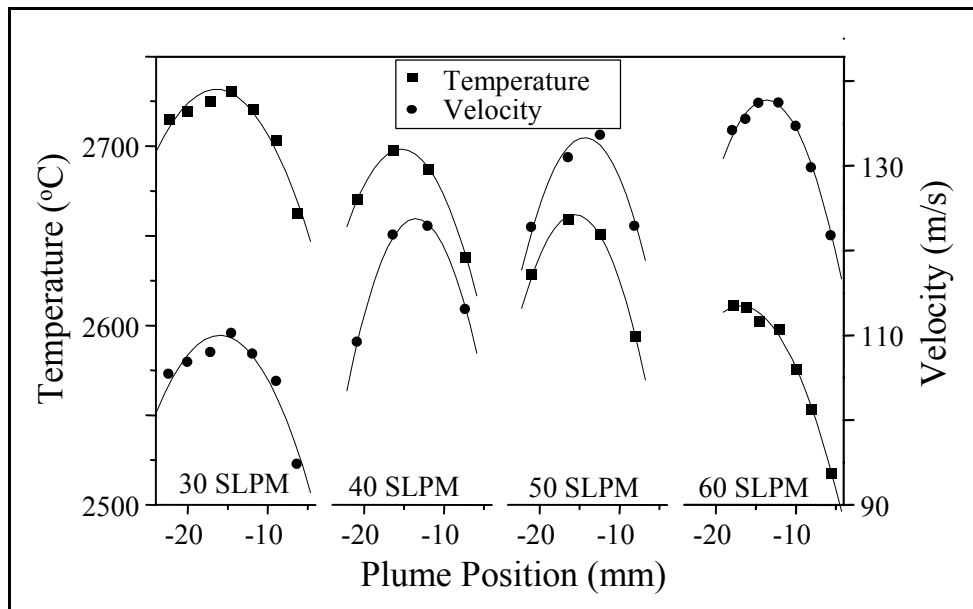


Figure 45: Mean particle temperature and velocity (from 10,000 particles measured using DPV 2000) as a function of plume position for different primary gas (N₂) flows for N₂-H₂ plasma gas mixture. Maximum could be observed in both T and V in each case. The plume position of the maximum is the same in each case. Compare Figure 44 for Ar-H₂

4.3.4.3 Feedstock Morphology

To investigate the effect of the powder particle characteristic on the particle injection behavior into DC plasma spray three different YSZ powders representing different morphologies and densities were studied. The three commonly used YSZ morphologies can be classified into two categories based on shape and density as (a) spherical Vs polyhedral and (b) low particle density Vs high particle density. This experiment enables examination of shape and density effects on plasma jet-particle interaction. Similar experiments were conducted using N₂-H₂ plasma for three morphologies of YSZ and the results are shown in Figure 46.

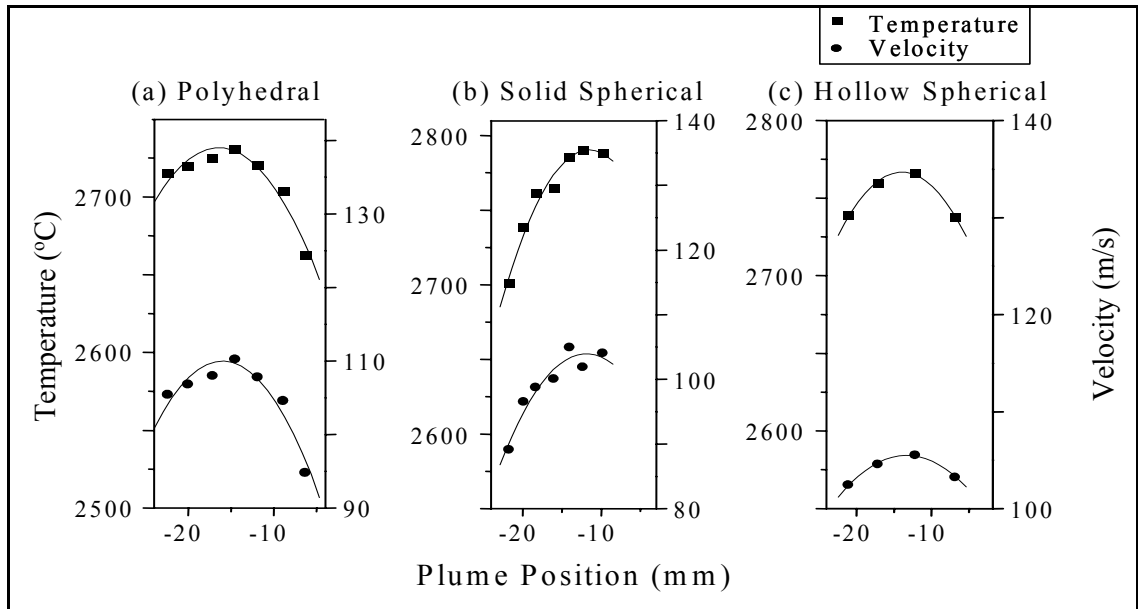


Figure 46: Mean particle temperature and velocity (from 10,000 particles measured using DPV 2000) as a function of plume position for different feedstock morphologies. Maximum could be observed in both T and V in each case at similar plume position

The results once again suggest the presence of an optimum plume position for all morphologies. Both solid spherical and hollow spherical feedstock have a common optimum at about -12 mm, whereas the polyhedral morphology feedstock displays an optimum at -14 mm. The origin of this minor difference is unclear and is perhaps related to the morphology, density and size distribution. Nevertheless the optimization phenomenon is generically applicable to all three morphologies (including for various primary gas flows; data not shown here).

4.3.4.4 Injection Angle

All the previous results were for orthogonal injection to the plasma axis (referred to as 0° in this study). The injector angle is used as a design variable to change the particle injection location in plasma sprays. It allows sampling different locations of the plasma jet for particle injection. To assess the effect of such a modification, three different injection angles were examined to determine if an optimum plume position exists.

An optimum plume position can be observed for all the three angles considered here (Figure 47), though the effects are not as clear as those observed for orthogonal injection. In the case of $+5^\circ$ downstream injection), optimum can be identified to be about -12 mm. The difficulty to over inject the particles is also evident. However, in the extreme case of $+20^\circ$ downstream injection, the overall temperature is low and the temperature change (as a function of plume position) is relatively insensitive illustrating a non-optimal plasma jet-particle interaction. Optimum plume position can be estimated to at about -7 mm which is significantly different compared to the orthogonal case.

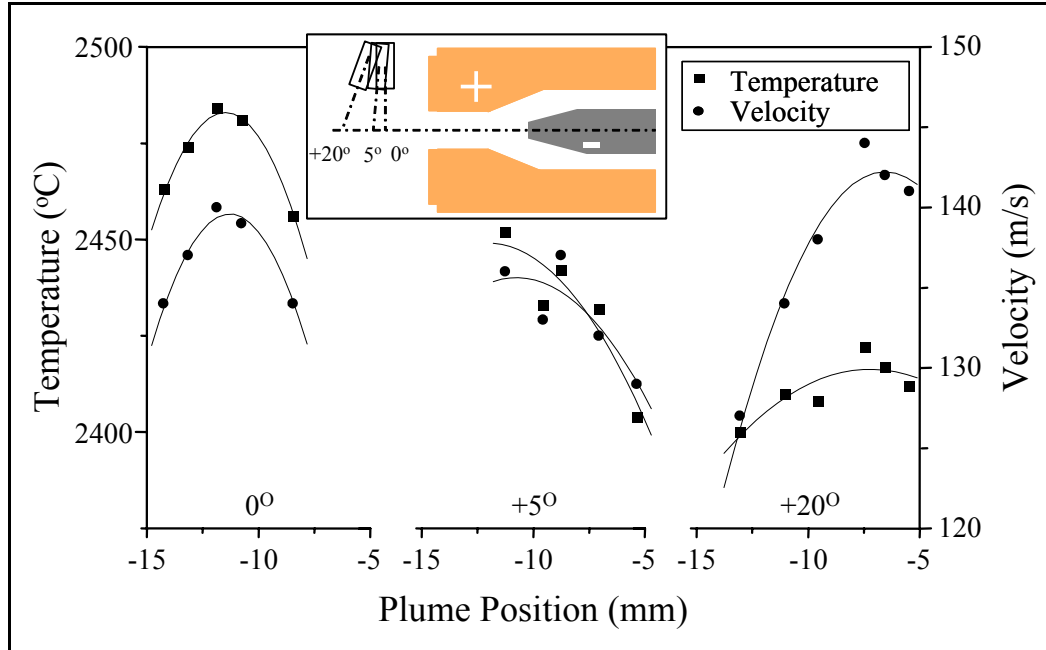


Figure 47: Mean particle temperature and velocity (from 10,000 particles measured using DPV 2000) as a function of plume position for different angles of particle injection. Inset shows a schematic of the injection angles. Maximum could be observed in both T and V in each case

4.3.4.5 Feed Rate

Process diagnostics is usually done at low feed rates (2 g/min) to maximize sensor data collection efficiency and to eliminate any bias associated with particle size selection. At higher feed rates, DPV 2000 tends to select more coarse particles due to the fact that larger particles emit higher intensity. In general the coarser particles tend to be colder and slower than the fine particles, which results in a suppressed estimate of particle temperatures and velocities. In this study a typical deposition condition of 30 g/min federate was examined.

Figure 48 compares the effect for the two extremes in feed rate for 30 SLPM primary gas flow for the FC powder. The results indicate that the plume position is consistent in both cases. The difference in temperature observed between the two feed rates can be attributed to the difference in input power, preferential size selection of the sensor and to plasma jet quenching.

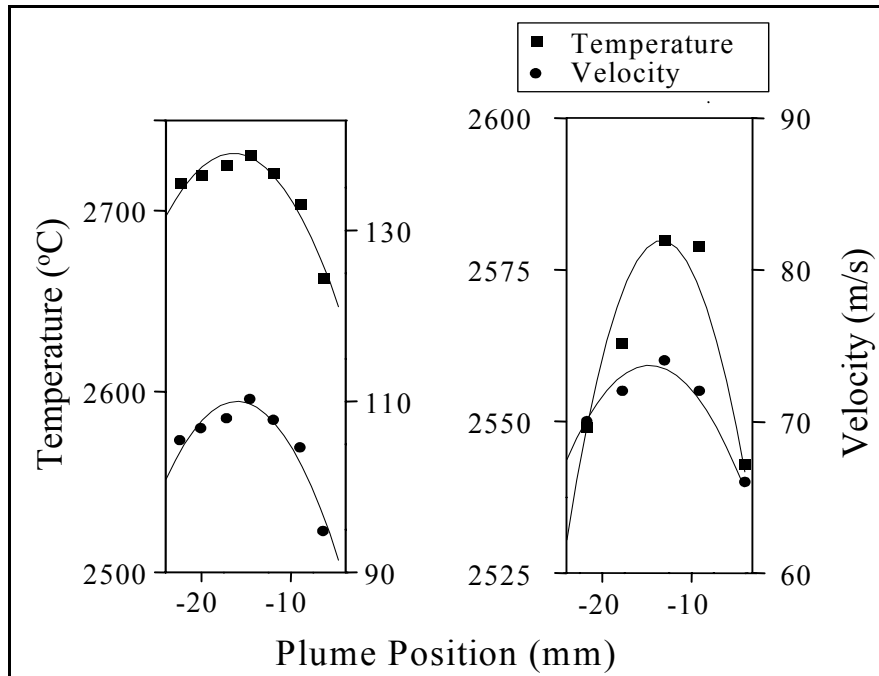


Figure 48: Mean particle temperature and velocity (from 10,000 particles measured using DPV 2000) as a function of plume position for different feed rates (left – low feed rate; right – high feed rate). Maximum could be observed in both T and V in each case at similar plume position

4.3.4.6 Other Material Systems

This phenomenon of optimum injection is applicable to not only to YSZ system but to other material systems as well. It is clearly observable in material systems where melting is an issue (usually due to a combination of high melting point, low thermal conductivity and large thermal mass of particles). This phenomenon has been observed in similar studies with TiO₂ and Alumina.

4.3.5 Implications of the Observed Phenomena

It is clear from the above observations that optimizing injection is a critical first step in examining the influence of the plasma-particle interactions. Without this step, it becomes difficult to establish “true” correlations between plasma spray parameters and resulting particle states (and eventually the coating properties). The proposed approach of independently optimizing injection (using plume position; controlled via carrier gas) for each of the plasma forming parameters allows for a robust method of establishing process maps and examining the influence of the key variables. The observed results show the deficiencies in contemporary methods of parameter optimization process monitoring and control strategies.

4.3.5.1 Enhanced Reliability in Particle State Measurement

To further understand the reliability in measurement of diagnostic data, two sets of experiments were compared. In one set, injection was optimized and then the plume position was intentionally varied to be on either side of the optimum (by varying carrier gas flow) for the same torch parameters in a single spray run. In a second set of experiments, injection was optimized for 7 measurements spread over a period of about 210 minutes in a single spray run.

The difference between the extremes of average particle T and V measured from these experiments are shown in Figure 49. It can be seen that the spread of data is negligible when injection is optimized. In contrast, small variation in plume position on either side of the optimum results in substantially increased variability in temperature and velocity. These results clearly illustrate the extent of variability in particle state arising from change in plume position.

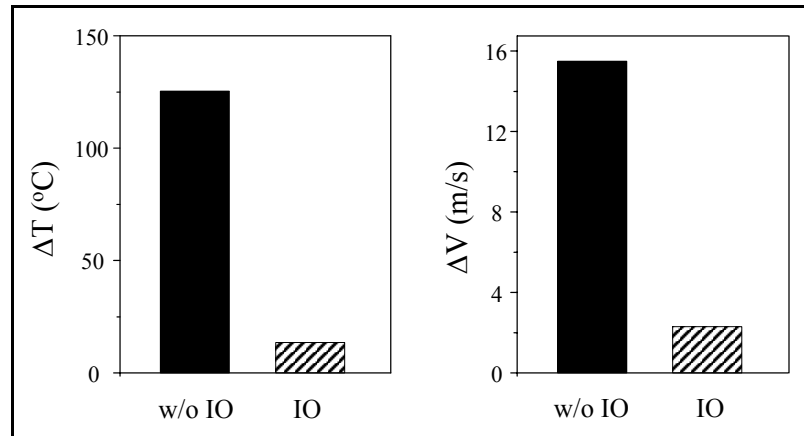


Figure 49: Controlling particle injection via plume position results in enhanced reproducibility in measured particle state (IO) as compared to intentional variation of plume position on either side of the optimum (w/o IO). w/o IO depicts the extreme case where carrier gas flow is maintained constant with time resulting in different plume positions due to change in the DC plasma jet

4.3.5.2 Enhanced Melting

All the previous results have reported the nominal average T and V from 10,000 particles. However, the DPV also provides the opportunity to obtain the T and V distributions. A detailed analysis of the particle temperature distributions for the optimum and non-optimum conditions is compared in Figure 50. It can be seen that the overall distribution is shifted to higher temperatures for the optimal injection situation.

Earlier studies by Streibl et al. examined the temperature distributions and concluded that the peaks allowed for rationalization of melting status of particles and a representative melting point can be defined from the analysis of the distribution [158]. The curve in dotted line is the melting peak identified by fitting the sub-distributions,

which corresponds to partially molten particles. This peak is almost non-existent in the case of optimum injection (for the same set of torch parameters in the same experimental run) with the distribution shifting to higher temperatures. This is an indication of increased molten content in the spray stream, which would result in improvement in deposit characteristics and deposition efficiencies.

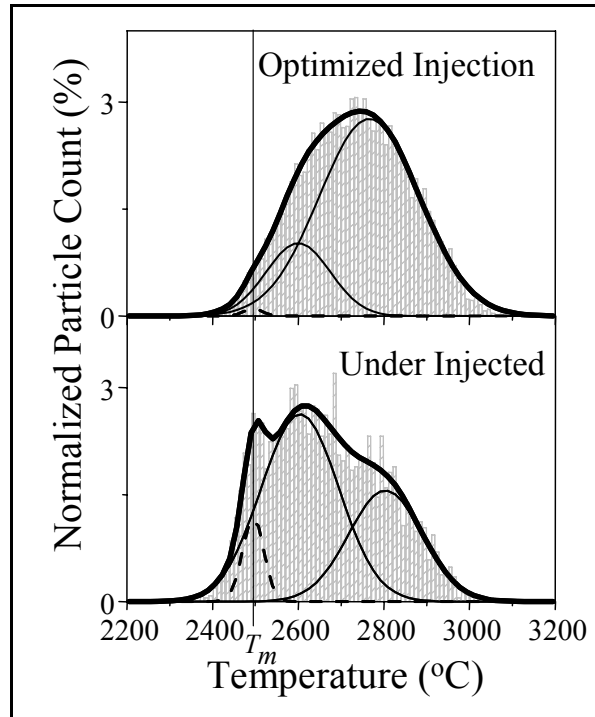


Figure 50: Temperature distributions for different particle injection shown with the underlying peaks [158]. Optimizing injection shifts the distribution to higher temperatures resulting in better melting and higher deposition efficiency. (Top - optimized injection; Bottom - under injected)

4.3.5.3 Reduced Overall Process Variability

To assess the improvement in process variability, two sets of experiments were conducted. In one set of experiments, injection was optimized for the first experiment and that value of carrier gas was used for the rest of the experiments conducted at the same plasma spray parameters (plume position was not fixed). In the second case, injection was optimized for every experiment at the same plasma spray parameters (plume position was fixed for every experiment). Variability has been defined as the difference between the maximum and minimum values of the measured response parameters (such as particle temperature, coating thickness, etc) and normalized to the average value of that parameter.

From Figure 51, it can be seen that despite modest reduction in variability of particle T and V, significant reduction in coating thickness variability is resultant due to control of the plume position. This is a notable finding that suggests a pathway for process

control strategy based on injection optimization. Additional information can be found in references [146, 184, 192, 193].

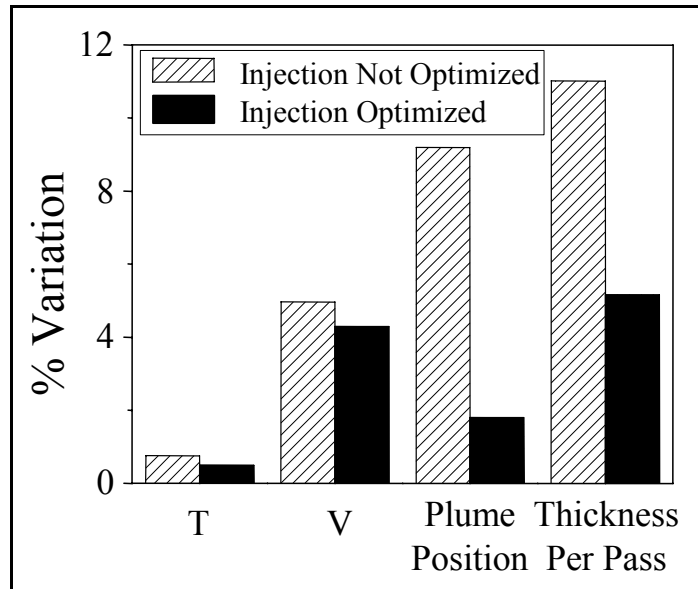


Figure 51: Variation (maximum range normalized over the average of that parameter) in properties from few repeated experiments. Controlling plume position results in reduced variability in thickness per pass with no significant improvement in the variability in particle state, indicating controlled coating build-up [192]

4.4 Summary and Conclusion

Particle injection is an important issue in the processing of materials in radial injection DC plasma spray systems. The orthogonal injection of solid low temperature particles create an asymmetric interaction with the plasma jet and results in complexities in establishing effective thermal and momentum transport. It is particularly critical for materials such as YSZ, which have high melting points and low thermal conductivity.

This study addresses this phenomenon through a detailed investigation of YSZ particles in an industry standard DC arc plasma spray device. This research was aided not only by the availability of advanced in-situ particle diagnostic tools but also by a novel 3D arrangement of both individual and ensemble sensors. They provide a new perspective into the process diagnostics.

The following specific observations and conclusions can be drawn from the results.

- Average particle T and V achieve maximum for any given set of parameters at comparable carrier gas flows. This is indicative of simultaneous maximum in heat and momentum heat transfer to particles, suggesting the presence of an optimum in the plasma jet

- The aforesaid maximum in T and V is invariant with respect to plume angle or plume position (at spray distance) for a variety of process conditions such as primary gas flows, gas chemistries, flow patterns of the plasma jet, feedstock morphologies, and angles of injection and feed rates
- Simple ensemble sensors enable us to observe the phenomena and as such provides a means to optimize the process

Furthermore, this study demonstrates that optimizing injection based on maxima in average T and V using plume position has the following implications and benefits

- Enables improved understanding of the plasma-particle interaction at the various process conditions due to the elimination of carrier gas from the equation
- Enhanced reliability of diagnostic measurements and data
- Enhanced melting or in general, optimum utilization of the plasma
- Reduced variability in the process resulting in more reproducible deposits
- Independence from hardware controls due to controlling the injection using in-flight data

Recent studies have shown that this procedure can also be employed for other ceramic materials and as such points a pathway for enhanced process understanding and control.

Chapter V

5 A Critical Examination of Particle State and Spray Stream

5.1 Process-Particle State Relation

5.1.1 Introduction

Plasma spray process is complex owing to the large number of variables involved. The process has been studied by many and variables that have profound influence on the process and on the coating characteristics have been identified from both engineering and scientific standpoints [100, 145, 146, 182, 196]. These variables could be clustered and categorized as shown in Figure 7. A scientific framework that links one stage of the process to the other is what we call a process map (shown in colored arrows). The relation between the hardware variables and the in-flight particle state and spray stream is what we refer to as a first order process map. In this section of this chapter, the implications of such a relation established by Vaidya [146] is explored.

5.1.2 Background

There are two basic requirements for the establishment of a first order process map. First, the process variables that have profound influence on the particle state and the spray stream have to be identified. From previous studies and from available literature on this process (including references [100, 148, 182]), the three primary torch parameters, namely total mass flow, ratio of secondary gas in the total volume flow and the arc current, have been identified to be critical in influencing the particle state and spray stream as a whole apart from particle injection. Second, the response parameters have to be identified and measured. Since it is widely appreciated that particle temperature (T) and velocity (V) influences the coating microstructure [28, 32, 35, 100, 102, 147, 149, 151, 193, 197], they were chosen as the response parameters in the present study to describe the particle state. Though normalized and non-dimensional parameters such as Melting Index [147, 161] and Reynolds number are *perhaps* better descriptors of the particle state, they cannot be measured directly unlike particle temperature and velocity.

5.1.2.1 First Order Process Maps

Extended central composite design of experiment (DoE) developed by Vaidya et al. [146] covering the safe operational range of the hardware (SM 7MB with N₂-H₂ straight flow) is shown in Figure 52. Experiments were done in a single run of the torch. DPV 2000 was used to measure the temperature and velocity of particles. Data from SPT was used to optimize injection for every process condition.

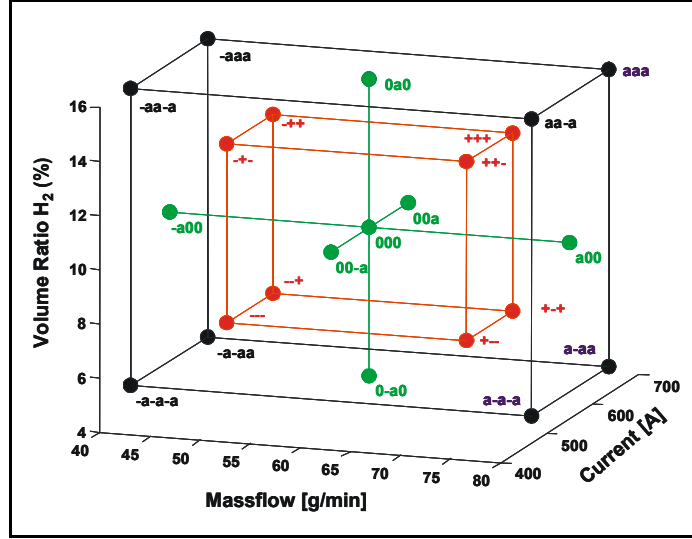


Figure 52: Extended central composite design of experiment using three significant plasma-forming torch parameters [146]

Figure 53 is a representation of a first order process map (of extreme points) for the polyhedral morphology (fused and crushed) feedstock. Quantitative relation between the plasma forming torch parameters and particle state was established using a linear fit comprising of individual primary parameters and their interaction combinations as represented in the Equation 4.

$$\begin{aligned}
 R_1 = & \bar{R}_1 + C_1 * (P_1 - \bar{P}_1) + C_2 * (P_2 - \bar{P}_2) + C_3 * (P_3 - \bar{P}_3) + C_4 * [(P_1 - \bar{P}_1) * (P_2 - \bar{P}_2)] \\
 & + C_5 * [(P_1 - \bar{P}_1) * (P_3 - \bar{P}_3)] + C_6 * [(P_2 - \bar{P}_2) * (P_3 - \bar{P}_3)] \\
 & + C_7 * [(P_1 - \bar{P}_1) * (P_2 - \bar{P}_2) * (P_3 - \bar{P}_3)]
 \end{aligned}$$

Equation 4

Where, 'R₁' is one the response parameter under consideration, 'P₁' is one of the primary process parameter considered in the DoE, \bar{P}_1 is the mean of P₁ and 'C₁' to C₇' are constants obtained from fit.

Significant parameters and their contributions were determined and are shown in Table 5 and Table 6. From Table 5, the influence of the parameters on the average particle temperature can be identified for each step change considered in DoE for any of the considered parameters. The same is shown in Table 6 for average particle velocity.

High values of accuracy (R^2) observed in both cases means that the fit describes the experimental data quite well.

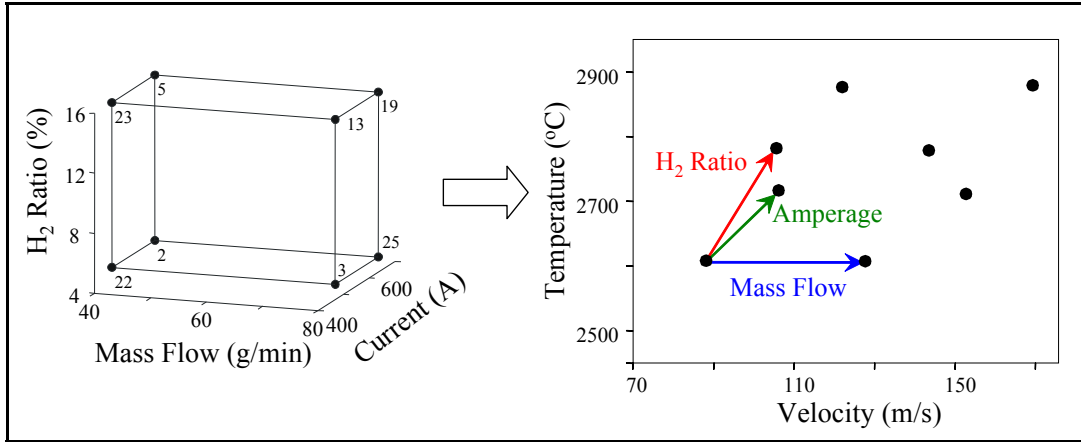


Figure 53: Torch parameter vectors in T-V space

Table 5: Contribution to average particle temperature (measured by DPV at flow center) from significant torch parameters and their combinations [146]

Term	Scaled Estimate
Intercept	2660.08
Mass Flow	- 28.01
H ₂ Ratio	78.44
Current	57.78
(Mass Flow – 60.0285) * (H ₂ Ratio – 10.5)	3.43
(Mass Flow – 60.0285) * (Current – 550)	5.32
(H ₂ Ratio – 0.5) * (Current – 550)	- 10.51
(Mass Flow – 60.0285) * (H ₂ Ratio – 10.5) * (Current – 550)	9.62
Accuracy of Fit (R^2)	0.98

Table 6: Contribution to average particle velocity (measured by DPV at flow center) from significant torch parameters and their combinations [146]

Term	Scaled Estimate
Intercept	123.74
Mass Flow	20.33
H ₂ Ratio	6.35
Current	12.51
(Mass Flow – 60.0285) * (Current – 550)	1.80
Accuracy of Fit (R^2)	0.98

This study is different from the previous studies [143, 147, 149, 151] for the following reasons.

- Controlled particle injection
- All experiments run in one ignition of the torch, eliminating the uncertainty brought about by arc dynamics due to re-ignition
- Systematic exploration of the operating space in terms of the three primary parameters (total mass flow, hydrogen ratio and current)
- Detailed particle and spray stream diagnostics using integrated setup

As an illustration of the complexity, versatility and scope of this processing route, an overview of a large number of process diagnostic results obtained is provided in Figure 54 [146]. This figure captures the results of a large number of experiments performed with multiple feed stocks and nozzle sizes. This is referred to as a global first order process map, which is link between process variables and the in-flight particle characteristics. Here, the particle velocity and temperature regions are distinguished as zones for different combinations of feed stock and nozzle sizes.

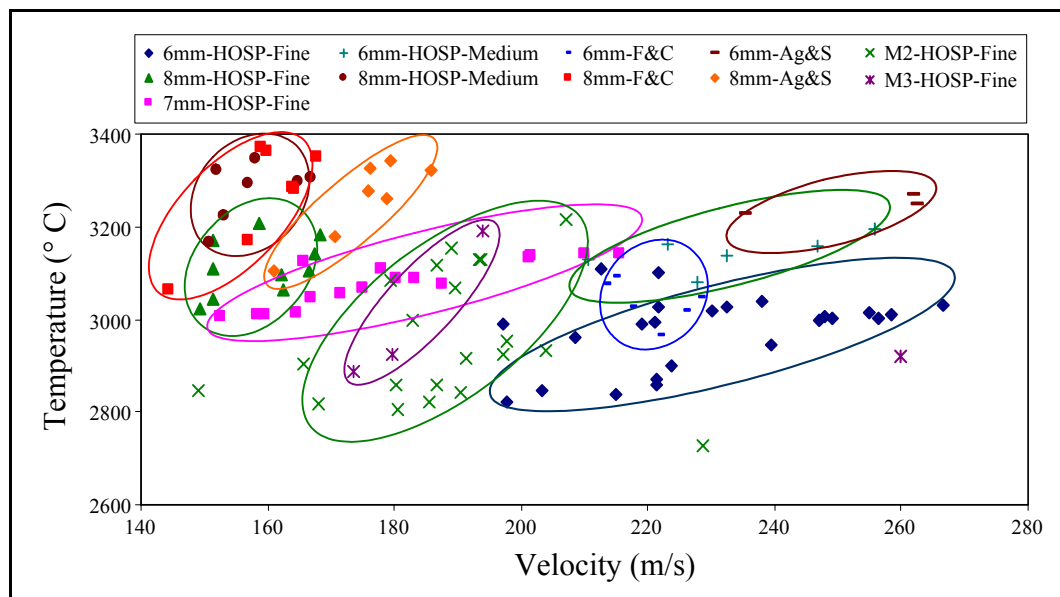


Figure 54: First order process maps from a variety of feedstock, hardware and torch parameters [146]

As is seen clearly from Figure 54, the overall range of particle states that can be attained using different combinations is quite large. For a given combination of feed stock and hardware configuration, there are limits of the particle states that are achievable within the safe operating range of that set up. The degree of correlation between velocity and temperature can also vary – as evident from the various ellipses in Figure 54. There is also overlap in the region of operation between different combinations. Typically, the smaller opening conventional nozzles resulted in larger extremes of particle velocity values whereas the larger diameter nozzles allowed greater flexibility in temperature range. It implies that there is considerable flexibility in terms of the type of particle states that can be generated and consequently in the type of splats and coatings that can form. In this study we consider one hardware setting to explore and understand the implications of the carefully

established relation between particle state and torch parameters for the three commonly used morphologies of YSZ.

5.1.3 Implications of First Order Process Maps

5.1.3.1 Assessment of Process Stability

The central condition of the DoE was repeated eight times, spread out randomly throughout the entire duration of the experiment. This set of data provides a means approach to assess the variability in repeated experiments in one non-stop run of the torch. For the polyhedral morphology powder, the error in temperature is 4.4% (~13 °C) and error in velocity is 2.8% (~2 m/s) in comparison to the entire range possible with the present set of hardware. This error accounts for

- The effect of nozzle wear during the operation of the torch and the stability of the process in one ignition of the torch (one run)
- The difference in response parameters due to the error in set point control for the plasma forming torch parameters
- The error in repeated measurements of the response parameters

However, the error reported does not include the influence of torch re-ignition because the experiments were done in a single torch ignition or the information about the accuracy of the sensor to measure the actual value (systematic or absolute error). The observed variability could/would set our limits in achieving any given temperature and velocity reproducibly.

5.1.3.2 Establishing Process Vectors

From the established first order process map, process parameters vectors have been determined in the T-V space as shown in Figure 53 for the polyhedral morphology YSZ. The following can be inferred from these process vectors

- Hydrogen ratio has the most influence on particle temperature, closely followed by amperage
- Altering mass flow is the only way to decrease particle temperature (for this morphology) while simultaneously resulting an increase in particle velocity. This is a very useful inference because of its use in process control strategies. Other morphologies behave slightly differently as will be shown later
- For a comparable step change of hydrogen ratio and amperage in the operational space (say 0 to a or -a to 0), larger change in particle temperature result from change in hydrogen ratio while larger change in particle velocity result from change in amperage

5.1.3.2.1 Implications of Process Vectors

First order map developed earlier by Vaidya [146] can be used to determine the torch parameter combination(s) that will result in a given combination of temperature and velocity. But it has been observed that the so identified parameters do not result in the expected temperature and velocity. This is due to torch re-ignition, which comprises of the influence of stochastics in arc attachment, and wear of nozzle and the associated arc dynamics.

Figure 55 shows such a tuning in process. It can be observed that the starting point did not result in the required temperature and velocity and that the tuning process resulted in the required values within a few iterations. The required vector is calculated (point 1 to 2 in Figure 55), one of the torch parameters fixed, the two torch parameter vectors are calculated and the process parameters adjusted accordingly. Hence, apart from its qualitative significance, these vectors form a guideline for process control involving control of average particle T and V.

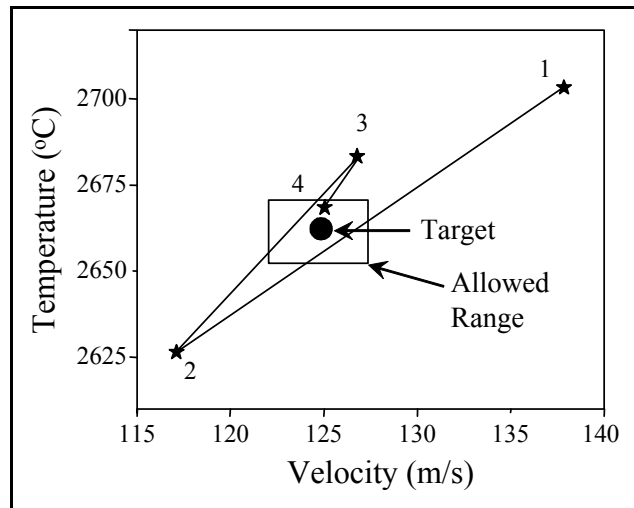


Figure 55: An illustration of the tuning-in procedure

5.1.3.3 Exploration of Process Limits

As mentioned earlier, the DoE was setup such that the ‘safe operational range’ of the hardware used was explored. This determines the limits of temperature and velocity that could be obtained using this hardware (Figure 56). The feedstock itself could be extended to different T-V regimes either by changing the nozzle geometry or by using completely different hardware configuration (different torch).

These boundaries set by the operating parameters could be used (as extremes) to assess the influence of spray stream on the coating microstructure and properties. This is addressed in the subsequent chapter.

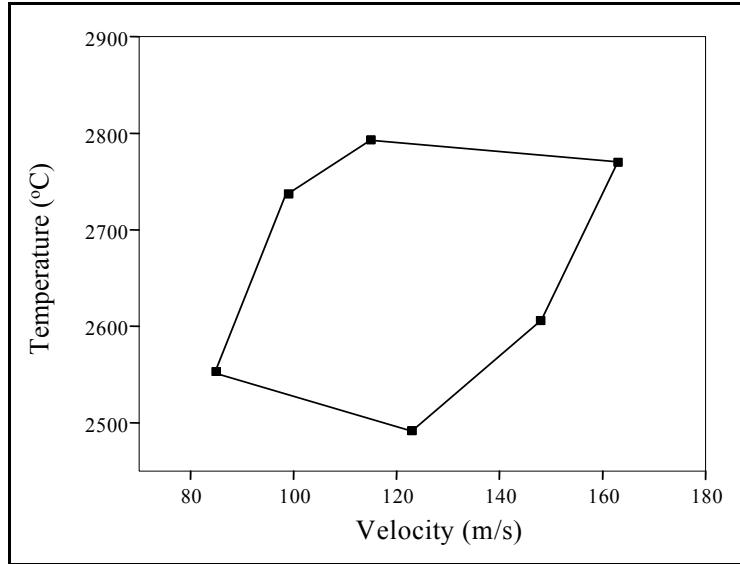


Figure 56: Process boundary in T-V space for FC feedstock

5.1.4 Comparison of Feedstock Morphologies

5.1.4.1 Process Instability

The center condition of the DoE that was repeated eight times for each of the different feedstock morphologies. From Figure 57 it can be observed that polyhedral morphology is least sensitive while hollow spherical morphology is very sensitive to changes in process conditions with time (with all parameters remaining the same).

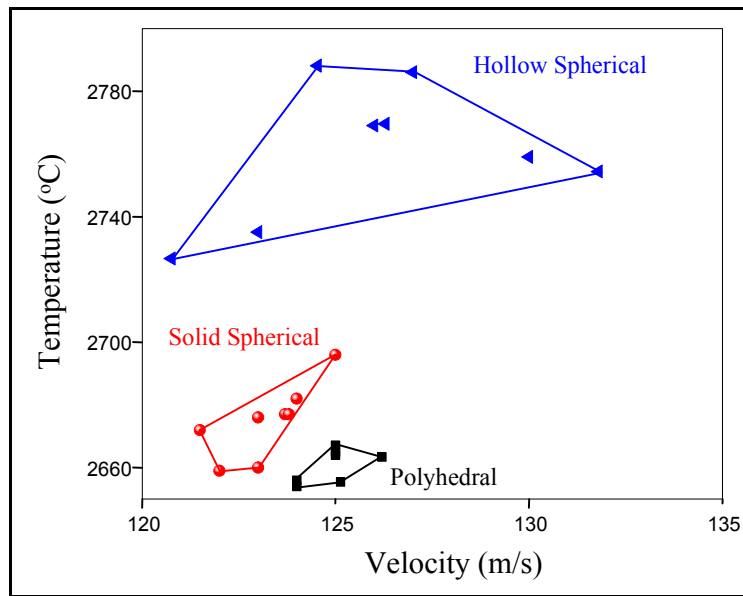


Figure 57: Process instabilities and errors

Time-dependent behavior of average particle temperature is shown in Figure 58. It can be seen that both polyhedral and solid spherical feedstock shows no or very less time dependence of temperature, which is shown by the lack of fit as well as by the slope of the fit. The hollow spherical feedstock, on the other hand, exhibits a clear time-dependent behavior; about 17°C decrease in average particle temperature per hour of the run time. Figure 59 shows the time dependent behavior of arc voltage for hollow spherical morphology feedstock which shows time dependent temperature behavior. There is a drop of about 0.5 V per hour, suggesting that the temperature drop is really a voltage dependence of the temperature and not direct time dependence. Particle velocity did not exhibit time/voltage dependence.

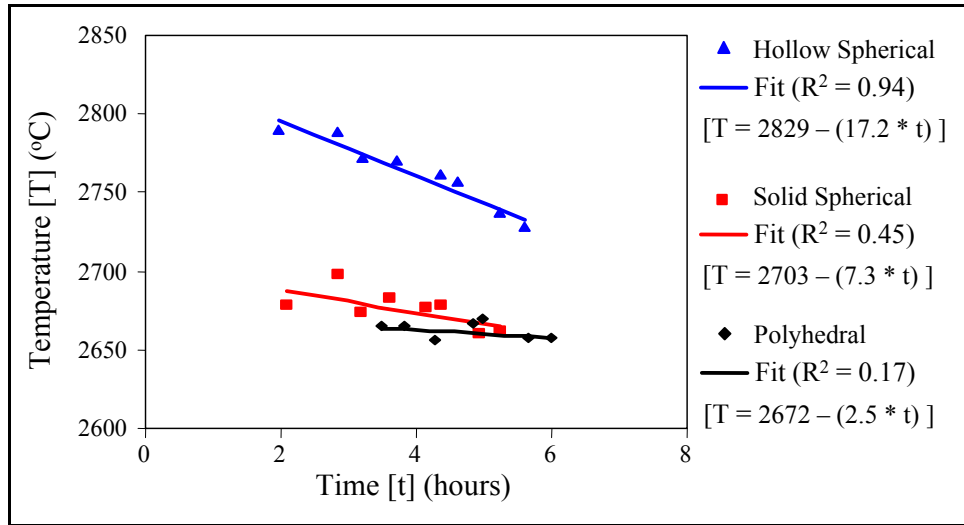


Figure 58: Time dependence of average particle temperature from repeated DoE center point condition (same process parameters) for the different morphological feedstock

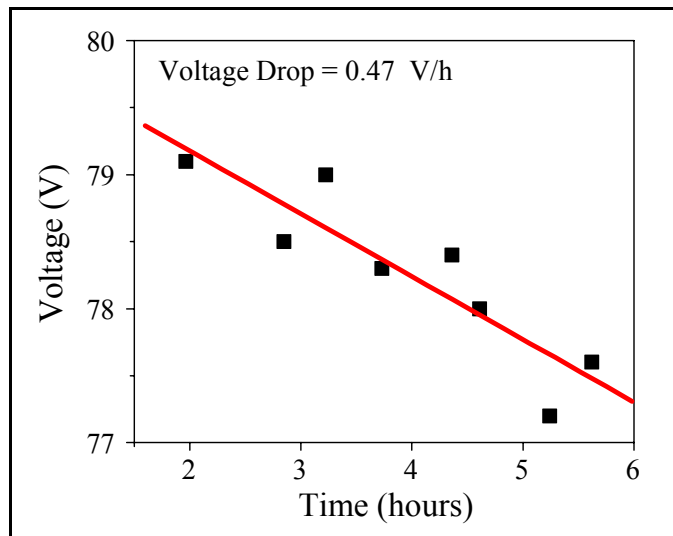


Figure 59: Time dependent behavior of voltage for hollow spherical morphology

5.1.4.2 Torch Parameter Vectors in T-V Space

Figure 60 shows the process parameters vectors in T-V space clustered suitably to enable clear comparison of the different morphological feedstock. This figure should be interpreted only in a relative sense because these vectors were calculated at a certain DoE condition, which results in different temperature and velocity for different morphological feedstock.

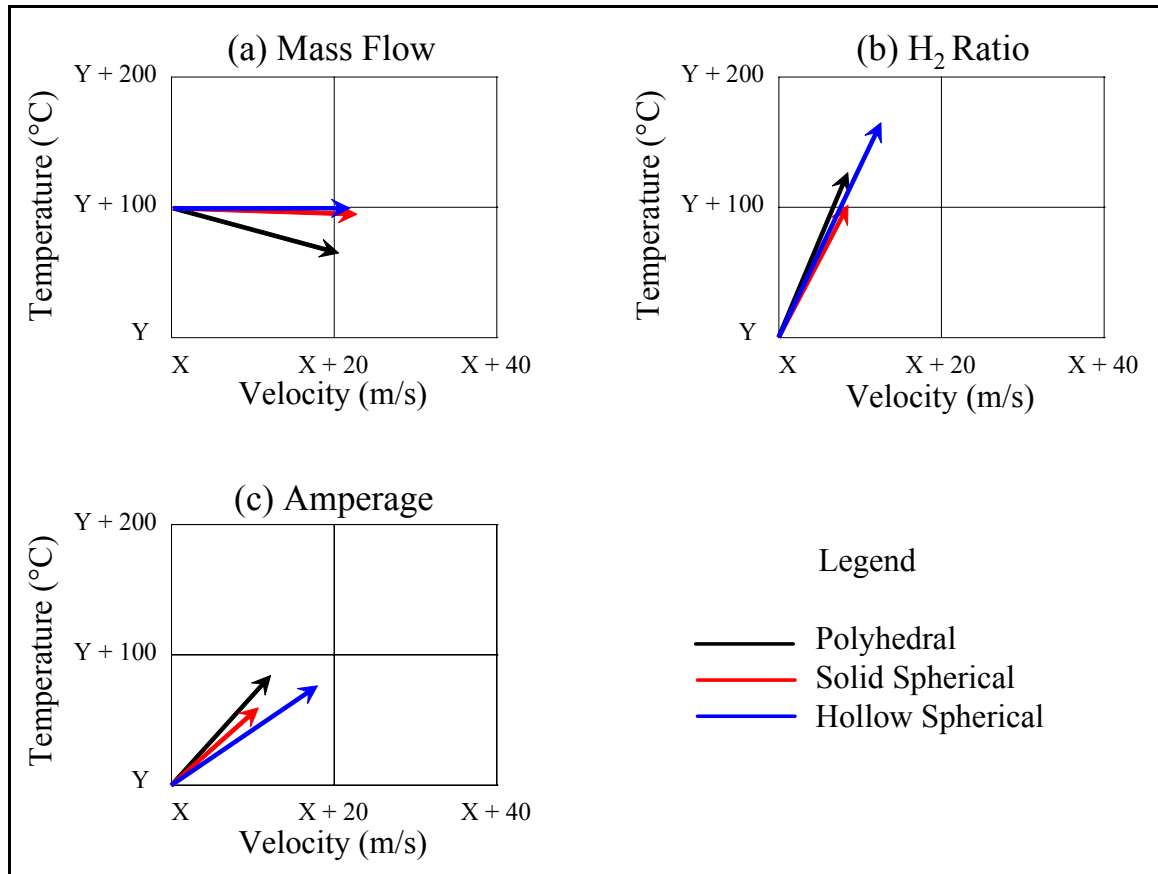


Figure 60: Comparison of process parameter vectors in T-V space. Fig (a) shows the behavior of each of the three morphology feedstock to change in mass flow. Fig (b) and (c) show similar behavior of each of the three morphology feedstock to change in hydrogen ratio and amperage (or current) respectively

It can be seen from Figure 60(a) that total mass flow does not have any influence on the particle temperature for both solid spherical and hollow spherical morphologies, whereas it decreases the average particle temperature for the polyhedral morphology feedstock. The magnitude of resultant velocity change is very similar for all three morphologies.

Figure 60(b) shows that the direction of the vectors is very similar for the three morphologies but the magnitudes are different (as against total mass flow). Hollow

spherical morphology shows most sensitivity to change in hydrogen ratio while the other two morphologies show similar changes.

Arc current change results in different directions and magnitudes for all the three morphologies (Figure 60(c)). This is different from influence of total mass flow and hydrogen ratio. Polyhedral morphology feedstock shows more sensitivity to particle temperature than velocity for a similar change in current while hollow spherical feedstock is more sensitive to particle velocity than temperature. Solid spherical morphology feedstock is in-between the other two in terms of direction and is lesser in magnitude.

5.1.4.3 T-V Space Resulting from Exploring Process Limits

From Figure 61 it can be seen that different morphologies behave differently in the plume to result in a different T-V space. Despite the differences, all three morphologies share a large common T-V space, which could be explored to design coatings.

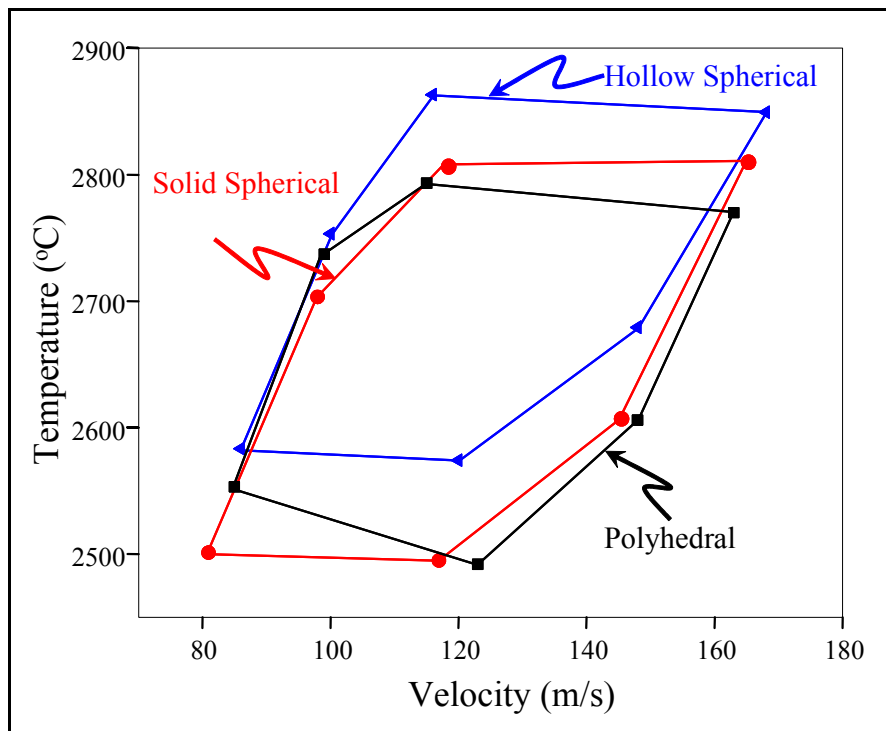


Figure 61: Behavior of all the three morphology feedstock overlaid in the T-V space

5.1.5 Summary and Conclusion

First order process map is a representation of the relation that exists between the particle state and the torch parameters and feedstock characteristics. This relation was established in previous studies at the Center for Thermal Spray Research for different YSZ feedstock. This study critically examined the implications of such a relation in terms of the process stability from repeated conditions, torch parameter vectors in particle state space and the boundaries of the process in terms of the particle state. Based on these implications, the three widely used morphologies of YSZ, namely polyhedral, solid spherical and hollow spherical, were compared.

This study shows that the process is stable within a single run of the torch due to avoiding re-ignition, which could result in arc attachment at a completely different region in the anode. The different feedstock morphologies are sensitive to the process to different extents. The hollow spherical morphology shows the largest error window of the three morphologies, establishing the high sensitivity of the feedstock to process changes.

Vectors of plasma forming torch parameter were established in the particle state space (T-V space) for the different morphology feedstock. This is a necessary step to controlling particle temperature and velocity. Increase in the total mass flow shifts the process to a higher velocity region while simultaneously decreasing the temperature slightly. Increasing hydrogen ratio and arc current increases both temperature and velocity of particles, but to different extents. Arc current increases the velocity more and temperature less than the hydrogen ratio. Different morphology feedstock has slightly different vectors but the overall trends are the same.

The boundaries of the particle state space have been established for the different feedstock morphologies by exploring the safe operational torch parameter space. Both polyhedral and solid spherical morphologies have very similar process space while the hollow spherical morphology results in a process space shifted higher on the temperature axis. The process space of all three morphologies overlap significantly resulting in a large particle state space that can be achieved with any of the feedstock morphologies.

Establishing the relation between the torch parameters and the particle state and understanding the implications of such a relation enables a better understanding of the plasma-particle interaction and the role of feedstock morphology. This forms the basis for a scientific framework for possible process control using only the in-flight state of the process.

5.2 Process Control Using In-flight Particle State: Observations and Considerations

5.2.1 Introduction

With the widespread availability of commercial process monitoring sensors and studies suggesting the significance of particle state and spray stream, these sensors are starting to find their way into industrial process monitoring and control. There exist different control strategies, predominantly based on controlling particle temperature and velocity, for tighter control of the process [25, 28, 35, 148, 181]. For true in-flight process monitoring and control completely independent of torch parameters, the process, sensors and the data output from sensors needs to be understood thoroughly along with the methodologies of process control.

Insufficiency of measured particle surface temperature to describe the molten status of particle is well established [160, 161, 197]. Yet at the spray stream level studies have suggested that average temperature and velocity control the microstructure and properties of coatings to a first approximation [148, 149, 151]. In a recent study at the Center for Thermal Spray Research (CTSR), it has been observed that the temperature distributions of particles are not normal curves. They are multi-modal in nature, exhibiting two or three peaks [158, 198]. Melting Index distributions are similarly multi-modal. Mean and standard deviation are sufficient to describe a normal or Gaussian distribution but are not sufficient to describe such multi-modal distributions.

These recent findings raise the question whether average particle temperature and velocity are sufficient to completely describe the spray stream completely. Towards addressing this question, a few key controlled systematic experiments were performed; average particle temperature and velocities were maintained similar by varying the torch parameters in a wide parameter space. This section reports the salient observations on the sufficiency of average particle temperature and velocity as parameters to describe the spray stream in order to satisfactorily explain the observed structure and properties of coatings.

5.2.2 Experimental Details

Air plasma spray torch 7MB (Sulzer Metco, Westbury, NY) with an 8mm 'G' nozzle was used with straight flow of N_2 - H_2 gas mixtures. Ytria Stabilized Zirconia (YSZ) feedstock fed from Plasma Technik Twin 10 feeder was injected external to the nozzle from the top radially into the plasma. Three different morphologies of YSZ, namely solid polyhedral (FandC), solid spherical (AandS) and hollow spherical (PD) with similar powder size distributions of 10-75 microns were chosen for the study. Process parameters are shown in Table 7.

Table 7: Process conditions and feedstock details

Experiment (Numbers)	Powder Morphology (Manufacturing Method) (Abbreviation)	Range of Torch Parameters Used
Set A (1 – 5)	Hollow Spherical (Plasma Densified) (PD)	N ₂ : 40.9 to 55.4 SLPM H ₂ : 1.7 to 12 SLPM I: 434 to 706 A
Set B	Solid Polyhedral (Fused and Crushed) (FC)	N ₂ : 39.3 to 48 SLPM H ₂ : 1.8 to 7.1 SLPM I: 466 to 634 A
Set C	Solid Spherical (Agglomerated and Sintered) (AS)	N ₂ : 43.1 to 52.5 SLPM H ₂ : 1.7 to 9.4 SLPM I: 548 to 763 A
Set D	Solid Polyhedral (Fused and Crushed) (FC)	N ₂ : 41.9 to 45.3 SLPM H ₂ : 6.9 SLPM I: 675 to 700 A

Injection was optimized using SPT sensor and the particle temperature and velocities were measured using DPV 2000. Coatings were made on grit blasted Al 6061 T6511 alloy strip of dimensions 228 mm x 25 mm x 3 mm using 20 g/min feed rate and 300 mm/s (robot) pass rate. Microstructural characterization was done using image analysis. Through thickness thermal conductivity, through thickness indentation modulus and in-place curvature modulus were measured.

5.2.2.1 Achieving Same Average Temperature and Velocity

Figure 62 shows one approach to the problem in the form of a simplified flow chart. Each of the steps and stages are explained in detail below.

As mentioned in the previous section, three significant torch parameters were quantitatively related to two particle characteristics via first order process map. This provides the possibility of achieving any specified temperature and velocity using a wide variety of torch parameter combinations (within the scope of the experimental data from which the equations were calculated). In order to solve this equation, one torch parameter has to be specified at regular intervals covering the entire operational range and the other two parameters can be calculated from the equation for the specified temperature (2661°C) and velocity (125 m/s). Figure 63 shows a curve fit for the discrete data points of nitrogen flow and current calculated by fixing hydrogen flow at the different values starting from lowest to highest (left to right along the X axis). Torch parameter vectors were also established in the temperature-velocity space as mentioned earlier (Figure 53).

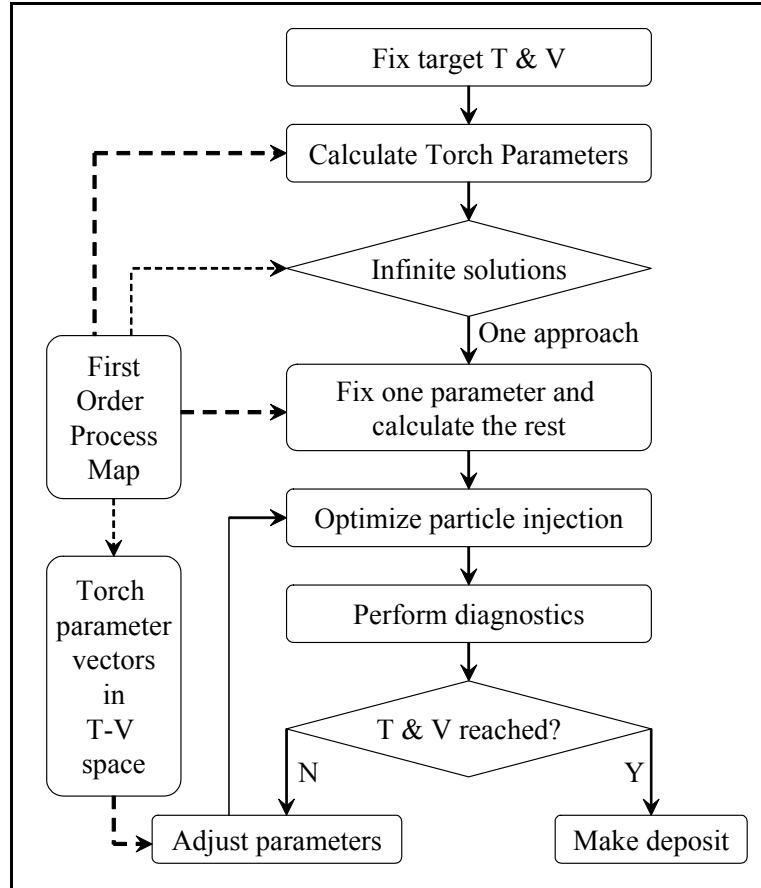


Figure 62: Procedure followed to achieve same average temperature and velocity. Solid line represents the solution path. Dotted lines represent the fundamental source of the issue/solution and the bold dotted lines represent the immediate source of solution

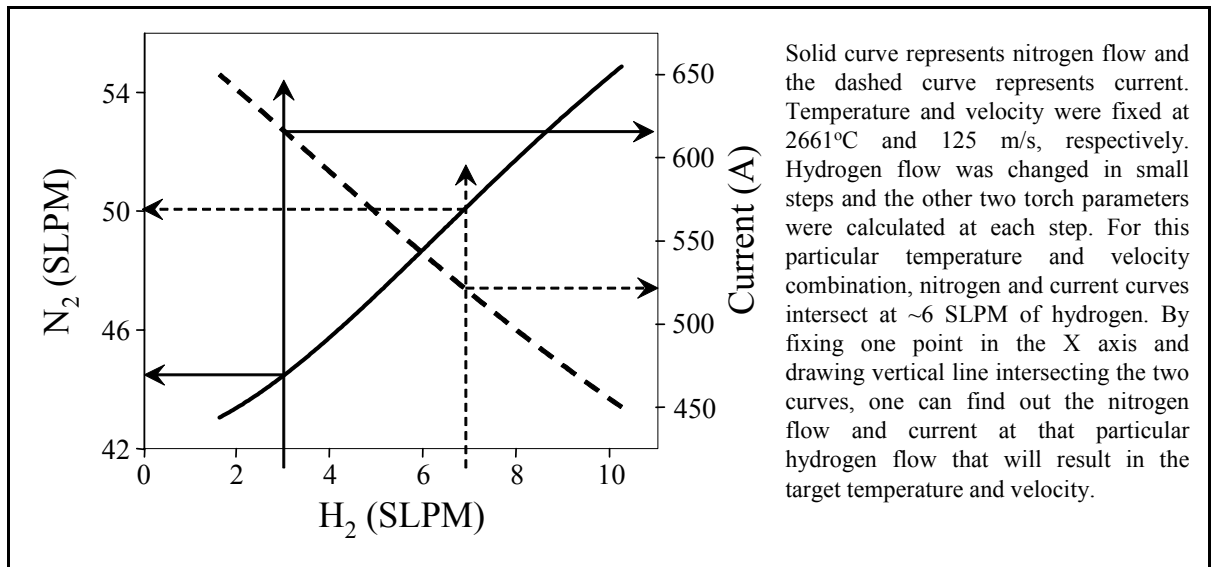


Figure 63: Visualization of the many possible solutions possible for the torch parameters to achieve the same target temperature and velocity

Hydrogen flow was fixed to calculate the parameter combinations for the hollow spherical and solid spherical feedstock while current was fixed for the polyhedral feedstock. It should be noted that the first order process map for the different morphologies resulted in slightly different relations between the torch parameters and the particle properties [146, 193], hence appropriate relations were used in the calculations.

Particle injection, was *optimized* for every change in torch parameters [199]. Injection was controlled separately from the three torch parameters such that the particle state is influenced only by the plasma forming torch parameters and not by carrier gas flow. This results in comparable trajectories resulting in similar diagnostic coordinates in the spray stream. This ensures the T and V measured is representative and suitable for comparison.

It is known that the in-flight particle characteristics are influenced by re-ignition and by nozzle life (wear) [166-168]. Hence the calculated torch parameters do not yield the anticipated temperature and velocity (refer point # 1 in Figure 55). To address this issue, the torch parameters were adjusted to achieve the required T and V (target) for each experiment. This was done using the torch parameter vectors in T-V space following an iterative procedure (Figure 55) to achieve the set the required temperature and velocity within a stringent margin of $\pm 10^\circ\text{C}$ and $\pm 2\text{m/s}$.

5.2.3 Results and Discussion

Of the three morphologies that were studied, hollow spherical feedstock (PD) shows higher sensitivity to the changes in process conditions compared to the other two. In this study, the parameters were varied most widely for the PD feedstock. Hence we our observations with the PD feedstock are discussed in detail below.

5.2.3.1 Assessing the Difference/Variability

The variation in average particle T and V for the different process conditions that resulted in the same average T and V is shown in Figure 64 for hollow spherical morphology powder (*Same T-V PD experiments – Set A*). Since the average particle temperature and velocity were controlled to within $\pm 10^\circ\text{C}$ and $\pm 2\text{m/s}$ respectively, the variation ($V = \Delta * 100 / \text{average}$; where $\Delta = (\text{max} - \text{min})$), 1.1% and 2.4% respectively, is very less. Average Melting Index and Reynolds Number, group parameters calculated from the thermo-physical and in-flight properties of individual particles, shows much higher variability.

In spite of the similar average particle temperature for experiment *set A*, ensemble or plume averaged temperature is observed to vary widely (Figure 64). Plume width calculated from the plume intensity profile (SPT) as the width at $(1/(I_{\text{max}})^2)$ at the spray distance of 130 mm is shown in (Figure 64). As much as 20 % variation could be observed for experiment *set A*.

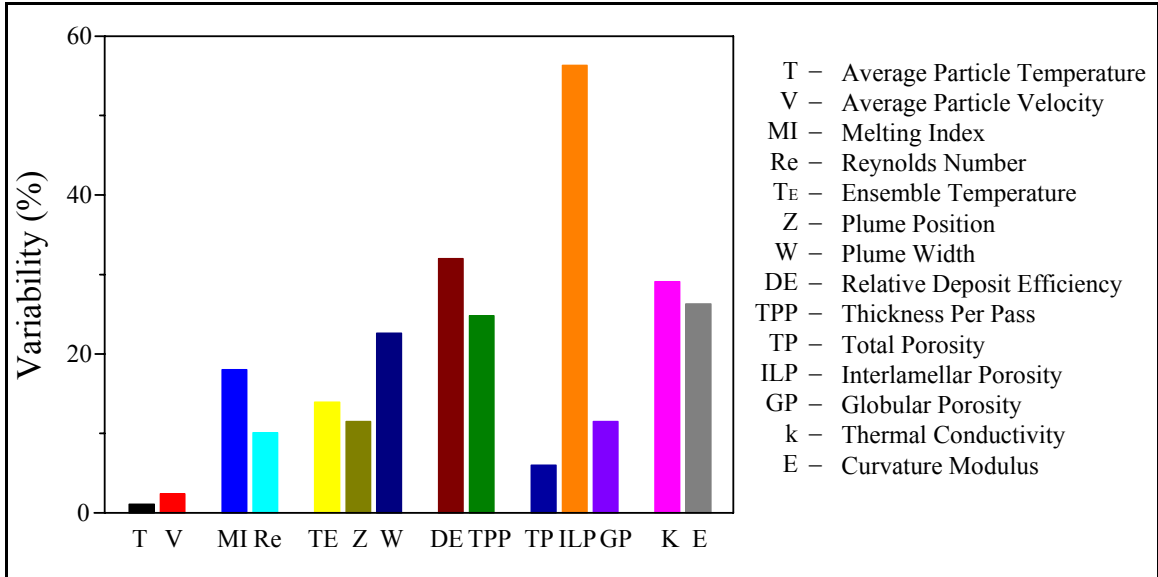


Figure 64: Variability in in-flight particle properties, ensemble plume properties, coating attributes, microstructure and properties of coatings in experiment set A (PD morphology)

A closer look at the distributions reveals the difference between the experiments. Particle velocity distributions are Gaussian ($R^2 \sim 0.8$) with mean about the point and are quite similar for the different experiments (Figure 65).

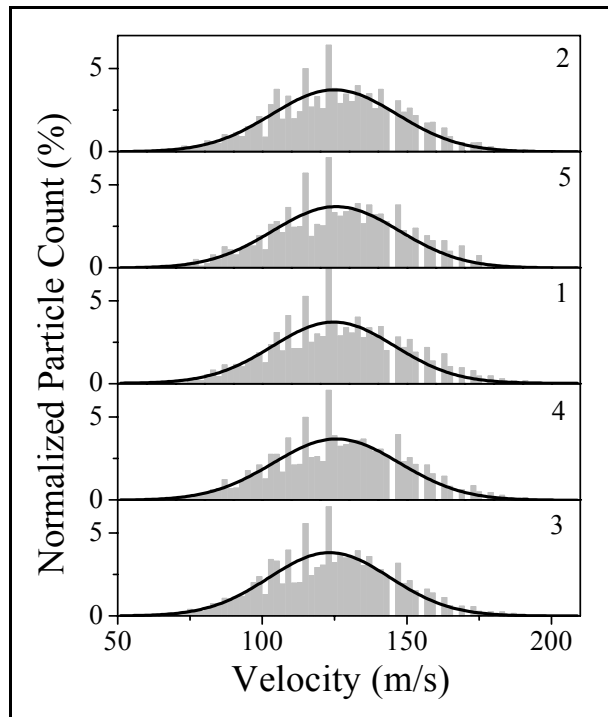


Figure 65: Velocity distribution of particles measured at the flow center using DPV. The distributions are Gaussian and quite comparable

The particle temperature distributions, on the other hand, appear to be multi-modal, consisting of three sub-distributions (Figure 66). The vertical line in Figure 66 is the melting point as determined from the temperature distributions measured using DPV 2000 [158]. One can observe the difference in the height, width and area under the ‘melting peak’ (red color) as well as the other peaks for the different experiments. Similar differences could be observed in the Melting Index distributions in Figure 67.

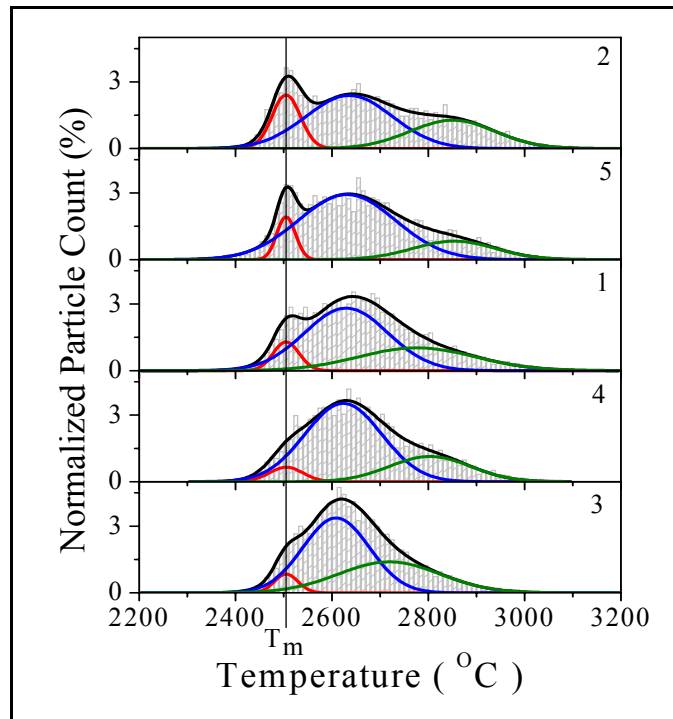


Figure 66: Particle temperature distribution arranged by increasing total input power from bottom to top. The distributions are multi-modal and are different from each other

Differences of the order of 25 to 30 % could be observed in deposition efficiency and coating thickness per pass for the different coatings (from experiment *set A*) (Figure 64). These, along with the variation in ensemble plume properties, suggest that the process is not the same though they have resulted in similar averages in particle temperature and velocity.

The total porosity in the coatings as determined by image analysis from 2D optical images shows small variability, not as significant as the basic coating attributes (Figure 64). Interlamellar porosity shows very high variability, which could be due the difference in coating assemblage that exist between the different coatings due to difference in spray stream and/or due to the resolution/limitations of measurement technique. The variability observed in thermal conductivity appears to corroborate the variability in interlamellar porosity, which plays a significant role in influencing the thermal transport.

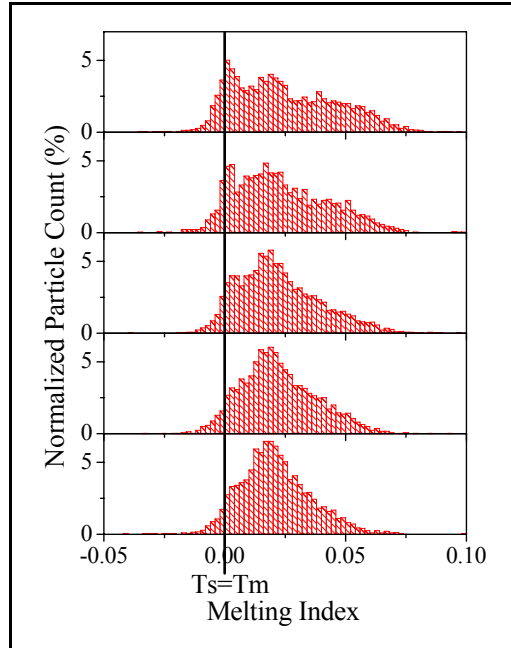


Figure 67: Melting Index distributions for the different experiments resulting in same average temperature and velocity arranged by increasing total input power from bottom to top. One can observe the multi-modal nature of the distribution and the relative differences

In-plane elastic modulus of coatings as determined from in-situ coating curvature measurements also shows high variability, similar to the coating attributes such as deposition efficiency. Through thickness elastic modulus determined using instrumented indentation also shows high variability (Figure 68).

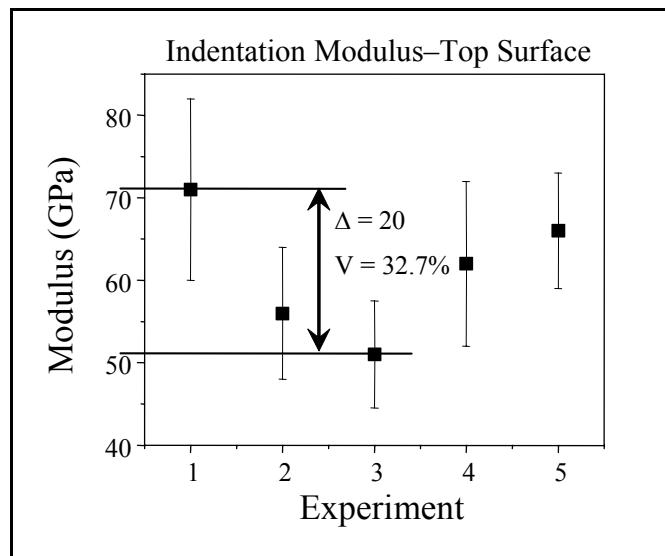


Figure 68: Through thickness elastic modulus from instrumented indentation showing significant variation for the five experiments which resulted in same average temperature and velocity

If average temperature and velocity were sufficient to describe the spray stream, such high variability in in-flight state (ensemble), coating build-up and properties would not be observed between these process conditions that resulted in the same average temperature and velocity.

5.2.3.2 Same T-V: Large Parameter Space Vs Smaller Parameter Space

Results from the previous set of experiments (*set A*) provided the range of variation possible in the spray stream, coating attributes, microstructure and properties when the average temperature and velocity were quite closely controlled by varying the plasma forming torch parameters in an *unrestricted wide parameter space*. Such a wide parameter space (large change in all three primary parameters) would not be typically used in process control though it is not uncommon to observe large changes in few parameters.

In order to understand how significant the observed variability of those coatings are, we compare here data from another set of experiments (*set D*), where the temperature and velocity were controlled similar to the previous experiments but within a *closely controlled and restricted narrow range* of plasma forming torch parameters. Figure 69 is a comparison of variability at different stages in the process for both sets of experiments.

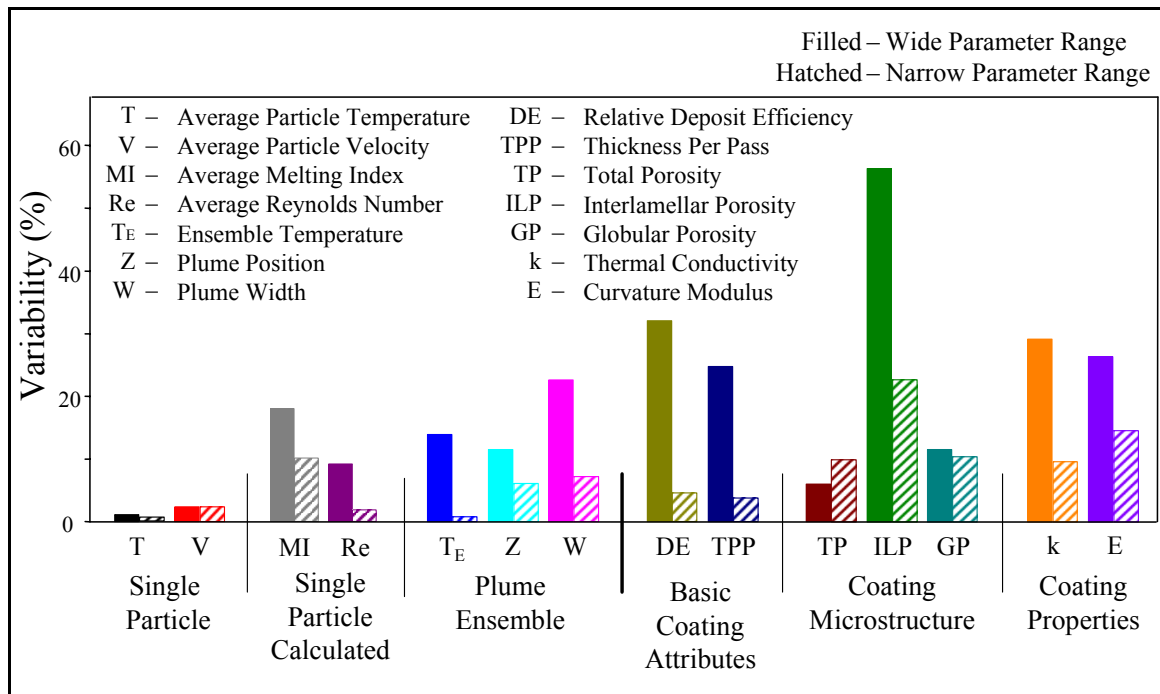


Figure 69: Achieving similar average temperature and velocity - comparison between using wide range of torch parameters Vs small range of parameters. Narrow parameter space results in lesser variability

Average temperature and velocity as well as plume position (Z) all show comparable variation due to the control exercised. Clear difference could be observed in ensemble temperature and plume width. From the in-flight status of the process, clear improvement in the ensemble properties could be observed when the parameters are controlled in a narrow space. This suggests a more streamlined and controlled process. Variability in relative deposition efficiency and thickness per pass corroborate this. Such a stringent and strict level of process control is atypical in industry.

Total porosity from experiment *set D* shows slightly higher variability compared to experiment *set A*. The variability in interlamellar porosity has halved, although still quite high. Variability in globular porosity is comparable to experiment *set A*. These are indicative of two things – (i) a more controlled coating assemblage between the different coatings when the parameter range is small and the temperature and velocity are controlled and (ii) the accuracy or precision of measurement of these microstructural features from image analysis of optical images may not be sufficient to clearly establish difference between coatings that are not significantly different.

Through thickness thermal conductivity and in-plane curvature modulus show reduced variability when temperature and velocity are controlled using a restricted narrower torch parameter space (*set D*). Again, the variability observed is not small though reduced. These are perhaps the limits of resolution of the respective techniques, which needs to be investigated further.

Despite the limitations, some significant differences could be observed in the in-flight state of the process and in the basic coating attributes, which are clear indication of the difference in the state of the process with and without restriction in process space.

5.2.3.3 Scope of the Phenomenon: Examining Feedstock Morphology

In order to understand if the observed variation in experiment *set A*, is unique to the hollow spherical morphology or if it a general phenomenon, similar experiments were conducted with the two other commonly used morphologies namely polyhedral (FC) (experiment *set B*) and solid spherical (AS) (experiment *set C*). Average particle temperature and velocity was maintained the same (within the range of $\pm 10^\circ\text{C}$ and $\pm 2\text{m/s}$ respectively) by varying the plasma forming torch parameters *widely*. In both these cases, the parameters were not varied as widely as in experiment *set A* with the PD feedstock.

Figure 70 shows the variability for the polyhedral morphology feedstock (FC). Melting Index shows significant variability comparable to the variability observed in thickness per pass. The ensemble temperature shows higher variability and plume width shows even higher variability. The extent of control established in controlling the plume position by injection optimization is reflected in the low variability in Z . The variability in microstructure and the properties are also high. It should be noted that the variation in torch parameters is smaller compared to experiment *set A* with PD feedstock.

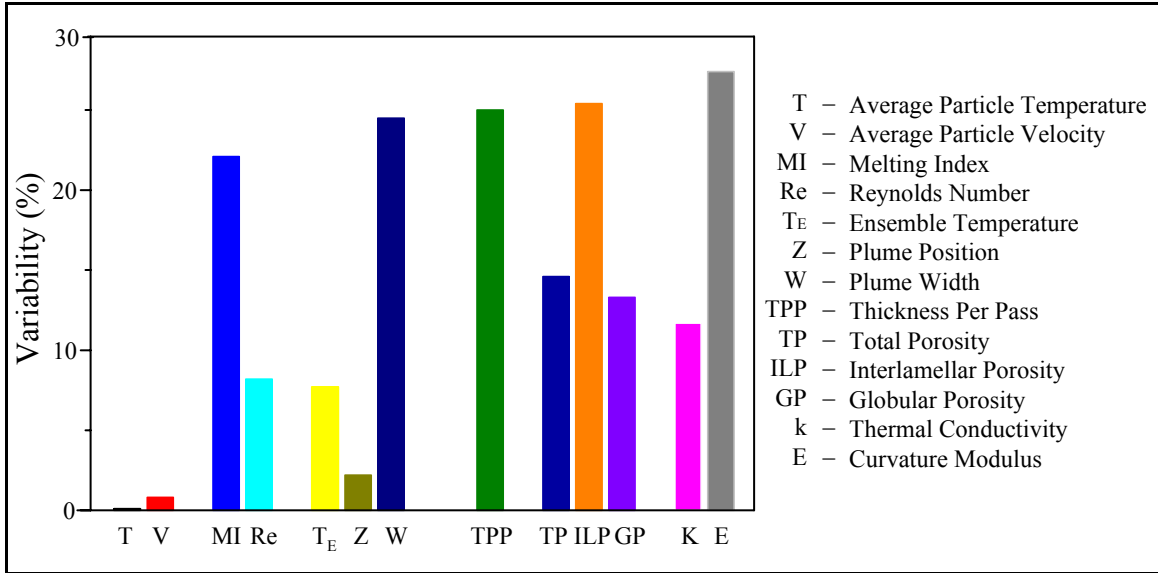


Figure 70: Assessment of variability within experiment set B – FC morphology

For the most part, *set C* experiments also exhibit high variability (Figure 71), especially in deposition efficiency and in thickness per pass of the coatings. The difference in this case is the relatively smaller variability in the plume properties and the very high variability in microstructural characteristics. Thermal conductivity shows low variability, while curvature modulus shows high variability. Melting Index shows significant variability, which could potentially hold the key to further the understanding.

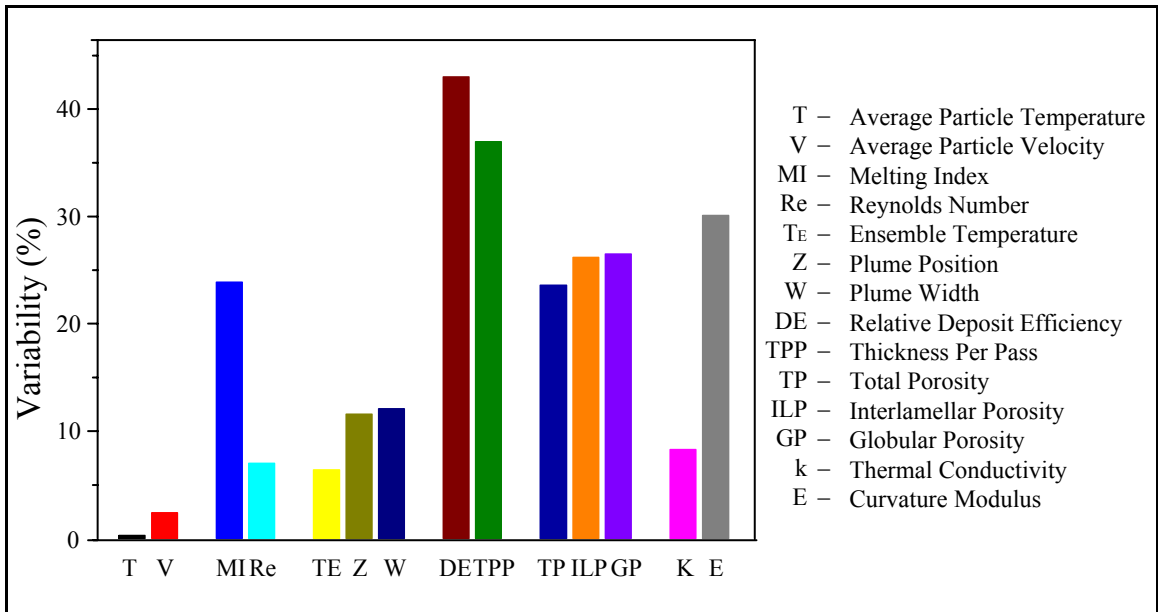


Figure 71: Assessment of variability within experiment set C – AS morphology

From these four sets of experiments, the following observations could be made

- Controlling average particle temperature and velocity does not appear to control completely the in-flight state of the process
- Basic coating attributes such as deposition efficiency and thickness per pass vary significantly
- Microstructural characterization does not appear to be very consistent though they project a higher variability overall. Perhaps limits of resolution/sensitivity reached in some cases. Needs further understanding
- Variability in thermal conductivity does not appear to correlate very well with the variability in microstructure. Needs further investigation to understand the microstructural characteristics and their relation to the properties
- Curvature modulus shows high variability even in the case of highly controlled process (*set D*). This could be due to reaching the limits of the curvature technique, which needs further understanding

5.2.3.4 Examining Correlations between Process and Coatings

The presence of large variation in coatings despite the controlled average particle temperature and velocity is established. It is clear that these variations are due to the changes in plasma forming torch parameters since the deposition conditions and substrate conditions were not changed. But the real source of these variations has not been understood in terms of in-flight state of the process. An attempt is made to understand any correlations that might exist between the process and the coatings for experiment *set A*. First we explore the relation between the torch parameters and the plume properties and then the plume properties on the deposition efficiency.

5.2.3.4.1 Torch Parameters Vs Ensemble Spray Stream Characteristics

The three most significant torch parameters – namely the total mass flow (TMF), hydrogen ratio (HR) and arc current (I) – have been correlated to the ensemble temperature by least square fit. Figure 72 shows the scaled estimates of the parameter and their combinations that have the most influence. It can be seen that all the three primary variables have a negative impact, which means that an increase in any of the three variables will result in a drop in temperature. This is in contrast to previous observations from first order process maps [146, 150], where HR and I show positive influence, while TMF shows negative influence of small magnitude.

When the ensemble particle temperature was plotted against the total input power (Figure 73), good correlation was observed with trends similar to several studies reported widely in the literature. A plot of the plume width as a function of the primary gas flow (Figure 74) shows widely reported trends with a very good correlation.

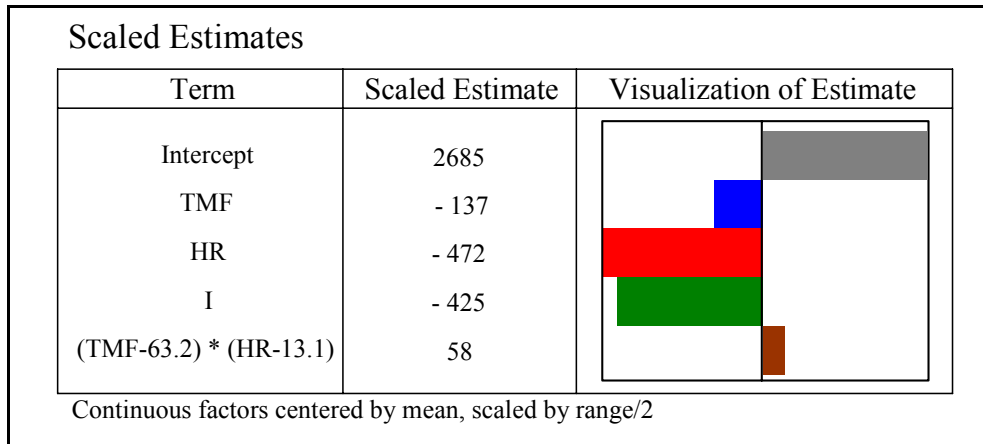


Figure 72: Ensemble temperature dependence on total mass flow, hydrogen ratio and current

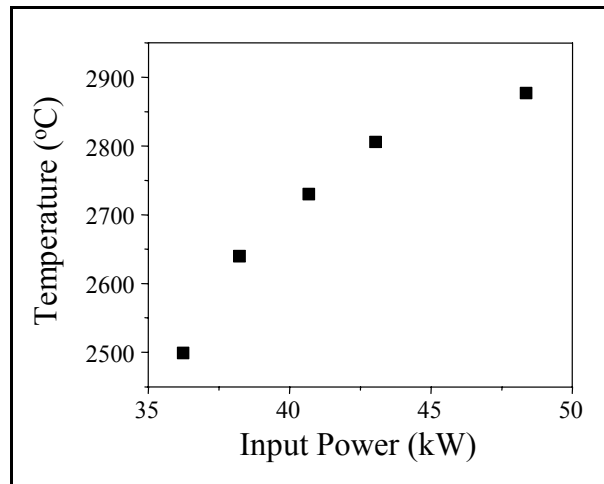


Figure 73: Ensemble temperature as a function of input power

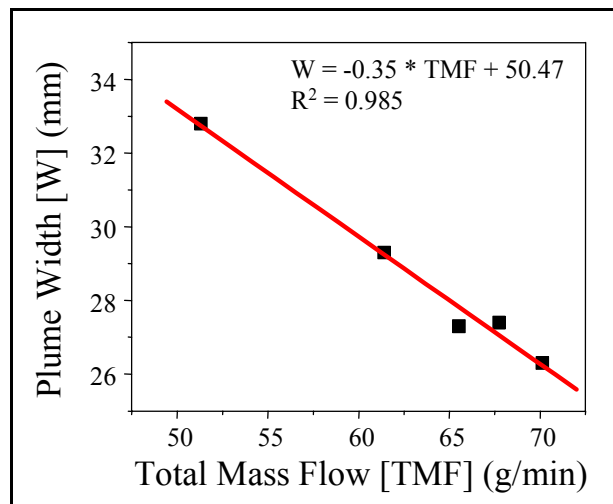


Figure 74: Plume width as a function of total mass flow

5.2.3.4.2 Ensemble Properties Vs Deposition Efficiency

Plume width has been observed to vary very linearly with total mass flow of gases (Figure 74). Lower total mass flows result in wider slower plasma jet, which results in better melting of particles due to low velocity and longer dwell times in the plasma. In this case though, the plume widths are different but the particle velocities are comparable. The process condition with wider plume has resulted in lower deposition efficiency (Figure 75), which is against the widely accepted trend. Relative deposition efficiency is observed to decrease as a function of increasing ensemble temperature (Figure 76), which is again not expected and against any current understanding [143, 146, 150, 151].

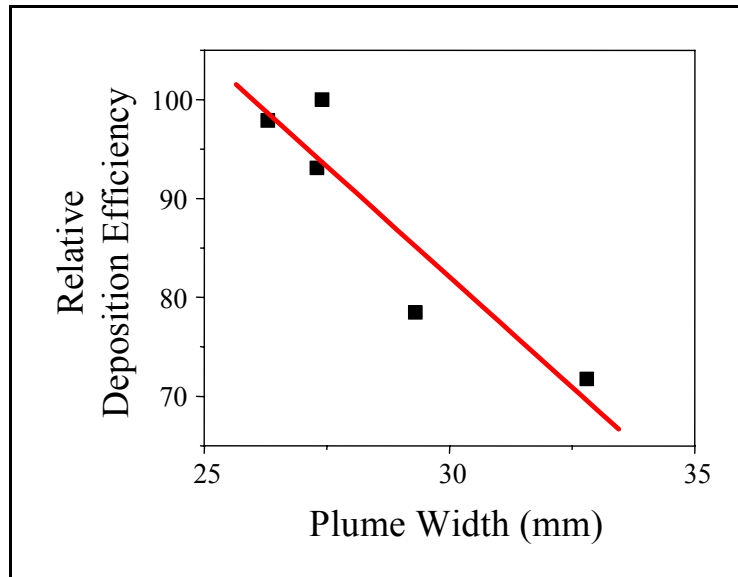


Figure 75: Deposition efficiency varying as a function of plume width

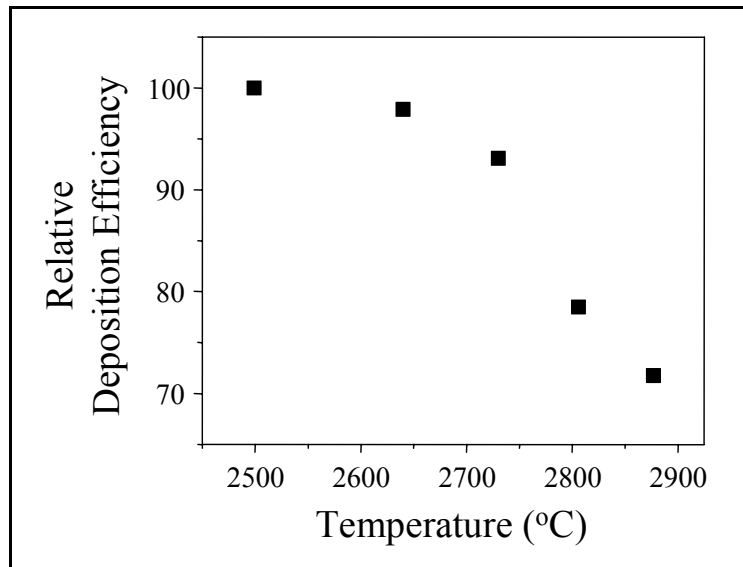


Figure 76: Deposition efficiency as a function of temperature

5.2.4 Summary and Conclusion

It is widely accepted that average temperature and velocity control the microstructure and properties of coatings to a first approximation. Based on some of the recent findings, we questioned the sufficiency of average temperature and velocity to describe the spray stream completely. To address this, systematic experiments were conducted such that similar average particle temperature and velocity were achieved by varying the plasma forming torch parameters widely. This was possible due to relating three independent plasma forming hardware variables to two particle state variables resulting in set of equations with multiple solutions.

The variability observed in the in-flight plume properties (ensemble temperature and plume width), coating attributes (deposition efficiency and thickness per pass), coating microstructure (porosity) and properties (thermal conductivity, in-plane curvature modulus) are significantly large. This is true for all three morphologies of YSZ feedstock, namely hollow spherical, polyhedral and dense spherical. On comparing this variability with the same from average temperature and velocity from narrow parameter range, one can understand/observe the severity/extent of variability. *This brings out the insufficiency – necessary but not sufficient – of average temperature and velocity to completely describe the spray stream.*

Current approach to process monitoring and control rely primarily on monitoring/controlling average particle temperature and velocity with the torch parameters varied within some allowed space, perhaps not as much as in this study. But this study points out the limitation of such an approach since the primary monitored/controlled variables are not sufficient and it is not a true in-flight process control since the torch parameters also need to be monitored.

An attempt to understand/explain the variation observed in coatings with respect to the in-flight plume properties and/or other established simpler parameters such as input power does not result in understandable correlations. Melting Index could not capture the in-flight state of the process / spray stream effectively. Though average particle temperature does not show much variation the distributions show noticeable differences. This clearly suggests that average temperature is not an accurate representation of the thermal component of the spray stream. These distributions along with other plume characteristics could hold the key to establishing a better link between the in-flight state of the process and the coatings.

This study also points out the limitations in the use of currently known and established parameters in explaining the link. It is perhaps due to the simplified “linear” nature of the parameters considered, which work well in a broader sense. This calls for methodologies to calculate parameters such as energy density and molten content of spray stream, which could better account for the complexities, non-linearity and dimensions of the process space in order to describe the spray stream to explain the observed coating characteristics.

5.3 Examining Temperature Distributions and Particle Melting

5.3.1 Introduction

Particle temperature distributions have been observed to be multi-modal, to completely describe which average is not sufficient. Group parameters such as Melting Index offer some insight into the melting of individual particles but not at the spray stream level [161]. Melting Index distributions are multi-modal too. This is perhaps the reason why temperature and velocity are insufficient (necessary but not sufficient) to describe the spray stream in order to completely depict the process downstream.

Due to the dynamic nature of the spray stream and its dependence on other primary variables it becomes necessary to understand and describe the spray stream in order to completely shift the monitoring and control to the in-flight state of the process. Studies have suggested the importance of temperature, velocity and molten state or molten fraction of the spray stream [28, 148]. Of these the only parameter that is not directly measurable is the molten fraction in the spray stream. In this study we explore the possibility of calculating this molten fraction from measured and calculated data based on analysis of temperature and Melting Index distributions. Attempt is made to compare the molten content in spray stream calculated from experimental analysis with that from simulation results using model established by Wan et al. [186].

5.3.2 Particle Melting Index

In-flight sensors have made possible measurement of temperature, velocity and size of individual particles as well as ensemble temperature, velocity, size, shape and trajectory of the spray stream. Velocity measurement is the most precise and size is the least precise, due to their respective principle of measurement, for single particle measurements. Particle temperature measured is not the temperature of the particle as a whole but it is the surface temperature of the particle with some contribution from the sub-surface due to non-contact pyrometry.

In the processing of high melting point low thermal conductivity materials, complete melting of the particles is of concern. Since the temperature measured does not tell about the melting status of the particle, a group parameter called Melting Index (MI) (Equation 5) was defined by Vaidya [147] as a simple combination of the particle temperature, size and dwell time (which is a function of the velocity of the particle and the spray distance; assuming constant acceleration of the particle) [147]. The validity of this group parameter was established by relating it to the splat characteristics [146] and deposition efficiency [194].

$$M.I. = \frac{T \Delta t_{fly}}{D}$$

Equation 5

Where, T is the measured (surface) temperature of the particle

D is the size of the particle

Δt_{fly} is the time of flight of the particle (Equation 6)

$$\Delta t_{fly} = \frac{2L}{V}$$

Equation 6

Where, L is the spray distance and V is the velocity of the particle

This was then numerically derived from first principles as a dimensionless group parameter by Zhang et al. [161] based on the ratio between the time required to melt a particle and the dwell time of the particle as shown in Equation 7.

$$M.I. = A \frac{24k}{\rho h_{fg}} \cdot \frac{1}{1 + 4/Bi} \cdot \frac{(T_s - T_m) \cdot \Delta t_{fly}}{D^2}$$

Equation 7

Where,

k is the thermal conductivity in liquid state (ideally at the T of the particle)

ρ is the density of the material in its liquid state (ideally at the T of the particle)

h_{fg} is the enthalpy of fusion

T_s is the measured surface temperature of the particle

T_m is the melting point of the material

D is the size of the particle

$$A = \frac{(T_f - T_m)}{(T_s - T_m)} \text{ (is taken as 1 due to unavailability of } T_f \text{)}$$

Equation 8

$$Bi = \frac{hD}{k_l}$$

Equation 9

h is the heat transfer coefficient

k_l is the thermal conductivity of the liquid material

By this definition, a Melting Index value of more than 1 will be completely molten and less than 1 should not be completely molten. But using the equation thus derived, it is possible to calculate a negative Melting Index due to the use of $(T_s - T_m)$ term instead of T_s . Melting point of the material used in the calculations for YSZ is almost always above the mean of the particle temperature distribution, resulting in negative numbers more often than not.

5.3.2.1 Identifying Particle State Regimes in the Melting Index Scale

The Melting Index calculated does not provide information on the exact extent of molten content of each individual particle. Even reference points are not available in the Melting Index scale even to identify the three categories of particles that could be present in the spray stream, namely completely molten, partially molten and unmolten.

To address these issues we turn to the particle temperature distributions. The particle temperature distribution for YSZ has been found to be multi-modal instead of normal distribution as it was always considered (Figure 77). When the distribution is fitted for its underlying distributions, it has been found that the peak of one sub-distribution occurs at about the same temperature for various process conditions (Figure 78). This temperature has been identified and verified to be the melting point of the material as measured by the sensor used [158, 200]. One can note the difference in melting point obtained from these distributions ($\sim 2500^\circ\text{C}$) and the melting point reported in literature (2680°C). The deviation from equilibrium/literature melting point has been attributed predominantly to the error in temperature measurement and the calibration of the sensor.

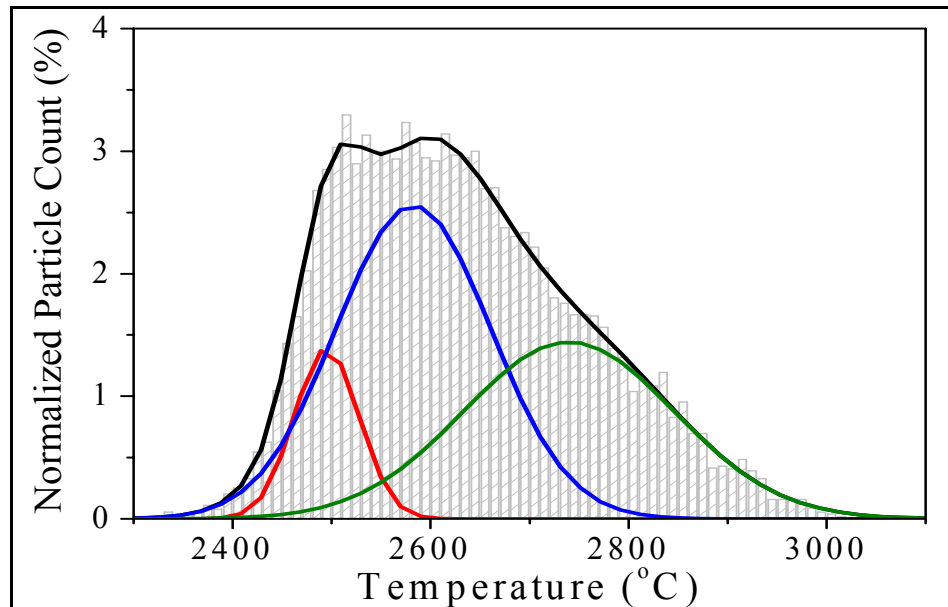


Figure 77: Temperature distribution fitted with the underlying peaks. Red color represents the melting peak consisting of partially molten particles

By using this melting point in Melting Index calculation, we can at least establish one reference point in the Melting Index scale – Melting Index of 0 means that the particle is partially molten because it lies within the melting peak.

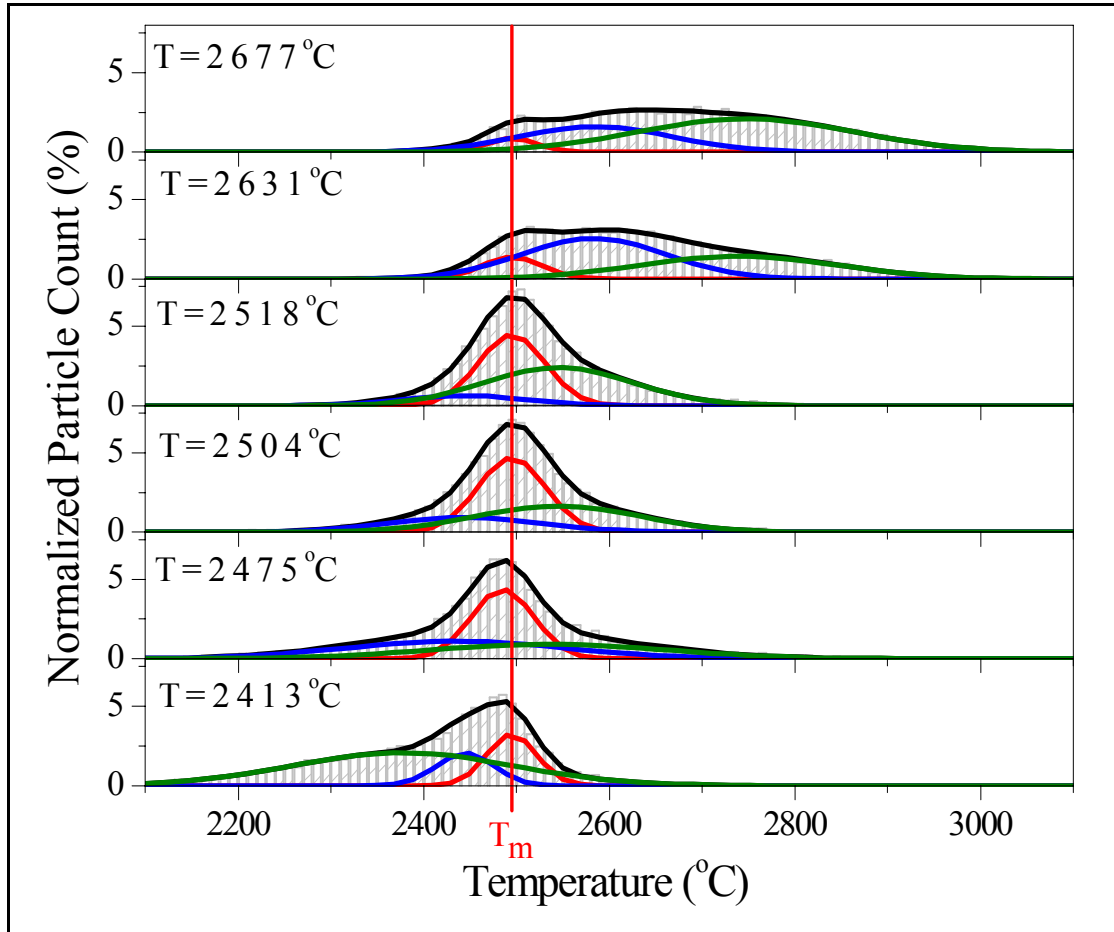


Figure 78: Particle temperature distribution against normalized particle count for the different process conditions exploring the extremes of the process space. Shift in temperature distribution from left to the right (low temperature to high temperature) can be observed with increasing average temperature (bottom to top)

To identify the Melting Index regime of partially molten particles, we plot the distribution of Melting Index and fit the underlying peaks for a few widely differing process conditions (Figure 79). As these Melting Index distributions shift from the unmelted side to the melted side on the Melting Index scale (for the different process conditions) one can observe the melting peak (red color) at the invariant Melting Index of zero. This peak comprises of partially molten particles. The blue and green peaks comprises of either completely molten particles or completely unmolten particles depending on whether they are along the positive axis or negative axis, respectively.

In cases where there is a significant portion of the entire distribution centered on the zero of Melting Index, the width of the melting peak for the different conditions is

similar. Based on this width of the melting peak the reference points on the Melting Index scale have been identified to be about ± 0.01 about the zero of Melting Index. Based on this, fully molten, partially molten and un-molten particles can be identified. This can be used to calculate the molten content of spray stream.

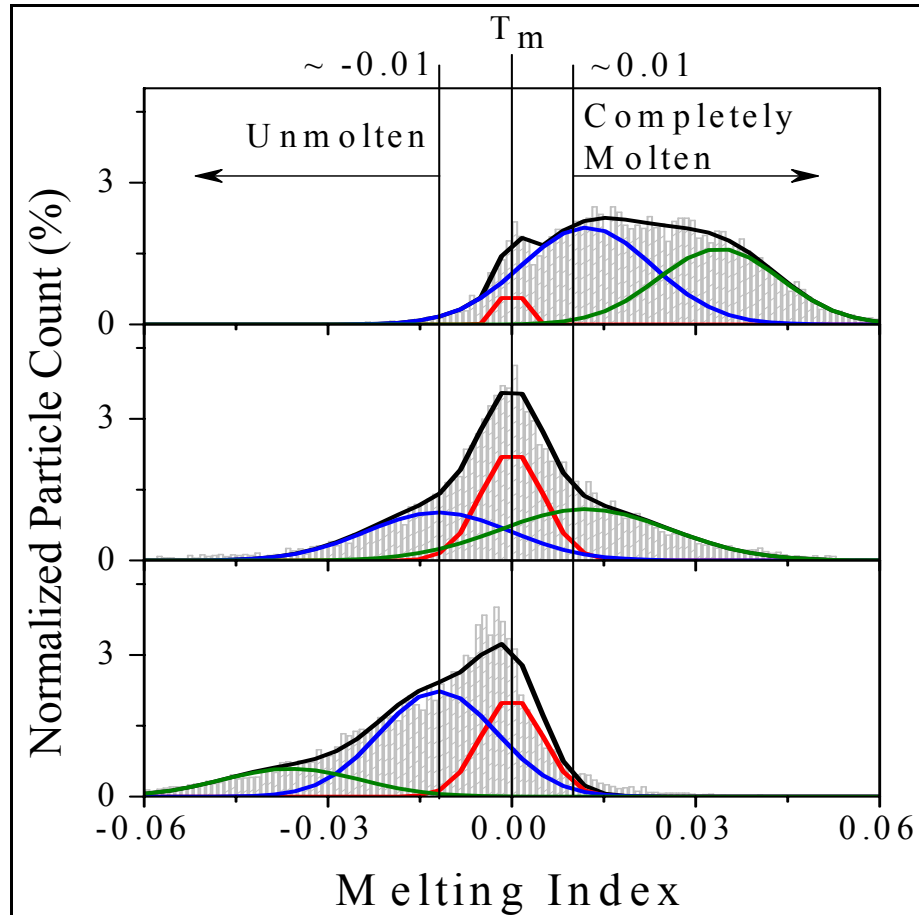


Figure 79: Melting index distribution with the melting status regions identified. Red peak – melting peak (partially molten particles); Blue peak and Green Peak and either completely molten or completely unmolten depending on whether are located in the positive or negative side respectively

5.3.3 Spray Stream Melting Index

From these observations it is clear that the particles that have crossed the melting barrier (red color peak) and contribute to the sub-distributions on the right side of the melting peak are completely molten, while those that have not contribute to the sub-distributions to the left and are unmolten. Those particles that contribute to the melting (barrier) peak are partially molten, typically to varying extents. This forms the basis for Spray Stream Melting Index (SSMI).

On a simpler note, if there are two process conditions such that the average temperature is almost the same while the velocities are very different, the condition at

lower velocity would be better melted due to longer dwell time in the plume. One such case is shown in Figure 80. It can be seen that the lower velocity condition has larger area to the right of the red color peak. This again shows that area to the right of the red color peak corresponds to the molten content in the spray stream and that the peak itself corresponds to the melting point.

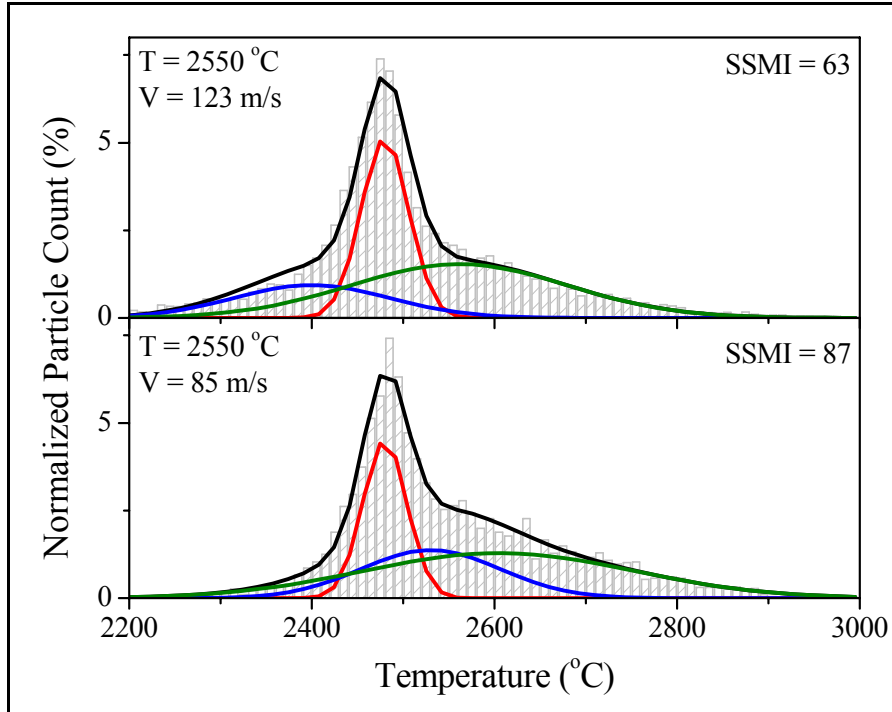


Figure 80: Particle temperature distribution for two different process conditions with same mean temperature but different mean velocities. One can observe the shift in the sub-distributions, which forms the basis for Spray Stream Melting Index

5.3.3.1 Calculating Spray Stream Melting Index From Distributions

Spray Stream Melting Index is calculated as the ratio of sum of area under the completely molten peaks and a factor of the area of the partially molten peak to the total area under the whole distribution (Equation 10).

$$\text{Spray Stream Melting Index} = \frac{(1 * A_m) + (0.5 * A_p)}{A} * 100$$

Equation 10

Where, A_m is the area under the molten peaks, A_p is the area under the partially molten peak and A is the total are under the distribution. 50 % of each particle under the partially molten peak is assumed to be molten.

5.3.3.1.1 Applicability

Since Spray Stream Melting Index is the molten content in the spray stream, it should correlate to the deposition efficiency of the coatings. An attempt has been made to correlate Spray Stream Melting Index to the relative deposition efficiency of coatings (Figure 81) for (i) second order process map - influence of spray stream, (ii) feedstock size distribution and (iii) similar average temperature and velocity for PD morphology.

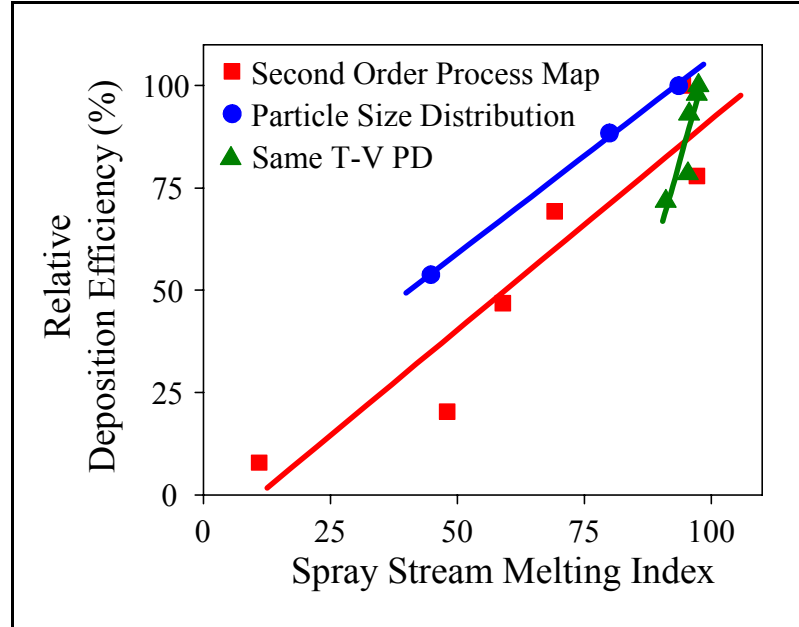


Figure 81: Correlating Spray Stream Melting Index to relative deposition efficiency for the coatings obtained from (i) Second Order Process Map – red square (refer section 6.2.1), (ii) Feedstock size distribution – blue circle (refer section 6.3.3.1.1) and (iii) Same T-V PD – green triangle (*Set A exp*; refer section 5.2.3.1)

In all cases considered here, Spray Stream Melting Index correlates well to the relative deposition efficiency. This validates the physical concept of Spray Stream Melting Index to describe molten content in the spray stream to ultimately explain the observed deposition efficiency as well the technique used to calculate it from temperature distributions.

The intercept of the linear fit in Figure 81 is not zero perhaps due to the limited range of the process explored with respect to melting, unaccounted factors influencing deposition such as splashing of splats and ricocheting of particles (different for these process conditions), limitations in sensing ‘all’ particles and/or the use of relative deposition efficiency instead of absolute. It can be seen that for the case of second order process maps, the intercept is closer to zero than the other cases since a fairly large process space was explored.

5.3.3.2 Calculating Spray Stream Melting Index Using Individual Particle Melting Index

Another approach to obtain Spray Stream Melting Index in a similar normalized form is using the volume ratio of molten particles in the Particle Melting Index distribution. This approach involves classifying each individual particle in the distribution as unmolten, partially molten and completely molten based the temperature of the particle with respect to the melting point obtained from the temperature distribution.

Particles within ± 0.01 from the zero have been considered to be partially molten based on the width of the melting peak for a wide range of process parameters. Particles with Particle Melting Index less than this range are considered unmolten and those above this range are considered completely molten. Ratio of the sum of molten volumes to the total volume expressed as percentage would give Spray Stream Melting Index. Because it is not possible to determine exactly what fraction of the particle is molten within the partially molten group, each particle is assumed to be 50% molten.

Figure 82 shows a plot of relative deposition efficiency as a function of Spray Stream Melting Index calculated from the volume based molten fraction for the second order process map experiments. Good correlation exists between the deposition efficiency and the Spray Stream Melting Index. It is worth to note that the accuracy of fit between deposition efficiency and Spray Stream Melting Index calculated from volume of individual particles ($R^2 = 0.93$) and from the distributions as a whole ($R^2 = 0.87$) are comparable. This suggests that the particle size distribution within each sub-distributions of the temperature distributions are comparable and are similar to the overall size distribution.

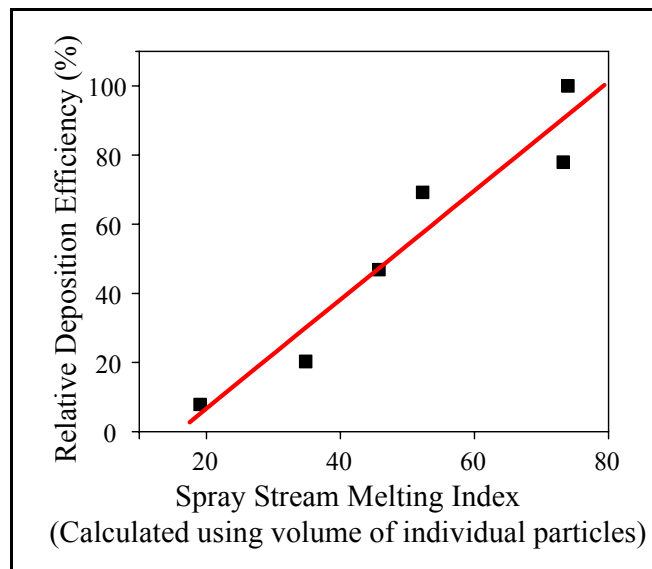


Figure 82: Comparison of volume percentage of molten particles obtained from the distribution and the deposition efficiency. Volume percentage of molten particles obtained from particle Melting Index of individual particles classified using the approach in Figure 79

Spray Stream Melting Index calculated using this method would be influenced by the calculation of particle volume (from measured particle size) for different feedstock morphologies. Since the Spray Stream Melting Index is normalized, the absolute sizes measured are not significant. But the volume calculated from size measurements on hollow spherical particles would be erroneous due to non-uniform shell thickness, presence of smaller particles within the hollow particles and the presence of solid spherical particles as well. In the case of polyhedral particles, the effective size measured may not be representative of the volume of the particle. Also the shape change in particles in-flight due to melting would influence the volume calculated from the diameter measured. Hence comparing morphologies using this method is not appropriate.

5.3.3.3 Applicability of Spray Stream Melting Index to Other Material Systems

The observation of melting point in the temperature distribution is the key to identifying the three different states of particles in the spray stream. Though it is not typical only to YSZ system, it has not been observed in other material systems as clearly. This is mainly due to the low conductivity and high melting point of YSZ.

Mn-Zn ferrite is a low melting low thermal conductivity material system, where one would not expect to observe the melting peak. But due to use of coarser feedstock in the size range of 20-200 μ (sample feedstock), the signature melting peak could be observed in the ferrite system by fitting the temperature distributions (Figure 83). The area covered by the coatings was somewhat irregular and not comparable across the different experiments. Hence the calculated Spray Stream Melting Index could not be related to the deposition efficiency. Though not completely validated, this suggests that the concept of Spray Stream Melting Index is not specific to YSZ and can be applied to other material systems

The particle temperature distributions have been observed to shift in a similar fashion for coarse molybdenum (Figure 84), which can be used to calculate the melting point and the spray stream Melting Index using a similar approach.

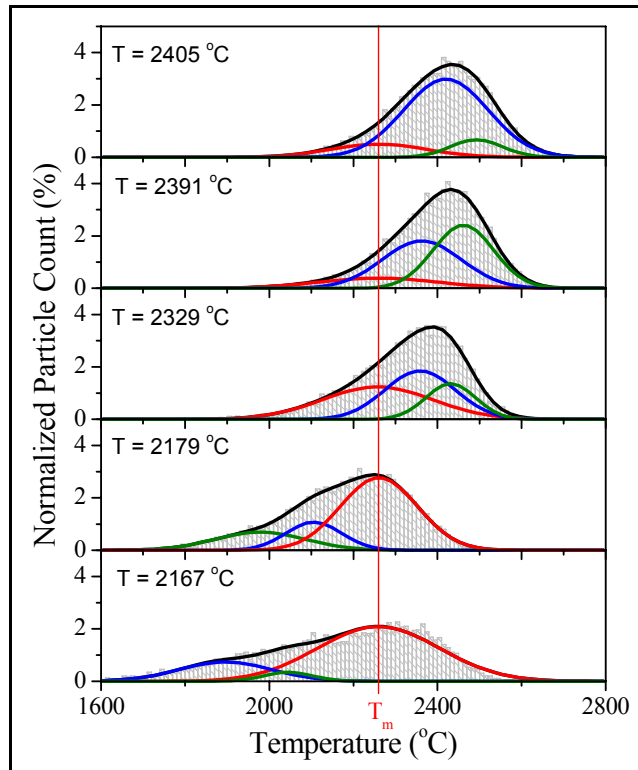


Figure 83: Particle temperature distributions for Ferrite system. Melting peak (in red) can be observed as well as the shift in distribution

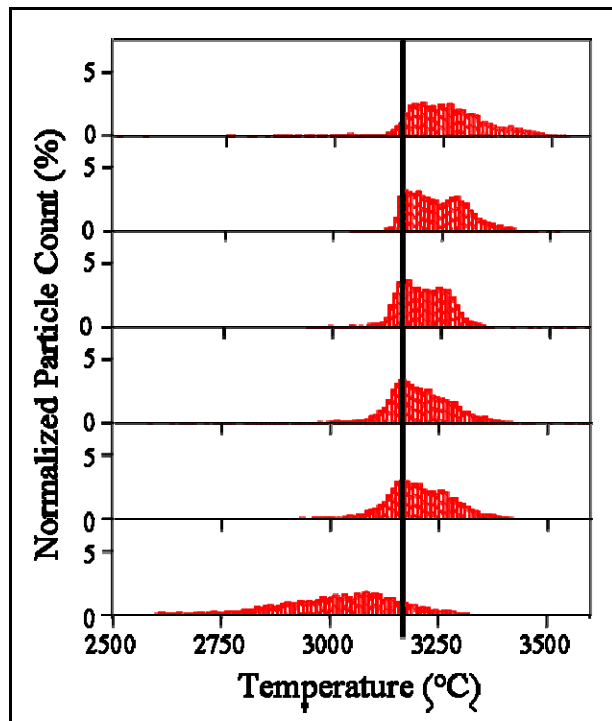


Figure 84: Particle temperature distribution for Mo under different process conditions. Shift in distribution could be observed

5.3.3.4 Comparing Experimental Data Analysis With Simulation

A series of experiments were conducted with the F4 torch using Ar-H₂ plasma with swirl flow with very different process conditions (extremes of the T-V space). The distributions from these experiments are shown in Figure 85. Three process conditions with very different distributions and SSMI (from these experiments) were chosen for simulation and comparison of molten content in the spray stream. From simulations, the location of the molten – unmolten interface and the molten – re-solidification interface are known for each particle. Hence the molten volume can be calculated for each particle, which can be normalized to the total volume of particles to obtain the ratio of molten content in the spray stream.

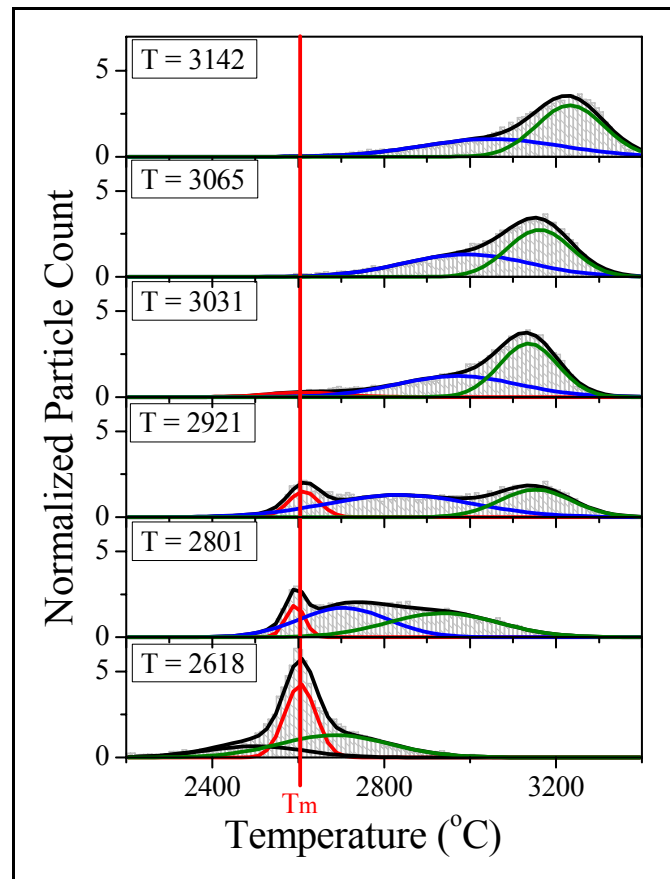


Figure 85: Particle temperature distribution for widely different process conditions for YSZ sprayed under Ar-H₂ plasma with a swirl flow. Shift in distributions can be observed with some distributions comprising only of completely molten particles

SSMI was calculated from experimental data of temperature distributions and particle Melting Index distributions as mentioned earlier. A plot of relative deposition efficiency and SSMI is shown in Figure 86. It can be seen that the experimental values (both methods; 100 mm spray distance) fit the observed deposition efficiency well ($R^2 \sim 0.9$). The simulated data (at 130 mm spray distance) does not fit the deposition efficiency well.

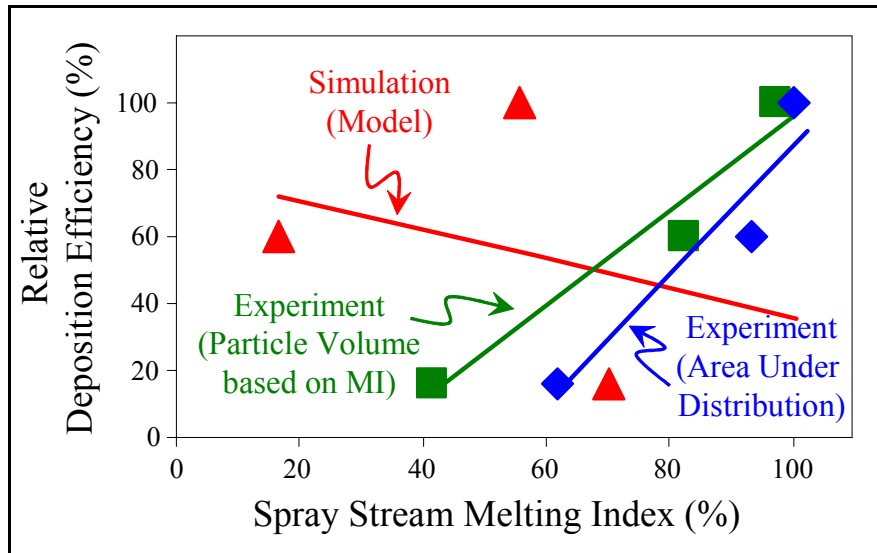


Figure 86: A plot of relative deposition efficiency Vs Spray Stream Melting Index (SSMI) for three process conditions. SSMI has been evaluated from experimental data using two different methods and from simulation data and compared. Both the experimental methods result in a good fit in the expected direction, whereas the simulation results show opposite trend with a poor fit

5.3.3.5 Limitations

Fundamental

- Once all the particles are either completely molten or unmolten, the Spray Stream Melting Index cannot be used to differentiate the distributions. Though the case of completely unmolten particles is very unlikely due to the highly uneconomical situation, completely molten scenario is possible in a wide variety of cases such as metals and/or fine particles. Spray Stream Melting Index can still be used to predict the deposit efficiency but the influence of superheating of particles on the splat formation and other related issues, such as in-flight oxidation, which also influences splat formation and coating build-up cannot be accounted for, and hence, the accuracy of prediction could be compromised
- Temperature of particles measured at the flow center has been used in these calculations. The ability of this distribution to represent the entire spray stream is limited. In the case of straight flow of gases (without swirl), the distribution of temperature measured at the flow center were similar to the distributions obtained by scanning across the entire spray stream
- Contribution from unmolten particles to the coating buildup and deposition efficiency are not considered though one can observe unmolten particles in the coating microstructure to a small extent

Data acquisition

- Spray Stream Melting Index is calculated from distributions of particle temperature, hence data from sufficient number of particles need to be acquired in order to be able to expose the peaks

- There exist limitations in particle sensing which could lead to insufficiency of temperature distribution to completely describe the spray stream (e.g. particles $< 5\mu\text{m}$ and the ‘cold’ particles are not measured).
- The ability of the sensor to locate the flow center could be compromised in the case of swirl flow of gases or when there is more than one flow center (which has been observed in 3 MB torch with swirl flow; it is not used in this study)

Data processing

- When the whole distribution is narrow and around the melting point (as measured from the distribution by the DPV) the whole distribution tends to be bimodal with the peaks of both the sub-distributions very close to the melting point. This makes it difficult to calculate the Spray Stream Melting Index for the different distributions that are similar but not the same, around the melting point. Though it can be argued that such distributions are rather rare in typical plasma spray processing of YSZ due to the resulting low deposition efficiency, it is one area where the ability of Spray Stream Melting Index is limited
- Under conditions where the distributions are bimodal but are not around the melting point, fitting three curves and two curves to calculate the Spray Stream Melting Index does not result in exactly the same Spray Stream Melting Index
- Manual post processing analysis is needed to fit the distributions to obtain Spray Stream Melting Index. After standardizing the fitting procedure and rigorous testing, it could be automated to calculate Spray Stream Melting Index to be used for real-time process monitoring/control

Other

- In predicting deposition efficiency, the influence of substrate conditions (chemistry, roughness, temperature etc...) is not accounted for. It is limited to assessing the influence of spray stream
- Of the partially molten particles, not 50% each particle is molten. There would be different extents of melting within that region. Hence that assumption could introduce some error

5.3.4 Summary and Conclusion

The temperature reported by the DPV 2000 sensor is based on measurement of surface temperature of the particle by non-contact two wavelength pyrometry. Since large gradients in temperature can exist within the particle due to the low thermal conductivity of YSZ, the surface temperature reported does not provide information on the melting status of the particle. Given that DPV 2000 concurrently measures size, temperature and velocity of particles, a more appropriate representation of the particle state can be made through the application of group parameters such as Melting Index (MI) and Reynolds Number (Re).

Melting index is a novel group parameter that essentially normalizes the measured temperature with reported size and dwell time (via velocity). Melting Index distributions are multi-modal, similar to particle temperature distributions. Hence average Melting Index does not clearly represent the melting status. This was also shown from the results in the previous section, where average temperature and velocity was maintained similar for five different coatings and Melting Index could not explain the observed deposition efficiency.

In this study, the multi-modal temperature and Melting Index distributions were analyzed to characterize the distributions. A melting signature has been observed in the distributions where the one of the fitted sub-distributions occur at the same temperature (melting temperature). The overall distribution could be sufficiently described by using three Gaussian sub-distributions in all cases except when the distributions are far away from the melting point, in which case the distributions could be sufficiently described using two sub-distributions. To a first approximation, the distributions shift depending on the average temperature (or Melting Index) but it has also been shown that the distributions could be manipulated significantly while retaining the same average temperature (and not significantly different average Melting Index). This is possible primarily due to the location of the experiments in the process space – higher degree of freedom at the center of the process space.

The distributions fitted for the sub-distributions points to an interesting approach to calculate the molten content of the spray stream. Those sub-distributions that at the higher temperature side of the melting peak are from completely molten particles, while those that are on the lower temperature side are from completely unmolten particles. This could be understood based on the location of each individual particle in a distribution with respect to the presence of a melting barrier at the melting point. Those particles that contribute to the melting peak are partially molten. Using this simple understanding, the molten content in the spray stream – Spray Stream Melting Index – can be calculated using temperature distributions based on the area under each sub-distribution. The same can also be calculated from individual particle Melting Index (calculated using the melting temperature identified from the distributions) by normalizing molten volume of all (individual) particles to the total volume of particles. Each method has its own limitations.

Spray Stream Melting Index calculated for a wide range of process conditions, feedstock size distributions has been shown to correlate well with the measured deposition efficiency (based on relative weight of coatings). This is an interesting finding given the significance of particle melting in splat formation and coating build-up. This approach provides a quantitative representation of the molten content in the spray stream, which can be used as an in-flight monitoring/control parameter as suggested by previous studies.

Chapter VI

6 Synthesis of Process Maps and Strategies to Alter Microstructure: Integrating Process Science and Material Properties

6.1 Introduction

As a consequence of the processing route, the coatings exhibit many different microstructural features that govern the final coating properties. We briefly outline three key aspects for further consideration in this chapter. They include influence of

- Particle state in-flight and spray stream characteristics
- Deposition conditions (deposition rate, angle of impact)
- Feedstock characteristics (morphology and size distributions)

6.1.1 Plasma Spray Conditions

It has long been appreciated that plasma spray offers a spectrum of process conditions and parametric states which allow “tuning” of the microstructure. However, this flexibility has also been an enigma in terms of process control. For instance, as a consequence of the process variations, the coatings exhibit many different microstructural features that govern the final coating properties. The differences in coating microstructure can arise due to the many process variables that affect the plasma flame including the primary plasma forming torch parameters and hardware design of the torch. Even when the plasma flame generated by a particular configuration of the torch is kept nominally the same, deposited coating structures vary considerably due to a difference in the feedstock characteristics and their interactions with the plasma flame [102, 146, 147].

Over the last decade, particle-flame interactions have been investigated quite extensively. A large number of measurement techniques have been developed and commercial instruments based on these have been applied to study the particle state in thermal spray processing [26, 32, 33, 152, 155-157]. The advent of such in-flight particle diagnostics has allowed assessment of the particle characteristics (velocities, temperatures, size distributions) and spray stream characteristics (plume width, intensity and trajectory). The influence of particle state on the deposit formation dynamics is much more complex and difficult for in-situ non-invasive measurement. As such the interrelationships between process state and deposit microstructure relies on correlations.

Nevertheless, the availability of these tools has significantly improved the sophistication of the plasma spray process with notable impact on reliability.

With the wide availability of these sensors in the 1990s, studies were focused on assessing the qualitative influence of the torch parameters on the particle state, namely temperature and velocity. The independence of particle temperature from velocity was established and qualitative understanding was established to control them independently [149]. Friis et al. [150] quantitatively related the influence of torch parameters (considering two of the three most significant torch parameters) on particle state and further extended it to understand the coating microstructure development in an effort to predict the coating structure and properties and to identify “process windows”. Vaidya [146] considered all of the three significant torch parameters (with optimized particle injection) and studied their influence on the particle state using a design of experiment. Figure 87 is a schematic representation of the progress in knowledge with respect to understanding the relation between torch parameters and particle state with the comprehensive use of sensors.

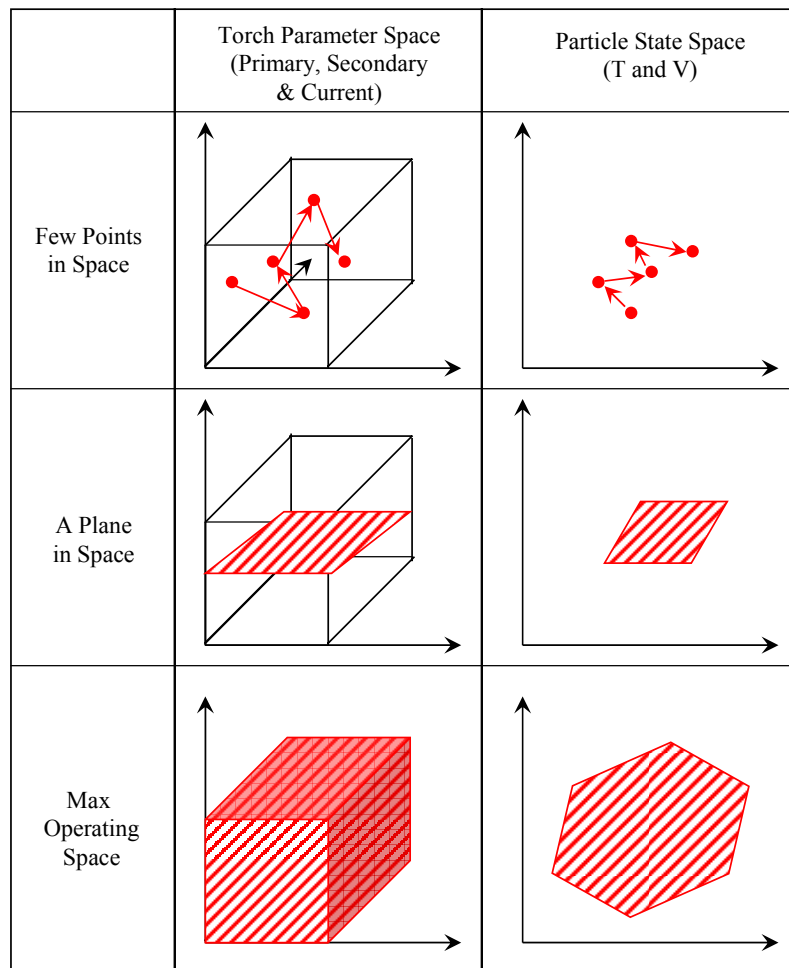


Figure 87: Schematic representation of the progressive knowledge in terms of exploring the process space using in-flight particle sensors

As a continuation of the first order process maps linking the torch parameters to the particle state, this study is directed at understanding the influence of particle state on the coating microstructure and properties. By exploring the possible range of microstructures and properties possible (for the given feedstock and hardware), the coating properties would be mapped to the particle state space. This would provide a means to select the process condition that would result in reliable coating.

6.1.2 Deposition conditions

In addition to feedstock characteristics and plasma spray parameters, substrate conditions and robotic manipulation also play a significant role in the deposit formation dynamics and the associated microstructure. Changes in deposition temperature can introduce large changes in coating properties. In an earlier paper Sampath et al. conducted a detailed integrated study on the effects of substrate temperature on the splat formation and coating properties for plasma sprayed YSZ. The deposition angle and robotic motion paths can affect both the shape of the deposition profile as well as the defect architecture [164]. Similarly deposition rate can affect the nature of the coating build-up process and affect the residual stresses. Several industrial corporations have sought to use these nuances to generate unique microstructures such as “dense vertically cracked coatings” or “segmented crack microstructure” to aid in coating compliance [140, 142, 144, 162, 201-204]. These technologies are now prevalent in industrial practice. In this study we consider the deposition conditions in detail and evaluate its influence on the coating properties.

6.1.3 Feedstock Characteristics

The feedstock material employed in the industry is made by a number of different processes. Each of these powder manufacturing methods results in unique powder morphology and different physical characteristics (such as shape of particle, density of powder and flowability). Depending on the manufacturing method, the purity and phase content of the powders are also different.

It is of significant interest to both the gas turbines and the thermal spray industry to understand the differences that arise due to the usage of these different powders, particularly since one can meet a requisite specification through any of the manufacturing approaches. Previous studies have indicated that when powders with different morphologies are injected into a plasma jet, the resulting particle characteristics (e.g. temperature and velocity) are very different [193]. As a consequence, the splat morphologies also vary which in turn result in distinct coating microstructures and therefore properties [102]. These past engineering studies also point to an intriguing possibility to combine starting morphology with process conditions so as to optimize the compliance and thermal conductivity of the coatings. Through the proposed process map concepts, it is feasible to achieve this goal as will be presented in subsequent sections.

6.2 Synthesis of Second Order Process Maps

6.2.1 Influence of Particle State

6.2.1.1 Experimental Details

The extremes in particle temperature and velocity resulting from extremes of process parameters from the design of experiment (section 5.1.2.1), were selected for this study. 7MB torch with N₂-H₂ plasma gas and polyhedral morphology feedstock were used. Injection was optimized for each experiment. Detailed diagnostics was done and deposits made on ICP samples. The deposits were characterized for microstructural features, thermal conductivity, through thickness indentation modulus and in-plane curvature modulus. Splats were collected on polished stainless steel substrates maintained at 270°C.

6.2.1.2 Results and Discussion

6.2.1.2.1 Establishing Particle State – Property Relation and Regimes

6.2.1.2.1.1 Particle State

Figure 88 shows a first order process map in terms of measured particle properties (average particle temperature and velocity) and calculated particle states (Melting Index and Reynolds Number). One can observe the widespread range of particle states covered in these experiments to understand the relation between particle state and coating properties. These data points are the extreme conditions from the first order process map presented in section 5.1.3.3.

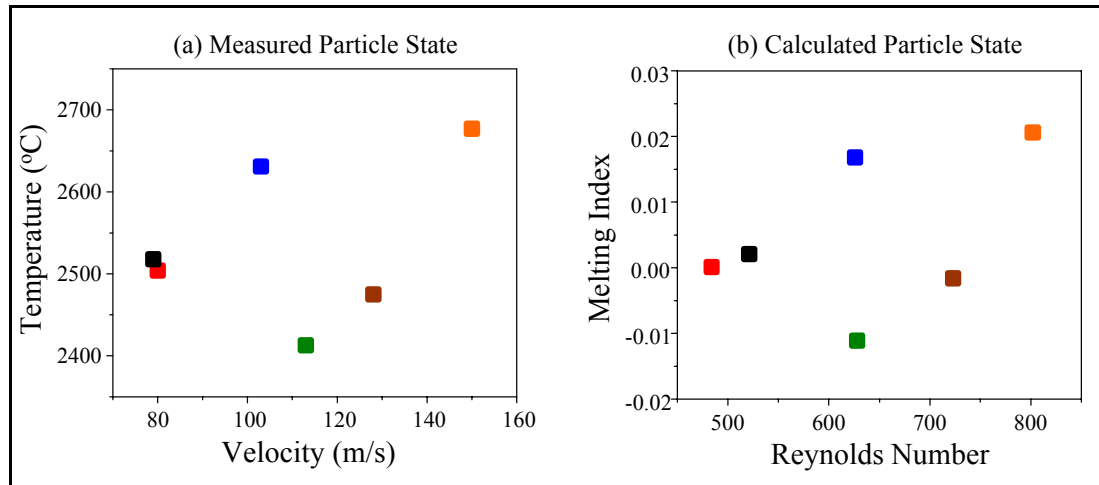


Figure 88: In-flight process space resulting from the extreme torch parameters. (a) Measured particle state - temperature and velocity and (b) calculated particle state – Melting Index and Reynolds Number

Particle velocity distributions are typically Gaussian whereas the particle temperature distributions are multi-modal shifting from one side of the melting point to the other (Figure 78) as the average temperature increases due to the change in torch parameters (corresponding to the points in T-V space in Figure 88). Melting Index distributions also exhibit multi-modal behavior and is shown in Figure 79. Detailed analysis of these distributions is presented in [158].

6.2.1.2.1.2 *Splats*

Figure 89 shows optical images of splats collected on stainless steel substrates superimposed on the MI-Re space. Disc shaped splats can be observed in all cases due to the high substrate temperature, though during making deposits the substrate temperatures were not identical in each of these case since the heating due to plasma jet is different for the different process parameters. Splashing could be observed at high Melting Index and Reynolds Numbers (orange color). Process conditions that resulted in low Melting Index and high Reynolds Number results in improper melting and hence the observed low area coverage of splats.

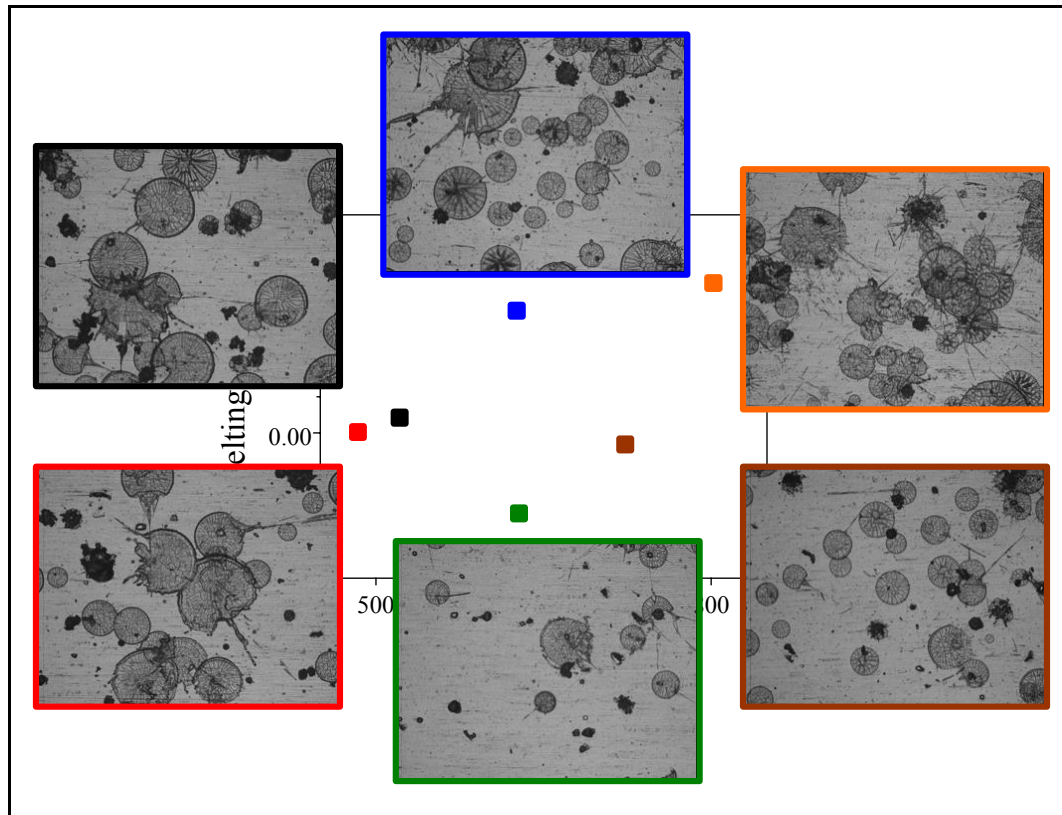


Figure 89: Splat micrographs superimposed on a plot of Melting Index Vs Reynolds Number. All images are at 200X. All splats are fairly disc shaped due to high substrate temperature (280°C). At very high MI and Re splashing can be observed (orange color). Low MI and high Re (green and brown color) results in poor melting, which is reflected in the area covered by the splats and by the smaller size of splats implying melting of fine particles

In order to quantify the splat morphology, flattening ratio was calculated from experimental measurements of splat volumes as well as from particle data from DPV using Madejski model [205] (section 3.4.1.1). In calculating FR from particle data, only particles with temperatures above 2550°C were used since only those particles would be molten and result in disc shaped splats, which were the ones measured experimentally. Figure 90 shows a plot of flattening ratio and Reynolds Number. Flattening ratio can be observed to increase with Reynolds Number. Experimental and calculated flattening ratios follow the same trend until very high Reynolds Numbers. The discrepancy in absolute values between experimental and calculated flattening ratio could be attributed to the choice of constants used in the calculation based on the model.

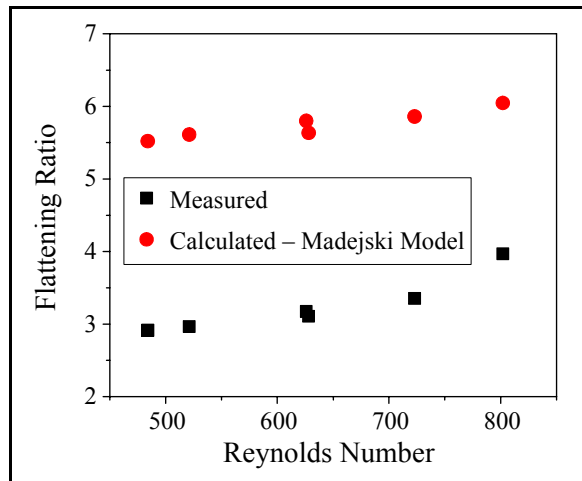


Figure 90: Splat Flattening Ratio (FR) as a function of Reynolds Number (Re). Red data points represent FR calculated from Madejski model and black data points represent measured FR from splats obtained on polished high temperature substrate. Good trend observed between measured and calculated values except at high Re

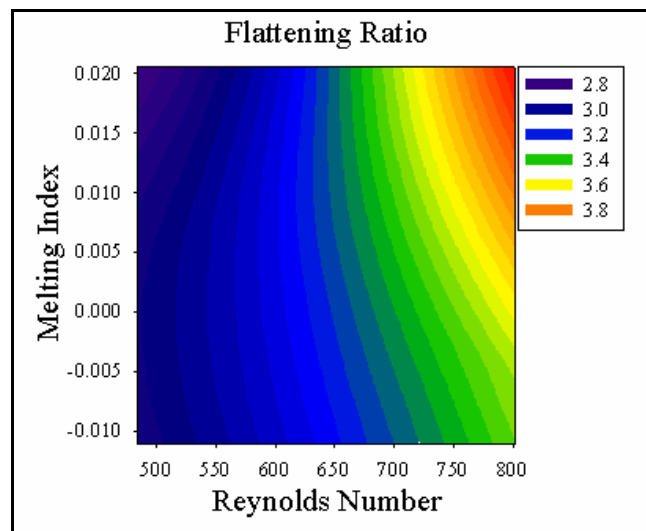


Figure 91: Contour plot of Flattening Ratio (FR) as a function of Melting Index (MI) and Reynolds Number (Re). Re has the most influence on FR

Figure 91 shows flattening ratio contours in the MI-Re space. This suggests a strong correlation between the flattening ratio and Re with some correlation to MI. This map can be used to select the flattening ratio required to achieve the number of interfaces per unit length.

6.2.1.2.1.3 Coatings

The basic attribute of coating build-up - deposition efficiency - is superimposed on the MI-Re space in fig. The deposition efficiency is higher when the MI is high and Re is low since it results in better melting due to longer dwell time in the plasma jet. The other extreme (low MI and high Re) results in the lower deposition efficiency due to shorter dwell time.

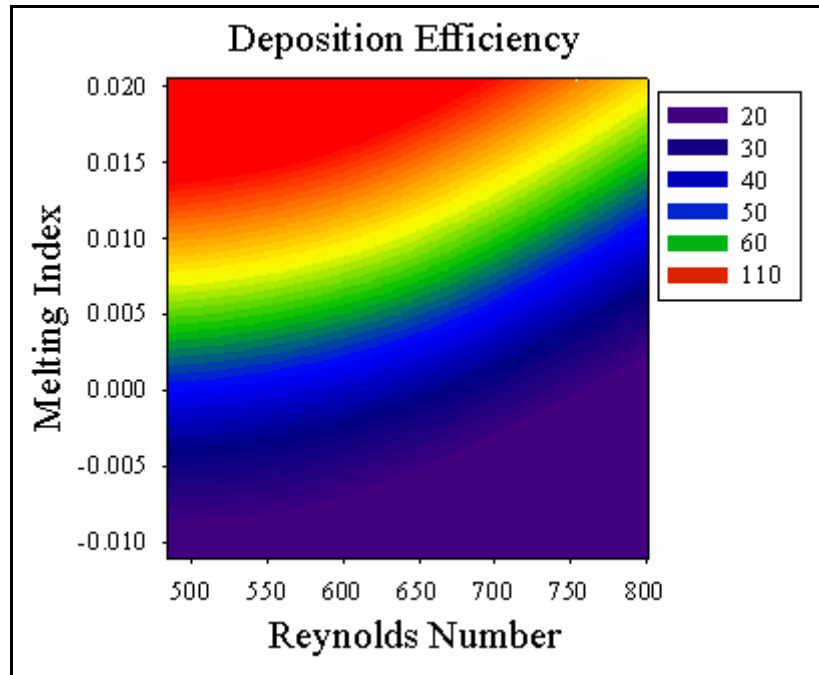


Figure 92: Relative deposition efficiency (DE) contour in Melting Index (MI) - Reynolds Number (Re) space. DE increases as MI increases and Re decreases due to improved melting resulting from longer dwell time of particles in the plume

Through thickness thermal conductivity, through thickness indentation modulus and in-plane curvature modulus are shown in Figure 93, Figure 94 and Figure 95 respectively in the MI-Re space. The two data points without property measurement (thermal conductivity and through thickness indentation modulus) are due to very low deposition efficiency and the resultant thin coating unsuitable for property measurement. In-situ curvature measurements were possible even on the thin coating though the accuracy would be less due to lesser deflection compared to thick coatings in other cases. Thermal conductivity as well as modulus increases with an increase in MI and Re due to the

improved wetting and spreading of fully molten particles and the higher impact velocities resulting in denser coatings.

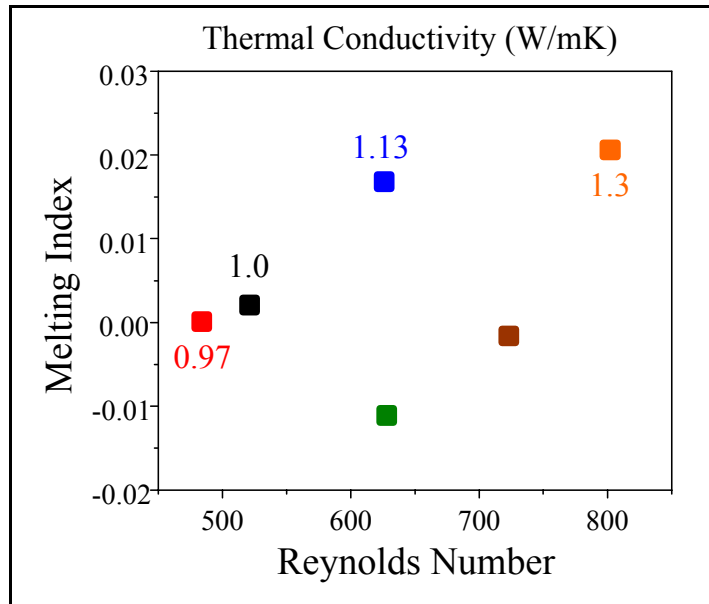


Figure 93: Through thickness thermal conductivity (k) measured by laser flash technique in the Melting Index (MI) – Reynolds Number (Re) space. MI contributes to k by better melting and hence better contact, wetting and spreading behavior of splats and Re contributes by better adhesion between splats during coating build-up

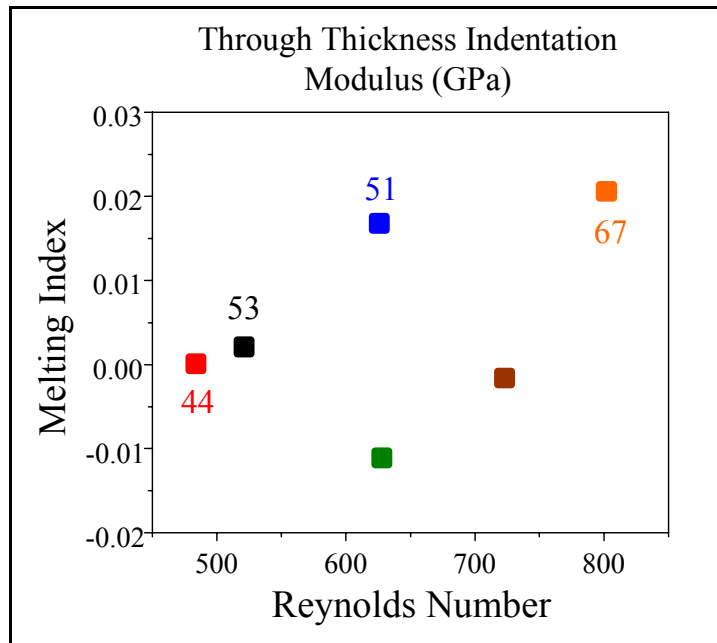


Figure 94: Through thickness modulus from instrumented indentation in the Melting Index (MI) – Reynolds Number space (Re). Modulus increases with both MI and Re. The jump in modulus from 44 to 53 is due to enhanced melting (44 is at the melting point whereas 53 is on the molten side)

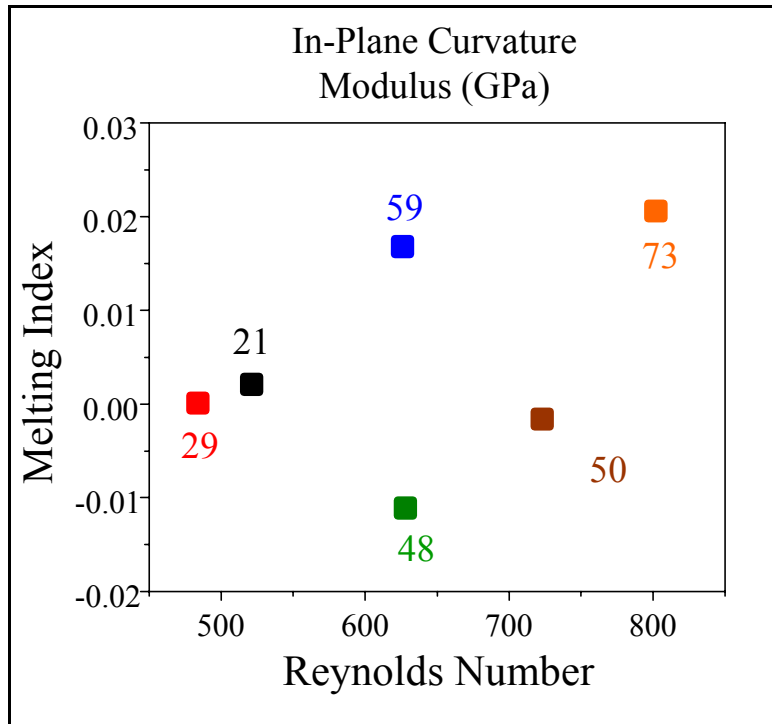


Figure 95: In-plane modulus from in-situ curvature shown in the Melting Index (MI) – Reynolds Number space (Re). Modulus increases primarily with Re though MI also has an influence

6.2.1.2.2 Identification of Regimes in the Particle State Space

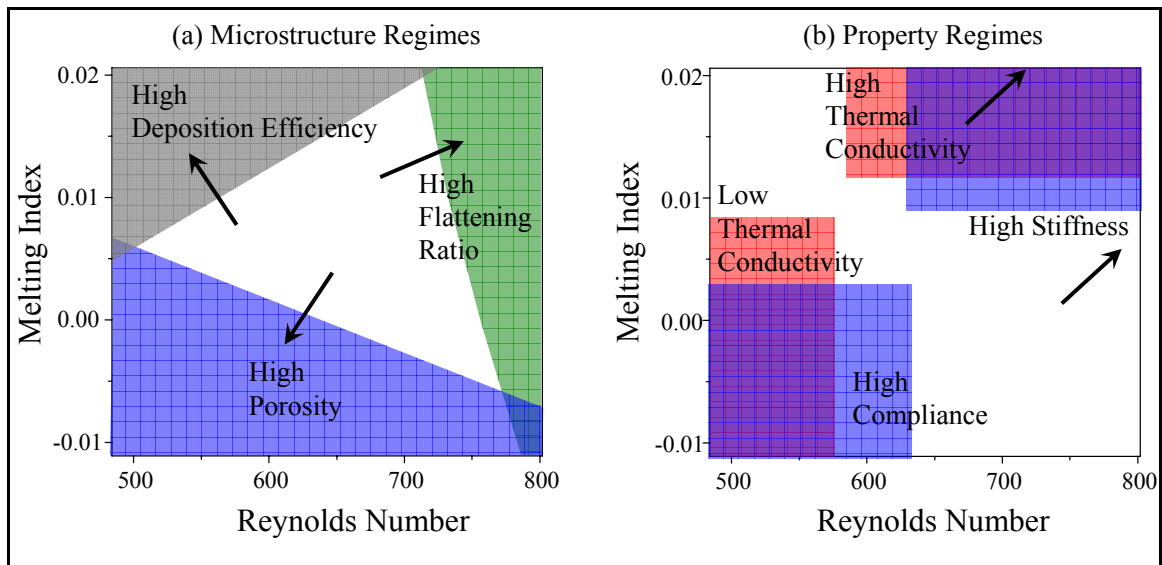


Figure 96: Microstructural (left) and property (right) regimes identified in the Melting Index (MI) – Reynolds Number (Re) space. Arrows indicate approximate direction of increase of property

Based on these measurements and results, characteristic regimes of coating properties has been identified and superimposed on the first order process map (Figure 96). Figure 96a shows the basic coating build-up and microstructure regimes and Figure 96b shows the property regimes. From this mapped regions, one can observe the qualitative correlation between the particle state, coating formation and microstructure and property regimes – (i) high porosity, low flattening ratio and lower deposition efficiency region results in low thermal conductivity and high compliance, (ii) high deposition efficiency, low porosity and high flattening ratio region results in high thermal conductivity and high coating stiffness. The compromise in achieving the required properties and achieving high operating efficiencies is also evident from this relation.

6.2.1.2.3 Identifying Design Window

These qualitative observations provide a simple way to identify the appropriate regime for the required coating. In order to optimize the process, a controlled and more comprehensive second order process map including full contour plots of property in the specific region needs to be established (Figure 97). This has been attempted with PD feedstock in this study due to its extensive use in the thermal spray industry for its ease of melting (hollow spheres) and the resulting low thermal conductivity and compliant coating. Though similar studies have been done in the past, they have been limited to identifying process windows based on microstructural features.

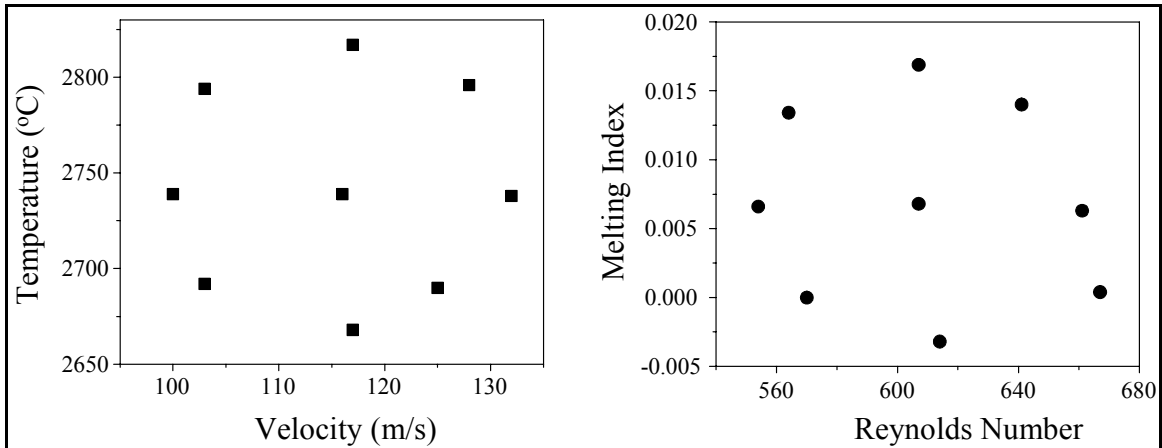


Figure 97: Particle state space designed and controlled to identify process windows for design

The following steps were followed in order to establish a controlled second order process map to identify appropriate process window.

- First order process map was established using a torch parameter design of experiment (similar to the one used in section 5.1.2.1 shown in Figure 53 following the same procedure including optimizing injection)
- The T-V region of interest was identified

- A T-V based design of experiment was adapted to established the second order process map (property maps)
- In order to control T and V, torch parameter vectors were established in the T-V space from the first order process map
- Appropriate tolerance window was set for each T-V condition to be achieved based on the error from the repeated experiments of the center condition of the first order process map
- Starting torch parameters were calculated for the selected/designed T-V conditions and then subsequently tuned to the required value

Controlled second order process maps relating particle state to thermal conductivity and in-plane and through thickness modulus are shown in Figure 98, Figure 99 and Figure 100 respectively. In order to identify appropriate process windows, the different property contours were superimposed as shown in Figure 101. This enables identification of different regions satisfying the same criteria set based on the three coating properties considered here. Figure 101 shows a few different combinations of parameters that can be achieved and the region in which they can be achieved.

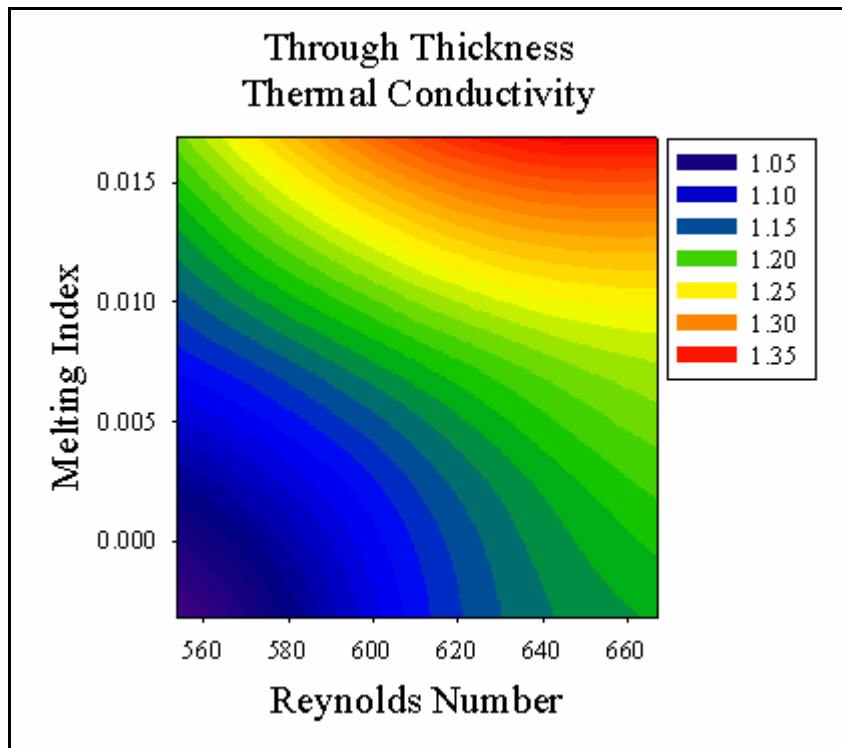


Figure 98: Contour plot of through thickness thermal conductivity in the Melting Index-Reynolds Number space

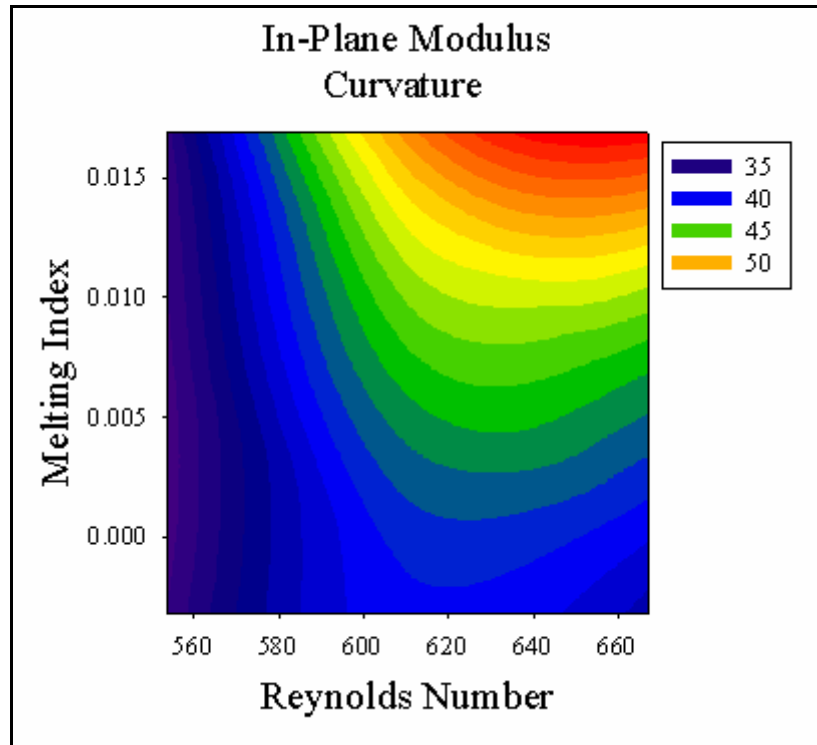


Figure 99: Contour plot of in-plane curvature modulus in the Melting Index-Reynolds Number space

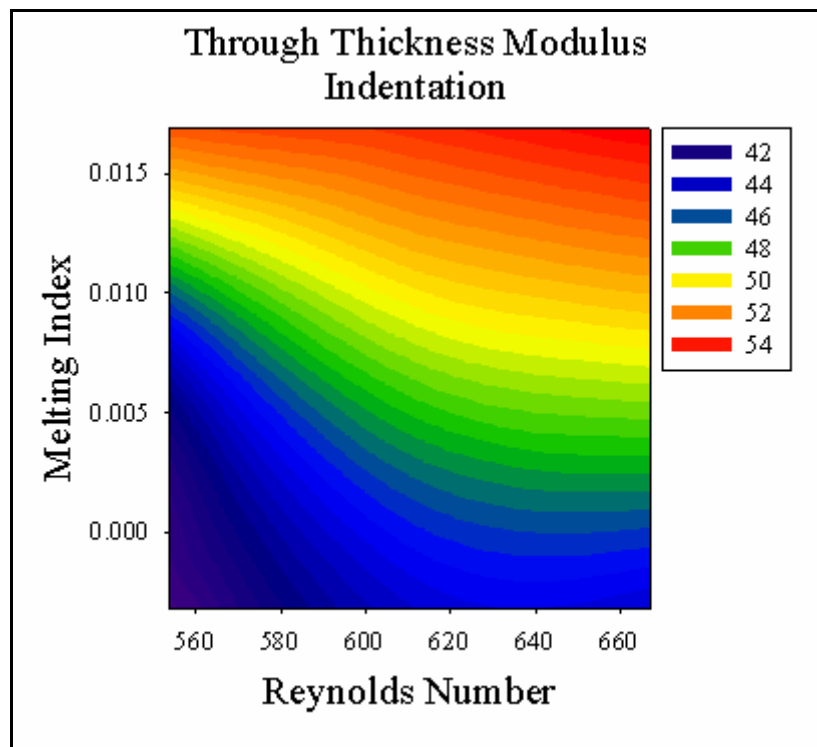


Figure 100: Contour plot of through thickness indentation modulus in the Melting Index-Reynolds Number space

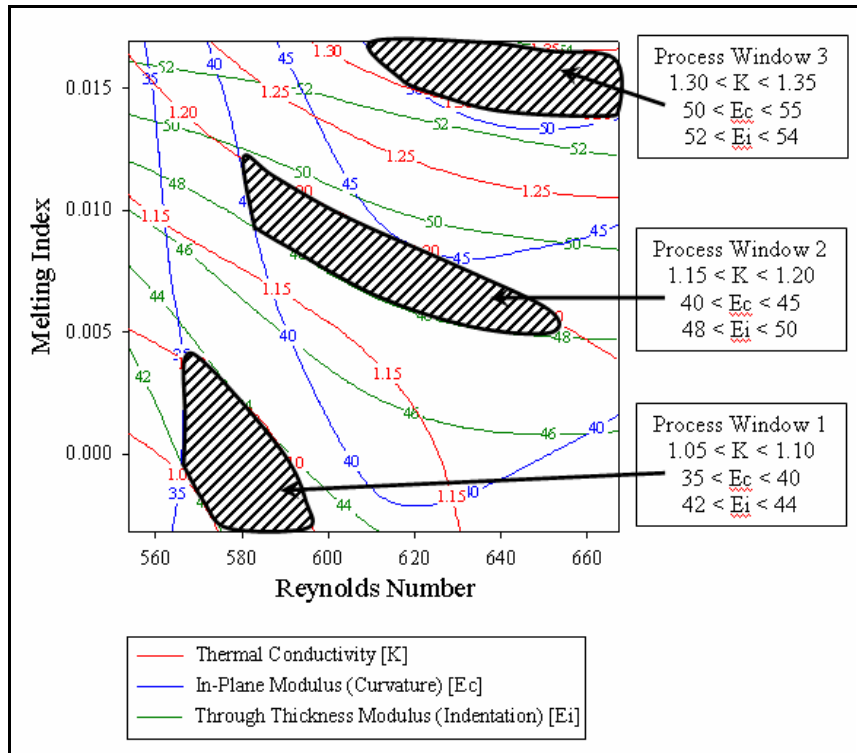


Figure 101: Identifying process window in the Melting Index – Reynolds Number space taking into account the thermal conductivity, in-plane modulus and through thickness modulus of coatings

6.2.1.3 Summary and Conclusion

It is widely appreciated that the in-flight state of plasma spray process has a substantial influence on splat formation and subsequent coating build-up. The in-flight state of the process can be varied very widely by using a range of process conditions, feedstock and hardware configurations. The influence of large particle state space on the coating build-up and properties has been investigated systematically in this study for a given feedstock and hardware configuration under comparable deposition conditions. This study is based on the systematic first order process map established in section 5.1.2.1 under near-ideal conditions with controlled optimum particle injection chapter 4.

The process conditions that resulted in the T-V extremes were chosen for establishing the second order process map – relating particle state to splat characteristics, deposition characteristics and coating properties. Difference in degree of splashing and flattening ratio were observed for the different process conditions. Splashing has been observed under high Reynolds Number conditions with higher Melting Index. Flattening ratio has been observed to increase as a function of Reynolds Number with limited dependence on Melting Index. Correlation has been established between these splat characteristics and particle state via contour maps in MI-Re space.

These specific extreme process conditions resulted in a very large difference in deposition efficiency (relative deposition efficiency between 10 and 100%). Deposition

efficiency has been observed to have nearly equal dependence on MI and Re increasing from low MI high Re to high MI low Re. Property measurements on these coatings show detectable change in thermal conductivity (1 to 1.3 W/mK) and significant change in through thickness indentation modulus (41 to 67 GPa) and in-plane curvature modulus (21 to 73 GPa). All the measured properties increase with increasing MI and Re.

Microstructural and property zones were identified in the MI-Re space based on measured data from these coatings. These zones help understand the behavior of the coatings to change in particle state as well as identify the zone that needs further understanding for designing coatings.

Subsequently, a smaller particle state space was identified for hollow spherical morphology feedstock and a systematic set of experiments were designed to explore the identified T-V space towards identifying appropriate process window, which could be used in designing coatings. Deposits made under carefully controlled T and V conditions (to meet the designed target) were characterized for through thickness thermal conductivity, through thickness indentation modulus and in-plane curvature modulus. Individual property contours in MI-Re space were superimposed on each other and in-flight particle state windows were identified for different sets of property requirements to validate the methodology.

6.2.2 Influence of Deposition Conditions

6.2.2.1 Introduction

Deposition conditions include variables such as feed rate, angle of impact, speed of torch movement (raster rate or pass rate) and step size and are considered to be dynamic or actively controllable during spraying. They influence the microstructure and properties of coatings both directly by altering the layering behavior and indirectly by influencing the substrate temperature.

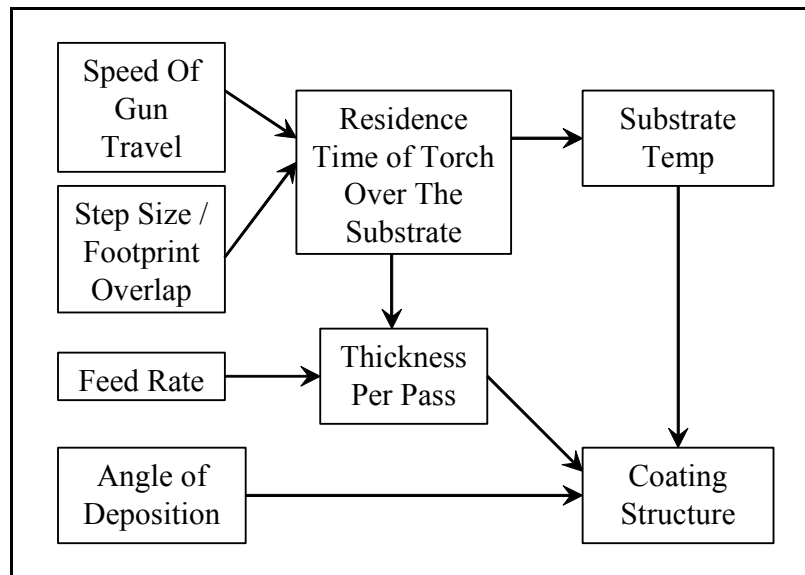


Figure 102: A schematic representation of the role of the different variables classified as deposition conditions on the coating microstructure and properties

Of these variables, step size influences the uniformity of coating and hence is controlled / optimized separately in accordance with the plume width, which is influenced by the choice of torch parameters. Due to the complex geometries of components, invariably the coatings have to be sprayed at different angles.

In order to understand the behavior of feed rate and pass rate, a combined parameter called the Deposition Rate has been developed. Deposition rate is a measure of the flux of particles impacting the substrate per unit length. As it can be seen in the equation below, any Deposition Rate can be achieved by different combinations of feed rate and pass rate.

$$\text{Deposition Rate (g/m)} = \frac{\text{Feed Rate (g/s)}}{\text{Pass Rate (m/s)}}$$

Deposition Rate can be adjusted in real time to influence the coating build-up and hence the interest. This study aims to understand the role of Deposition Rate on the coating structure and properties.

6.2.2.2 Experimental Details

In order to understand if Deposition Rate influences the coating properties, a simple set of experiments were designed with two variables at three levels as shown schematically in Figure 103. All experiments were performed with the 7MB torch with straight flow of N₂-H₂ gases. The center condition of the DoE (Figure 52) was used and injection was optimized for every experiment. Deposits were made at 130 mm spray distance on grit blasted Al 6061 T6511 substrates placed on the ICP sensor.

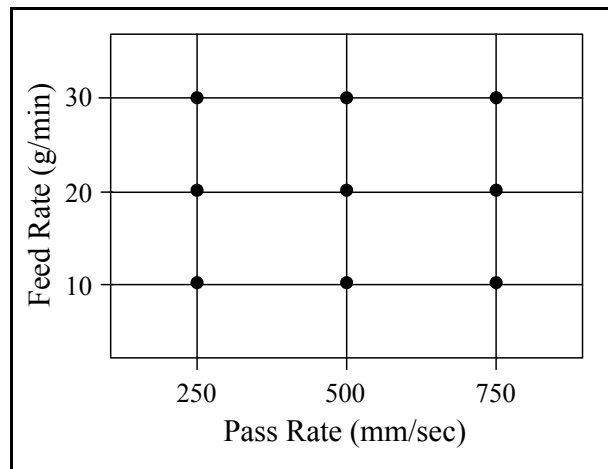


Figure 103: Schematic of design of experiment and the parameters used

6.2.2.3 Results and Discussion

Figure 104 shows a contour plot of the variation in thickness per pass of the coating with the feed rate and pass rate. The thickness per pass contours, to a first approximation, varies with the iso Deposition Rate lines. This is expected because the Deposition Rate is a combination of pass rate and feed rate, both of which influence the coating build-up and at the same plasma forming torch parameters they would correlate well with the thickness per pass and the deposition efficiency (Figure 105).

The objective of using the iso-lines and verifying the relation between the Deposition Rate to thickness per pass is to verify if the coating properties show a similar trend or not. If the coating properties showed the same trend as the thickness per pass, it would mean that the coating properties are influenced only by the Deposition Rate and that the feed rate or the pass rate does not influence the properties separately.

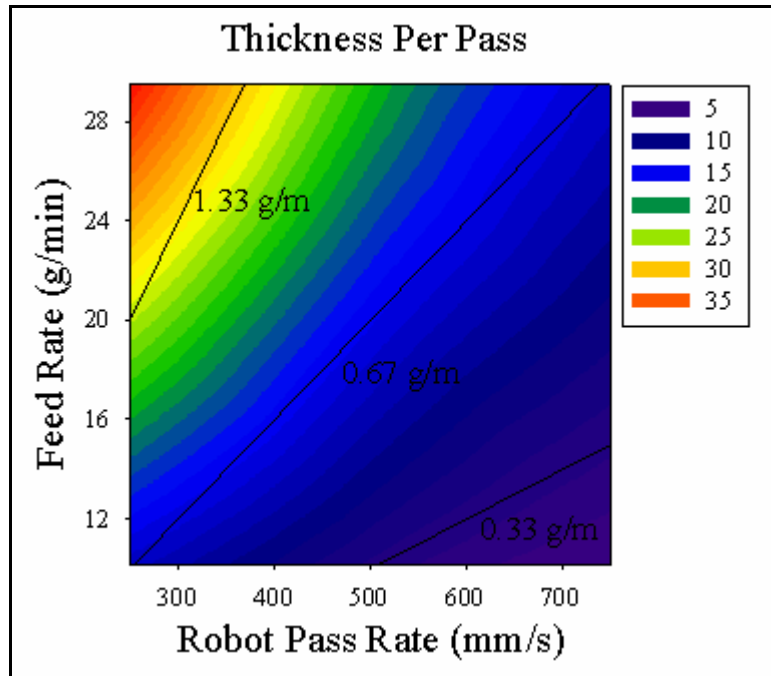


Figure 104: Contour plot of the response of thickness per pass of the coating to the feed rate and pass rate. No clear trend could be established and the contours do not follow the iso-Deposition Rate lines

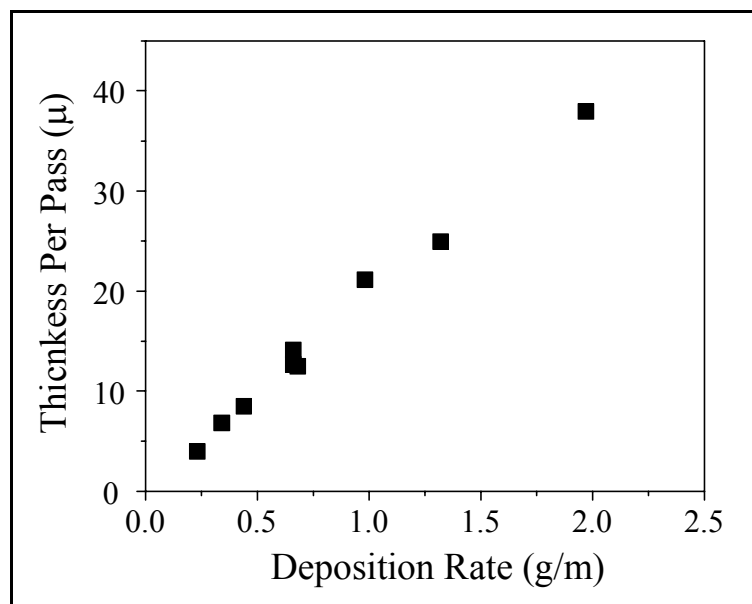


Figure 105: Relation between Deposition Rate and Thickness Per Pass

Figure 106 and Figure 107 shows the contour plots of the through thickness thermal conductivity and in-plane modulus from curvature of the coatings respectively. Thermal conductivity shows some correlation with the Deposition Rate in that higher thermal conductivity is achieved with higher thickness per pass or lesser pass-pass interfaces.

This suggests that pass-pass interface plays a significant role in plasma sprayed YSZ similar to alumina coatings made by HVOF [206]. Higher thermal conductivity observed at the lowest thickness per pass (high pass rate and low feed rate) could not be explained. In-plane curvature modulus does not exhibit any clear trend with the Deposition Rate. Detailed microstructural investigation is necessary for further understanding of the discrepancy in thermal conductivity as well as the in-plane modulus.

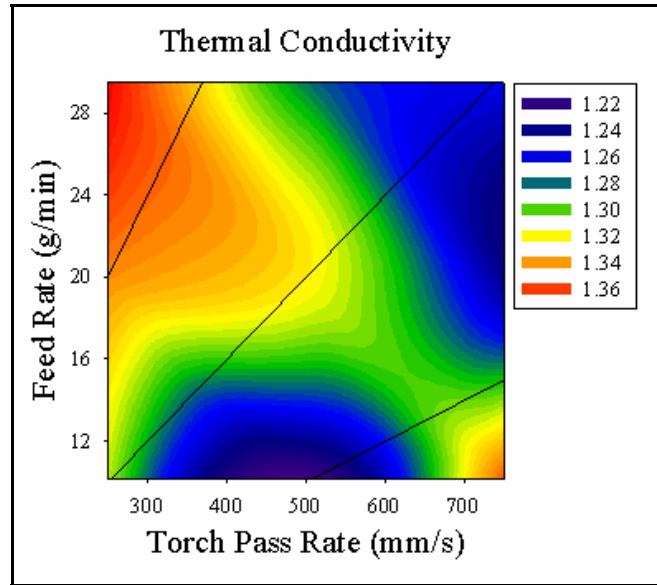


Figure 106: Contour plot of the response of through thickness thermal conductivity of the coating to the feed rate and pass rate. Though no clear trend could be established, higher Deposition Rates appear to increase the thermal conductivity

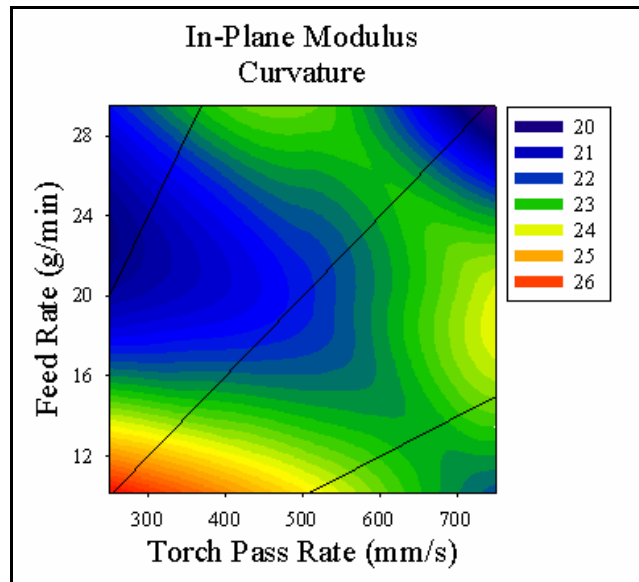


Figure 107: Contour plot of the response of in-plane modulus (from curvature) of the coating to the feed rate and pass rate. Though no clear trend could be established in comparison with the iso-Deposition Rate lines

Though the variation in the properties across the Deposition Rates is small, they are considerably different in comparison with the difference observed between the experiments done at the standard condition one before and one after these nine experiments (in order to rule out process reproducibility issues). This suggests that Deposition Rate does not sufficiently represent the coating build-up process. It is an important finding since during commercial manufacturing the thickness per pass is adjusted either by adjusting the feed rate or by adjusting the pass rate. These would not result in the same coating.

6.2.2.3.1 Angle of Impact

During spraying of actual components such as the turbine blades, the impacting surface is not always perpendicular to the spray stream. It is known that the orientation of the crack network depends on the angle of impact of particles [163, 164]. In order to understand the influence of deposition angle on the in-flight state of the process and coating build-up two experiments were done – 90° and 70° angle of impact.

Figure 108 shows the flow contour along the cross section of the spray stream at the spray distance (130 mm). For the 70° angle, the spray stream is cross-sectioned at an angle and hence the 20% larger plume width along the Y axis. This results in a wider spray footprint and ~35% reduction of the peak deposition flux per unit area at the flow center. This would influence the coating build-up and thickness per pass.

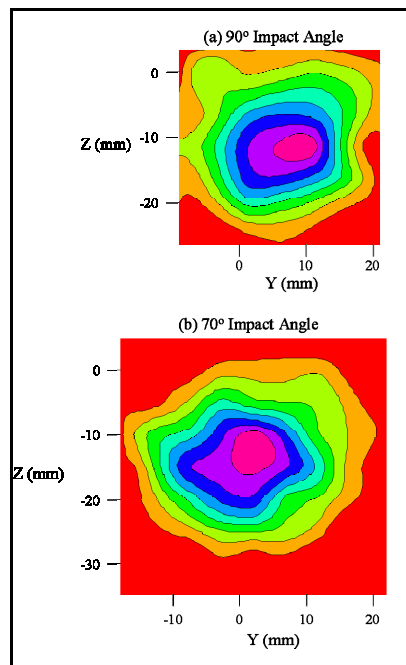


Figure 108: Contour plots of cross-section DPV scan showing particle flux or spray stream shape. A 20% increase in plume width in the Y direction is observed for a 70° angle of impact in comparison with the standard or 90° for the same torch conditions due to the orientation of the spray stream to the diagnostics

The influence of the change in angle (and hence the change in flux results) on the coating properties is shown in Figure 109. Compared to the standard (coating sprayed at 90°), the coating sprayed at an angle (70°) shows decreased deposition efficiency (Figure 109a). This is likely due the change in flux per unit area and the change the spray distance within the footprint (though it couldn't be captured clearly in the particle state). In-plane curvature modulus (Figure 109b) and thermal conductivity (Figure 109c) also decreases with the change of angle.

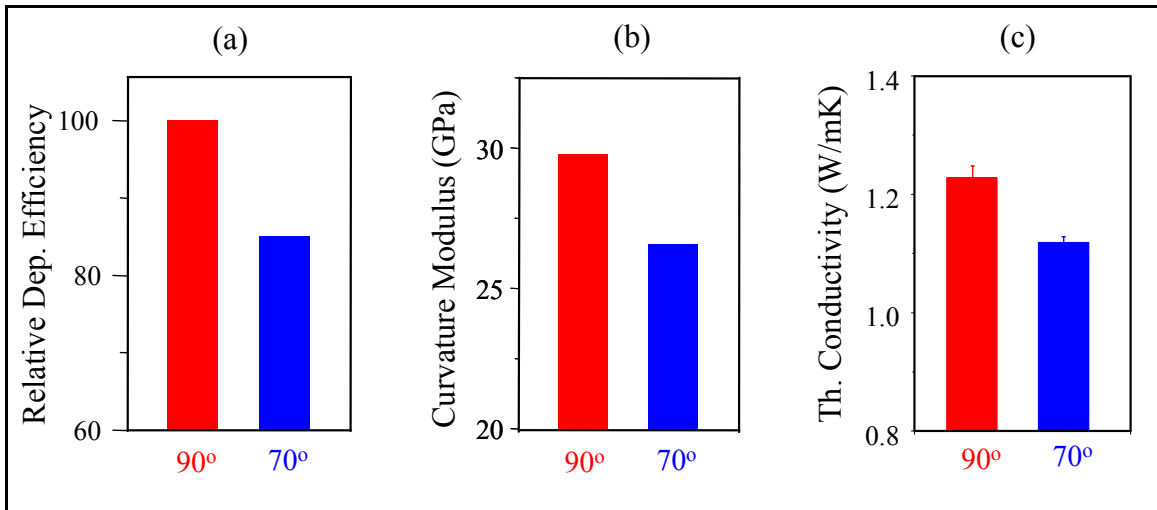


Figure 109: Variation in properties for a small change in the angle of impact

6.2.2.4 Summary and Conclusion

Deposition conditions are the cluster of variables that influences coating structure and properties but does not influence the in-flight state of the process. Particle flux per unit time deposited, the relative motion between the torch and the substrate, and the angle of impact of the particles belong to this category. Some of these variables can be controlled in real-time to influence the coating build-up while the rest of the variables also need to be considered in designing coatings.

The flux of particles was grouped with the relative raster to obtain the Deposition Rate representing the flux per unit length of the substrate. Deposition Rate was varied systematically within typical plasma spray range resulting in lamellar coating microstructure and without any significant quenching of the plasma to understand its influence on the coating build-up. These experiments were performed to specifically understand if it sufficient to achieve the same thickness per pass of coating by any combination of pass rate and feed rate.

The results show that the thickness per pass of the coating correlated well with Deposition Rate as shown by the correlation between the iso-Deposition Rate lines and the thickness per pass contours. Coating properties, specifically in-plane elastic modulus

determined using in-situ curvature and through thickness thermal conductivity, did not correlate well with the Deposition Rate (or the iso-Deposition Rate line). Benchmark experiments conducted using standard spray parameters (including deposition conditions) before and after this experimental set validates the difference observed in properties are due to change in deposition conditions and not due to the process reproducibility issues. Despite the lack of correlation, the difference observed between these coatings clearly suggests that controlling the Deposition Rate does not sufficiently control the coating build-up and properties.

The other significant variable that belongs to the deposition condition is angle of impact. In this study a small change in the angle of impact (70°) was done and the results compared with the standard condition (90° impact angle). The results show that due to the angle, the spray footprint is about 20% larger resulting in lesser flux of particles per unit area, which influences the thickness per pass and the number of pass-pass interfaces for a given coating thickness. Apart from this, the shadowing effect of particles causes a drop in deposition efficiency. Microstructural study is underway to quantitatively relate the microstructural change to the observed property difference.

6.3 Approaches to Significantly Modify the Microstructure and Properties

6.3.1 Introduction

One of the effective ways to influence the transport properties in thermal barrier coatings is by tailoring the splat-splat interfaces. Previous studies have established the effectiveness of interfaces on impeding thermal transport. Concurrent studies are underway to assess the contribution of interfaces and porosity on the thermal transport properties on a wide variety of coatings made as a part of this study. Splat-splat interface not only influences the thermal transport properties but also the mechanical behavior of coatings due to the nature of bonding of the splats and the existence of defect at the interface. Both, the type of defect structure at the interface and the number of such interfaces per unit length influence the coating properties [39, 58].

Examining the particle state-microstructure-property space resulting from the change in plasma forming torch parameters is one of the simple yet efficient ways to tailor the layering (section 6.2.1). It was shown that the torch parameters can be altered to vary deposition efficiency, microstructure and properties significantly. As mentioned in section 1.3.3 (Figure 7) torch parameters are one sub-section of one of the cluster of variables that influence the spray stream and the process downstream. There exist other options to influence the particle state, spray stream and the coating build-up and properties and hence tailor the microstructure and properties of coatings.

The addition of feedstock cluster of variables such as the morphology and size distribution introduces another dimension to the particle state-microstructure-property space. Previous studies have indicated that when powders with different morphologies are injected into a plasma jet, the resulting particle characteristics (e.g. temperature and velocity) are different [102, 193]. As a consequence, the splat morphologies also vary which in turn result in distinct coating microstructures and therefore properties.

Another approach is to alter the Reynolds Number of the particles to influence the spreading and flattening behavior [118, 121, 122, 147, 161, 207]. For a given set of torch parameters, this can be achieved by either changing the particle size using different feedstock size distributions or by changing the velocity of particles by using nozzles of different geometries. The influence of these changes on the particle state, splat flattening behavior and coating properties will be addressed in this section.

6.3.2 Experimental Details

Different feedstock size distributions and morphologies of YSZ were used in this study along with different nozzles to alter the splat layering. Sulzer Metco 7MB torch was used in the first part of this study with N₂-H₂ plasma gas mixtures with straight gas

flow to understand the influence of feedstock morphology and size distribution. Sulzer Metco PT-F4 MB torch was used in the later parts of this study with Ar-H₂ plasma gas mixtures with swirl flow to understand the influence of different nozzle dimensions and towards obtaining DVCs. In all cases particle injection was external with radial injection of powder into the plasma and was optimized (refer chapter 4). Sulzer's Plasma Technik Twin 10 powder feeder was used throughout this study. Details about the different feedstock morphologies and size distributions can be found in section 3.2.1.1.

Integrated sensor setup consisting of DPV 2000, SPT and IPP was used in this study (refer section 3.3.1.2). DPV data was recorded at the flow center as well as throughout the cross-section via scan.

For the study of feedstock morphology and size distribution, center condition from the design of experiment discussed in section 5.1.2.1 was used. For the studies on different nozzle and towards obtaining DVCs the center condition of a design of experiments for the F4 torch using Ar-H₂ gases was used. In order to vary the Deposition Rate, feed rate was kept constant and the robot pass rate was changed.

Coatings were made on beam samples 225 mm x 25 mm x 3.3 mm and their deflection was monitored using ICP. All relevant parameters were maintained constant between the different experiments. Cooling air jets mounted alongside the torch were used for all coatings. In order to control the substrate temperature while changing the pass rate, the cooling air pressure was altered.

6.3.3 Results and Discussion

6.3.3.1 Altering Number of Splat-Splat Interfaces Per Unit Length

The number of splat-splat interfaces per unit length is inversely proportional to the thickness of the splat. The splat thickness is a function of the flattening behavior of the particles, which depends to an appreciable extent on the Reynolds Number of the particles [118, 121, 122, 147, 161, 207]. Reynolds Number is expressed as shown in equation below.

$$\text{Reynolds Number} = \frac{\rho v D}{\mu}$$

Where, ρ is the density, v is the velocity, D is the size and μ is the viscosity of the particle at the temperature of the particle

For a given material, the density (ρ) and viscosity (μ) are fixed assuming the particles are dense solids and are completely molten. That being said, there are two different ways

to alter the Reynolds Number – (i) by changing the size of the particles, which could be extended to different feedstock distributions and (ii) by changing the velocity of the particles, which can be achieved by using nozzles of different dimensions.

6.3.3.1.1 Altering Particle Size: Different Feedstock Size Distributions

The three different feedstock size distributions were processed at the same plasma-forming torch parameters under optimized injection condition. Figure 110 shows the location of these different size distributions are shown in T-V space and MI-Re space. The fine distribution gets propelled faster and better melted while the coarse particles are slower and are less molten. The ensemble distribution is in between the two since it is a mix of the other (size) distributions. This can be observed from Figure 110 and from the distributions shown in the distribution Figure 111.

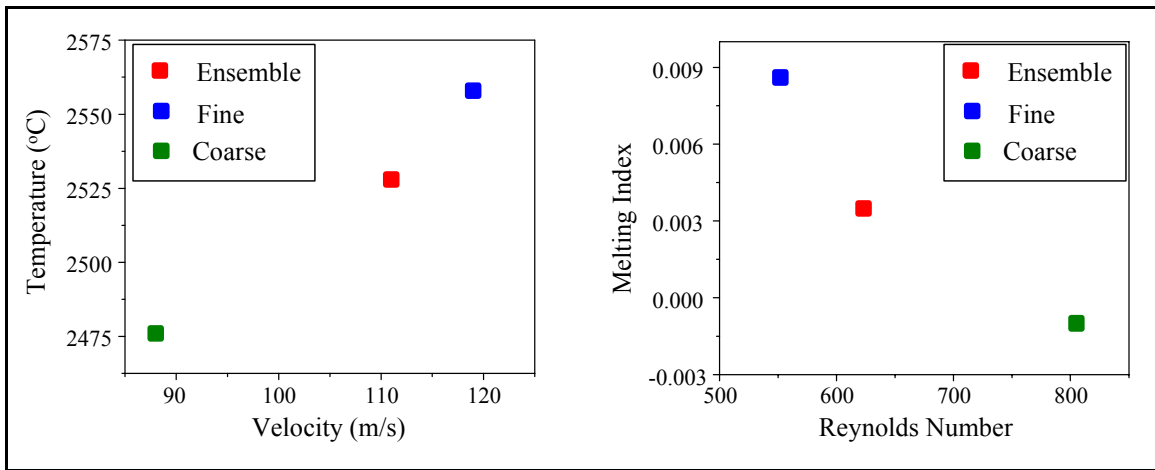


Figure 110: Different feedstock size distributions represented in the T-V space (left) and in the MI-Re space (right)

Flattening ratio was calculated from measured splat dimensions as well as using Madejski model from the in-flight particle data and the results are shown in Figure 112. The flattening ratio for the different size feedstocks are comparable though coarse particle shows moderately higher value than the other two feedstocks. This is due to the higher Reynolds Number observed for the coarse particles. It has to be noted that a constant value was used for the viscosity of the particles though they are temperature dependent. This is perhaps why the fine particles show much lower Reynolds Numbers but not significantly lower flattening. These differences observed influence the number of splat-splat interfaces per unit length, which ultimate influence the properties in addition to the other microstructural contribution.

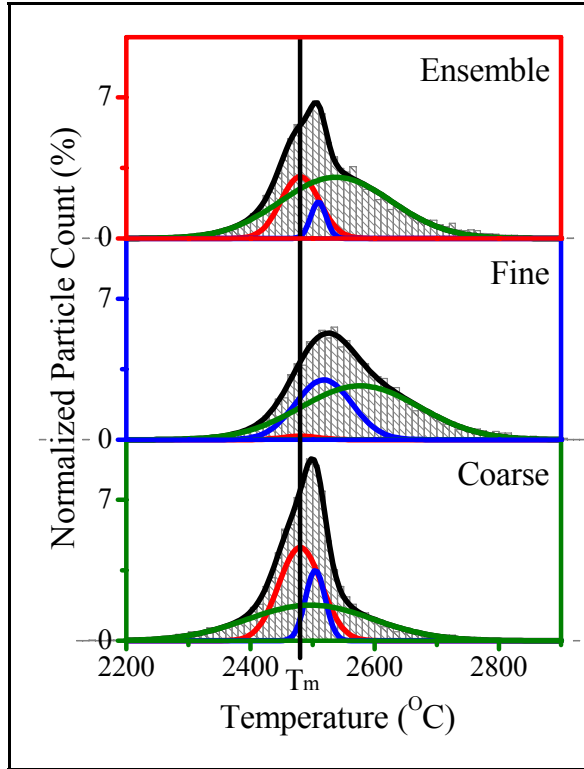


Figure 111: Particle temperature distribution obtained from 10,000 particles at the flow center for the three different feedstock size distributions. The melting point is shown by the vertical line. One can observe the shift in distributions implying different extents of melting

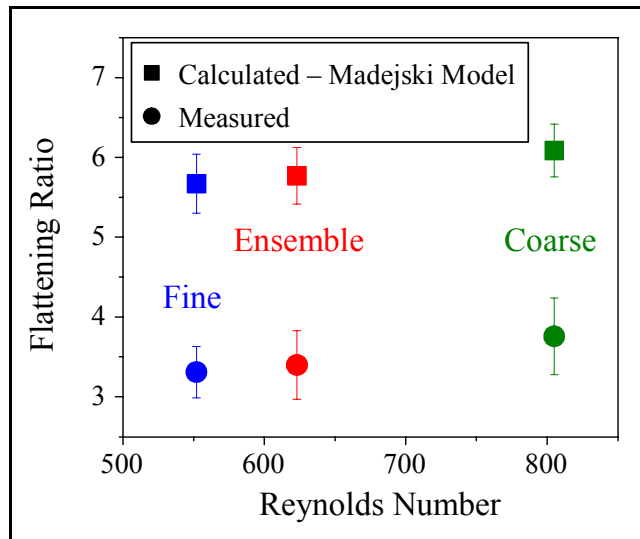


Figure 112: Splat flattening ratio for the different feedstock size distributions. The coarse distribution shows moderately higher flattening ratio due to very high Reynolds Number

The (relative) deposition efficiencies and the thickness per pass are shown in Figure 113 for these different size feedstocks. The coarse feedstock exhibits the least melting and hence the least deposition efficiency of the three, while the fine feedstock is at the

other extreme. Since the size distribution of the ensemble feedstock is similar to a physical mix of the other two feedstocks, the deposition efficiency and the thickness per pass are in the middle. The deposition efficiencies correlate to Spray Stream Melting Index very well.

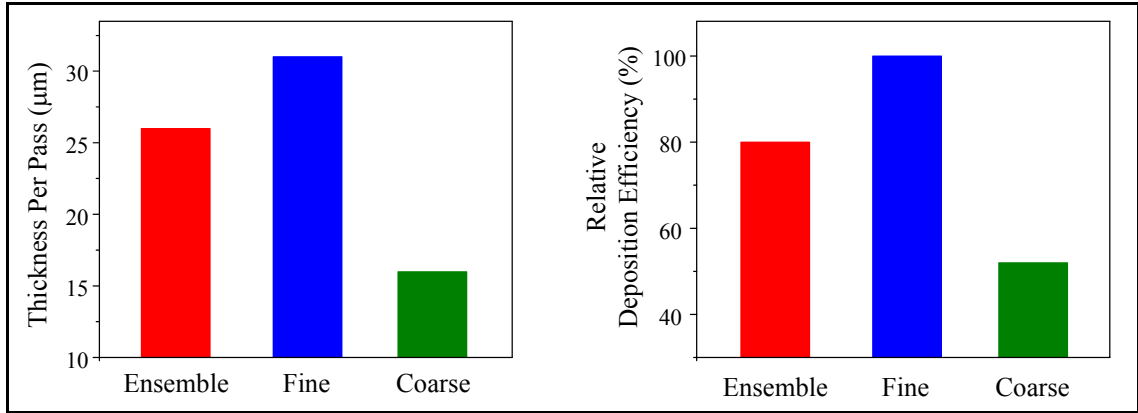


Figure 113: Thickness per pass and deposition efficiency (DE) for the different feedstock size distributions. Fine distribution shows highest DE while coarse particles show the lowest. Since the ensemble is a mixture of the coarse and the fine distributions, it is in between. This correlates well with the melting assessed from the temperature and Melting Index distributions

The in-plane elastic modulus measured using curvature technique and the through-thickness modulus measured using instrumented indentation is shown in Figure 114 for the different size distribution feedstocks. Significant changes could not be observed though the ensemble feedstock shows slightly higher modulus in both orientations. This is an interesting observation considering the fact that the melting behavior and the deposition rates (thickness per pass) are considerably different for these feedstocks.

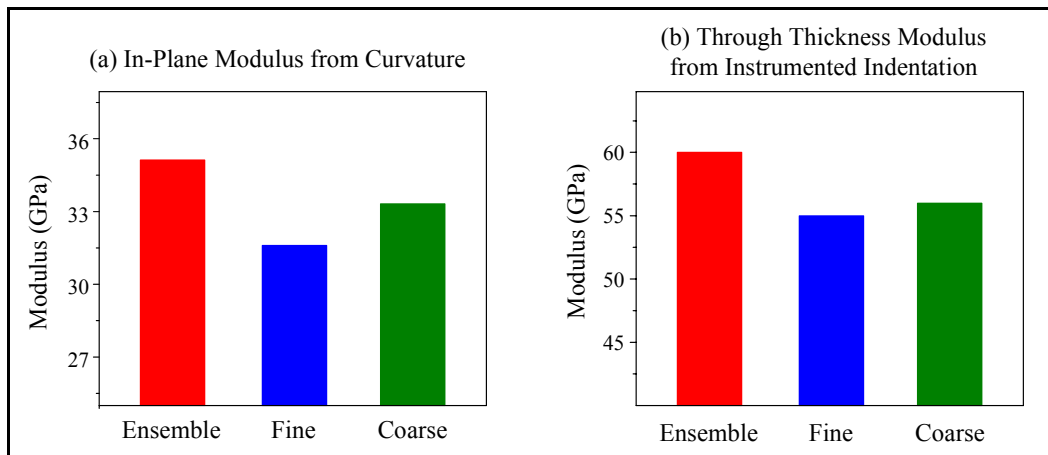


Figure 114: In-plane elastic modulus from curvature and through thickness modulus from indentation for the different feedstock size distributions. In both orientations ensemble feedstock shows the highest modulus closely followed by the other two size distributions

Through thickness thermal conductivity shows noticeable change between the three feedstocks (Figure 115). Coarse feedstock shows higher thermal conductivity and the fine feedstock shows lower values. This is very likely due to the resultant influence of the resistance to thermal transport by the interfaces (number of interfaces per unit length through thickness) and porosity (pores and cracks). A simple calculation of the average splat thickness which is inversely proportional to the number of interfaces shows that the fine feedstock has three times the number of interfaces as the coarse feedstock. This is perhaps the reason why coarse feedstock shows higher thermal conductivity despite the (expected) increase in porosity due to incomplete melting (as seen in the temperature distribution). This study points out the effectiveness of inter-splat interfaces in resisting thermal transport.

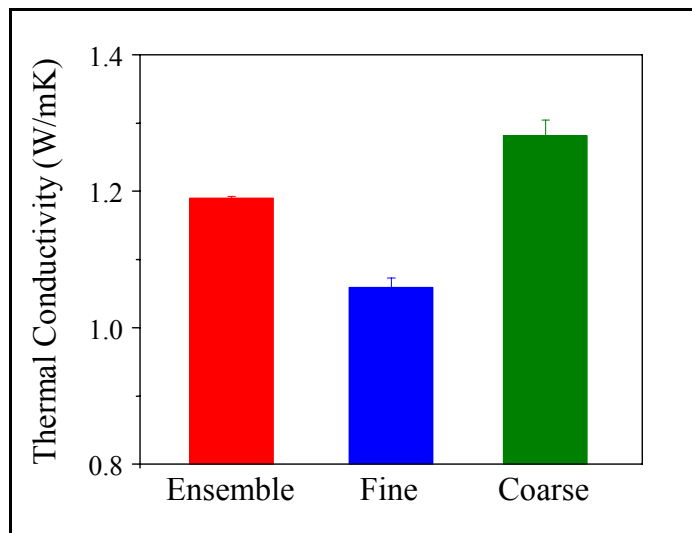


Figure 115: Through thickness thermal conductivity for the different feedstock size distributions. Coarse feedstock shows the highest thermal conductivity, fine shows the lowest and ensemble is in between

6.3.3.1.2 Altering Particle Velocity: Different Nozzle Exit Diameters

The second method to influence the number of interfaces is by achieving higher extents of flattening for any given feedstock. This is achieved by increasing the impact velocity by using different nozzle geometries (8mm and 6mm) with all other parameters remaining the same. Figure 116 shows the temperature-velocity space obtained by exploring the torch parameter space. The 6mm nozzle results shifts the T-V space towards higher velocity without any significant impact on the temperature. Detailed experiments were conducted at one point in the T-V space for each nozzle, which resulted from the same plasma-forming torch parameters. Average MI and Re at these two points show that MI is not influenced much whereas Re increases significantly for the 6mm nozzle. Similar observation could be made from the distributions in Figure 117 and the Spray Stream Melting Index calculated from the distributions in Figure 118.

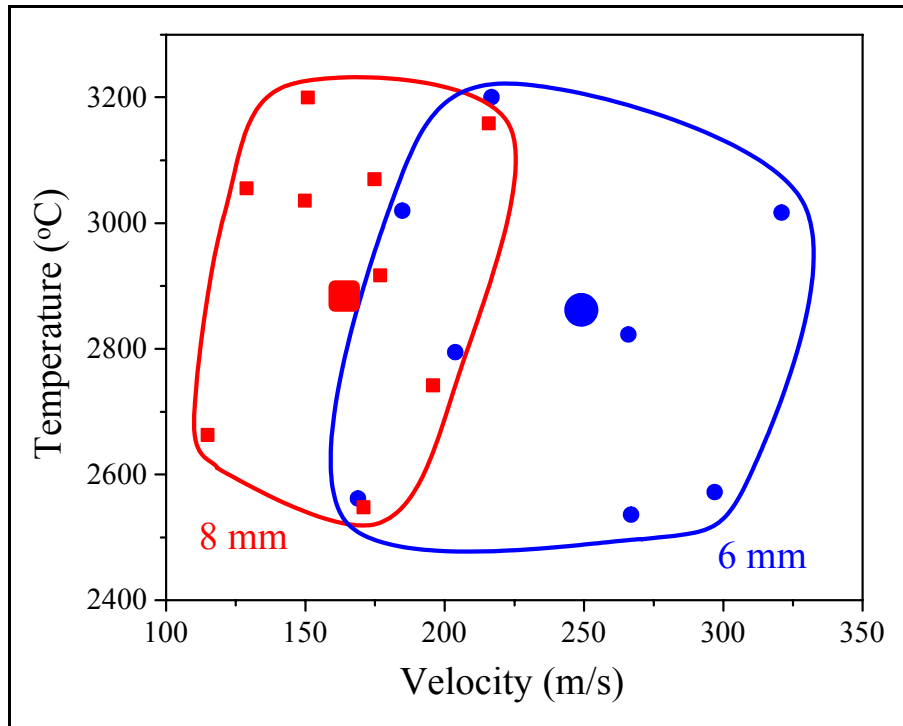


Figure 116: The temperature-velocity space for the two different nozzles used. The data point in bold represents the temperature and velocity at which the splats and deposits were made

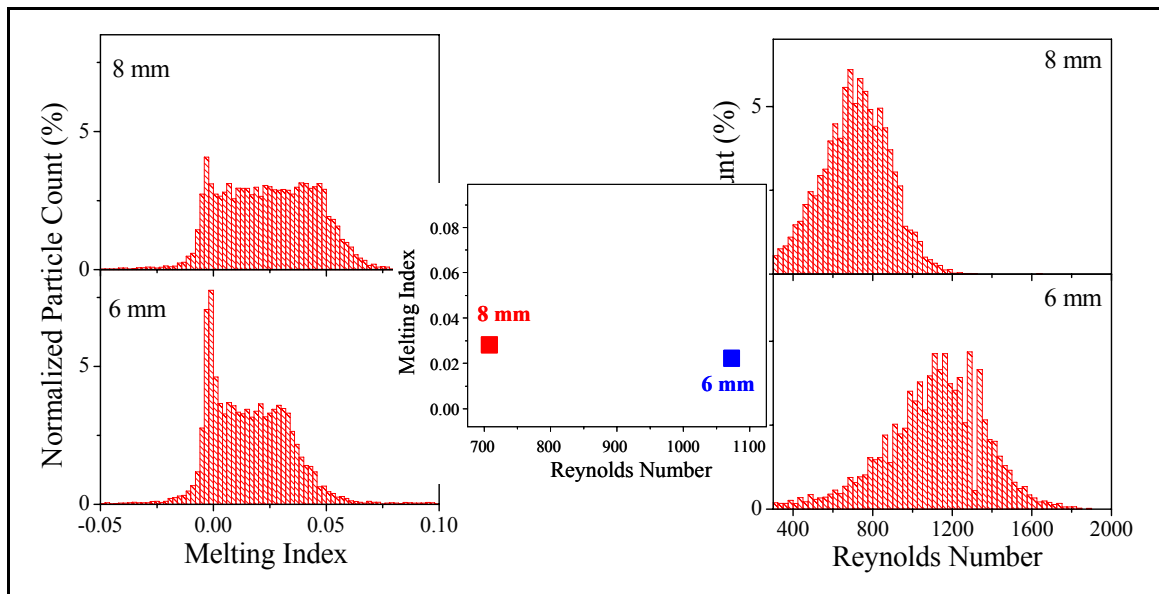


Figure 117: Distributions of particle Melting Index (left) and Reynolds Number (right) are shown with an inset figure showing of the average MI and Re for the different nozzle diameters used. 6mm nozzle results in marginally lower melting while drastically increasing the Reynolds Number

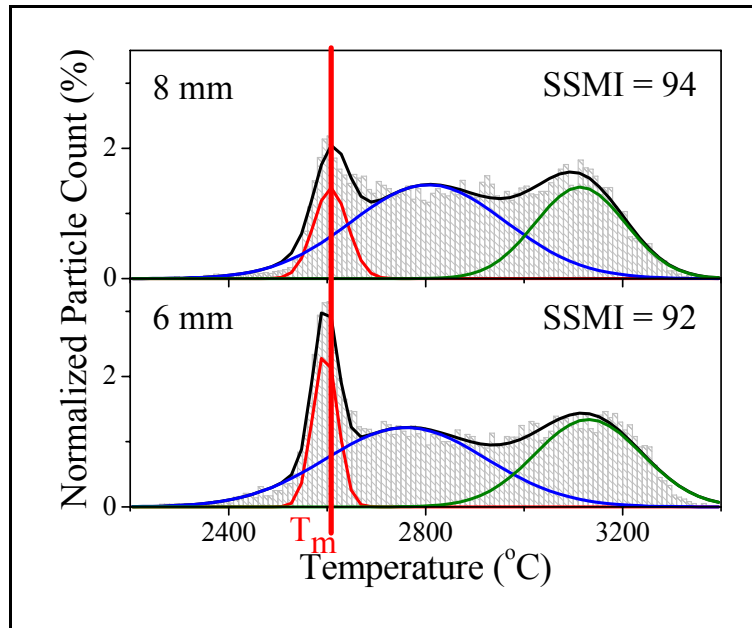


Figure 118: Spray Stream Melting Index calculated from the temperature distributions of 6mm and 8mm nozzle. No significant difference is observed

Measured and calculated flattening ratios are shown in Figure 119 as a function of the Reynolds Number. Increase in flattening ratio can be observed for the 6mm nozzle which shows higher Reynolds Number. Since same feedstock (size distribution) was used, this change in flattening ratio results in only a moderate increase in the number of interfaces per unit length for the 6mm nozzle.

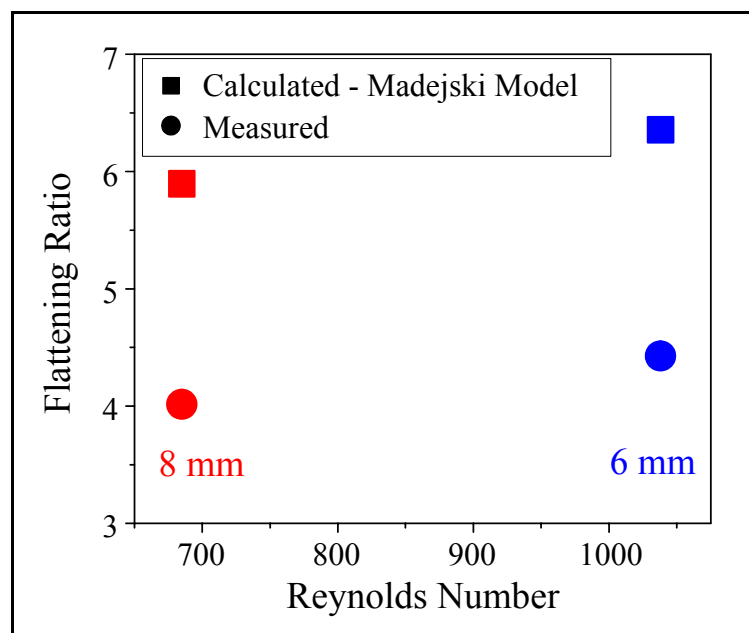


Figure 119: Splat flattening ratio measured (circle) and calculated (square) as a function of Reynolds Number for 6mm and 8mm nozzles. Higher Re results in higher flattening ratio for the 6 mm nozzle

Though same coating thickness was obtained in both the cases (using different number of passes) the thickness per pass are different for 8mm nozzle and 6mm nozzle (Figure 120a). The lesser thickness per pass for 6mm can be attributed to the higher flattening ratio, splashing and ricocheting of particles due to higher impact velocities and the associated Reynolds Number. In-plane modulus shows a noticeable increase for the 6mm nozzle (Figure 120c), which could be due to the enhanced inter-splat bonding and reduced porosity as a result of the impact velocity and also. Thermal conductivity shows a significant decrease (Figure 120b) for 6mm nozzle. The difference in thermal conductivity is more than half that observed earlier in the process maps exploring the entire operational range of torch parameters. This shows the influence of impact velocity in determining and altering the microstructure and properties. Microstructural work is needed to clearly understand the reason for the decrease.

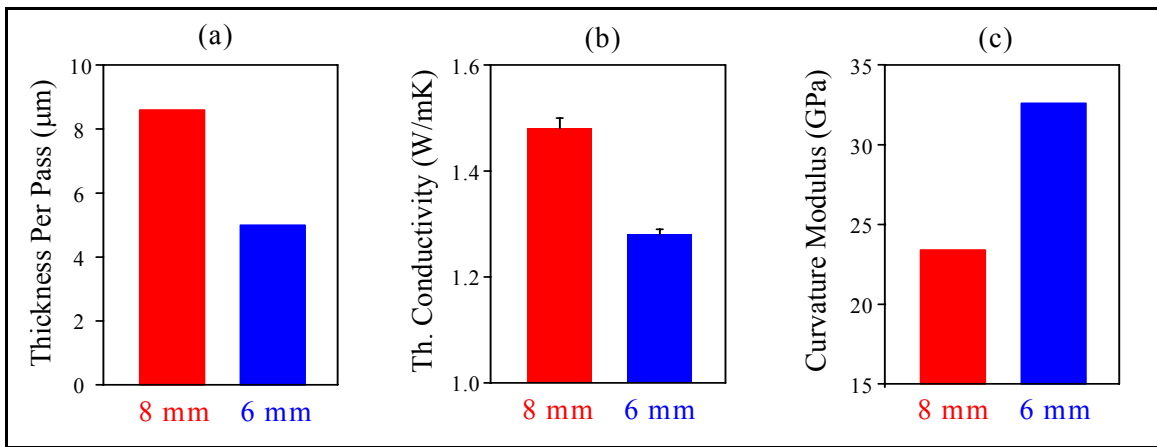


Figure 120: Properties of deposits made with 6 mm and 8 mm nozzles

6.3.3.2 Altering the Interlamellar Defect Features Using Different Feedstock Morphology

Three different morphology feedstocks (polyhedral, solid spherical and hollow spherical) were processed such that the average temperature and velocity were very similar (within a very narrow allowed range) while maintaining the hydrogen flows constant. The process control methodology explained in section 5.2.2.1 was used with three different sets of torch parameter – particle state relations to achieve the same temperature and velocity with the three different morphology feedstocks.

Figure 121 shows the selected temperature and velocity and the allowed range in the context of maximum T-V space obtained by exploring the process space. Figure 122 shows the different morphologies in MI-Re space (scale has been selected for clarity to bring out the small difference that exists between the morphologies). Since PD particles are lighter, they achieve higher velocities and hence the higher Reynolds Number. There is certain error associated with the calculation of MI and Re for PD morphology due to the hollow nature of particles.

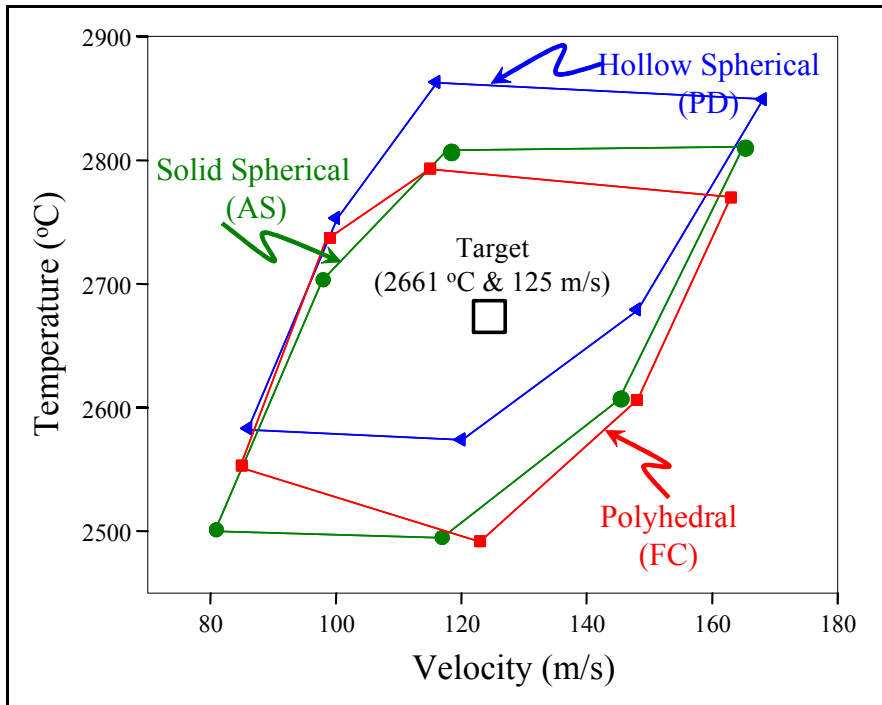


Figure 121: T-V space for the different morphology feedstock. All three morphologies share a large common T-V space. Same average particle T and V (2661 °C and 125 m/s) were achieved within a narrow tolerance limit of ± 10 °C in T and ± 2 m/s in V (schematically represented by the box in the center of the T-V space)

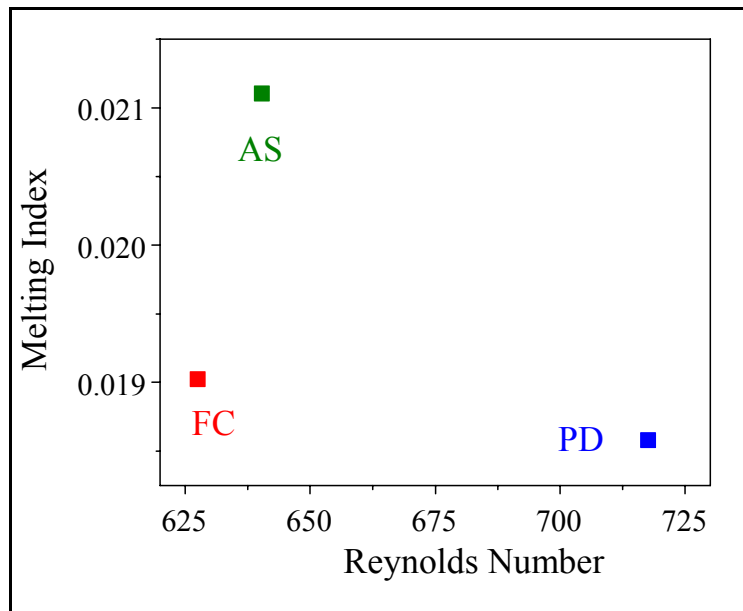


Figure 122: Average Melting Index and Reynolds Number for the different morphology feedstock. The values appear to be very different due to the scale. In comparison to the overall range possible from the first order process map, the MI values are similar while the Re values are moderately different for PD

The similarity in average Melting Index between the different morphology feedstocks can be observed in their overall distributions (Figure 123). But the solid spherical morphology shows more partially molten content than the rest (area under the red color peak). Also most of the particles are at very high melting status for solid spherical and hollow spherical (area under green color peak), while for polyhedral morphology most of the particles are at a lower melting state (blue color peak). Though the overall distributions appear similar the different shifts within these distributions could influence the flattening behavior due to melting status and the associated viscosity difference.

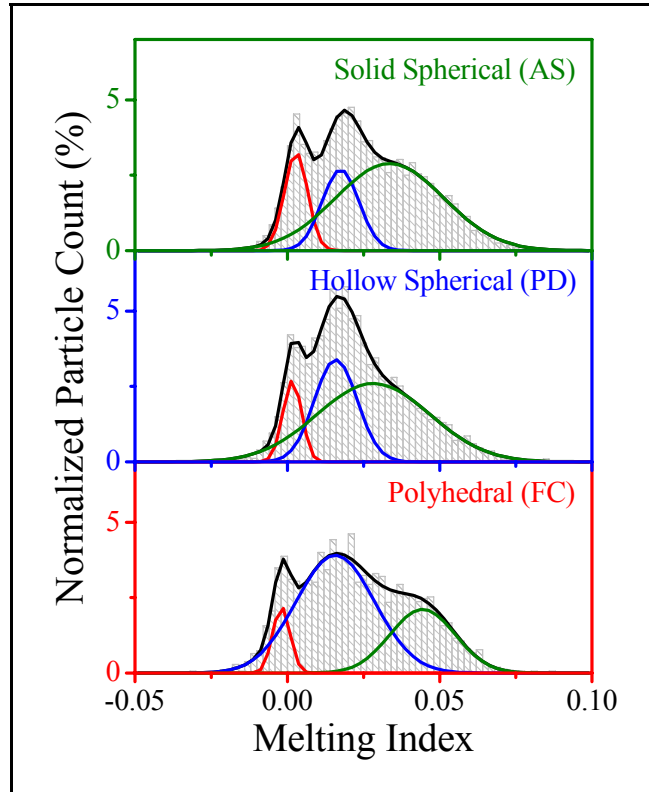


Figure 123: Melting Index distributions for the different morphology feedstock. The distributions appear similar except for a small difference at high temperature for hollow spherical (PD) morphology

A plot of the properties of the coatings obtained from the different feedstock morphologies is shown in Figure 124. The thickness per pass of the coating is highest for hollow spherical morphology and lowest for solid spherical, while the polyhedral morphology is in between (fig a). Higher thickness per pass for hollow spherical morphology is perhaps due to the higher interlamellar porosity. Lower thickness per pass for solid spherical morphology could be attributed to less melting, which could be observed in the Melting Index distributions.

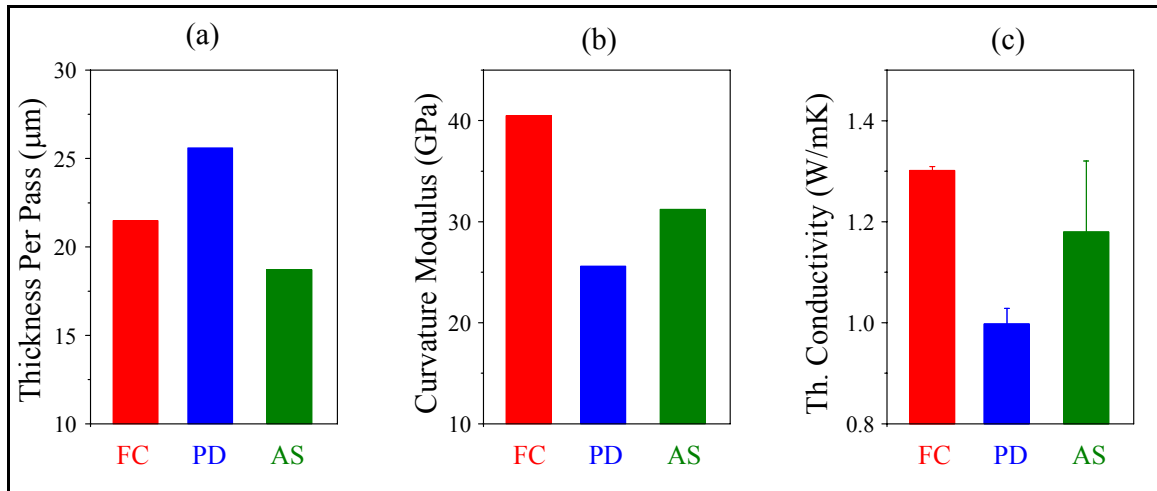


Figure 124: Properties obtained for the different morphology feedstock

The interface defect structure can further be modified by using hollow spherical feedstock with a uniform thin shell, which will result in a more compliant structure. Studies are underway with this type of feedstock.

6.3.4 Summary and Conclusion

There are many critical variables that influence the microstructure and properties of coatings, which need to be considered carefully for effectively tailoring the coating. This study is aimed at engineering the microstructure by modifying the nature and quantity of the splat-splat interfaces and the associated defect structure. Few key parameters that influence the splat formation (impact, wetting and spreading) are considered in order to alter the number of splat-splat interfaces per unit length in the thickness direction.

The most influencing parameter that controls the number of interface per unit length is the splat thickness, which is in turn controlled by the starting particle size and the flattening ratio. Flattening ratio has been shown to correlate to the Reynolds Number in previous studies [118-122, 147, 161, 207]. By definition Reynolds Number is influenced by particle size and velocity for a given material assuming completely molten particles at the same viscosity. Hence in this study, different particle size distributions (influences the splat thickness directly due to starting particle size as well as indirectly by the difference in flattening ratio) and different particle velocities (directly influences the flattening ratio) are considered. Comparison is made from the in-flight state of the processes to the coating properties and an attempt is made to quantitatively establish the differences.

For size distributions, fine, coarse and ensemble feedstock of polyhedral morphology (FC) were processed at the same plasma-forming torch parameters. Average temperature and velocity are higher for fine particles and more particles are completely molten, while the coarse distributions achieve slower velocity and lower temperature resulting in lesser particles being completely molten. Though the difference in flattening ratios is not

significant, the splat thickness from coarse feedstock is roughly three times that from fine feedstock, thus coarse feedstock results in lesser number of interfaces per unit length. But the porosity due to improper melting (evident from the particle temperature distributions and deposition efficiency) also influences the properties. Through thickness and in-plane modulus of coatings do not exhibit significant difference while through thickness thermal conductivity is noticeable different. Fine feedstock shows the least thermal conductivity while coarse feedstock shows high thermal conductivity, which could be attributed to the difference in number of interfaces per unit length and to some extent the porosity.

The flattening ratio has been altered in this study by varying the Reynolds Number by significantly varying the particle velocity by the use of different nozzle exit dimensions. 8mm and 6mm nozzle exit diameters were used to process the ensemble polyhedral (FC) feedstock under same process conditions. Using 6mm nozzle resulted in about 60% increase in average particle velocity and Reynolds Number. This resulted in change in flattening ratio of half that of the entire process space using one feedstock and hardware, which is significant. This not only resulted in more number of interfaces per unit length but also in improved bonding between splats resulting in lower thermal conductivity and higher modulus.

Finally to alter the interlamellar defect features and the number of splat-splat interfaces, different feedstock morphologies were processed at similar average temperature and velocity using similar secondary gas flows and comparable torch parameters. Hollow spherical morphology feedstock results in thinner splats with higher interlamellar porosity and hence reduces the thermal conductivity as well as modulus. The hollow spherical particles considered in this study do not have a uniform shell thickness. Studies are underway with laboratory prepared hollow spherical particles of thin uniform shell [208, 209], which would result in considerably thinner splats and much higher number of interfaces.

Chapter VII

7 Assessment of Process Variability

7.1 Variability at Different Stages in the Process

7.1.1 Introduction

Reproducibility is necessary if the process has to be integrated into the component design stage. It is important for achieving prime-reliance in tailored coatings, which implies that the life of the coating and hence the component is predictable. Other benefits of a reproducible process includes reduced operating costs, enabling stable process for better understanding of other less dynamic yet significant process variables influencing the coating build-up such as the substrate conditions and deposition conditions (Figure 125). Therefore understanding reproducibility and assessment of the existing variability of the plasma spray process is important [61, 100].

To facilitate such understanding, the various sub-processes or variable clusters that have significant influence on the coating performance have been identified and are shown in Figure 125. Process variability has been systematically assessed at each significant step of the process, namely the particle/plume, coating microstructure and coating property stages. Significant effort has been directed at the plasma-particle interaction stage due to the fact that spray stream is complex and dynamic making it difficult to measure, assess and control the particle state. Stochastic nature of the feedstock and understandable yet uncontrollable drift in the process due to nozzle wear adds to the complexity [100, 166-168].

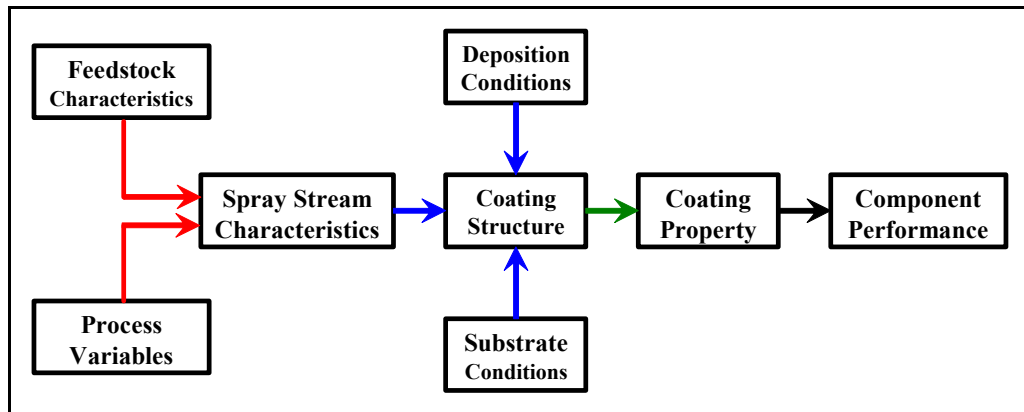


Figure 125: Process understanding from a design perspective. Significant variables have been identified and clustered for better focus

Improvements in quality and specifications of the hardware and feedstock have contributed to an overall improvement in reliability of the process as a whole. But controlling the process to tighter process specifications is necessary to ensure reliable coatings. There exist at least a few different process control methodologies. Some control the process at the hardware level and some at the in-flight particle level [25, 28, 32, 35, 148, 149]. In this study we consider four methods, two in each of the aforesaid categories, to assess their effectiveness in controlling the process.

7.1.2 Experimental Details

7.1.2.1 Process and Sensors

In this study a Sulzer-Metco 7MB torch with an 8mm ‘G’ nozzle was used with a non-swirl gas distribution. A mixture of nitrogen (N₂) and hydrogen (H₂) gas was used for plasma generation to study Ytria Stabilized Zirconia (YSZ) feedstock of 10-75 microns with polyhedral morphology particles (fused and crushed) (HW1532; Saint-Gobain, ceramics and grains division, Worcester, MA).

Detailed diagnostics was performed using the different sensors that are set up in an integrated fashion at the Center for Thermal Spray Research (CTSR). Measurement of particle T and V using DPV 2000 on very large number of particles (10,000 typically) were averaged and was used for particle state control. Ensemble sensors such as the Inflight Particle Pyrometer and Spray Plume Trajectory sensor (IPP and SPT) were also used. Schematic of the integrated sensor set-up at CTSR and details about the sensors and the procedure followed can be found in the experimental techniques chapter.

7.1.2.2 Coating and Characterization

For each experiment deposits were obtained on grit blasted 3mm thick Al 6061 T6 substrates of dimensions 225 mm x 25 mm at 130 mm standoff. The deposition procedure and all the related parameters were maintained the same for all the experiments. No specific effort was directed towards achieving a specific substrate temperature though one cooling air jet mounted on the torch was used to cool the coating. Because the experiments were in the similar operational parameter range and the same procedure was followed for all the experiments, the substrate temperatures were within comparable range (~300°C) for all sets of experiments except for the fixed voltage method. In the case of fixed voltage method experiments, the operation parameters are at a different location in the process space compared to the rest and hence the substrate temperature was lower (~210°C).

The defect structures of the deposits were characterized using digital image analysis of optical micrographs. The mechanical properties have been assessed in the form of indentation modulus and curvature modulus from instrumented indentation and in-situ

curvature sensor respectively. Thermal conductivity was measured by laser flash technique as a measure of the functional property of the sprayed YSZ coatings.

7.1.2.3 Process Control Methods

7.1.2.3.1 Fixed Parameter Method

The torch parameters, namely primary flow (N_2), secondary flow (H_2) and arc current (I), were fixed for a series of six experiments. Particle injection was optimized for the first experiment and then that carrier gas flow was used for the subsequent five experiments. This method will be referred to as the FP method in this chapter.

7.1.2.3.2 Fixed Voltage Method

Here the objective was to control the voltage and hence the total input power by varying the H_2 flow. N_2 and I were kept constant. Two experiments were performed five nozzle hours apart in order to result in significant change in H_2 flow to obtain the same voltage. Injection was optimized for both the experiments. This method will be referred to as the FV method in this chapter.

7.1.2.3.3 Optimized Injection Method

In this method, the three torch parameters were fixed and carrier gas flow was optimized for each of the four experiments. Simply put, the angle made by the plume with the nozzle axis (i.e. trajectory) is controlled by changing the carrier gas flow irrespective of the flow value. In an earlier study at CTSR, it was observed that the particles achieve maximum temperature and velocity when injected such that they follow a certain trajectory, implying maximum heat and momentum transfer to particles for any given parameter combination. More information on this can be found in a classified presentation made at CTSR, which will be made available in an article under preparation. This method will be referred to as the OI method in this chapter.

7.1.2.3.4 Optimized T-V Method

This procedure involves achieving constant average particle temperature and velocity as measured by DPV 2000 at the flow center at the spray distance. The average particle temperature and velocity to be achieved were chosen to be $2661^\circ\text{C} \pm 10^\circ\text{C}$ and $125 \text{ m/s} \pm 2 \text{ m/s}$ for four experiments.

Restarting the torch at the same process condition that resulted in these temperatures and velocities did not ensure same particle properties (point 1 in Figure 126). In order to

‘steer’ the process to the predetermined particle velocity and temperature the torch parameters were adjusted using a model that was developed from a previous systematic study. This method will be referred to as the OT method in this chapter.

The radial variation of plasma plume characteristics and the resulting variation in particle properties are well established. Hence it is necessary to control the particle trajectory in the plume, thus enabling particle diagnostics at the same or similar coordinates. This was done by *optimizing the injection* for every process condition until achieving the target.

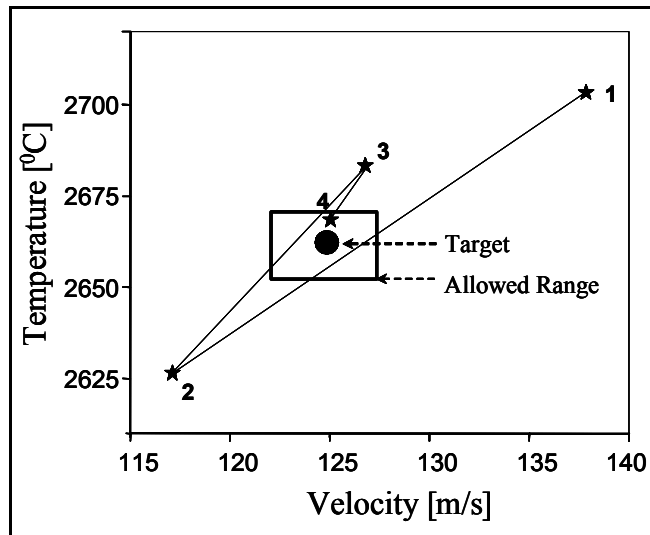


Figure 126: Illustration of the procedure used to adjust the temperature and velocity. Target and the allowed range are marked in the figure

7.1.2.4 Summary of Process Conditions Used

Table 8: Summary of torch parameters used in the different process control methods for the angular morphology YSZ feedstock. Sensor based process control is italicized in table

	Nitrogen Flow (SLPM)	Hydrogen Flow (SLPM)	Current (A)	Voltage (V)	Carrier Gas (SLPM)
Fixed Parameter Method	47.6	5.6	550	76 – 78	5.18
Fixed Voltage Method	31.9	1.7 – 6.0	466	66 – 67	3.18 – 2.44
Optimized Injection Method	47.6	5.6	550	81 – 83	3.23 – 3.60
Optimized T-V Method	41.9 – 45.3	6.9	675 - 700	71 – 73	4.15 – 4.81

7.1.3 Results and Discussion

7.1.3.1 Establishing Basis for Comparison

In order enable objective comparison between the different methods considered here, a standard has to be set for comparison. For this reason, maximum variability or *range* has been considered (calculated as the difference between the maximum value and the minimum value of the considered property). *Range* does not provide objective comparison for the different parameters due to the difference in absolute values of the variables. For example, temperature is three orders of magnitude higher than thermal conductivity and two orders of magnitude higher than modulus. Hence the *range* has been normalized to the *process map range* (range calculated for the property under consideration from the extremes as a result of varying the plasma forming torch parameters between safe operational extremes). In this study we refer to this as *variability*. This is one of the benefits of establishing the process maps and the interrelation between the hardware, in-flight state and coating

$$\text{Variability in P} = \frac{(P_{\max} - P_{\min})}{(PM_{\max} - PM_{\min})}$$

Where, P is the property under consideration from repeated experiments and PM is the property under consideration from process map experiments (exploring the safe operational range of the hardware; section 6.2.1)

Standard Deviation has not been used in this case because of fewer experiments conducted (data points) and because each data point itself is an average of few values. The range of properties from varying parameters other than in-flight particle parameters (such as substrate roughness, substrate temperature and other deposition conditions) have not been taken into account because this study is aimed at assessing the variability in the process caused mainly due to the spray stream and their influence downstream.

7.1.3.2 Assessing Variability: In-Flight

7.1.3.2.1 Average Properties

7.1.3.2.1.1 *Single Particle Properties*

Aforementioned variability was calculated for average particle temperature and velocity (from typically 10,000 particles) and is shown in Figure 127. Variability in average particle temperature (Figure 127a) is about 5 %, which is small compared to the maximum range of temperatures obtainable by widely varying the plasma forming torch parameters. Of the four methods considered herein, OI method seems has the least variability while FP method has the most variability. This is perhaps due to controlling the trajectory by optimizing injection in the OI method.

Variability in average particle velocity (Figure 127b) is slightly higher than the variability in particle temperature. FV method has the least variability followed by OT method. Both FP method and OI method have the highest variability. In the case of OT method, the maximum variability is set by the user in terms of allowed limit while tuning-in and controlling the process to achieve same average temperature and velocity. The variability calculated with the allowed range is about 5%, while the observed variability is about 4%. This explains why this is lower than FP method. Controlling the trajectory (OI method) doesn't appear to reduce the variability in average particle velocity. In FV method the intention was to only control the voltage and hence the input power. But the resulting average temperature and velocity were very close to each other and hence the lower variability in the case of the current experiments. This suggests the presence of a possible link between the input power and the average particle temperature and velocity even for different sets of plasma forming torch parameters.

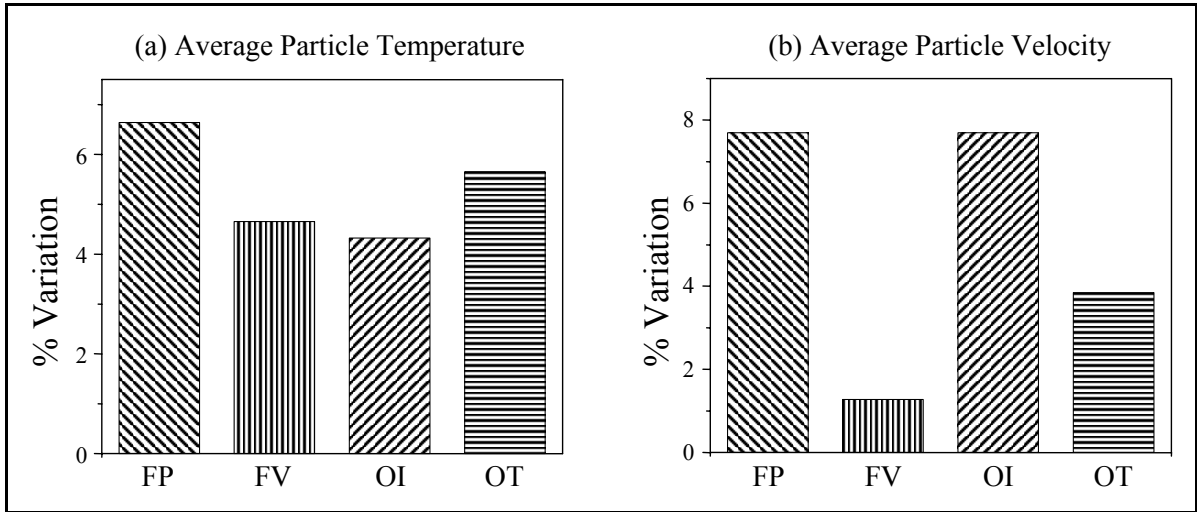


Figure 127: Variability in average particle properties from single particle measurements at the flow center as measured by DPV2000 for the different process control methods. Variability in temperature and velocity is shown in fig a (left) and fig b (right) respectively. Temperature does not show any significant difference whereas velocity shows difference

7.1.3.2.1.2 Ensemble Properties

Variability in ensemble plume properties, temperature (measured by IPP) and plume width (measured by SPT) are shown in Figure 128. The variability in ensemble temperature (Figure 128a) is clearly a few times higher than the single particle averaged counterpart. The variability in plume width (Figure 128b) also shows higher variability compared to the variability observed in average particle temperature and velocity.

Fixing the average particle temperature appears to constructively influence the ensemble temperature, resulting in the lowest variability among the four methods. This is perhaps due to the ability of the ensemble sensor to capture the changes in the plume as a whole. Variability in plume width (Figure 128b) appears to be significantly influenced by

controlling or optimizing the process as is shown by the higher variability of OI and OT methods. FV method shows the least variability.

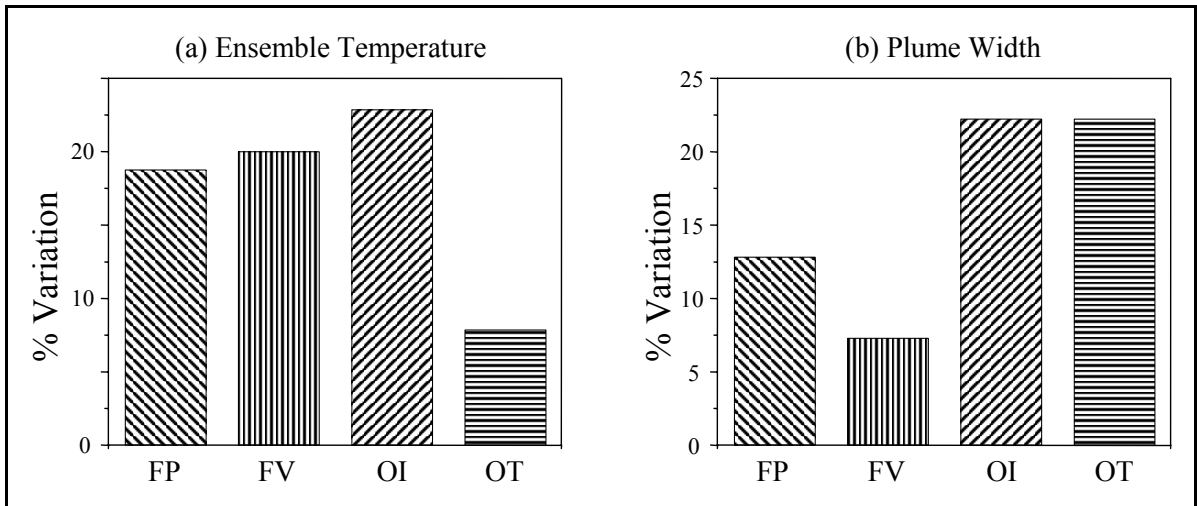


Figure 128: Ensemble plume properties. Plume ensemble temperature measured by IPP 2000 (fig a) shows less than half the variability of other methods for the OT method. Plume width measured by SPT (fig b) shows least variability for FV method

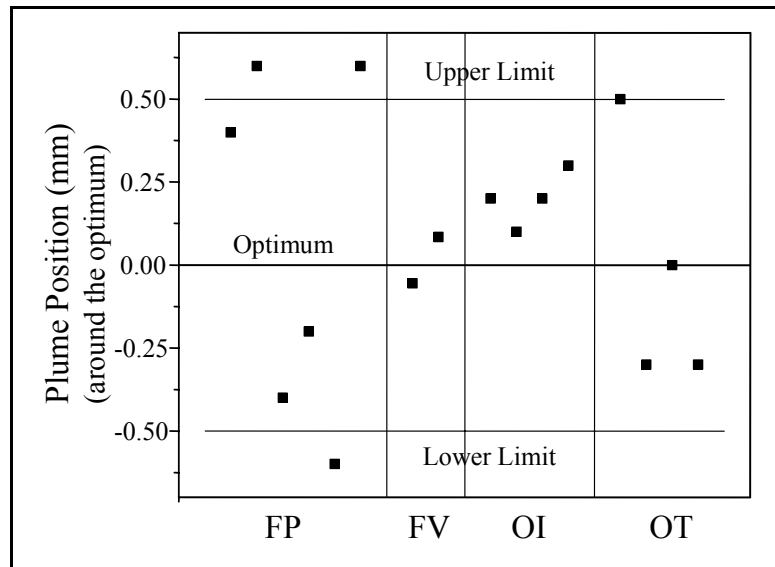


Figure 129: Plume position subtracted from the optimum plume position. FV and OI method show the least variability while FP method shows the highest variability

Plume position subtracted from the optimum plume position is shown in Figure 129. For this parameter the variability cannot be normalized with the maximum range possible because injection is optimized for every experiment exploring the operational space and hence ideally the maximum range should be zero. For all methods other than FP method, injection was optimized. OT method shows the highest variability amongst the three. But

the variation is within the allowance (± 0.5 mm) for optimizing the injection. FP method shows the highest variability of all methods, though not appreciably higher than the permitted range. Due to the dynamic nature of plasma, the plume position keeps changing rapidly and hence is difficult to control, especially when the parameters are altered.

7.1.3.3 Distributions

Distributions of particle properties (temperature and velocity) provide better insight into the in-flight state of the process than just the average values of particle and plume properties. It has been observed that the particle velocity behaves as a normal distribution and that there is no noticeable difference between the distributions within each method considered herein. It is known that the particle temperature distributions are not normal distributions [158, 200]. They are multi-modal and can be fitted with few Gauss functions.

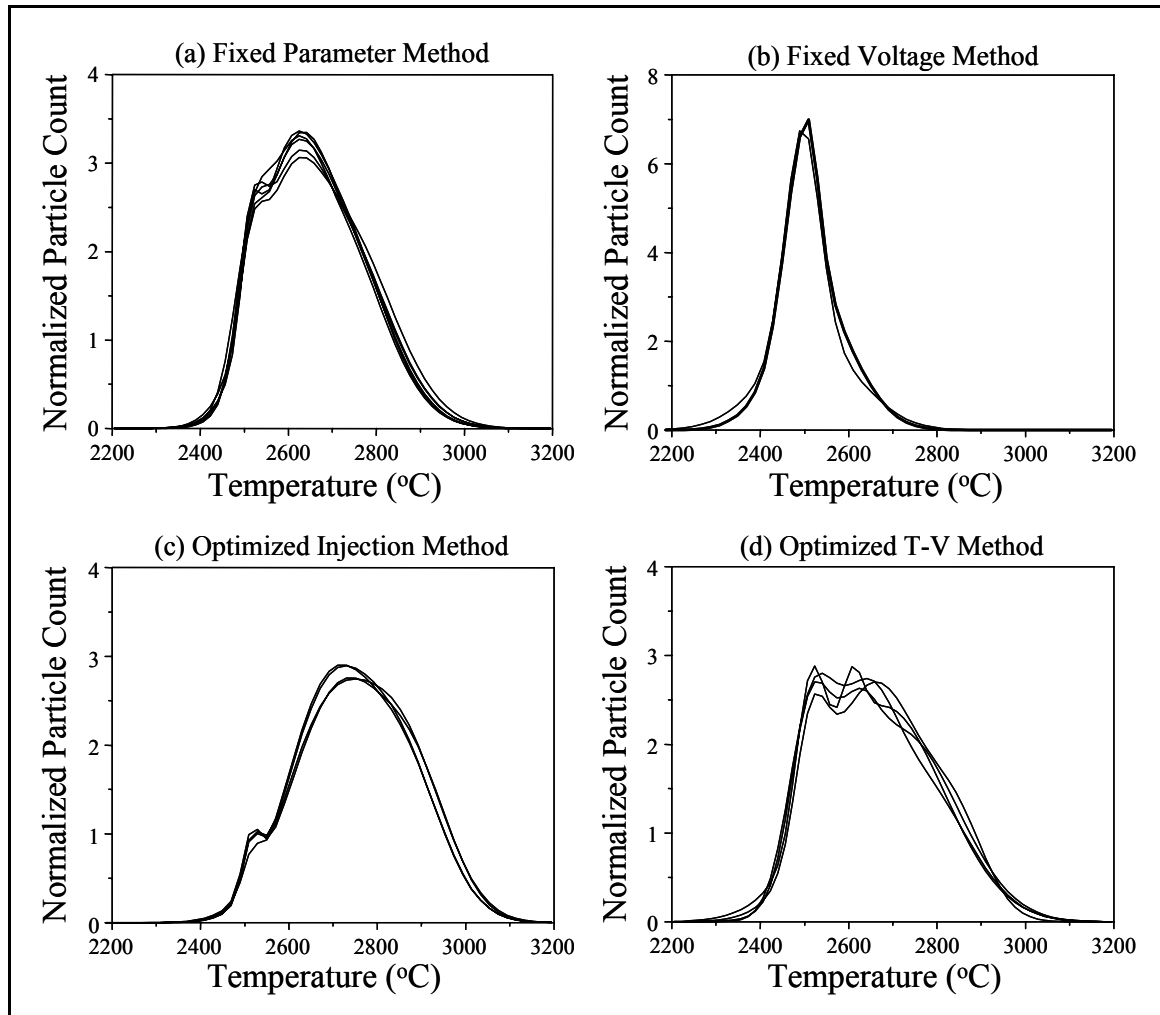


Figure 130: Particle temperature distributions overlaid from individual experiments for each process control method. No clear distinction could be observed amongst the different methods

Figure 130 shows the individual temperature distributions from experiments overlaid for each of the different methods. The melting point of YSZ has been observed to be $\sim 2500^{\circ}\text{C}$ from fitting the underlying peaks in the distributions of particle temperatures as measured using DPV 2000. The deviation from the theoretical value (2680°C) is primarily due to the error from two-wavelength pyrometry and the calibration of DPV 2000. The first peak in the distributions (only peak in the case of FV method) can be observed at $\sim 2500^{\circ}\text{C}$. For more information, refer to articles [158, 200].

For all four methods, the temperature distribution appears to be similar. A closer look at the overall distribution with their underlying peaks, FV methods shows some significant difference between the distributions and is shown in Figure 131. For the higher hydrogen condition, peak P2 is larger and is shifted to higher temperatures, which would be expected to show better melting. This has been verified by the observed variability in deposition efficiency, where the higher hydrogen condition has resulted in 40% higher deposition efficiency than the low hydrogen condition. This suggests that melting and deposit efficiency are very sensitive to small changes in temperature distributions especially close to the melting point. This also suggests that the FV method may not be the right choice to control the process in order to control the deposit formation.

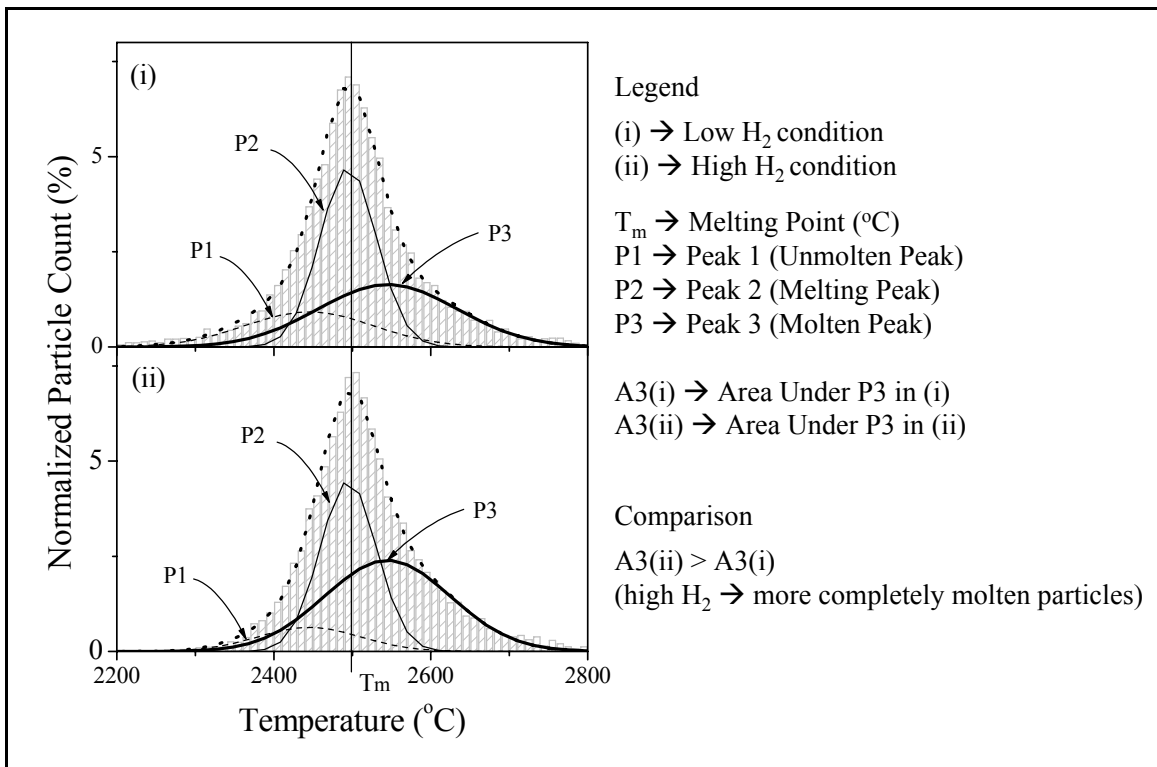


Figure 131: Detailed comparison of particle temperature distributions in the FV method. (i) Low H_2 (ii) High H_2 . The distributions have been fitted with three underlying peaks. Completely molten content in (ii) is higher than in (i) and ratio of area under P3 to P1 is clearly much higher for (ii)

7.1.3.4 Assessing Variability: Coating Attributes and Microstructure

7.1.3.4.1 Coating Build-up: Thickness Per Pass

Thickness per pass does not have significant influence on the basic aspects of splat formation such as the flattening or fragmentation within the normal limits of operation. But it does influence the layering and coating build-up and hence the transport properties of coatings. Thickness per pass influences the brick-wall structure of the coatings and hence needs to be tailored carefully to control the properties. It is also a measure of relative deposition efficiency, if all others variables and parameters are kept constant.

Figure 132 shows the variability in thickness per pass of the various coatings in each method. FV method results in the most variability, while OT method shows the least. Methods involving active control of the process at the in-flight stage show significantly less variability. OI method results in a considerable reduction in variability considering the simplicity of control involved. On the other hand, rigorous and strenuous efforts to optimize the T-V results only in a marginally better reduction in variability than the OI method. This shows the effectiveness of injecting the particles optimally in the plasma.

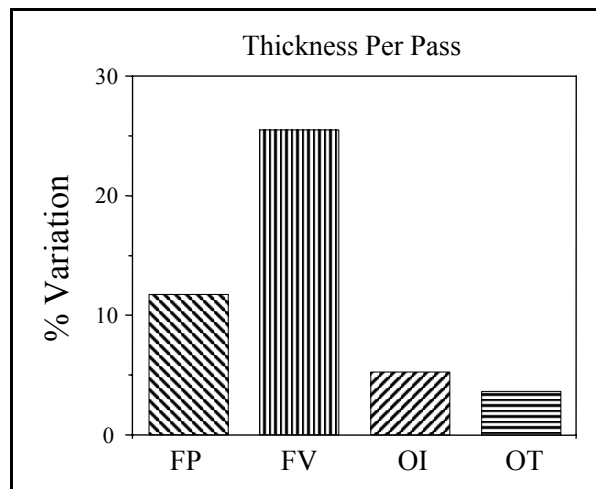


Figure 132: Variability in thickness per pass of the coatings produced by the different methods. Controlling the in-flight state results in better control of thickness per pass/deposition efficiency

7.1.3.4.2 Microstructure

It is widely accepted that coating microstructure influences the properties of coatings, especially in defect dominated systems such as thermal sprayed coatings. In the case of plasma sprayed YSZ, porosity and cracks are the most dominant defects. Though total porosity does not satisfactorily explain the measured properties, variability in total porosity has been compared here as a measure of the microstructural variability.

The variability in total porosity obtained by image analysis on optical images at 200X is shown in Figure 133. It can be seen that the methods implementing control of particle state have resulted in lesser variability. The FV method shows the highest variability, suggesting that the slight difference observed in temperature distribution have significantly influenced the coating build-up and microstructure.

The overall variation in total porosity is much higher than the variability observed in particle state. This is very likely the synergistic effect of underestimation of variability in particle state due to limitations in sensing particles, stochastic nature of the coating build-up process and error in image analysis from optical images at lower magnifications.

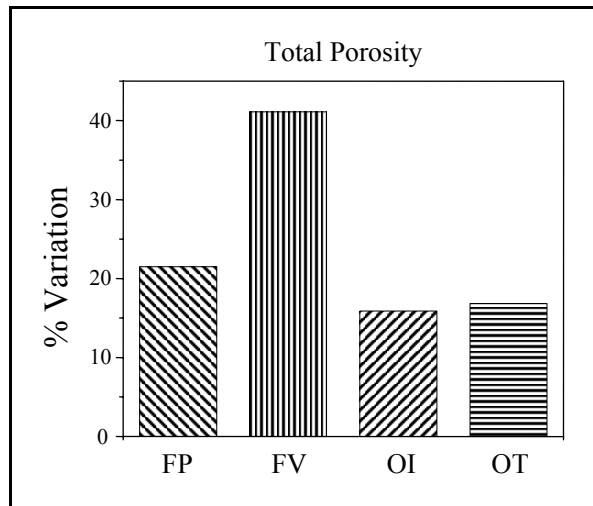


Figure 133: Variability in total porosity for the four different methods. Controlling the in-flight state (OI and OT) shows the least variability

7.1.3.5 Assessing Variability: Coating Properties

Elastic modulus has been determined through-thickness by instrumented indentation and in-plane based on the curvature technique. Thermal conductivity along the thickness direction has been as measured by laser flash technique. In essence, one mechanical (modulus) and one functional property (thermal conductivity) are considered for reproducibility assessment.

Figure 134a shows the variability in indentation modulus along the thickness direction on the top surface of the coatings. The variability is rather high for all the four methods and noticeably different only for the FV method. In-plane curvature modulus in Figure 134b also shows higher variability for all methods but considerably higher for OT method.

Both the elastic modulus values and the resultant variability cannot be directly compared to one another due to differences in principles and techniques, measurement volume, and the anisotropic behavior of coatings. A rather simple observation is made in

that both the modulus values have higher variability as against the smaller variability observed for the particle properties. In both cases of modulus, optimizing particle injection does not appear to make a difference. Controlling the particle state (OT method) appears to worsen the variability, more so in the modulus in-plane. These observations are perhaps due to the compounded effect of the variability in microstructure and the resolution, sensitivity and limitation of each method and equipment.

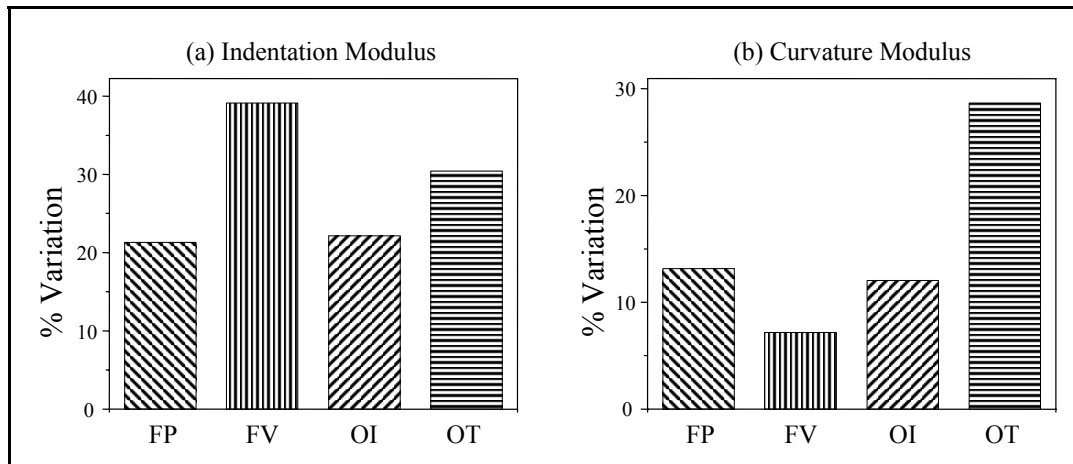


Figure 134: Variability in elastic modulus of coatings (a) via instrumented indentation along the thickness direction and (b) via curvature method in the plane of the coating

The observed variation in thermal conductivity is shown in Figure 135. Overall variability is higher compared to the variability in particle state and similar to the variability in microstructure. Hardware based control of voltage (FV method) results in the least variability. Controlling the particle injection does not influence the variability. Controlling the particle state appears to increase the variability in thermal conductivity.

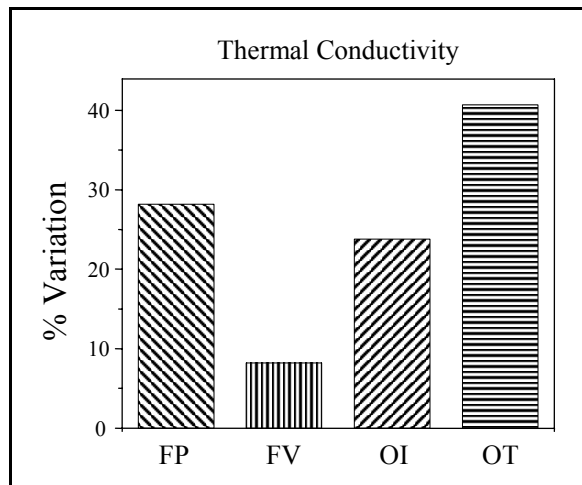


Figure 135: Variability in thermal conductivity for the different methods. Clearly, fixed voltage method shows the least variability and optimized T-V method shows highest variability (~4 times of FV and ~1.5 times that of traditional approach or FP)

7.1.4 Summary and Conclusion

Few of the commonly used process control methods, namely fixed parameter method and fixed voltage method (hardware level control), and some of the less commonly implemented methods, namely optimized injection method and optimized T-V methods (particle/plume level control based on feedback from sensors), have been compared in light of process reproducibility/variability. The effectiveness of each of the method to control the process as a whole in the short-term has been assessed at the three vital stages in the process, namely particle/plume stage, coating microstructure stage and coating property stage.

Maximum variability has been considered since treating the few data points from each method as normal distribution is not very appropriate. A basis has been suggested for comparing the different properties / response parameters at the different stages in the process by normalizing the maximum variability against the maximum range of properties obtainable for the hardware under consideration. Any change in hardware could alter the range of particle states, microstructures and properties. But if this variability is normalized with the new possible range at each stage in the process, the trends would still be similar. The relative variability between the particle state, microstructure and properties would also remain unaltered compared to normalizing the variability in property to the average of the property.

FV method shows lower variability in particle state but very large variability in coating attributes and mixed variability in properties. The actively controlled methods (OI and OT) show moderate variability in particle state, lower variability in coating attributes but shows higher variability in properties. In general, the variability observed in the coating microstructure and properties are significantly higher compared to the variability in particle and plume properties. This could be due to one or more of the following reasons

- Only average particle temperature and velocity have been considered and the distributions have not been quantified to allow clear assessment of the particle properties. Better data evaluation methods could provide better insights
- Insufficiency of average particle temperature and velocity to describe the spray stream
- Stochastic variability in the coating build-up process
- Limitations in sensing particles
- Limitations in characterizing the complex microstructure
- Reaching the limits of the measurement method

The results are somewhat contradictory at the different stages and no method can be concluded as the best considering all the stages in the process. But based on one of the basic aspect of coating formation – deposition efficiency – controlling the spray stream is better compared to having no control or hardware level control. The capability, resolution and limitations needs to be assessed for all the measurement and characterization techniques for better understanding of the results.

7.2 Examining the Variation in Splat Characteristics within the Spray Footprint

7.2.1 Introduction

The dynamic nature of air plasma spray process introduces variability at different stages in the process to different extents. At the spray stream stage, axial and radial variations of the plasma jet characteristics play a significant role in introducing variability in the spray stream via plasma-particle interactions. External radial injection adds to the issue by introducing trajectory based segregation of particle size. These variations, along with the stochastic nature of the build-up process, influence the variability in coating microstructure and properties.

Experimental and computational studies have identified the extent of radial and axial variations in the plasma plume and also their role in particle properties at the different locations in the plume [178, 179, 186, 210-213]. For any given feedstock material of a specific morphology, there is a distribution associated with the particle state at every location in the cross section of the plume at a given axial distance from the nozzle exit. This is due to the size distribution of the feedstock and also due to the radial variations in the plasma plume and the corresponding plasma-particle interaction at any given axial distance from the nozzle exit. Recent finding that the temperature distribution is not a normal distribution (Figure 136) [158] only adds to the importance of those distributions and their influence on splat and coating properties across the spray footprint.

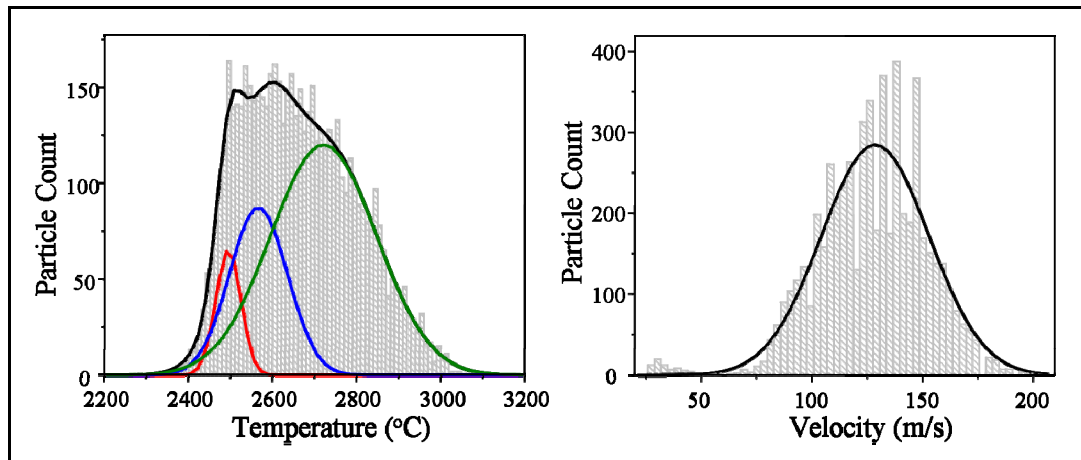


Figure 136: Temperature and velocity distributions representing the range of variability possible

It is known that splats are the building blocks of coatings and any influence on splat characteristics affect the coating assemblage, nature of the interface, the defect structure and hence the coating properties. Studies have documented the influence of particle state, as an ensemble, on the splat characteristics in order to understand/explain the coating

characteristics and properties [116, 118, 119, 121, 122, 141, 165, 188, 190]. There have been studies where the individual particles have been tracked from the in-flight stage to the splat impact, formation and beyond [31, 36, 214, 215]. Single splats have been characterized for their composition, phase, stress state, mechanical behavior under instrumented indentation [194].

There is very limited information on the spatial characteristics of splats (at different locations in the footprint of spray stream). In essence it is studying the splats at the individual particle level but for an entire array of splats whose location in the spray stream is known. Thus the extent of variability that the particles introduce to the coating microstructure can be understood by studying the snapshot of the spray stream in the form of splats. This is important for a better understanding of the coating build-up phenomena and the variations in coating properties. Each material system has different set of functional properties influenced by different microstructural and crystallographic features of the coating. Also due to the different thermo-physical properties of materials the particle state gets influenced in different ways. To understand the different aspects of the process influencing the variability in splats and coatings, we study a few of these material systems to identify the extent of variability in the different attributes.

7.2.2 Experimental Details

7.2.2.1 Process Details

A few different materials were processed using Sulzer Metco 7MB torch with an 8 mm ‘GH’ nozzle with a swirl flow of Argon and Hydrogen gas mixtures. Table 9 below shows the parameters used for the different materials. Feed rate of 2 – 5 g/min was used for diagnostics and splat collection at 100 mm spray distance.

Table 9: Feedstock and process parameters used in the study

Material	Powder Details	Size (μ)	Current (A)	Primary Argon (SLPM)	Secondary Hydrogen (SLPM)	Carrier Argon (SLPM)
Amorphous Alloy NiCrBSiMo	Abracor	20-180	400	40	3	3.9
Alpha Alumina	Vista 340S	20-50	400	35	4	6.3
Gamma Alumina	Vista 2901	10-70	400	35	4	6.3
YSZ	Saint-Gobain Lab Sample	63	575	47.6	5.9	4
Ni-Cr (50-50)	Praxair 1260F	20-60	400	40	3	4.7

7.2.2.2 Diagnostics

DPV 2000 was used for the collection of in-flight particle temperature and velocity. DPV scan was performed (49 point covering 30 mm^2 area) on the spray stream cross-section at the spray distance and particle temperature and velocity were measured at each point (refer section 3.3.1.1.1). The spray stream was thus mapped at the in-flight stage. Additionally the particle temperature and velocity were measured at the flow center. Ensemble spray stream temperature and width were measured using IPP 2000 and SPT.

7.2.2.3 Splat collection

A simple mechanical shutter mechanism was used to collect a snapshot of the spray stream (refer section 3.1.2.2). A snapshot of the plume at the in-flight stage and as splats is what we call a *splat map* (Figure 137). Polished stainless steel substrates $75 \times 75 \text{ mm}^2$ maintained at 250°C were used for collecting splat.

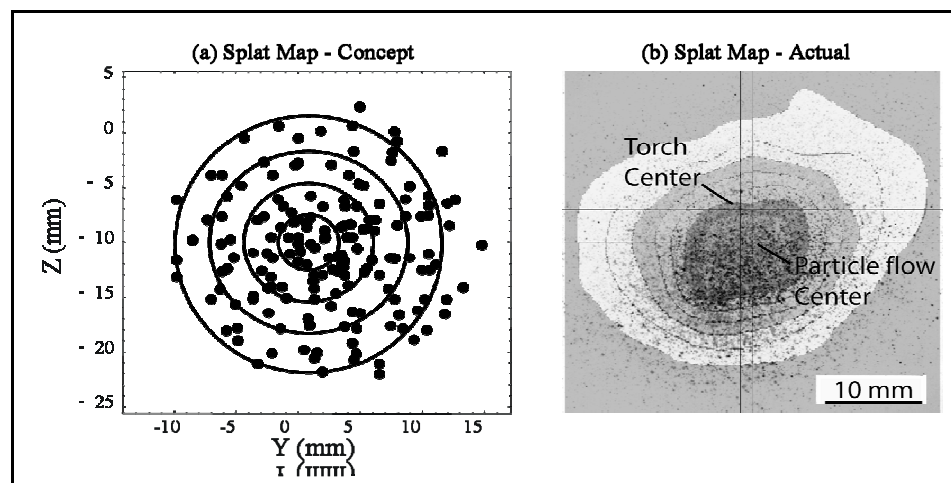


Figure 137: Splat Map – Schematic (fig a) and Actual (fig b)

7.2.2.4 Characterization

Splat map thus obtained have been characterized for morphology using optical microscopy and for flattening behavior using scanning white light interferometry using Zygo. General Area Detection Diffraction System (GADDs) was used to understand the phase content in the splats from the different regions. X-Rays of CoK_α wavelength was focused to 500 square microns to cover a few splats over a small region of the splat map. The region under consideration was exposed at each angle for the same duration. It should be noted that splats did not cover the entire surface and the splat thickness were in the order of a few microns (~ 2 to 5 microns). This resulted in strong substrate (stainless steel) peaks in all cases. The results are presented at CuK_α wavelength due to the familiarity of XRD data at that wavelength.

7.2.3 Results and Discussion

7.2.3.1 Diagnostics Vs Splat Map: Comparing Flow Pattern

Figure 138 on the top shows a flow contour from particle diagnostics using DPV and the bottom half shows the corresponding splat snapshot. To a first approximation, the shape and orientation of the splat snapshot correlates well to that of the in-flight particle flow pattern. This provides some level of confidence in both the particle diagnostics and the splat snapshot.

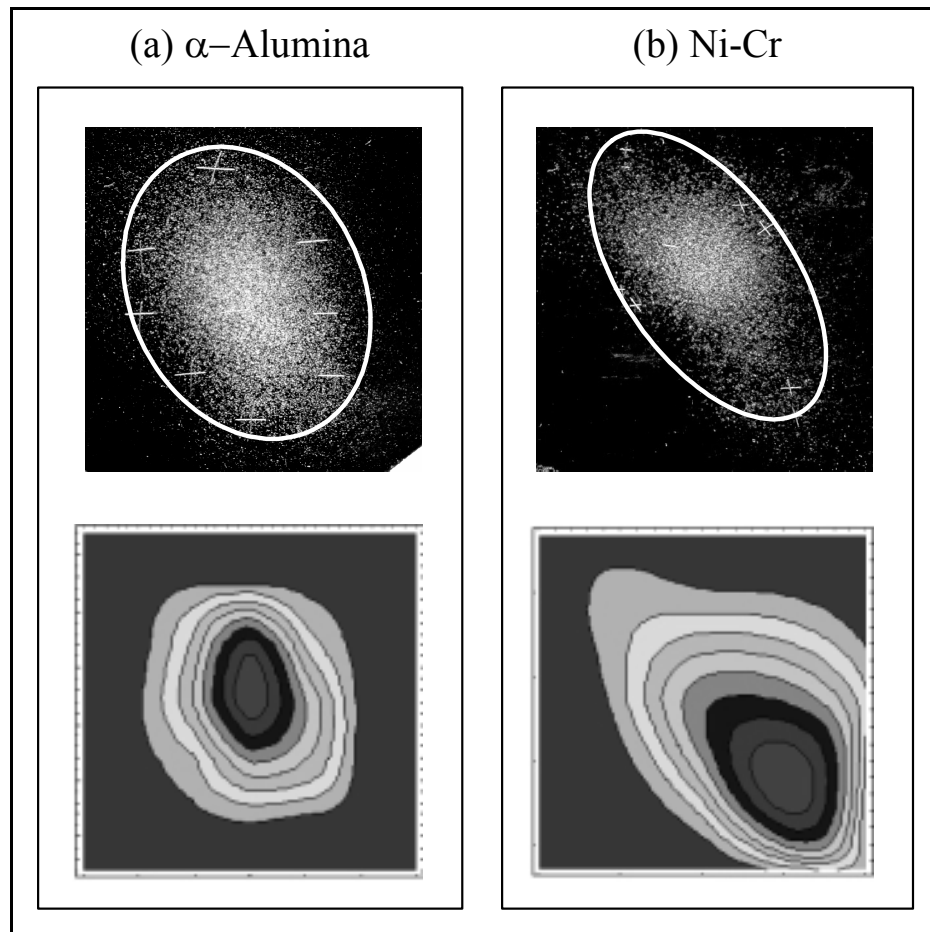


Figure 138: Correlation between particles in the plume as captured by a cross-section scan by DPV 2000 and the splats. The pictures on the top are photographed splat maps and are not shown to scale. The bottom pictures are contour maps of the particle flow at the standoff. In fig b, the entire plume has not been captured in particle diagnostics due to the plume being wider than the scanning grid (as revealed by the contour maps in the post-processing). The flow contours appear to capture the shape of the splat map for both the ceramic system (fig a) and metallic system (fig b)

The flow center location obtained from diagnostics and from visual examination of the splat map does not appear to correlate very well (Figure 139). This could be due to

the fact that diagnostics preferentially senses larger particles which are more intense due to the larger surface area. The finer particles are thus missed to some extent in the particle diagnostics. On the other hand, this could also be due to the swirl in the plume and the rotation of arc resulting in hot zones at different locations in the plume cross-section (YZ plane) at different instances of time. It should be noted that the splat collection was done in about 50ms, which is, to a first approximation, in the same time scale as the arc root fluctuations. Hence the observed phenomenon could be due to any of the two reasons or both. The other pitfall is in correlating the torch coordinates on the substrate.

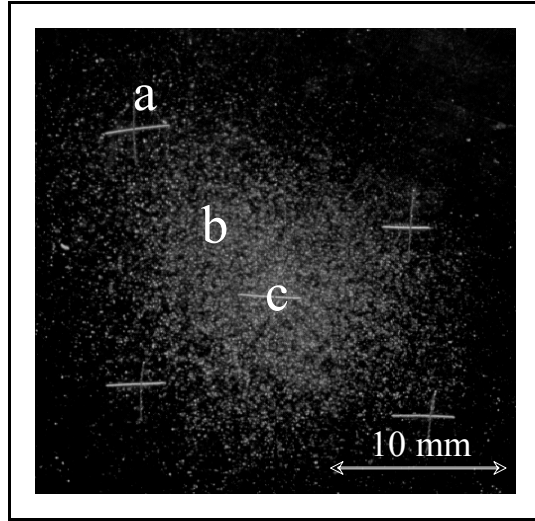


Figure 139: Splat map with coordinates from DPV contour map superimposed for Abracor amorphous alloy. 'a' corresponds to the nozzle axis, 'b' to the flow center measured from DPV and 'c' to the 'visual' flow center from the splat map. There exists discrepancy between flow centers detected using DPV (point 'b') and splat map (point 'c')

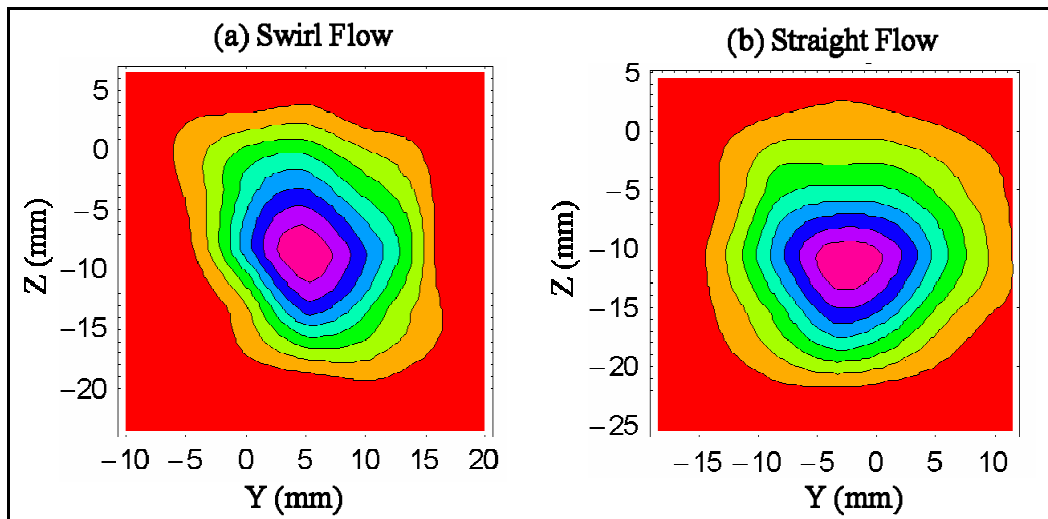


Figure 140: Flow contours of particles measured using DPV scan across the spray stream for YSZ. Straight flow shows circular contours while swirl flow results in elliptical contours

Experiments have been performed under straight flow of plasma gases with some of these feedstock materials. The flow contours measured using DPV match the observed splat profile. Moreover the flow contours are circular to a first approximation and not elongated as in the case of swirl flow of plasma gases (Figure 140).

7.2.3.2 Splat Morphology

The splat map obtained from amorphous alloy (Abracor) feedstock was divided into nine zones of almost the same substrate area for characterization. The splats in each zone were carefully observed under optical microscope and a representative splat from each zone is shown in Figure 141. At the first look it can be seen that the splat morphology is not the same in all the zones. Splats show that the particles in-flight were completely molten in some regions and partially molten in the other regions as demonstrated by the missing cores. It can also be observed that all the molten particles did not result in the same splat morphology. Some regions show more or less disc shaped splats (with a curled edge) with almost no splashing, whereas the splats are splashed in other regions formed by fully molten particles.

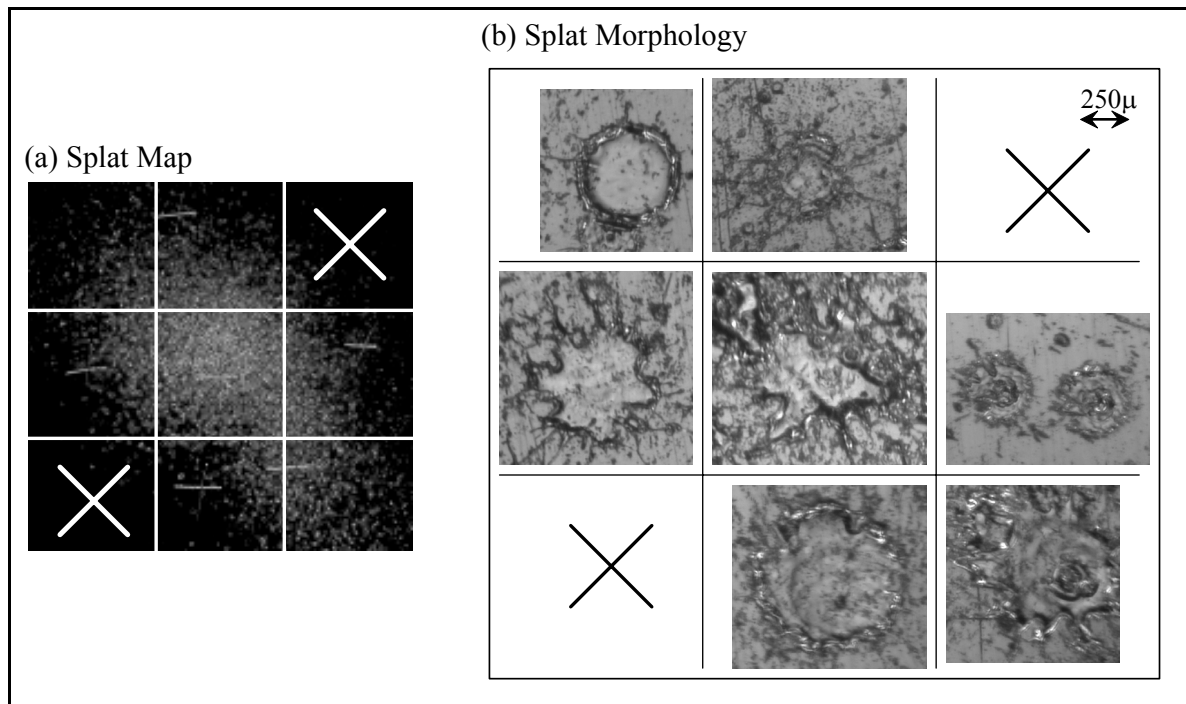


Figure 141: Optical micrographs of representative splats from the different regions in the splat map for Abracor. Splat morphology can be observed to vary from disc shaped to splashed to splashed with missing core in the different regions

The center region had very high splat density (relative surface area covered by the splats) and the rest of the regions provided splat density usually considered suitable for further characterization. Though this is not a new observation, the point to note here is

that the splat morphology at the central region is not the same as the splat morphology in other regions. Flattening ratio is measured only from disc shaped single splats with no or very less splashing. One should keep this in mind when interpreting results from splats obtained by the traditional swipe method of splat collection as the results could be biased.

7.2.3.2.1 Flattening Ratio

Flattening ratio has been calculated from representative splats in the different zones in the splat map for Abracor and YSZ. Small difference could be observed in the flattening ratio measured at two different locations in the splat map for Abracor (Figure 142).

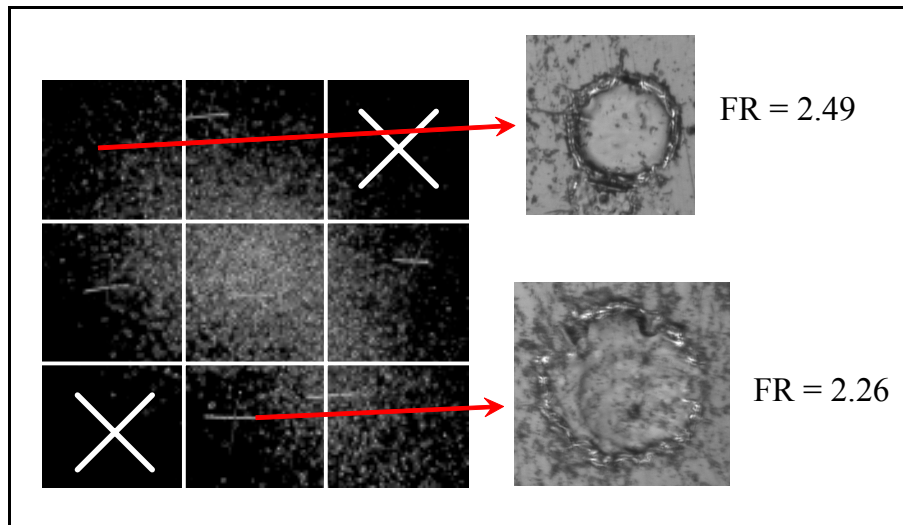


Figure 142: Flattening ratio measured at different regions in the splat map

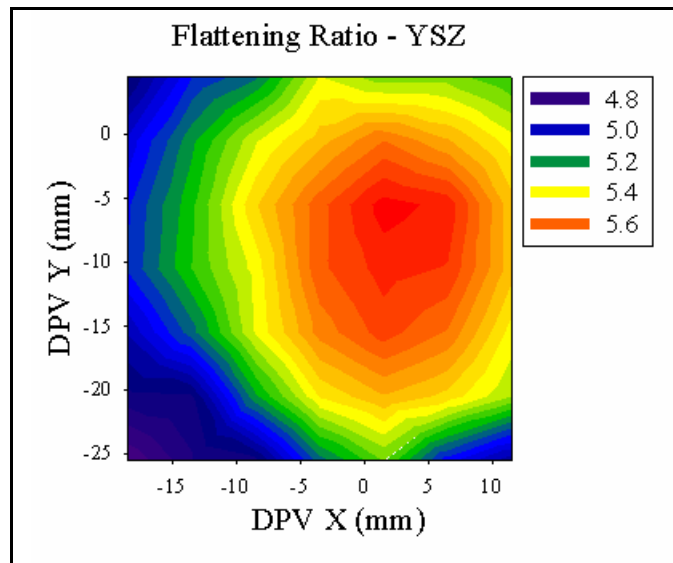


Figure 143: Flattening ratio (Madejski model) distribution across the spray stream for YSZ

Flattening ratio calculated using Madejski model [205] for YSZ is shown in Figure 143. The difference between the maximum and the minimum in flattening ratio in the splat map is more than half the difference between the extremes in process map. This shows the extent of variability that can arise from difference in particle states within the spray footprint.

7.2.3.3 Phase

Powder diffraction was done on a group of splats in the different regions of the splat map for amorphous alloy and alpha alumina and the integrated intensity profiles are shown in fig and fig respectively. Due to improper choice of substrate (stainless steel) and since the splats are thin (splat thickness $< 5 \mu\text{m}$) the strongest peaks are from the substrate. Despite the contribution of substrate, the regions marked 1 and 2 in fig show different extents of amorphous content (bump). Corresponding difference could be observed in the splat morphology. In the case of alpha alumina feedstock, same regions 1 and 2 show difference – region 1 shows the presence of gamma alumina while region 2 does not show gamma. This shows the differences that exist in the different regions in the splat map despite the limitations in the experiments (contribution from substrate and different extents of splat coverage in the different regions). This observed difference is due to particle state, which is in turn due to the interaction of the particles with the different plasma zones. Studies are underway to establish the correlation between particle state and splat characteristics.

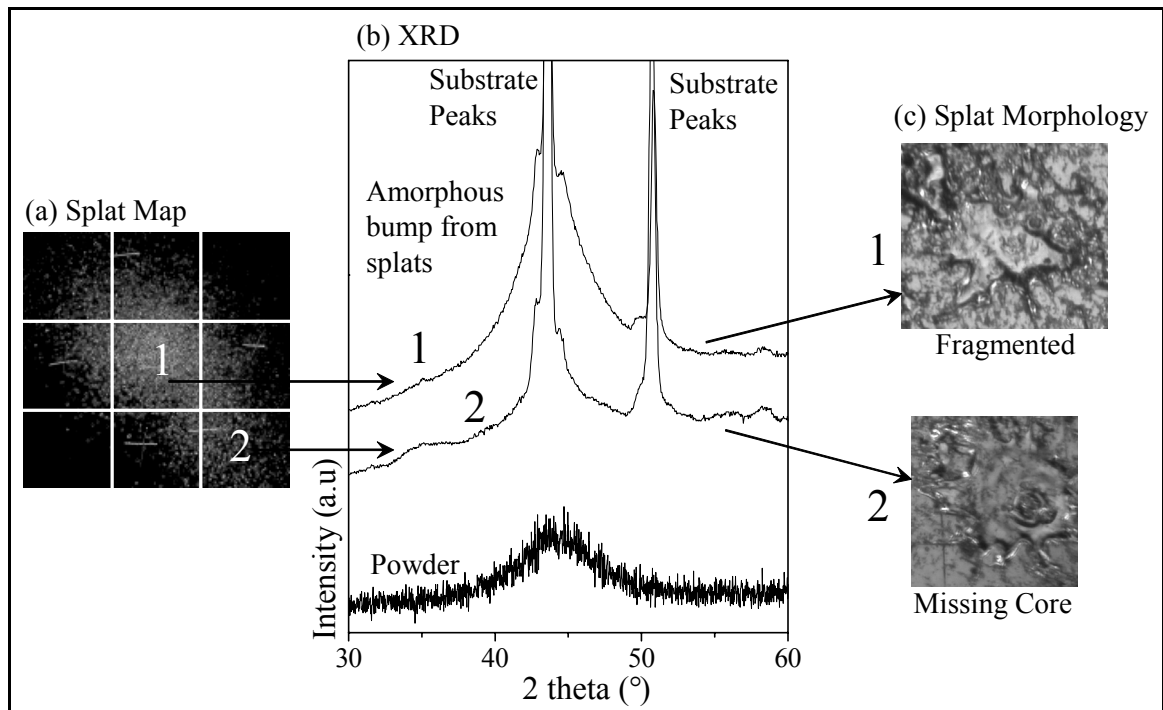


Figure 144: Integrated powder XRD profile of amorphous alloy. Different extents of amorphous content could be observed in regions 1 and 2

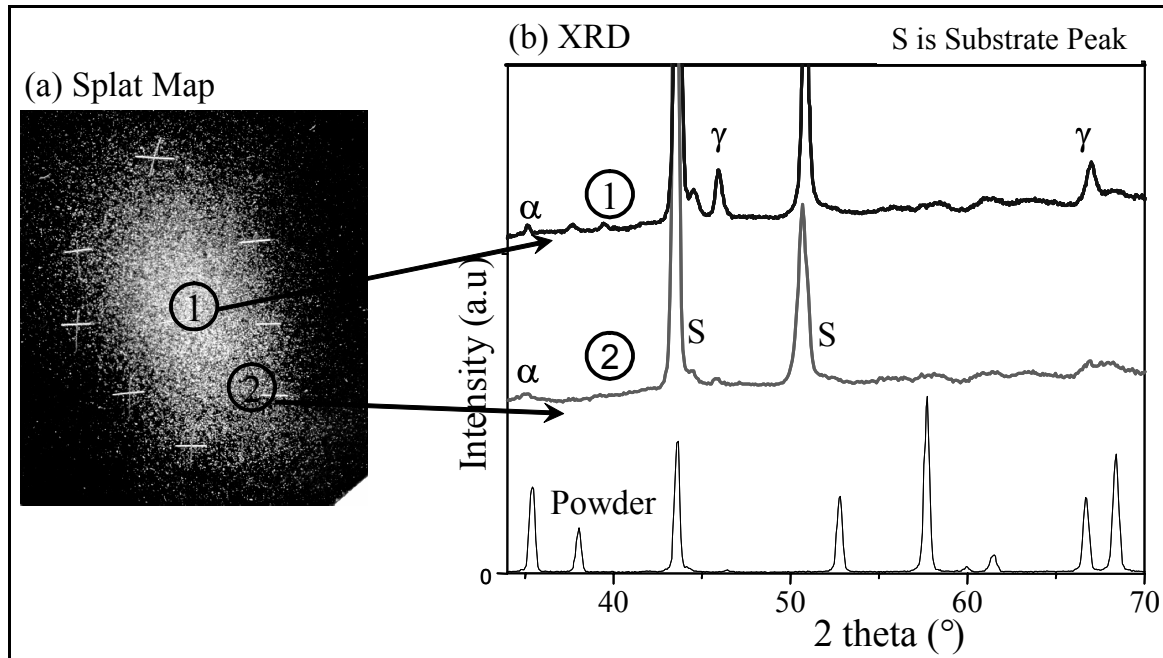


Figure 145: Integrated powder XRD profile of alpha alumina. Gamma phase is present in region 1 but is not present significantly in region 2

7.2.4 Summary and Conclusion

It is known that particles injected in a plasma stream follow differing trajectories which in turn leads to different thermal and kinetic history before they impinge on the substrate. The variation in particle characteristics across the spray stream results in variation in splat characteristics across the spray footprint. In this study an attempt was made to understand the spatial variability that exists in the 'splat map' (spray footprint) by a combination of detailed in-flight diagnostics and collecting a snapshot of splats using a shutter mechanism that exposes the substrate for a very small period of time (~50 ms).

The first simple observation is the difference in areal density of splats within the splat map. This is to be expected given the particle trajectory, interaction of the injected particles with the plasma jet and the resulting difference in particle properties and plasma jet promoted segregation in the spray stream. The shape of the splat map obtained through the snapshot shutter method agrees well with the flow contour obtained from cross-sectional scan of the spray stream (at the spray distance). This suggests that the particle diagnostics captures the in-flight particle state effectively with respect to splat formation.

Morphology was studied at the different regions in the splat map using the optical microscope for splats made with a few different materials. These results show that appreciable differences exist within the different regions. In coarse amorphous alloy feedstock, this change could be observed more clearly than the other feedstock. Due to

the experiments done with swirl flow of plasma gases, a clear symmetric change was not observed in the splat morphology. For the same reason, correlation between particle state and splat morphology could not be made.

Flattening ratio was measured for the amorphous alloy splats since they showed the most difference in morphology. Only a small difference could be observed between representative splats from the different regions. Whereas flattening ratio calculated for YSZ processed under straight flow plasma conditions from the particle state using Madejski model shows significant symmetric variation in flattening ratio as shown by the flattening ratio contour. The difference in flattening ratio between the center and the radial extreme is more than half the change observed in average flattening ratio at the extreme process conditions in the design of experiment. This suggests that the flattening behavior is significantly influenced by the plasma-particle interaction within the spray footprint.

It should be noted that most of the studies on splat flattening ratio to understand its relation to the process conditions has been done using splats obtained from the swipe method where the torch is passed swiftly over the substrate. Splats obtained through this method have very high areal density in the center of the splat trail and low density at the edges. Since single splats are necessary to measure flattening ratio, splats from the regions with less areal density have been used to measure flattening ratio. This is not completely representative of the process condition and comparison made between splats processed at different process conditions is not accurate. This is perhaps the reason for the high standard deviation reported in previous studies [114]. The splat map method of splat collection enables proper comparison of splat characteristics between the different process conditions since comparison can be made based on splat measurements at specific known locations in the splat map.

Some difference could be observed in the phase content of the splats from different regions. Though this study is encouraging, the results presented here are not accurate due to the contribution from the substrate and due to sampling only a few splats by XRD. Larger area needs to be covered in order to sample more volume of splats (such as $3 \times 3 \text{ mm}^2$ instead of the currently used $0.8 \times 0.8 \text{ mm}^2$). Recently splat maps have been obtained using straight flow of gases for a wide variety of materials avoiding the limitations of previous studies such as using appropriate substrates (Si wafer) for phase studies.

This study points out the issues with current ways of characterizing splats to understand the effect of processing conditions on the splat characteristics. This variation within the splat map is perhaps the most significant reason for the variability observed between coatings presented in the previous section of this chapter. The variability in coatings could potentially be minimized by simply blocking the radial extremes of the spray stream in order to avoid the particles/splats with widely different properties from the vast majority of the particles at the flow center. Since the particle distribution in the plasma jet is considered to be three dimensional Gauss profile, blocking the radial extremes of the spray stream would not be expected to influence the deposition efficiency drastically.

Chapter VIII

8 Discussion of Salient Observations

The results presented earlier in this dissertation were geared towards tailoring coatings and achieving reliability in coatings via process reliability. Some interesting observations have been made during the study, which are discussed in this chapter to enable integrated understanding of the individual studies.

8.1 Particle Injection

In chapter 4, an intriguing phenomenon was presented – injection ‘sweet-spot’. It has been observed to be invariant with respect to a host of process variables that significantly influence particle injection. It is clear that such an optimum will occur if there is maximum heat and momentum transfer between the plasma and particle. Since most of the critical plasma-particle interactions happen in the hot zone where experimental studies are limited, we recourse to process modeling to examine the phenomenon in collaboration with Prof. H. Zhang.

There are primarily two zones in the plasma jet that the particles experience – the plasma zone where the particles receive most of the thermal and kinetic energy and hot gas zone where melting continues and both thermal and kinetic energy of the particles keep decreasing and could result in re-solidification (not considering evaporation of particles) (Figure 146). Particles following trajectory marked by 1 in Figure 146 is a case of under injection resulting in improper penetration resulting in smaller dwell times in both the plasma zone and in the hot gas zone. The other extreme is the particles following trajectory marked by 3 in Figure 146, where most of the particles are over injected resulting in through penetration of the plasma zone and less dwell time in the hot gas zone due to being along the radial extreme of the hot gas zone. Particle trajectory marked by 2 in Figure 146 represents the optimum condition as a function of maximum dwell time in the plasma zone and in the hot gas zone as well. This is perhaps the reason why despite the increase the particle velocity particles reach higher temperatures resulting in an optimum injection condition. The same is also observed in simulations [216] as shown in Figure 147.

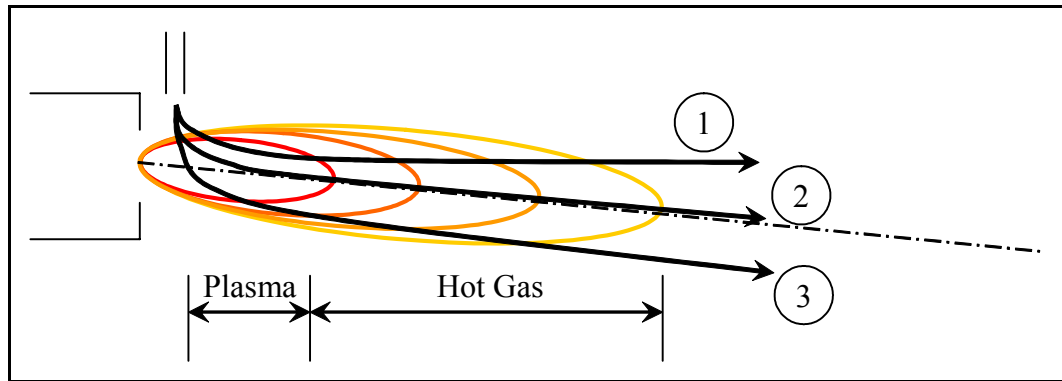


Figure 146: Schematic of particle injection and spray stream trajectory

As to the origin of maximum heat and momentum transfer at the same plume position (angle of the trajectory), computational modeling based on the LAVA 3D program at Stony Brook provides the answer [179, 216]. Figure 148 shows a plot of the tan of the plume angle as a function of the carrier gas flow and the ratio of injection velocity at the exit of the injector to the plasma jet velocity at the point of injection along the spray for few different primary gas flows using LAVA 3D. It can be seen that the plume angle and the velocity ratio at the optimum (maximum temperature and velocity) are comparable across the different primary gas flows. This suggests that the velocity ratio governs both the angle of the spray stream and the momentum transfer to the particles and that there exists a velocity ratio where momentum transfer reaches maximum.

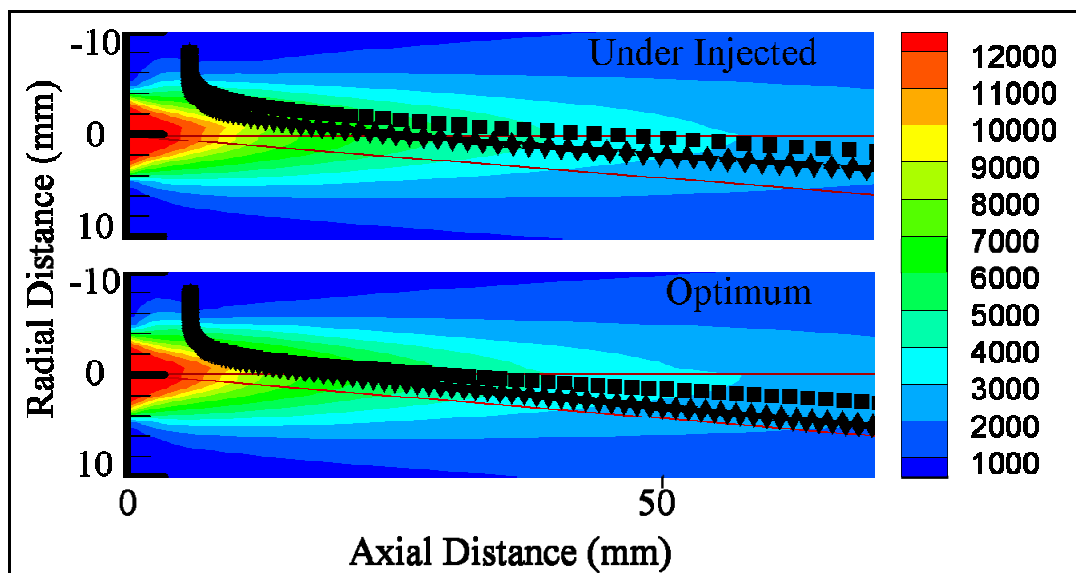


Figure 147: Simulation results showing plasma temperature profiles and the interaction of the injected particles (at two different carrier gas flows – top: under injected and bottom: optimum injection) resulting in different trajectories. Different extent of penetration in the hot zone can be observed as well as the spread of the trajectory consisting of different particle sizes

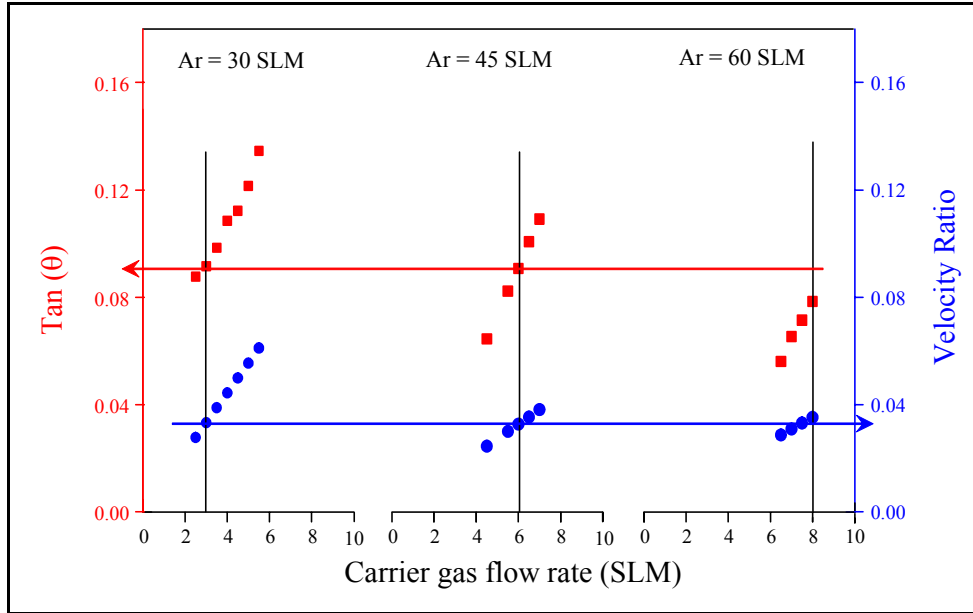


Figure 148: Tan of plume angle and ratio of initial vertical velocity to the horizontal velocity at the spray distance as a function of carrier gas flow for different primary gas flows. The vertical black lines correspond to the optimum injection. Blue horizontal line intersecting the velocity ratio axis shows that optimum injection occurs at the same value of velocity ratio. The red horizontal line intersecting the tan (θ) axis shows that the optimum occurs at the same plume angle

This combined experiment and simulation studies have enabled understanding of the plasma-particle interaction during particle injection and the occurrence of the sweet-spot in the resultant in-flight particle state as a function of the angle of the trajectory.

8.2 Examining Particle State and Spray Stream

As discussed in the statement of the problem, the process diagnostics equipment resort to measurement of particle temperatures or particle velocities through either single particle type measurements or ensemble measurements. In most cases, one tends to use the average velocity and temperature to establish correlations with microstructure and properties. Of particular concern is that temperature measured is usually only on the surface contributing to potential inaccuracies associated with the surface measurements. In order to understand the sufficiency of average temperature and velocity to describe the spray stream, a series of experiments were conducted with the different feedstock morphologies. The results showed a large variation in coating properties and deposition characteristics when the average temperature and velocity were controlled by varying the torch parameters widely. Based on those results the insufficiency of average temperature and velocity was established. The source of the variation in deposition characteristics and coating properties are addressed here by considering the following questions.

8.2.1 Validity of the Measured Particle Temperatures

It is known that the temperature measured is the particle surface temperature. Though particle temperature does not provide a sufficient understanding of the melting status, the measured temperature itself is not invalid. Calibrated two wavelength pyrometry is known to be fairly accurate for high emissivity materials such as oxides of metals (ceramics) including YSZ [27, 217, 218]. Absence of chemical reaction such as oxidation (and the resulting material with different properties) works in favor of proper measurement for YSZ. Due to measurements at longer spray distance, the contribution from plasma and scattering of plasma by the particles are minimal.

The spectral emissivity is not well known as a function of temperature for solid and liquid material. Hence accuracy of measurement could be compromised especially at higher temperatures due to pronounced parabolic nature of the spectral emissivity in general [27]. Due to these factors, the absolute temperature measured could be inaccurate but the relative differences measured between the different process conditions are accurate.

It is known that measuring different regions in the spray stream can result in different particle temperature and velocities. In order to consistently measure at the same location in the spray stream, particle injection was optimized for every set of process parameters. This results in controlled and comparable trajectories in all cases eliminating error in location of measurement if the flow center could be identified reliably. The “auto-centering” procedure of DPV is very reliable in identifying the flow center in straight flow systems especially with high intense (high emissivity and high temperature) powder particles. Thus it can be concluded that the measurement of particle states are reliable and valid.

8.2.2 Difference between Ensemble Temperature and Average Particle Temperature

The difference between single particle measurement and ensemble measurement is the measurement volume and the number of particles that contribute to the measured intensity. When measurement is made on one particle, emissivity does not play a role since the ratio of the intensity is used with gray body assumption. When intensity is measured from an ensemble of particles, two issues are observed

- **Spatial Variation:** The cylindrical measurement volume captures particles that are at the center as well as the radial extremes of the spray stream. This results in averaging out the intensity from relatively hot (center of spray stream) and cold particles (radial extremes)
- **Emissivity Difference:** Due to the aforementioned reason and due to the simultaneous measurement of intensity from multiple particles the use of gray

body assumption is questionable. Using gray body assumption results in overestimation of temperature [26].

Thus the difference observed in ensemble temperature for the same average particle temperatures (difference between the experiments; not the absolute difference). Due to large volume of measurement and the associated averaging effect (despite the absolute error), it could capture the changes in process. But the result (Figure 76) shows that the ensemble temperature does not explain the trend in melting and deposition behavior.

8.2.3 Source of the Variation

Melting Index showed higher variability for all the morphologies considered, which leads us to believe that it holds the key to understanding the relation between the in-flight state of the process and the deposit efficiency since it is a non-dimensional group parameter taking into account the particle temperature, velocity and size. Average Melting Index calculated from individual particle measurements has been plotted against the relative deposition efficiency in Figure 149. One can observe the drop in deposition efficiency as the Melting Index increases, which is against current understanding. It should be noted that the change in Melting Index for these experiments are relatively small compared to the range of possible values (from process map), which suggests that the Melting Index has not effectively captured the changes observed. This is in contrary to the findings of Vaidya [146], Li [194] and Zhang [161]. Since the substrate and deposition related variables were identical, this is due to a difference in the particle state that has not been captured by Melting Index. The difference in the degree of splashing between these process conditions with comparable (known) particle characteristics would not be expected to be large enough to explain the observed difference.

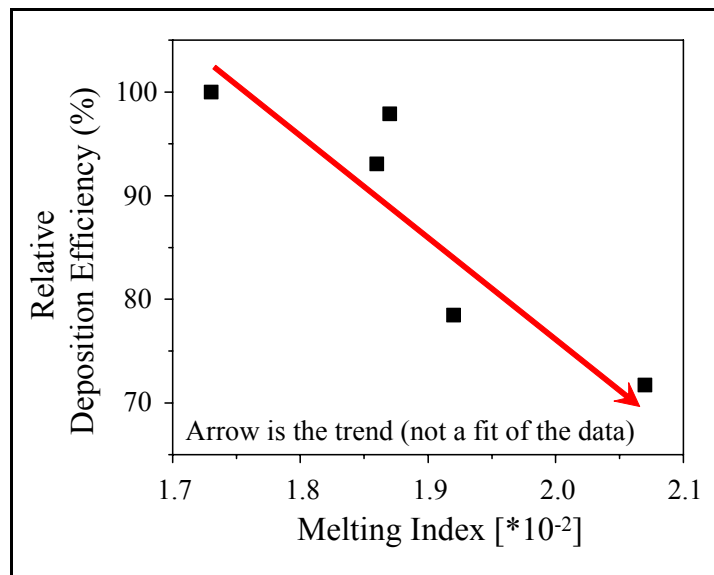


Figure 149: Relative deposition efficiency as a function of Melting Index for experiment set A. Deposition efficiency decreases with increasing Melting Index

A close look at the temperature (Figure 66) and Melting Index (Figure 67) distributions shows that they are considerably different between the different conditions and. These distributions (with detailed analysis) can explain the basic deposition characteristics to a first approximation. But what caused the distributions to be different?

The change in plume characteristics captured by plume width suggests that the plasma jet characteristics are different resulting in different interaction with particles though their averages are the same at the spray distance. A probable explanation is the difference in plasma jet characteristics, such as the energy density and its spatial distribution, which influences the particle state differently. The distribution of particle flux (contour map) and temperature (contour map) across the spray stream at the spray distance are shown in Figure 150 and Figure 151 respectively for the five different experiments where the same average particle temperature and velocity was achieved using HOSP feedstock. The shape of the particle flux distribution is different in each case and so is the location of maximum flux in the cross-sectional plane, implying the plasma fluid flow profiles are different. The temperature profiles are somewhat different but they are relatively flat over a large region near/at the flow center (compare with Figure 150).

The other source of variation could be the consideration of particle temperature and velocity at the flux center. Though particle characteristics measured at the flux center (or flow center) can explain most of the trends and relative difference in coatings it appears to breakdown in this dimension of the process space considered. Comparison of particle temperature distribution measured at the flow center with the distribution measured from a systematic array of points in the plane of spray stream cross-section, both at the spray distance, captures the difference (Figure 152). The extent of difference would be influenced by the characteristics of plasma.

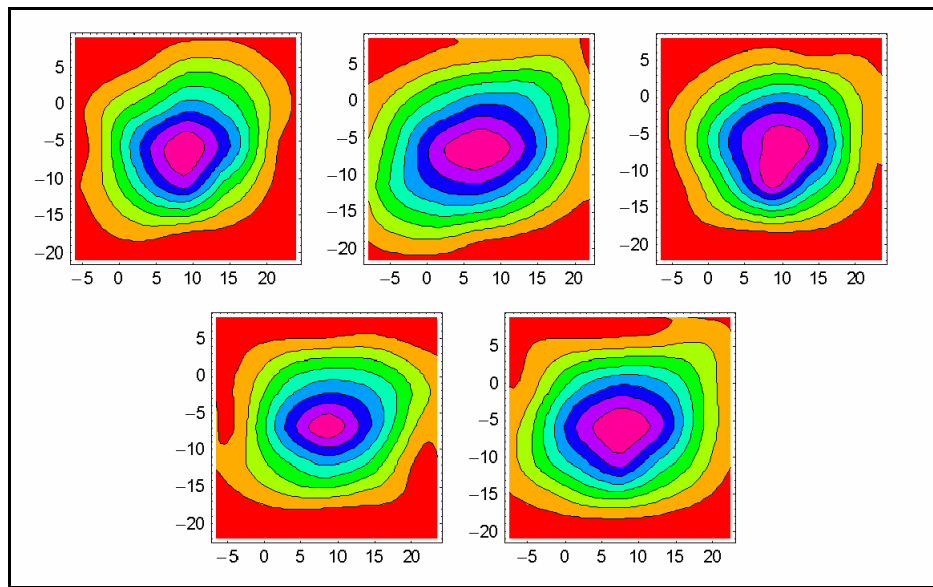


Figure 150: Contour maps of particle flux across the spray stream at the spray distance for the 5 experiments (section 5.2.3.1) where average temperature and velocity were same but the deposits were different. Difference in overall shape and location of the flux center could be observed

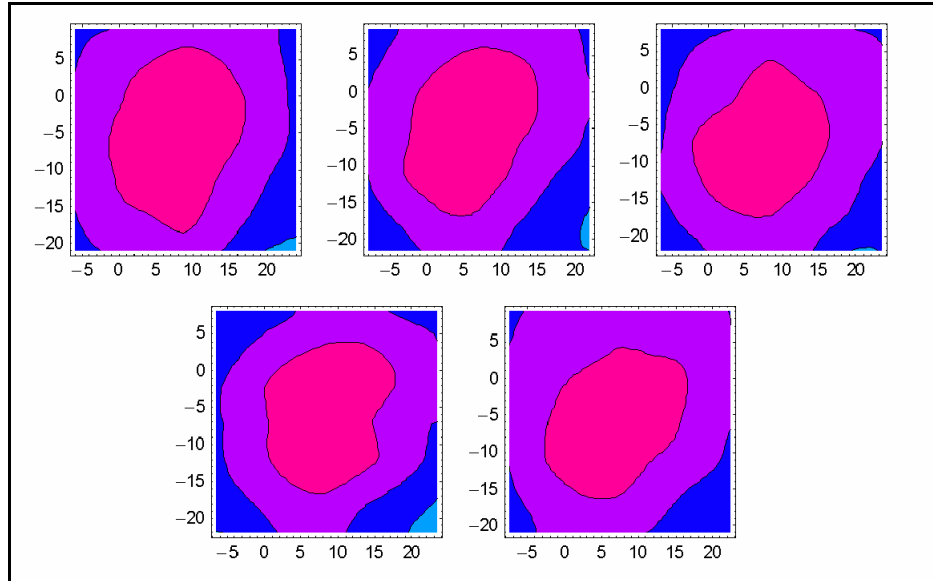


Figure 151: Contour maps of particle temperature across the spray stream at the spray distance for the 5 experiments (section 5.2.3.1) where average temperature and velocity were same but the deposits were different. Difference in shape does not appear to be very significant. There is a large ‘flat’ region at the flow center

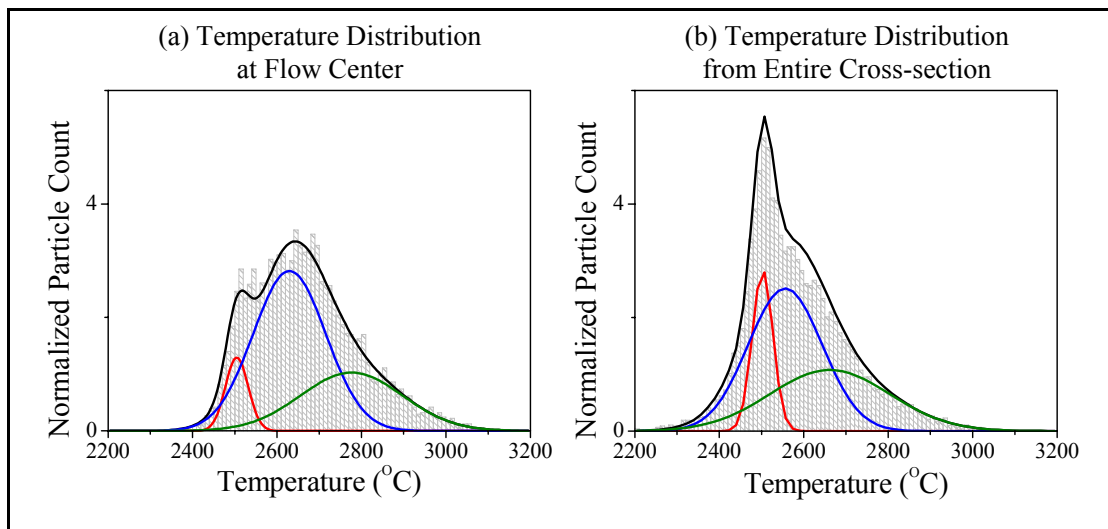


Figure 152: Particle temperature distribution from particles measured (a) at the flow center and (b) across the spray stream. The difference in distribution is clear

Describing the in-flight state of the process completely is very important to identify the appropriate parameters that need to be monitored and controlled. For the most part, only particle temperature and velocity are the only parameters that can be measured apart from the spray stream width, trajectory and intensity. A simple method to monitor the process would be by establishing the allowable range of each parameter and monitoring each parameter. For true in-flight process monitoring (only in-flight states; no hardware parameter limits), parameters of scientific importance needs to be identified and

methodologies to control them established. This study points out the limitations in using the currently identified directly measurable parameters - average T and V.

A possible explanation for the observation of differences could be the existence of these data points along a third axis of the particle state (apart from T and V or MI and Re), which is typically not necessary to understand major changes in properties as a function of currently known descriptors of particle state. Parameters such as Spray Stream Melting Index and Energy Density of the plasma jet could be the third axis of particle state.

8.3 Investigating Temperature Distributions

The interaction of powder particles of different morphologies (same chemical composition, size distribution and similar plasma conditions with similar particle injection conditions) with the plasma is different due their mass and specific surface area (ratio of surface area to volume) of each particle. Due to this difference there exists difference in in-flight particle states. Based on the results presented in section 5.1.4 a few questions arise.

8.3.1 Difference in Shift of T-V Space between PD and AS Morphology Feedstock

It is interesting to observe the non-identical shift between the solid spherical morphology and hollow spherical morphology in Figure 153. There is larger difference between the two morphologies at lower temperature compared to higher temperature.

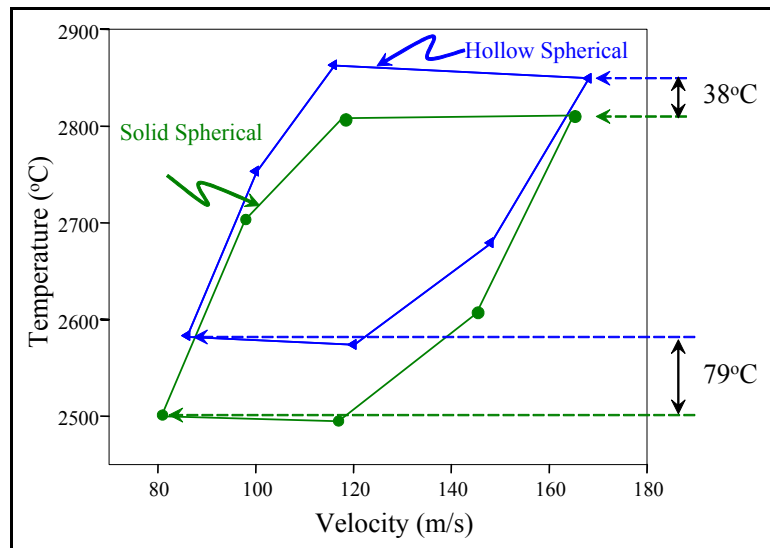


Figure 153: Shift in T-V space for solid spherical and hollow spherical morphologies

We know that the temperature distribution is multi-modal with a signature melting peak. Hollow spherical powder is easier to melt due to the absence of the core compared to the solid spherical. It is more pronounced when the process conditions are such that the distributions are around the melting point (average close to melting point), since more hollow particles melt and cross the melting barrier whereas more solid spherical particles remain in the melting peak resulting in a lower average temperature (Figure 154).

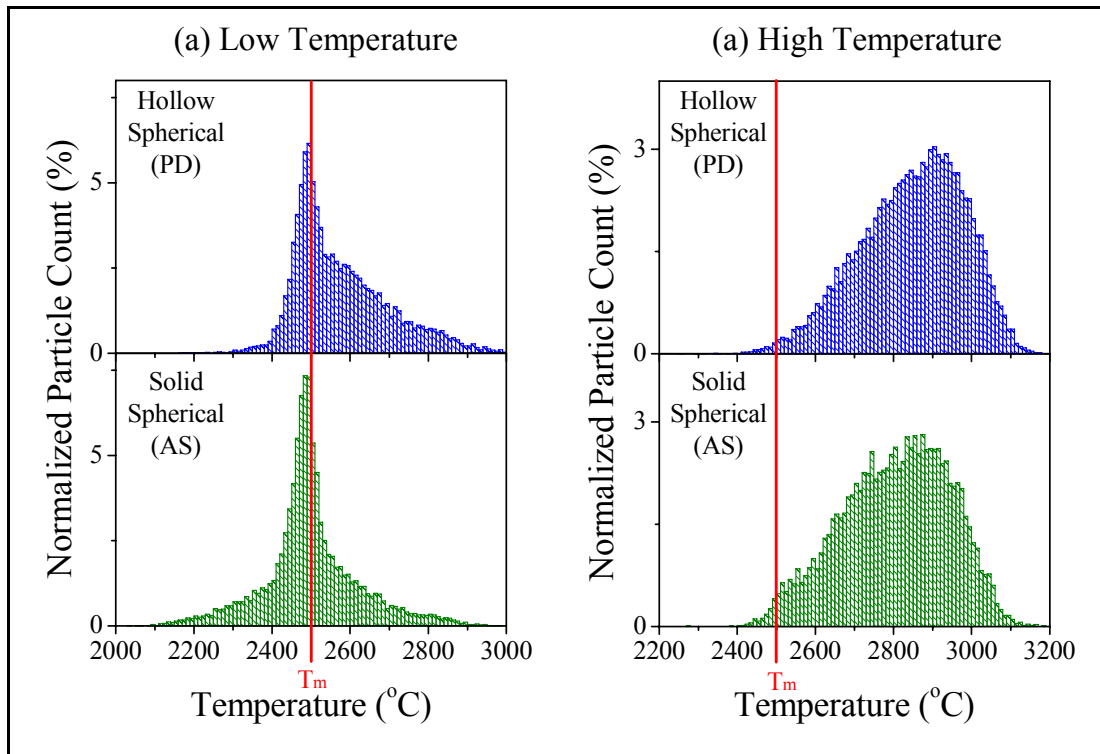


Figure 154: Temperature distributions for hollow spherical morphology and solid spherical morphology at the two extreme process conditions. Melting and shift in temperature distributions is the reason for the observed shift in T-V space in Figure 153

At same average temperature and velocity, the temperature distributions are observed to be similar for the different morphologies [158]. Whereas at the same plasma-forming torch parameters the distributions are different due to the difference in the extent of melting as a result of the difference in morphologies. This results in different average temperature since temperature distributions are not simple continuous probability density functions.

8.3.2 Difference in Behavior of Hollow Spherical Particles

In order to understand how the hollow spherical morphology feedstock behaves in-flight and which particle sizes contribute to what part of the temperature distribution, the

distributions have been plotted in JMP 5.1 statistical analysis software. This software allows selecting a certain range of values in one distribution to observe how that contributes to the other distributions. Figure 155 shows a plot of particle size (D), temperature (T) and velocity (V) for three different size ranges selected ((i) to (iii)).

From these distributions (Figure 155) one can observe that particles less than 20 microns (condition (i)) and greater than 60 microns (condition (ii)) contribute to the same region in the temperature distribution where the second of the three peaks would be. On the other hand most particles between 20 and 40 microns contribute to higher temperature region represented by the third of the three peaks. The velocity distributions appear to agree with the expected trend – fine particles are faster while coarser particles are slower.

This difference in contribution of different sized particles to the same region in temperature distribution (Figure 155) can be understood if we take into account the morphology of the feedstock – hollow spheres. It is known that the hollow spherical particles are not uniformly hollow throughout the size distribution and the finer particles tend to be dense or solid spherical. This result suggests that particles less than 20 microns are solid spherical and hence their melt status is not what would be expected from hollow spherical particles of less than 20 micron and that the cut-off occurs at about 20 microns.

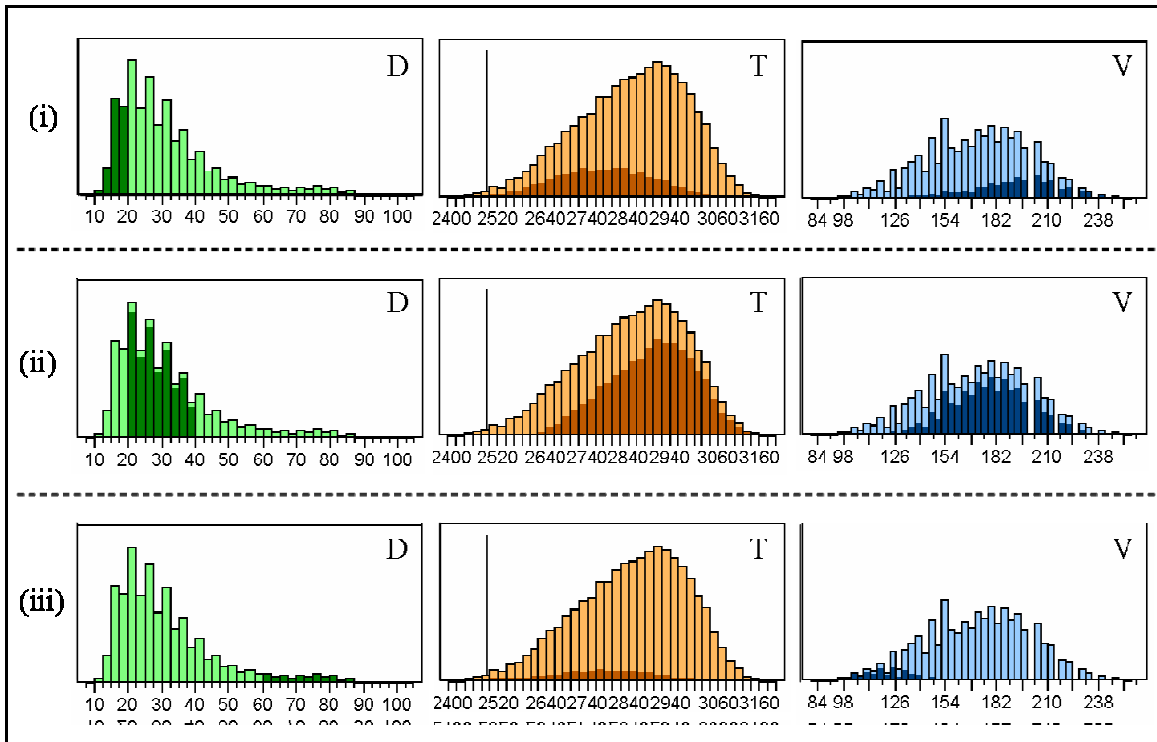


Figure 155: Distributions of particle size (D), temperature (T) and velocity (V) for hollow spherical morphology feedstock at one process condition. Different particle sizes have been selected (in darker color) to understand which part of the temperature and velocity distribution they contribute. The vertical line in T is the melting point. Particles less than 20 microns and greater than 60 microns both contribute to the second of the three peaks in T distribution, while particles between 20 and 40 microns contribute to the third of the three peaks

8.4 Examining the Possibility to Assess Melting States from Measured Particle Temperature

There are primarily three states of particles in-flight as shown in Figure 156 – un-molten (S1) or completely re-solidified (S4 and S5'), partially molten (S2, S3 and S4') and completely molten (S3'). Partially molten particles can have single solidification interface moving towards the core of the particle (S4') or two solidification interfaces moving in the opposite direction (S3). Former happens when completely molten particles re-solidify while latter happens when a partially molten particle starts to re-solidify. This is primarily due to the forced air convection effects on the outer surface of the particle dominating the particle cooling compared to the thermal conductivity effect within the particle for low thermal conductivity ceramics like YSZ [186].

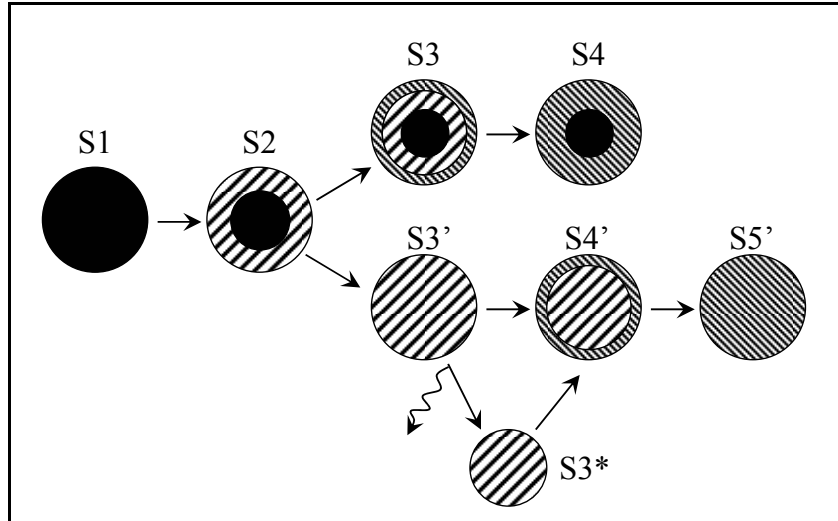


Figure 156: A schematic of the possible particle states with respect to particle behavior in-flight taking into account melting, re-solidification and vaporization (Figure adapted from reference [186])

It is known that the particles remain at the melting point longer when undergoing phase change from solid to liquid or liquid to solid due to the required energy transfer in the form of latent heat of melting or latent heat of fusion respectively. This is the reason for the observation of the melting peak in the temperature distributions [158]. Hence the particle will remain at the melting point in both cases of re-solidification (S3 and S4'), where the amount of molten content would be different for each case. Hence the measured particle temperature would not be able to distinguish the melting states.

Melting Index on the other hand is based on the time it takes to completely melt the particle and the time of flight of the particle. Re-solidification is not accounted for in Melting Index since the surrounding of the particle is not considered. The term 'A' in the analytically derived Melting Index (section 5.3.2) is assumed to be 1, which is true only if

$T_{\text{flame}} = T_{\text{particle}}$. But it is well known that this condition is not true throughout the axial distance. Hence Melting Index would also not be able to distinguish the different particles states within the partially molten category.

As we know, ‘A’ can assume significantly different values as shown in Table 10. The issue with the assumption of $A = 1$ is that it could influence the Melting Index completely contradictory to the melting states as shown by cases 5 and 6 in the table. Other possible values of ‘A’ can also significantly influence the Melting Index as shown by cases 1 to 4 in the table. These call for careful re-consideration of Melting Index incorporating the possible options.

Though the different extents of partially molten particles cannot be distinguished by the particle temperature or Melting Index, their distributions can be used to identify the three major categories of particles to a first approximation based on the occurrence of the melting peak. Thus the distributions can be quantified to a first approximation to estimate the molten content of the spray stream as a whole (Spray Stream Melting Index section 5.3.3) but it is not possible to accurately determine the molten content in the spray stream.

Table 10: Possible combinations of relations between flame temperature, particle surface temperature and particle melting temperature involved in the calculation in ‘A’

Case	Value of A		MI	Comments	
(1) $T_f > T_m$ and $T_s > T_m$	+	$\ll 1$	+	Typical conditions observed for APS processing of YSZ. Each particle will be more than 50% molten and perhaps completely molten	
		~ 1			$T_s \gg T_m$
					$T_s \sim T_m$
		$\gg 1$			
(2) $T_f > T_m$ and $T_s < T_m$	-	$\ll 1$	+	Though the Melting Index is positive, the conditions observed are somewhat typical to low enthalpy high power plasma that does not result good melting	
		~ 1			$T_s \ll T_m$
					$T_s \sim T_m$
		$\gg 1$			
(3) $T_f < T_m$ and $T_s > T_m$	-	$\ll 1$	-	If T_f was never $> T_m$, $T_s > T_m$ is not possible. It is perhaps the beginning of re-solidification. Particle would be expected to be molten for the most part (as in case 1) and $MI > 0$	
		~ 1			$T_s \gg T_m$
					$T_s \sim T_m$
		$\gg 1$			
(4) $T_f < T_m$ and $T_s < T_m$	+	$\ll 1$	-	This could be due to low process conditions with no melting or it could be an extreme case of re-solidification. These would not result in the same molten content of particle	
		~ 1			$T_s \ll T_m$
					$T_s \sim T_m$
		$\gg 1$			
(5) $T_f = T_m$	0	0	0	All calculated combinations of MI would suggest a partially molten particle (~50% molten). But very different melting states can be achieved satisfying these criteria	
(6) $T_s = T_m$	I	I	0		

8.5 Process Control Based on Voltage/Power

In the study of process variability under different process control methodologies, the method involving controlling voltage and power to be constant resulted in similar average temperature and velocity as well as similar Melting Index and Reynolds Number (Figure 157). Coatings made at these process conditions exhibit different deposition efficiencies and elastic modulus while the thermal conductivity values are similar.

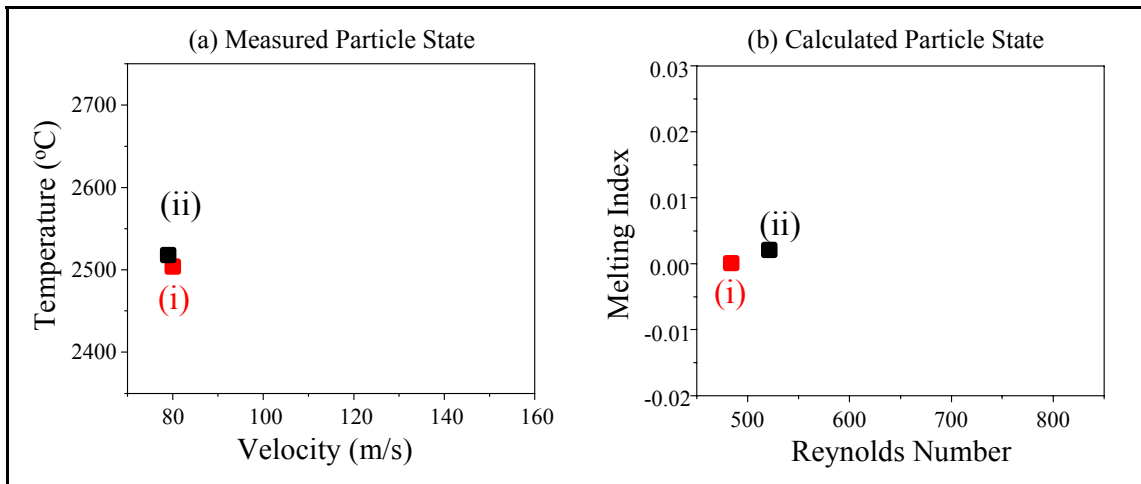


Figure 157: Particle state space for the two process conditions that were controlled to have similar voltage and power. Both conditions also resulted in similar average particle states (shown in the scale of the process maps)

Figure 131 reveals the area under the peak P3 (in relation to the total area) is higher for one process condition than the other. On quantification, the amount of molten content in the spray stream (SSMI) is different for the two process conditions (Figure 158).

The reason for the difference in distributions is evident in the difference in spray stream characteristics shown in Figure 159. The flow contours and temperature contours are different for condition (i) and (ii). The central region in the temperature contour consists of particles above 2480°C, which is above the melting point of YSZ determined from the particle distribution. It can be seen that this region is widespread in condition (ii) than in (i) implying that more particles are molten.

Further, linking the particle and spray stream characteristics to the torch parameters, process condition (i) and (ii) are at the same torch parameters except for the hydrogen flow and the degradation of the nozzle (which is not a well quantified or directly controllable parameter). Both wear of the nozzle and the difference in volume ratio of hydrogen influence the plasma flow contours and hence the plasma-particle interaction. Additionally, it is known that hydrogen flow alters the enthalpy of the plasma, which when combined with the plasma shape characteristics influence the energy density and the heat transfer characteristics.

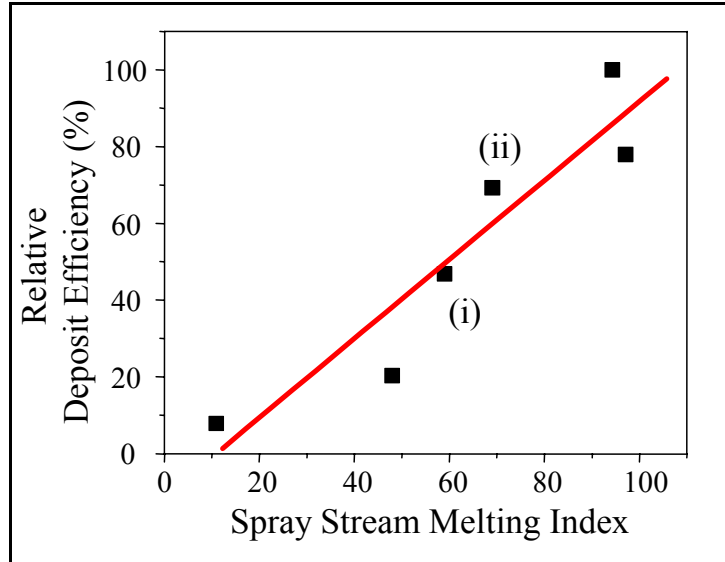


Figure 158: Plot correlating Spray Stream Melting Index (SSMI) to deposition efficiency (DE). The two data points pertaining to the discussion in this section are marked. Since two data points will always give a 100% fit, additional data covering the entire operational space (altering the SSMI from possible minimum to maximum) is shown to provide perspective of the goodness of fit.

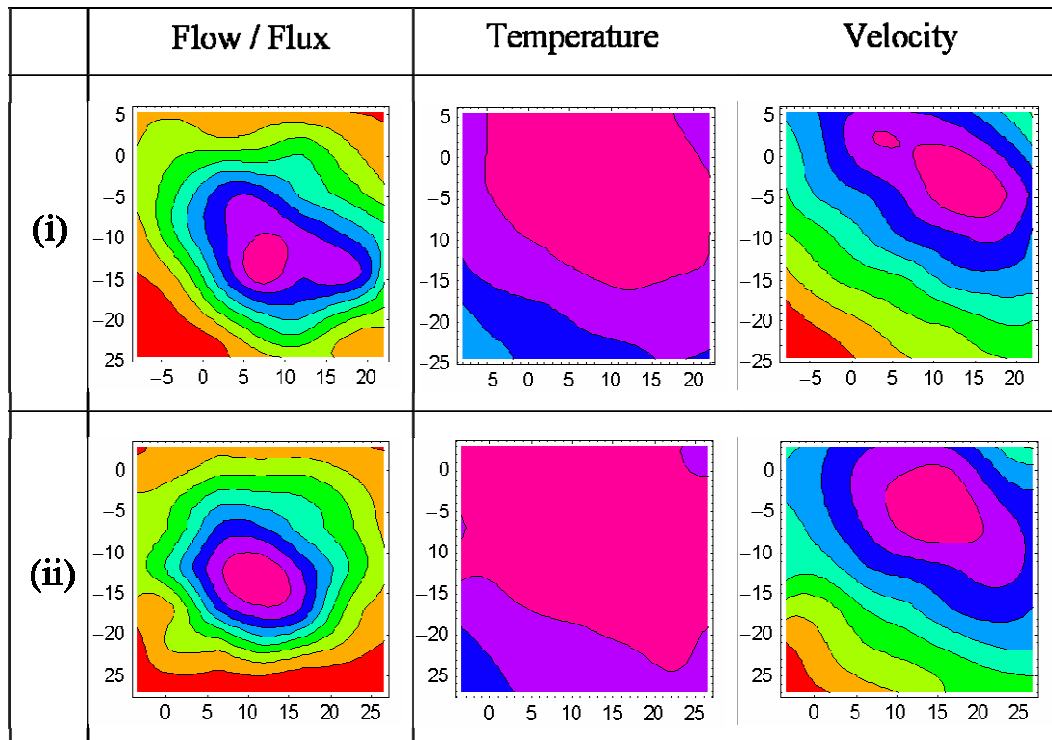


Figure 159: Spray steam contour plots for particle flow/flux, temperature and velocity for the two different process conditions that resulted in comparable average particle characteristics. Difference can be observed in flow pattern as well as the temperature contour

8.6 High Variability in Coating Properties

The extent of variability present at the different stages in the process (average particle state, particle state distribution, ensemble spray stream characteristics, deposition characteristics, microstructure and properties) has been assessed for the different process control methods (section 7.1). The variability observed at the different stages in the process is shown in Figure 160 for the traditional method with no process control (same as Fixed Parameter FP method discussed in section 7.1.2.3.1). The variability in average particle temperature (T) and velocity (V) were about 6-7% while the variability in thickness per pass (TPP) was about 11% and the variability in microstructure and properties were above 20%. This is thrice the variability in in-flight particle state. The reason for such a difference is investigated here.

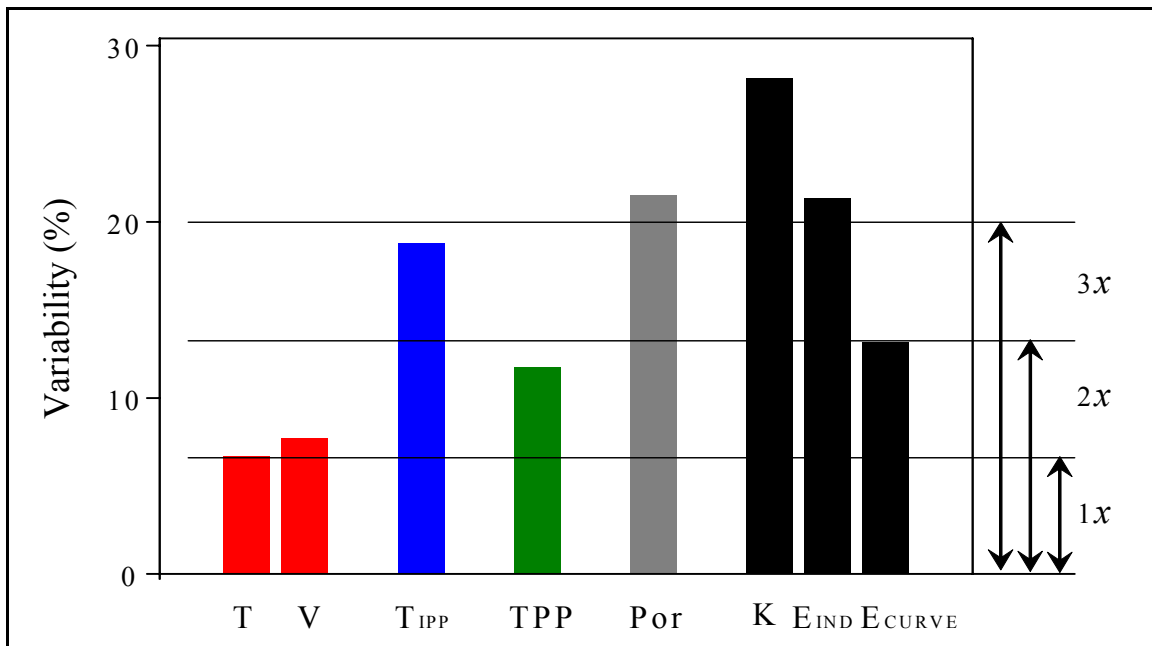


Figure 160: Variability observed at the different stages for repeated experiments with no process control (data from FP method discussed in section 7.1.2.3.1)

Coating build-up is a complex process due to the stochastics associated with the deposition of millions of particles per second to make the coating. The in-flight particle state varies across the cross-section of the spray stream due to trajectory based plasma-particle interaction, injection induced particle segregation and the wide starting feedstock size distribution. This adds to the complexity of the coating build-up since not all stochastically impinging particles are identical.

The defect microstructure in coatings has been quantified via image analysis of optical micrographs. Issues with the quality of the surface finish, brightness and contrast of images obtained, image resolution and area covered in the coating all influence the accuracy of the result. It is widely accepted that microstructural quantification is not very

accurate. If we consider, for example, the measurement of through thickness thermal conductivity using laser flash technique (Figure 161), the variability observed for a standard bulk sample is about 65% (from 9 measurements), the variability for one YSZ coating sample is about 50% (from 9 measurements) and the variability for six different samples (for thermal conductivity measurement) prepared from the same large YSZ coating sample is about 60% (from 1 measurement per sample). The variability observed for the repeated experiments in the in the FP method is well within this range.

Hence the variability associated with deposition characteristics such as the thickness per pass or deposition efficiency could just be due the aforementioned non-uniformity and stochastics. The use of narrower particle size distributions would be expected to result in lesser variability. Moreover as shown in this dissertation, average particle temperature and velocity are not sufficient descriptors of in-flight state of the process. This adds to the complexity in interpreting the results.

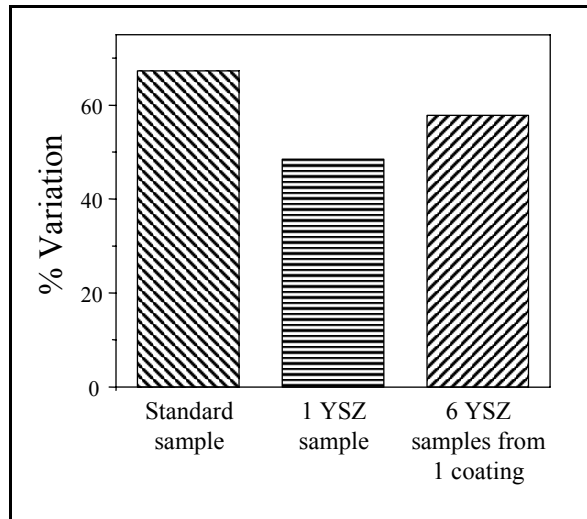


Figure 161: Fidelity of laser flash technique to measure thermal conductivity for plasma sprayed YSZ coating. Only in figure 'b' coefficient of variation is used (in the whole section)

The variability observed in properties (thermal conductivity) is due to instrumental limitations. Similar instrument/method error-calibrating experiments needs to be performed for the other techniques/properties and similar studies performed with smaller size distribution feedstock to conclusively understand the source of variation in coating properties.

Chapter IX

9 Synthesis

9.1 Integration of Results

To achieve reliable and predictable coating microstructure and properties, the coatings need to be tailored and the process needs to be controlled. In order to achieve that, the complexities of the process in terms of the various sub-processes (coating build-up, splat formation, development of in-flight particle characteristics, particle injection) and interrelated variables needs to be broken down, understood and re-integrated into perspective to enable complete understanding. The critical issues influencing coating build-up and property development (in-flight state of the process, deposition conditions and substrate conditions) need to be identified understood and controlled.

Figure 162 schematically shows the key issues identified and studied in this dissertation, which in an integrated sense addresses design of coatings and achieving coating dependability through process reliability.

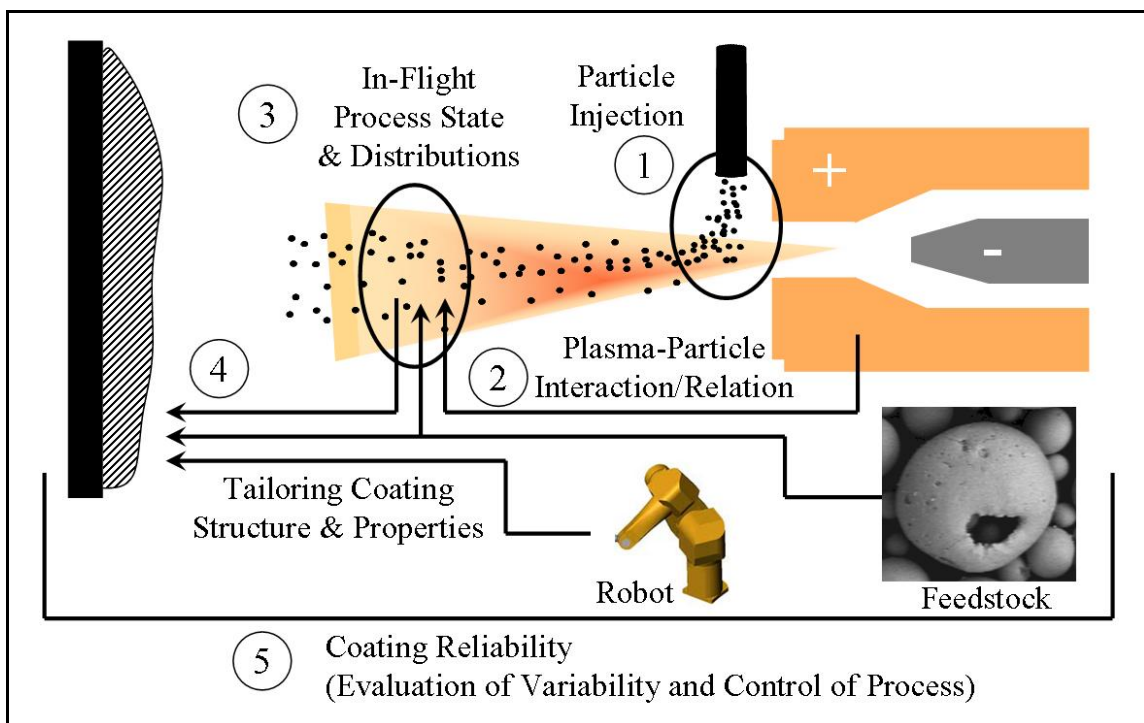


Figure 162: A schematic of the critical issues studied and their integration to coating design

Particle injection is a critical first step, which once controlled results in a more stable process and allows for critical examination of the real influence of plasma characteristics on the in-flight particle state. It is known that the different hardware configurations result in different in-flight particle states. This calls for complete description of spray stream (the in-flight state of the process as a whole). The insufficiency of average particle temperature and velocity has been established in this study. Particle temperature distributions have been examined critically in order to provide better understanding towards complete description of spray stream. Group parameters have been used to describe the particle state and their relation to coating properties has been established using the concept of process maps. This allows for identification of process windows to achieve the desired combination of design relevant properties. All this design of coatings would be incomplete without the systematic evaluation of variability at the different stages in the process. This was the last focus of this study. The variability on particle state, ensemble spray stream characteristics, deposition characteristics, coating microstructure and properties have been assessed under different extents of process control. This also serves as an evaluation of different process control methodologies.

9.2 Conclusions

This dissertation addressed a few key issues towards designing reliable thermal barrier top coats for possible prime reliance. Some issues of interest such as radial injection of particles into a plasma jet and the resultant particle characteristics, plasma-particle interaction for a wide range of process and feedstock conditions, characteristics of particle temperature distributions, process-particle state-coating microstructure and property relations and process variability at the different stages in the process were examined. Salient results from this investigation are listed below

- A variety of particle and spray stream sensors such as DPV 2000 for single particle measurement, and SPT and IPP, Accuraspray G3 for ensemble measurement and Control Vision for visual examination were used in an integrated fashion. This careful arrangement of sensors captures the various in-flight states and characteristics of interest uniquely with some redundancy for cross-correlation. In-situ coating property sensor was used in conjunction with these in-flight process sensors to correlate the observed particle characteristics to the coating microstructure and properties
- Particle injection was examined for the case of radial external injection using the experimental integrated sensor set-up and the resultant particle state and spray stream characteristics were studied. An optimum injection criterion was established based on the spray stream angle (or position at a specific spray distance) for a wide range of plasma conditions (total mass flow, enthalpy), different chemistries (Ar-H₂ and N₂-H₂) and types of plasma gas flows (straight and swirl flow), feedstock characteristics (density and shape of particles) and injection characteristics (angles of injection)

- The phenomenon of occurrence of optimum with respect to both heat and momentum transfer has been studied in association with process simulation and the reason for the observed simultaneous maximum in particle temperature and velocity established. The various benefits of optimum injection such as true understanding of the relation between plasma-forming torch parameters and particle state, enhanced reliability of in-flight data measurement and process stability downstream, and improved melting and process efficiency have been established
- Implications of the relation between plasma-forming torch parameters and particle state have been studied for the different feedstock morphologies and comparisons made with respect to the attributes of the relation such as the process stability, torch parameter vectors in particle state space, and expanse and overlap of the particle state space. This was further used to develop an iterative process control methodology for controlling the in-flight particle state based on empirical models developed previously
- The sufficiency of average particle temperature and velocity to completely describe the spray stream and hence the observed coating characteristics was explored using a systematic set of experiments enabled by process control using the previously mentioned outcome. The results brought out the intriguing possibility of achieving different temperature distributions while achieving the same average particle temperature. From the examination of the coating microstructure and properties, average particle temperature and velocity was identified to be necessary but not sufficient descriptor of the particle state
- Analysis of the temperature distributions showed that the distributions are multi-modal, typically tri-nodal, with a signature melting sub-distribution. Based on this observation, a simple empirical formulation was developed to extract the amount of molten content in the spray stream as a whole (not for individual particles) and validated on data from a wide range of process and feedstock conditions for YSZ. This approach has been shown to be valid for other material systems as well
- Second order process maps – relation between particle state and coating microstructure and properties – have been established based on group particle parameters such as Melting Index, Reynolds Number and Kinetic Energy, microstructure, and design relevant properties such as through thickness thermal conductivity, in-plane modulus (from curvature) and through thickness modulus (from instrumented indentation). Property regimes have been identified, distilled and controlled maps established for identifying process windows. Similar maps for understanding the relation between deposition conditions and microstructure and properties have also been established. Preliminary findings show that controlling the deposition rate is not sufficient to control the microstructure and properties
- Few methods for distinctly modifying the microstructure have been explored and controlled experiments performed to understand the particle state, splat

characteristics, coating build-up and microstructure and properties. Results suggest that the coating properties can be modified significantly by altering the particle impacting characteristics such as the Reynolds Number and Kinetic Energy by changing the feedstock size distribution and nozzle exit dimensions. Feedstock morphology, specifically hollow spherical feedstock, has been shown to influence the interlamellar defect feature and hence the through thickness thermal conductivity

- Variability at the different stages of the process has been explored systematically over a short time period to understand the influence of the process on coating reliability. Few process control strategies exercising different extents of control at different stages in the process have been explored. Controlling both particle state and particle injection results in the best control on the coating build-up and deposition efficiency. Simply controlling particle injection reduces the process variability by 50%. Controlling the process based on power and voltage appears to be least effective of all the methods considered within the scope of the experiments
- The influence of the three dimensional variation in spray stream on the splat characteristics has been investigated by collecting a snapshot of the entire spray footprint using a shutter mechanism. Preliminary results point to interesting differences in basic splat characteristics such as flattening and fragmentation, and in the phase evolution of splats at the different regions in the ‘splat map’. The differences need to be quantified and related to particle state under ‘clean’ processing conditions

Chapter X

10 Suggestions for Future Work

Interesting opportunities emerge for further research to better understand the process and coating microstructure and properties based on the studies conducted in this dissertation. Some suggestions are presented here for further consideration.

10.1 Improvements to Definition of Particle

Though derived from first principles, there are practical issues in the successful use of Melting Index to describe the melting status of the particle. In addition to the limitations in obtaining the necessary thermo-physical properties at elevated temperatures for thermal sprayed materials, calculating Melting Index has some deficiencies that need to be addressed in order to bring out the anticipated benefits. Here we explore some of the issues and discuss possible approach towards enhancing particle Melting Index.

10.1.1 Powder Morphology

The derivation of Melting Index is based on solid spherical particles. But feedstock comes in other morphologies such as polyhedral and hollow spheres with and without uniform shell thickness. In its current form the equation cannot accommodate for these particle characteristics.

To address this issue, a shape factor could be incorporated into the equation in the form of an additional term, which would be 1 for solid spherical and different for the other morphologies. One approach would be to use the volume to surface area ratio and normalize it based on solid spherical particles. Hollow spherical particle with the same size as the solid spherical particle will have a shape factor of less than 1. The extent of melting and hence the Melting Index for the same temperature and velocity will be higher for hollow spherical morphology. Determining the shape factor of polyhedral particles is somewhat difficult. Experimental measurements of apparent density and the concept of equivalent diameter could be used.

10.1.2 Thermal History of Particles

As mentioned earlier, the value of 'A' is taken to be 1 because of the non-availability of flame temperature at the point of measurement of the particle properties in the plume.

If flame temperature were to be available for calculations, the term 'A' could result in negative, zero and positive values and could vary as much as say 0.1 and 10. For both positive and negative values of A, positive and negative values are possible for Melting Index. Careful consideration of all the combinations reveal the inconsistency that 'A' brings to the calculation of Melting Index.

The time of flight estimated from experimental data on particle velocity has its limitations in addition to the fundamental limitation of taking the whole time of flight of the particle instead of the time of flight in the 'hot zone'. For this, the 'hot zone' needs to be defined for the different process conditions and simple analytical models needs to be established to calculate the axial distance up to which the particle is in the hot zone. This distance could be used along with appropriate analytical/empirical model to estimate the time the particle has resided in the hot zone based on the particle velocity.

The heat transfer coefficient 'h' is also taken as a constant, though it may not have as much influence as the flame temperature. These call for incorporation of thermal history of particles instead of the flame temperature at just the measurement location and a constant heat transfer coefficient.

10.2 Definition of Spray Stream and Process Control

10.2.1 Single Particle Sensor Vs Ensemble Sensor

It is not certain if the temperature and velocity measured using single particle sensors and ensemble sensors completely represent the process or if one is better than the other though correlations have been observed to exist between the sensors. Science based monitoring and control needs thorough understanding of the process, sensors and their data output and the methodologies of process control.

10.2.2 Choice of In-Flight Parameters to Completely Describe the Spray Stream for True In-flight Process Control

The results from this study showed the insufficiency of average particle temperature and velocity to describe the spray stream completely in order to explain the observed coating characteristics. Simple empirical approaches have been considered and some possible options presented. A few potential parameters that need to be understood better and explored for the possibility to describe the spray stream completely and for process control strategy are suggested below.

10.2.2.1 Spray Stream Melting Index

The Spray Stream Melting Index (SSMI) has been empirically obtained to represent the amount of molten content in the spray stream as a whole (not at the individual particle level). It has been observed to correlate well to the deposition efficiency for a wide variety of process and feedstock conditions for plasma sprayed YSZ. This approach has been shown to be valid for other material systems such as MnZn Ferrite and Molybdenum. It remains to be seen if the addition of SSMI to one thermal and one kinetic factor would result in a singularity with respect to the observed coating characteristics and properties.

The results also show that the SSMI calculated from simulations does not correlate well with the observed deposition efficiency. This discrepancy needs to be examined critically in order to understand the source of the discrepancy and enhance the model.

10.2.2.2 Axial Slope of Particle Characteristics

A possible reason for the observation of different temperature distributions with the same average/mean could be that the particle temperature profiles as a function of axial distance are different due to difference in plasma jet characteristics and the associated plasma-particle interaction (Figure 163). The ensemble measurements that were obtained at two different spray distances for these experiments did not exhibit any appreciable difference in slope of the temperature profile assuming a linear drop in temperature with axial distance. It is known that the plasma/hot gas interaction with the particles is complex and so the axial temperature profile may not be linear (after the particle has achieved maximum temperature).

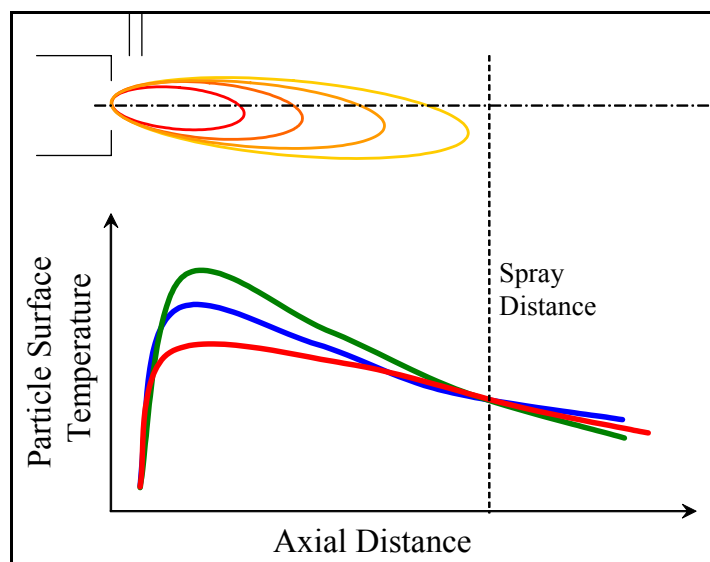


Figure 163: A schematic of different slopes of particle surface temperatures due to difference in plasma characteristics merging at the spray distance to result in same temperature

This needs to be explored both experimentally and via simulations. Model guided experiments needs to be performed and the results compared to understand the validity and significance of the slope of temperature as a possible control parameter. From an implementation standpoint, it would be very simple since it calls for diagnostic measurement at two different spray distances. Quantitative relations needs to be established between the slope of temperature and velocity and the plasma-forming torch parameters in order to implement a possible process control strategy using this parameter. This could also be incorporated into the equation for Melting Index in the proposed ‘thermal history’ component.

10.2.2.3 Energy Density

From the systematic experiments where average particle temperature and velocity was controlled, the three dimensional spray stream characteristics have been observed to be different. This is primarily due to the difference in the plasma jet characteristics and the ensuing plasma-particle interaction. The area of spread of the available energy in the plasma jet (in terms of width of the spray stream) was observed to be different for the different cases. Energy Density, which is the ratio of energy or enthalpy in the system (plasma jet) and the area of spread of the energy, would be an appropriate terminology (borrowed from the ‘high energy density processes’ such as laser welding/cutting etc) to understand the differences between these experiments.

Estimation/calculation of Energy Density for the different process conditions is not possible without recourse to computation/simulation. Trends obtained from a simple first attempt to calculate the Energy Density using plasma power (product of current and voltage) and spray stream width (both experimentally measured) is encouraging. Simple analytical solutions need to be established to calculate Energy Density, perhaps based on experimentally measurable parameters. Such an Energy Density term would be applicable to plasma processes as well as flame and combustion processes such as HVOF.

10.3 Shift in In-Flight Particle State With Time

It is known that the in-flight particle state changes with time due to degradation of nozzle with time and other process stochastics. Repeated sets of first order process maps for one feedstock morphology conducted at different lifetimes of a single nozzle would provide valuable information on the shift and skew of the T-V space with time. The torch parameter vectors evaluated at different nozzle lifetimes need to be compared, since most of the process control is based on the assumption that the vectors do not change with time.

10.4 Determining Adhesion and Cohesion Behavior of Coatings via In-Situ Curvature Monitoring

During heat cycling of a thick (~1.4 mm) YSZ coating on Al substrate (~3.3 mm thick), the coating delaminated (Figure 164) at fairly low temperatures. This can be detected in the displacement/distance profile as a function of time. The stress at which the coating failed (calculated from the temperature Vs curvature data) could serve as an indication of the adhesive bond strength (if the coating failed at the coating-substrate interface) or cohesive bond strength (if the coating failed within the coating along splat-splat interface). At the very least it could serve to identify whether adhesion strength is higher than cohesion strength.

(In-situ) Curvature monitoring could potentially be used to determine the adhesion/cohesion properties of coatings (not just YSZ). This observation needs to be explored further in order to understand the mechanics involved since it could potentially help understand the failure of TBCs in service.

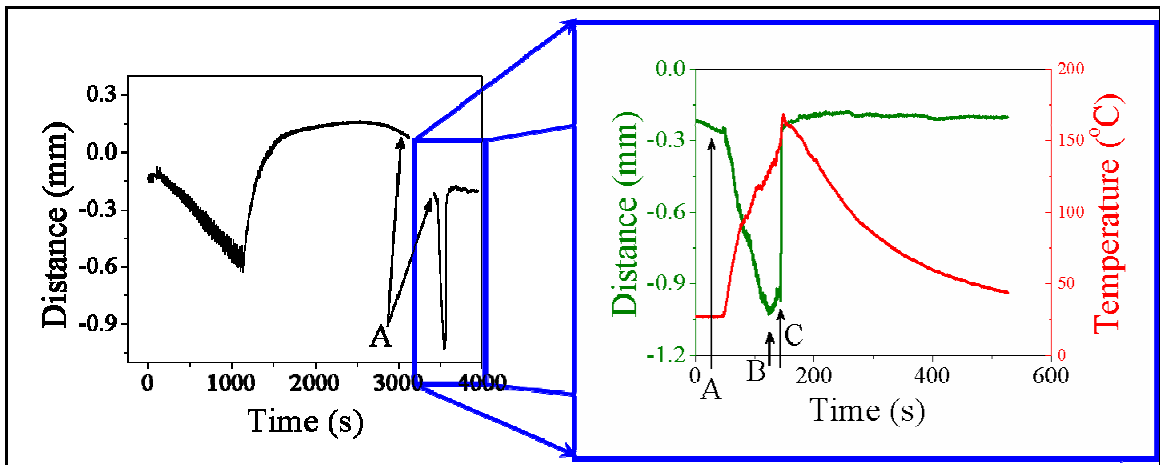


Figure 164: A plot of distance of the sample from the laser Vs time during preheating, spraying and cooling, and thermal cycling (left) and during thermal cycling (right). At the end of the coating cooling, stress relaxation/balance is still happening even after reaching room temperature (point A) although no visible delamination was observed at the end of coating cooling. In the inset plot on the right, onset of delamination (point B) as well as delamination failure (point C) (full spallation - adhesive failure) could be detected in the distance (or displacement profile) even at relatively low temperatures

10.5 Splat Map

Splat map is a unique method to collect and analyze splats since it enables spatial location based comparison between different process conditions. Detailed investigation of splat characteristics within the splat map would provide the opportunity to understand, and more important control, the variability observed in plasma sprayed coatings. Splat

morphology, including flattening ratio and fragmentation degree, and phase evolution needs to be examined critically and related to its origin – the particle state. A threshold radius could be established considering the observed difference in splat properties and the particle flux as a function of radial distance. Controlled experiments permitting particles within the threshold radius to form deposit (Figure 165) could provide valuable information in understanding and controlling variability in coatings.

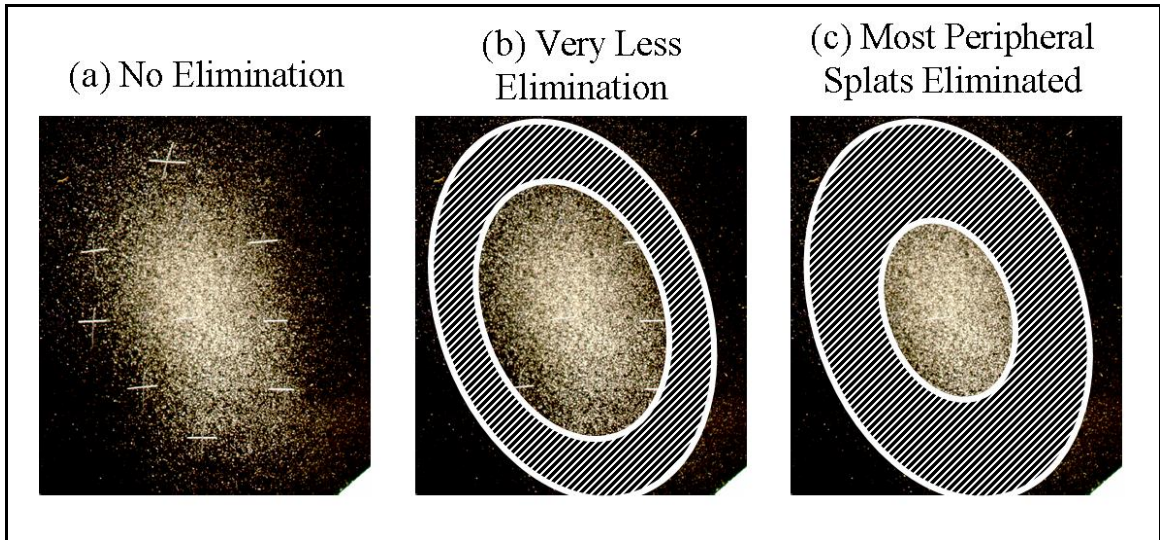


Figure 165: Elimination of splat from the periphery that contribute to coating build-up to reduce variability

10.6 DVC Threshold in Deposition Rate

Few experiments conducted for YSZ on Hastelloy X substrate with high Deposition Rate (about an order of magnitude higher than the typical plasma spray processing regime) showed interesting results. The curvature-temperature relation showed stiffening of coatings at higher strains during thermal cycling post deposition (Figure 166). Further, large area is enclosed between the curvature-temperature relation during heating and cooling. Interestingly the final curvature is not the same as the initial curvature (before and after heat cycling to relatively low temperatures $\sim 400^{\circ}\text{C}$) (Figure 167). These are contradictory to what has been observed for YSZ coatings on Al substrates and warrants careful investigation.

The aforementioned stiffening of coatings at high strains could mean that the coatings have transitioned from layered to DVC. In most studies where dense vertically cracked coatings (DVCs) were obtained by plasma spray processing of YSZ, the parameters have been varied somewhat non-systematically. Systematic studies with minimum number of significant group parameters (such as Deposition Rate) to obtain DVCs has not been undertaken. This would not only enable determining threshold Deposition Rate (Figure 168) but also help understand the basic criteria for DVC formation and the sequence of

events and their mechanisms with respect to the formation and survivability of DVC microstructure.

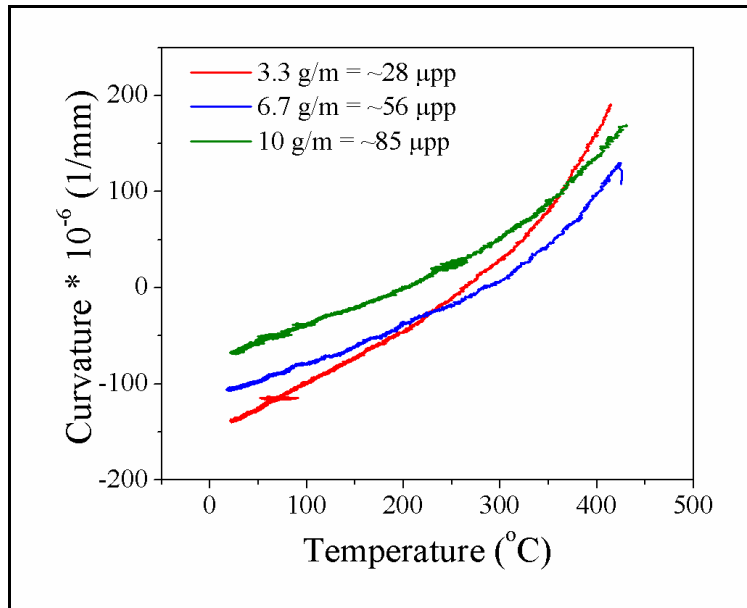


Figure 166: Stiffening of the coatings at higher temperatures (strains)

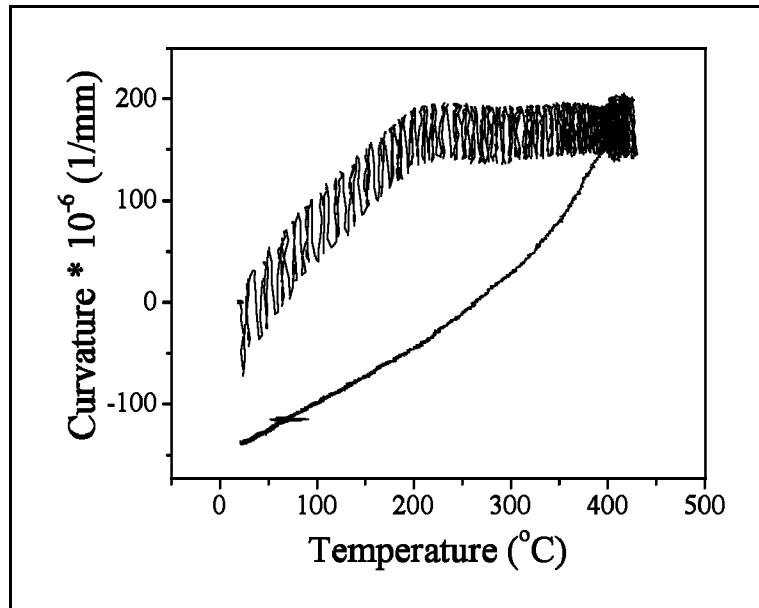


Figure 167: Large area enclosed between heating and cooling curves. No hysteresis observed

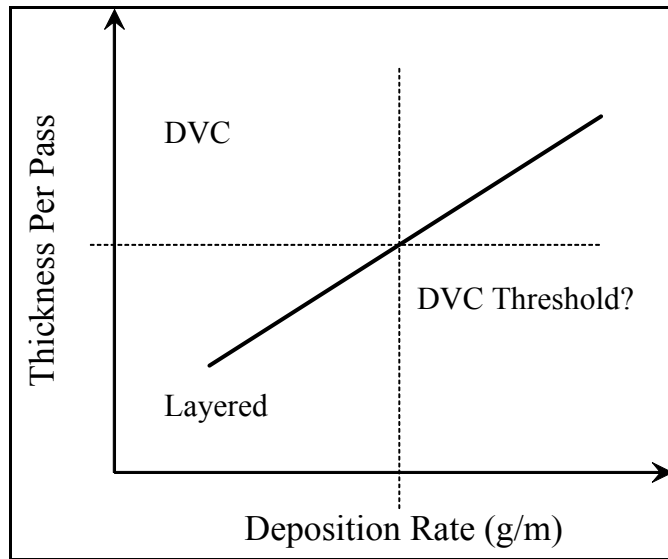


Figure 168: Schematic probing the existence of a threshold value of Deposition Rate resulting in transition from layered coatings to dense vertically cracked (or segmented crack) coatings

In its current form, Deposition Rate accounts for the flux change due to the rate of movement of torch in only one dimension. Taking into account the area of the footprint in terms of flux of the particles per unit area and then considering the linear motion would account for the spray distance.

Chapter XI

11 Bibliography

- 1 X. Q. Cao, R. Vassen, and D. Stoeber, Ceramic materials for thermal barrier coatings, *Journal of the European Ceramic Society*, 2004. **24**(1): p. 1-10.
- 2 R. A. Miller, Current status of thermal barrier coatings -- An overview, *Surface and Coatings Technology*, 1987. **30**(1): p. 1-11.
- 3 R. A. Miller and C. C. Berndt, Performance of thermal barrier coatings in high heat flux environments, *Thin Solid Films*, 1984. **119**(2): p. 195-202.
- 4 R. A. Miller and C. E. Lowell, Failure mechanisms of thermal barrier coatings exposed to elevated temperatures, *Thin Solid Films*, 1982. **95**(3): p. 265-273.
- 5 D. M. Zhu and R. A. Miller, Thermal-barrier coatings for advanced gas-turbine engines, *Mrs Bulletin*, 2000. **25**(7): p. 43-47.
- 6 A. G. Evans, D. R. Mumm, J. W. Hutchinson, G. H. Meier, and F. S. Pettit, Mechanisms controlling the durability of thermal barrier coatings, *Progress in Materials Science*, 2001. **46**(5): p. 505-553.
- 7 H. Herman and N. R. Shankar, Fundamental-Aspects of Thermal Barrier Coatings, *American Ceramic Society Bulletin*, 1984. **63**(12): p. 1475-1475.
- 8 D. R. Clarke, Materials selection guidelines for low thermal conductivity thermal barrier coatings, *Surface & Coatings Technology*, 2003. **163**: p. 67-74.
- 9 D. R. Clarke and C. G. Levi, Materials design for the next generation thermal barrier coatings, *Annual Review of Materials Research*, 2003. **33**: p. 383-417.
- 10 D. R. Clarke, C. G. Levi, and A. G. Evans, Enhanced zirconia thermal barrier coating systems, *Proceedings of the Institution of Mechanical Engineers Part a-Journal of Power and Energy*, 2006. **220**(A1): p. 85-92.
- 11 J. D. Ballard, J. Davenport, C. Lewis, W. Nelson, R. H. Doremus, and L. S. Schadler, Phase Stability of Thermal Barrier Coatings Made From 8 wt. Yttria Stabilized Zirconia: A Technical Note, *Journal of Thermal Spray Technology*, 2003. **12**: p. 34-37.
- 12 K. J. Huang, J. T. Chang, A. Davison, K. C. Chen, J. L. He, C. K. Lin, A. Matthews, and A. Leyland, Thermal cyclic performance of NiAl/alumina-stabilized zirconia thermal barrier coatings deposited using a hybrid arc and

- magnetron sputtering system, *Surface and Coatings Technology*, 2006. **201**(7): p. 3901-3905.
- 13 P. L. Ke, Q. M. Wang, J. Gong, C. Sun, and Y. C. Zhou, Progressive damage during thermal shock cycling of D-gun sprayed thermal barrier coatings with hollow spherical ZrO₂-8Y₂O₃, *Materials Science and Engineering: A*, 2006. **435-436**: p. 228-236.
 - 14 E. H. Jordan, L. Xie, X. Ma, M. Gell, N. P. Padture, B. Cetegen, A. Ozturk, J. Roth, T. D. Xiao, and P. E. C. Bryant, Superior thermal barrier coatings using solution precursor plasma spray, *Journal of Thermal Spray Technology*, 2004. **13**(1): p. 57-65.
 - 15 L. D. Xie, E. H. Jordan, N. P. Padture, and M. Gell, Phase and microstructural stability of solution precursor plasma sprayed thermal barrier coatings, *Materials Science and Engineering a-Structural Materials Properties Microstructure and Processing*, 2004. **381**(1-2): p. 189-195.
 - 16 L. D. Xie, X. Q. Ma, E. H. Jordan, N. P. Padture, D. T. Xiao, and M. Gell, Deposition mechanisms of thermal barrier coatings in the solution precursor plasma spray process, *Surface & Coatings Technology*, 2004. **177**: p. 103-107.
 - 17 L. D. Xie, X. Q. Ma, E. H. Jordan, N. P. Padture, D. T. Xiao, and M. Gell, Deposition of thermal barrier coatings using the solution precursor plasma spray process, *Journal of Materials Science*, 2004. **39**(5): p. 1639-1646.
 - 18 A. G. Evans, M. Y. He, and J. W. Hutchinson, Mechanics-based scaling laws for the durability of thermal barrier coatings, *Progress in Materials Science*, 2001. **46**(3-4): p. 249-271.
 - 19 A. Rabiei and A. G. Evans, Failure mechanisms associated with the thermally grown oxide in plasma-sprayed thermal barrier coatings, *Acta Materialia*, 2000. **48**(15): p. 3963-3976.
 - 20 H. Herman and N. R. Shankar, Survivability of Thermal Barrier Coatings, *Materials Science and Engineering*, 1987. **88**: p. 69-74.
 - 21 C. G. Levi, Emerging materials and processes for thermal barrier systems, *Current Opinion in Solid State & Materials Science*, 2004. **8**(1): p. 77-91.
 - 22 C. G. Levi, E. Sommer, S. G. Terry, A. Catanoiu, and M. Ruhle, Alumina grown during deposition of thermal barrier coatings on NiCrAlY, *Journal of the American Ceramic Society*, 2003. **86**(4): p. 676-685.
 - 23 D. R. Clarke, R. J. Christensen, and V. Tolpygo, The evolution of oxidation stresses in zirconia thermal barrier coated superalloy leading to spalling failure, *Surface & Coatings Technology*, 1997. **94-5**(1-3): p. 89-93.

- 24 R. Vassen, F. Traeger, and D. Stover, Correlation between spraying conditions and microcrack density and their influence on thermal cycling life of thermal barrier coatings, *Journal of Thermal Spray Technology*, 2004. **13**(3): p. 396-404.
- 25 P. Fauchais, J. F. Coudert, and M. Vardelle, Diagnostics of plasma spray process and derived on-line control, *High Temperature Material Processes*, 2002. **6**(2): p. 247-265.
- 26 J. R. Fincke, D. C. Haggard, and W. D. Swank, Particle temperature measurement in the thermal spray process, *Journal of Thermal Spray Technology*, 2001. **10**(2): p. 255-266.
- 27 J. R. Fincke, C. L. Jeffery, and S. B. Englert, In-Flight Measurement of Particle-Size and Temperature, *Journal of Physics E-Scientific Instruments*, 1988. **21**(4): p. 367-370.
- 28 J. R. Fincke, W. D. Swank, R. L. Bewley, D. C. Haggard, M. Gevelber, and D. Wroblewski, Diagnostics and control in the thermal spray process, *Surface & Coatings Technology*, 2001. **146**: p. 537-543.
- 29 J. R. Fincke, W. D. Swank, and C. L. Jeffery, Simultaneous Measurement of Particle-Size, Velocity, and Temperature in Thermal Plasmas, *Ieee Transactions on Plasma Science*, 1990. **18**(6): p. 948-957.
- 30 P. Gougeon and C. Moreau, In-Flight Particle Surface Temperature Measurement: Influence of the Plasma Light Scattered by the Particles, *NTSC*, 1993 (Anaheim, California, USA),
- 31 C. Moreau, P. Cielo, M. Lamontagne, S. Dallaire, and M. Vardelle, Impacting Particle Temperature Monitoring during Plasma Spray Deposition, *Measurement Science & Technology*, 1990. **1**(8): p. 807-814.
- 32 C. Moreau, P. Gougeon, M. Lamontagne, V. Lacasse, G. Vaudreuil, and P. Cielo, On-Line Control of the Plasma Spraying Process by Monitoring the Temperature, Velocity and Trajectory of In-Flight Particles, *Thermal spray Industrial Applications: Proceedings of 7th National Thermal Spray Conference*, 1994 (Boston, MA, USA), ASM International
- 33 S. Zimmermann and K. Landes, A particle image shape imaging (PSI) investigation of particles in a plasma jet, *Materials Science and Engineering a-Structural Materials Properties Microstructure and Processing*, 2004. **383**(1): p. 153-157.
- 34 B. M. Cetegen and W. Yu, In-situ particle temperature, velocity, and size measurements in DC arc plasma thermal sprays, *Journal of Thermal Spray Technology*, 1999. **8**(1): p. 57-67.

- 35 M. Vardelle and P. Fauchais, Plasma spray processes: diagnostics and control?, *Pure and Applied Chemistry*, 1999. **71**(10): p. 1909-1918.
- 36 M. Vardelle, A. Vardelle, P. Fauchais, and C. Moreau, Pyrometer System for Monitoring the Particle Impact on a Substrate during a Plasma Spray Process, *Measurement Science & Technology*, 1994. **5**(3): p. 205-212.
- 37 A. J. Allen, J. Ilavsky, G. G. Long, J. S. Wallace, C. C. Berndt, and H. Herman, Microstructural characterization of yttria-stabilized zirconia plasma-sprayed deposits using multiple small-angle neutron scattering, *Acta Materialia*, 2001. **49**(9): p. 1661-1675.
- 38 P. Ctibor, O. Roussel, and A. Tricoire, Unmelted particles in plasma sprayed coatings, *Journal of the European Ceramic Society*, 2003. **23**(16): p. 2993-2999.
- 39 A. Kulkarni, Z. Wang, T. Nakamura, S. Sampath, A. Goland, H. Herman, J. Allen, J. Ilavsky, G. Long, J. Frahm, and R. W. Steinbrech, Comprehensive microstructural characterization and predictive property modeling of plasma-sprayed zirconia coatings, *Acta Materialia*, 2003. **51**(9): p. 2457-2475.
- 40 A. A. Kulkarni, A. Goland, H. Herman, A. J. Allen, J. Ilavsky, G. G. Long, and F. De Carlo, Advanced microstructural characterization of plasma-sprayed zirconia coatings over extended length scales, *Journal of Thermal Spray Technology*, 2005. **14**(2): p. 239-250.
- 41 J. Ilavsky, A. J. Allen, G. G. Long, H. Herman, and C. C. Berndt, Characterization of the closed porosity in plasma-sprayed alumina, *Journal of Materials Science*, 1997. **32**(13): p. 3407-3410.
- 42 J. Ilavsky, C. C. Berndt, and J. Karthikeyan, Mercury intrusion porosimetry of plasma-sprayed ceramic, *Journal of Materials Science*, 1997. **32**(15): p. 3925-3932.
- 43 J. Ilavsky, G. G. Long, A. J. Allen, H. Herman, and C. C. Berndt, Use of small-angle neutron scattering for the characterization of anisotropic structures produced by thermal spraying, *Ceramics-Silikaty*, 1998. **42**(3): p. 81-89.
- 44 J. Ilavsky, G. G. Long, A. J. Allen, L. Leblanc, M. Prystay, and C. Moreau, Anisotropic microstructure of plasma-sprayed deposits, *Journal of Thermal Spray Technology*, 1999. **8**(3): p. 414-420.
- 45 S. Deshpande, A. Kulkarni, S. Sampath, and H. Herman, Application of image analysis for characterization of porosity in thermal spray coatings and correlation with small angle neutron scattering, *Surface & Coatings Technology*, 2004. **187**(1): p. 6-16.

- 46 A. Kulkarni, S. Sampath, A. Goland, H. Herman, and B. Dowd, Computed microtomography studies to characterize microstructure-property correlations in thermal sprayed alumina deposits, *Scripta Materialia*, 2000. **43**(5): p. 471-476.
- 47 S. Kuroda, T. Fukushima, and S. Kitahara, Simultaneous Measurement of Coating Thickness and Deposition Stress During Thermal Spraying, *Thin Solid Films*, 1988. **164**: p. 157-163.
- 48 J. Matejcek and S. Sampath, In situ measurement of residual stresses and elastic moduli in thermal sprayed coatings - Part 1: apparatus and analysis, *Acta Materialia*, 2003. **51**(3): p. 863-872.
- 49 J. Matejcek, S. Sampath, D. Gilmore, and R. Neiser, In situ measurement of residual stresses and elastic moduli in thermal sprayed coatings - Part 2: processing effects on properties of Mo coatings, *Acta Materialia*, 2003. **51**(3): p. 873-885.
- 50 L. Pawlowski and P. Fauchais, The Least-Square Method in the Determination of Thermal-Diffusivity Using a Flash Method, *Revue De Physique Appliquee*, 1986. **21**(2): p. 83-86.
- 51 L. Pawlowski and P. Fauchais, Thermal Transport-Properties of Thermally Sprayed Coatings, *International Materials Reviews*, 1992. **37**(6): p. 271-289.
- 52 Y. C. Tsui and T. W. Clyne, An analytical model for predicting residual stresses in progressively deposited coatings .1. Planar geometry, *Thin Solid Films*, 1997. **306**(1): p. 23-33.
- 53 H. Wang and R. B. Dinwiddie, Reliability of laser flash thermal diffusivity measurements of the thermal barrier coatings, *Journal of Thermal Spray Technology*, 2000. **9**(2): p. 210-214.
- 54 F. Kroupa, Effect of nets of microcracks on elastic properties of materials, *Kovove Materialy-Metallic Materials*, 1995. **33**(6): p. 418-426.
- 55 F. Kroupa and J. Plesek, Bending of beams with elastically non-linear coatings, *Journal of Thermal Spray Technology*, 2002. **11**(4): p. 508-516.
- 56 F. Kroupa and J. Plesek, Nonlinear elastic behavior in compression of thermally sprayed materials, *Materials Science and Engineering a-Structural Materials Properties Microstructure and Processing*, 2002. **328**(1-2): p. 1-7.
- 57 T. Nakamura and Y. Liu, Determination of nonlinear properties of thermal sprayed ceramic coatings via inverse analysis, *International Journal of Solids and Structures*, 2007. **44**(6): p. 1990-2009.

- 58 Z. Wang, A. Kulkarni, S. Deshpande, T. Nakamura, and H. Herman, Effects of pores and interfaces on effective properties of plasma sprayed zirconia coatings, *Acta Materialia*, 2003. **51**(18): p. 5319-5334.
- 59 R. Mcpherson, A Model for the Thermal-Conductivity of Plasma-Sprayed Ceramic Coatings, *Thin Solid Films*, 1984. **112**(1): p. 89-95.
- 60 A. Kulkarni, On The Porosity-Property Correlations In Thermo-Structural Coatings: Towards An Integrated Approach, Ph.D. Thesis, State University of New York at Stony Brook, 2002
- 61 A. Vaidya, T. Streibl, A. Kulkarni, M. Friis, V. Srinivasan, and S. Sampath, *Assessing Plasma Spray Variability and Reliability: Towards an Integrated Approach*, presented by S. Sampath, Sensors 2004, Montreal, Canada, 2004
- 62 M. Ahrens, S. Lampenscherf, R. Vassen, and D. Stover, Sintering and creep processes in plasma-sprayed thermal barrier coatings, *Journal of Thermal Spray Technology*, 2004. **13**(3): p. 432-442.
- 63 D. S. Balint and J. W. Hutchinson, An analytical model of rumpling in thermal barrier coatings, *Journal of the Mechanics and Physics of Solids*, 2005. **53**(4): p. 949-973.
- 64 C. C. Berndt and H. Herman, Failure during Thermal Cycling of Plasma-Sprayed Thermal Barrier Coatings, *Thin Solid Films*, 1983. **108**(4): p. 427-437.
- 65 E. P. Busso, L. Wright, H. E. Evans, L. N. McCartney, S. R. J. Saunders, S. Osgerby, and J. Nunn, A physics-based life prediction methodology for thermal barrier coating systems, *Acta Materialia*, 2007. **55**(5): p. 1491-1503.
- 66 S. R. Choi, J. W. Hutchinson, and A. G. Evans, Delamination of multilayer thermal barrier coatings, *Mechanics of Materials*, 1999. **31**(7): p. 431-447.
- 67 S. Darzens, D. R. Mumm, D. R. Clarke, and A. G. Evans, Observations and analysis of the influence of phase transformations on the instability of the thermally grown oxide in a thermal barrier system, *Metallurgical and Materials Transactions a-Physical Metallurgy and Materials Science*, 2003. **34**(3): p. 511-522.
- 68 H. B. Guo, R. Vassen, and D. Stover, Thermophysical properties and thermal cycling behavior of plasma sprayed thick thermal barrier coatings, *Surface & Coatings Technology*, 2005. **192**(1): p. 48-56.
- 69 J. W. Hutchinson and A. G. Evans, On the delamination of thermal barrier coatings in a thermal gradient, *Surface and Coatings Technology*, 2002. **149**(2-3): p. 179-184.

- 70 J. Ilavsky, G. G. Long, A. J. Allen, and C. C. Berndt, Evolution of the void structure in plasma-sprayed YSZ deposits during heating, *Materials Science and Engineering A*, 1999. **272**(1): p. 215-221.
- 71 A. A. Kulkarni, A. Goland, H. Herman, A. J. Allen, J. Ilavsky, G. G. Long, C. A. Johnson, and J. A. Ruud, Microstructure-property correlations in industrial thermal barrier coatings, *Journal of the American Ceramic Society*, 2004. **87**(7): p. 1294-1300.
- 72 V. Lughi, V. K. Tolpygo, and D. R. Clarke, Microstructural aspects of the sintering of thermal barrier coatings, *Materials Science and Engineering a-Structural Materials Properties Microstructure and Processing*, 2004. **368**(1-2): p. 212-221.
- 73 D. R. Mumm, M. Watanabe, A. G. Evans, and J. A. Pfaendtner, The influence of test method on failure mechanisms and durability of a thermal barrier system, *Acta Materialia*, 2004. **52**(5): p. 1123-1131.
- 74 N. P. Padture, M. Gell, and E. H. Jordan, Thermal Barrier Coatings for Gas-Turbine Engine Applications, *Science*, 2002. **296**(5566): p. 280-284.
- 75 J. E. Schilbe, Substrate alloy element diffusion in thermal barrier coatings, *Surface and Coatings Technology*, 2000. **133-134**: p. 35-39.
- 76 K. W. Schlichting, N. P. Padture, E. H. Jordan, and M. Gell, Failure modes in plasma-sprayed thermal barrier coatings, *Materials Science and Engineering A*, 2003. **342**(1-2): p. 120-130.
- 77 B. Siebert, C. Funke, R. Vassen, and D. Stover, Changes in porosity and Young's Modulus due to sintering of plasma sprayed thermal barrier coatings, *Journal of Materials Processing Technology*, 1999. **93**: p. 217-223.
- 78 F. O. Soechting, A design perspective on thermal barrier coatings, *Journal of Thermal Spray Technology*, 1999. **8**(4): p. 505-511.
- 79 D. Stover and R. Vassen, Thermal barrier coatings for gas turbines, *Materialwissenschaft Und Werkstofftechnik*, 2001. **32**(8): p. 649-649.
- 80 V. Teixeira, M. Andritschky, W. Fischer, H. P. Buchkremer, and D. Stover, Analysis of residual stresses in thermal barrier coatings, *Journal of Materials Processing Technology*, 1999. **93**: p. 209-216.
- 81 V. K. Tolpygo and D. R. Clarke, Morphological evolution of thermal barrier coatings induced by cyclic oxidation, *Surface and Coatings Technology*, 2003. **163-164**: p. 81-86.
- 82 R. Vassen, G. Kerkhof, and D. Stover, Development of a micromechanical life prediction model for plasma sprayed thermal barrier coatings, *Materials Science*

- and Engineering a-Structural Materials Properties Microstructure and Processing*, 2001. **303**(1-2): p. 100-109.
- 83 P. K. Wright and A. G. Evans, Mechanisms governing the performance of thermal barrier coatings, *Current Opinion in Solid State and Materials Science*, 1999. **4**(3): p. 255-265.
- 84 T. Xu, M. Y. He, and A. G. Evans, A numerical assessment of the durability of thermal barrier systems that fail by ratcheting of the thermally grown oxide, *Acta Materialia*, 2003. **51**(13): p. 3807-3820.
- 85 D. Zhu and R. A. Miller, Investigation of thermal fatigue behavior of thermal barrier coating systems, *Surface and Coatings Technology*, 1997. **94-95**: p. 94-101.
- 86 A. M. Khoddami, A. Sabour, and S. M. M. Hadavi, Microstructure formation in thermally-sprayed duplex and functionally graded NiCrAlY/Yttria-Stabilized Zirconia coatings, *Surface and Coatings Technology*, 2007. **201**(12): p. 6019-6024.
- 87 C. C. Berndt and R. A. Miller, Failure analysis of plasma-sprayed thermal barrier coatings, *Thin Solid Films*, 1984. **119**(2): p. 173-184.
- 88 W. G. Mao, C. Y. Dai, Y. C. Zhou, and Q. X. Liu, An experimental investigation on thermo-mechanical buckling delamination failure characteristic of air plasma sprayed thermal barrier coatings, *Surface and Coatings Technology*, 2007. **201**(14): p. 6217-6227.
- 89 M. Martena, D. Botto, P. Fino, S. Sabbadini, M. M. Gola, and C. Badini, Modelling of TBC system failure: Stress distribution as a function of TGO thickness and thermal expansion mismatch, *Engineering Failure Analysis*, 2006. **13**(3): p. 409-426.
- 90 J. Rosler, M. Baker, and M. Volgmann, Stress state and failure mechanisms of thermal barrier coatings: role of creep in thermally grown oxide, *Acta Materialia*, 2001. **49**(18): p. 3659-3670.
- 91 R. Vaen, G. Kerkhoff, and D. Stover, Development of a micromechanical life prediction model for plasma sprayed thermal barrier coatings, *Materials Science and Engineering A*, 2001. **303**(1-2): p. 100-109.
- 92 S. Ahmaniemi, M. Vippola, P. Vuoristo, T. Mantyla, F. Cernuschi, and L. Lutterotti, Modified thick thermal barrier coatings: Microstructural characterization, *Journal of the European Ceramic Society*, 2004. **24**(8): p. 2247-2258.

- 93 S. Ahmaniemi, P. Vuoristo, T. Mantyla, F. Cernuschi, and L. Lorenzoni, Modified thick thermal barrier coatings: Thermophysical characterization, *Journal of the European Ceramic Society*, 2004. **24**(9): p. 2669-2679.
- 94 C. Funke, J. C. Mailand, B. Siebert, R. Vassen, and D. Stover, Characterization of ZrO₂-7 wt% Y₂O₃ thermal barrier coatings with different porosities and FEM analysis of stress redistribution during thermal cycling of TBCs, *Surface & Coatings Technology*, 1997. **94-5**(1-3): p. 106-111.
- 95 S. V. Joshi and M. P. Srivastava, On the thermal cycling life of plasma-sprayed yttria-stabilized zirconia coatings, *Surface and Coatings Technology*, 1993. **56**(3): p. 215-224.
- 96 J. Liu, J. W. Byeon, and Y. H. Sohn, Effects of phase constituents/microstructure of thermally grown oxide on the failure of EB-PVD thermal barrier coating with NiCoCrAlY bond coat, *Surface and Coatings Technology*, 2006. **200**(20-21): p. 5869-5876.
- 97 F. Tang and J. M. Schoenung, Evolution of Young's modulus of air plasma sprayed yttria-stabilized zirconia in thermally cycled thermal barrier coatings, *Scripta Materialia*, 2006. **54**(9): p. 1587-1592.
- 98 V. Teixeira, M. Andritschky, W. Fischer, H. P. Buchkremer, and D. Stover, Effects of deposition temperature and thermal cycling on residual stress state in zirconia-based thermal barrier coatings, *Surface & Coatings Technology*, 1999. **121**: p. 103-111.
- 99 P. Fauchais, Formation of Plasma-Sprayed Coatings, *Journal of Thermal Spray Technology*, 1995. **4**(1): p. 3-6.
- 100 P. Fauchais, Understanding plasma spraying, *Journal of Physics D-Applied Physics*, 2004. **37**(9): p. R86-R108.
- 101 H. Herman, Plasma-Sprayed Coatings, *Scientific American*, 1988. **259**(3): p. 112-117.
- 102 A. Kulkarni, A. Vaidya, A. Goland, S. Sampath, and H. Herman, Processing effects on porosity-property correlations in plasma sprayed yttria-stabilized zirconia coatings, *Materials Science and Engineering a-Structural Materials Properties Microstructure and Processing*, 2003. **359**(1-2): p. 100-111.
- 103 S. Sampath and H. Herman, Rapid solidification and microstructure development during plasma spray deposition, *Journal of Thermal Spray Technology*, 1996. **5**(4): p. 445-456.
- 104 T. A. Taylor, Thermal properties and microstructure of two thermal barrier coatings, *Surface and Coatings Technology*, 1992. **54-55**: p. 53-57.

- 105 A. Vardelle, C. Moreau, and P. Fauchais, The dynamics of deposit formation in thermal-spray processes, *Mrs Bulletin*, 2000. **25**(7): p. 32-37.
- 106 G. X. Wang, V. Prasad, and S. Sampath, Rapid solidification in thermal spray deposition: Microstructure and modelling, *Sadhana-Academy Proceedings in Engineering Sciences*, 2001. **26**: p. 35-57.
- 107 P. Fauchais, M. Vardelle, J. F. Coudert, A. Vardelle, C. Delbos, and J. Fazilleau, Thermal plasma deposition from thick to thin coatings and from micro- to nanostructure, *Pure and Applied Chemistry*, 2005. **77**(2): p. 475-485.
- 108 J. Matejcek and S. Sampath, Intrinsic residual stresses in single splats produced by thermal spray processes, *Acta Materialia*, 2001. **49**(11): p. 1993-1999.
- 109 J. Matejcek, S. Sampath, P. C. Brand, and H. J. Prask, Quenching, thermal and residual stress in plasma sprayed deposits: NiCrAlY and YSZ coatings, *Acta Materialia*, 1999. **47**(2): p. 607-617.
- 110 H. Zhang, X. Y. Wang, L. L. Zheng, and X. Y. Jiang, Studies of splat morphology and rapid solidification during thermal spraying, *International Journal of Heat and Mass Transfer*, 2001. **44**(24): p. 4579-4592.
- 111 S. Sampath and X. Jiang, Splat formation and microstructure development during plasma spraying: deposition temperature effects, *Materials Science and Engineering a-Structural Materials Properties Microstructure and Processing*, 2001. **304**: p. 144-150.
- 112 J. Mostaghimi and S. Chandra, Splat formation in plasma-spray coating process, *Pure and Applied Chemistry*, 2002. **74**(3): p. 441-445.
- 113 H. Zhang, X. Y. Wang, L. L. Zheng, and S. Sampath, Numerical simulation of nucleation, solidification, and microstructure formation in thermal spraying, *International Journal of Heat and Mass Transfer*, 2004. **47**(10-11): p. 2191-2203.
- 114 X. Y. Jiang, Y. P. Wan, H. Herman, and S. Sampath, Role of condensates and adsorbates on substrate surface on fragmentation of impinging molten droplets during thermal spray, *Thin Solid Films*, 2001. **385**(1-2): p. 132-141.
- 115 S. Sampath, X. Y. Jiang, J. Matejcek, A. C. Leger, and A. Vardelle, Substrate temperature effects on splat formation, microstructure development and properties of plasma sprayed coatings Part I: Case study for partially stabilized zirconia, *Materials Science and Engineering a-Structural Materials Properties Microstructure and Processing*, 1999. **272**(1): p. 181-188.
- 116 J. Mostaghimi, M. Pasandideh-Fard, and S. Chandra, Dynamics of splat formation in plasma spray coating process, *Plasma Chemistry and Plasma Processing*, 2002. **22**(1): p. 59-84.

- 117 J. Cedelle, M. Vardelle, B. Pateyron, and P. Fauchais, Study of droplet behaviour at impact in plasma spraying, *High Temperature Material Processes*, 2004. **8**(3): p. 353-379.
- 118 P. Fauchais, M. Fukumoto, A. Vardelle, and M. Vardelle, Knowledge concerning splat formation: An invited review, *Journal of Thermal Spray Technology*, 2004. **13**(3): p. 337-360.
- 119 L. Bianchi, A. C. Leger, M. Vardelle, A. Vardelle, and P. Fauchais, Splat formation and cooling of plasma-sprayed zirconia, *Thin Solid Films*, 1997. **305**(1-2): p. 35-47.
- 120 L. Bianchi, A. Denoirjean, F. Blein, and P. Fauchais, Microstructural investigation of plasma-sprayed ceramic splats, *Thin Solid Films*, 1997. **299**(1-2): p. 125-135.
- 121 R. C. Dykhuizen, Review of Impact and Solidification of Molten Thermal Spray Droplets, *Journal of Thermal Spray Technology*, 1994. **3**(4): p. 351-361.
- 122 M. Fukumoto, E. Nishioka, and T. Matsubara, Flattening and solidification behavior of a metal droplet on a flat substrate surface held at various temperatures, *Surface and Coatings Technology*, 1999. **120-121**: p. 131-137.
- 123 M. Fukumoto, E. Nishioka, and T. Matsubara, Effect of interface wetting on flattening of freely fallen metal droplet onto flat substrate surface, *Journal of Thermal Spray Technology*, 2002. **11**(1): p. 69-74.
- 124 M. Fukumoto, E. Nishioka, and T. Nishiyama, New criterion for splashing in flattening of thermal sprayed particles onto flat substrate surface, *Surface and Coatings Technology*, 2002. **161**(2-3): p. 103-110.
- 125 L. Li, X. Y. Wang, G. Wei, A. Vaidya, H. Zhang, and S. Sampath, Substrate melting during thermal spray splat quenching, *Thin Solid Films*, 2004. **468**(1-2): p. 113-119.
- 126 Y. Huang and M. Fukumoto, Transition in flattening behavior of thermally sprayed particles impinging on flat substrate surface, *Journal of the Japan Institute of Metals*, 1998. **62**(4): p. 397-403.
- 127 M. Viana, P. Jouannin, C. Pontier, and D. Chulia, About pycnometric density measurements, *Talanta*, 2002. **57**(3): p. 583-593.
- 128 A. J. Allen, G. G. Long, H. Boukari, J. Ilavskya, A. Kulkarni, S. Sampath, H. Herman, and A. N. Goland, Microstructural characterization studies to relate the properties of thermal-spray coatings to feedstock and spray conditions, *Surface & Coatings Technology*, 2001. **146**: p. 544-552.

- 129 H. Boukari, A. J. Allen, G. G. Long, J. Ilavsky, J. S. Wallace, C. C. Berndt, and H. Herman, Small-angle neutron scattering study of the role of feedstock particle size on the microstructural behavior of plasma-sprayed yttria-stabilized zirconia deposits, *Journal of Materials Research*, 2003. **18**(3): p. 624-634.
- 130 F. Cernuschi, S. Ahmaniemi, P. Vuoristo, and T. Mantyla, Modelling of thermal conductivity of porous materials: application to thick thermal barrier coatings, *Journal of the European Ceramic Society*, 2004. **24**(9): p. 2657-2667.
- 131 W. Chi, S. Sampath, and H. Wang, Ambient and high-temperature thermal conductivity of thermal sprayed coatings, *Journal of Thermal Spray Technology*, 2006. **15**(4): p. 773-778.
- 132 Y. J. Su, H. Wang, W. D. Porter, A. R. D. A. Lopez, and K. T. Faber, Thermal conductivity and phase evolution of plasma-sprayed multilayer coatings, *Journal of Materials Science*, 2001. **36**(14): p. 3511-3518.
- 133 R. E. Taylor, X. Wang, and X. Xu, Thermophysical properties of thermal barrier coatings, *Surface & Coatings Technology*, 1999. **121**: p. 89-95.
- 134 Y. Tan, J. P. Longtin, and S. Sampath, Modeling Thermal Conductivity of Thermal Spray Coatings: Comparing Predictions to Experiments, *Journal of Thermal Spray Technology*, 2006. **15**: p. 545-552.
- 135 W. C. Oliver and G. M. Pharr, Measurement of hardness and elastic modulus by instrumented indentation: Advances in understanding and refinements to methodology, *Journal of Materials Research*, 2004. **19**(1): p. 3-20.
- 136 W. C. Oliver and G. M. Pharr, An Improved Technique for Determining Hardness and Elastic-Modulus Using Load and Displacement Sensing Indentation Experiments, *Journal of Materials Research*, 1992. **7**(6): p. 1564-1583.
- 137 M. Eskner and R. Sandstrom, Measurement of the elastic modulus of a plasma-sprayed thermal barrier coating using spherical indentation, *Surface and Coatings Technology*, 2004. **177-178**: p. 165-171.
- 138 A. Gouldstone, N. Chollacoop, M. Dao, J. Li, A. M. Minor, and Y.-L. Shen, Indentation across size scales and disciplines: Recent developments in experimentation and modeling, *Acta Materialia*, 2007. **55**(12): p. 4015-4039.
- 139 V. Harok and K. Neufuss, Elastic and inelastic effects in compression in plasma-sprayed ceramic coatings, *Journal of Thermal Spray Technology*, 2001. **10**(1): p. 126-132.
- 140 A. Tricoire, A. Vardelle, P. Fauchais, F. Braillard, A. Malie, and P. Bengtsson, Macrocrack formation in plasma-sprayed YSZ TBCs when spraying thick passes, *High Temperature Material Processes*, 2005. **9**(3): p. 401-413.

- 141 P. Fauchais, M. Vardelle, A. Vardelle, and L. Bianchi, Plasma spray: Study of the coating generation, *Ceramics International*, 1996. **22**(4): p. 295-303.
- 142 P. Fauchais, M. Vardelle, A. Vardelle, L. Bianchi, and A. C. Leger, Parameters controlling the generation and properties of plasma sprayed zirconia coatings, *Plasma Chemistry and Plasma Processing*, 1996. **16**(1): p. S99-S125.
- 143 M. Friis and C. Persson, Control of thermal spray processes by means of process maps and process windows, *Journal of Thermal Spray Technology*, 2003. **12**(1): p. 44-52.
- 144 H. B. Guo, R. Vassen, and D. Stover, Atmospheric plasma sprayed thick thermal barrier coatings with high segmentation crack density, *Surface & Coatings Technology*, 2004. **186**(3): p. 353-363.
- 145 S. Sampath, X. Y. Jiang, J. Matejcek, L. Prchlik, A. Kulkarni, and A. Vaidya, Role of thermal spray processing method on the microstructure, residual stress and properties of coatings: an integrated study for Ni-5 wt.%Al bond coats, *Materials Science and Engineering a-Structural Materials Properties Microstructure and Processing*, 2004. **364**(1-2): p. 216-231.
- 146 A. Vaidya, Process Maps for Thermal Spray: A Fundamental Approach to Process – Property Relationships, Ph.D. Thesis, Stony Brook University, 2004
- 147 A. Vaidya, G. Bancke, S. Sampath, and H. Herman, Influence of Process Variables on the Plasma Sprayed Coatings: An Integrated Study, *International Thermal Spray Conference (ITSC)*, 2001 (Singapore), ASM International, Materials Park, OH
- 148 C. Moreau, Towards A Better Control Of Thermal Spray, *ITSC*, 1998 (Nice, France),
- 149 M. Prystay, P. Gougeon, and C. Moreau, Structure of plasma-sprayed zirconia coatings tailored by controlling the temperature and velocity of the sprayed particles, *Journal of Thermal Spray Technology*, 2001. **10**(1): p. 67-75.
- 150 M. Friis, P. Nylen, C. Persson, and J. Wigren, Investigation of particle in-flight characteristics during atmospheric plasma spraying of yttria-stabilized ZrO₂: Part 1. Experimental, *Journal of Thermal Spray Technology*, 2001. **10**(2): p. 301-310.
- 151 M. Friis, C. Persson, and J. Wigren, Influence of particle in-flight characteristics on the microstructure of atmospheric plasma sprayed yttria stabilized ZrO₂, *Surface & Coatings Technology*, 2001. **141**(2-3): p. 115-127.
- 152 C. Moreau, M. Lamontagne, and P. Cielo, Method and apparatus for monitoring the temperature and velocity of plasma sprayed particles, USA, Pat. No. 5, 180, 921

- 153 J. R. Fincke and R. A. Neiser, Advanced diagnostics and modeling of spray processes, *Mrs Bulletin*, 2000. **25**(7): p. 26-31.
- 154 J. A. Brogan, C. C. Berndt, W. C. Smith, R. V. Gansert, S. Raghu, S. Sampath, and H. Herman, Real-time imaging of the plasma spray process - Work in progress, *Journal of Thermal Spray Technology*, 1995. **4**(4): p. 374-376.
- 155 J. Zierhut, K. D. Landes, W. Kroemmer, and P. Heinrich, Particle Flux Imaging (PFI) In-Situ Diagnostics for Thermal Coating Process, *Thermal Spray : Surface Engineering via Applied Research*, 2000 (Montreal, Quebec, Canada), ASM International
- 156 J. F. Bisson, M. Lamontagne, C. Moreau, L. Pouliot, J. Blain, and F. Nadeau, Ensemble In-Flight Particle Diagnostics Under Thermal Spray Conditions, *International Thermal Spray Conference (ITSC)*, 2001 (Singapore), ASM International
- 157 E. Hamalainen, T. Vattulainen, T. Alahautala, R. Hernberg, P. Vuoristo, and T. Mantyla, Imaging Diagnostics in Thermal Spraying - SprayWatch System, *Thermal Spray : Surface Engineering via Applied Research*, 2000 (Montreal, Quebec, Canada), ASM International
- 158 T. Streibl, A. Vaidya, M. Friis, V. Srinivasan, and S. Sampath, A Critical Assessment of Particle Temperature Distributions During Plasma Spraying: Experimental Results for YSZ, *Plasma Chemistry and Plasma Processing*, 2006. **26**(1): p. 73-102.
- 159 L. Pawlowski, D. Lombard, and P. Fauchais, Structure-Thermal Properties - Relationship in Plasma Sprayed Zirconia Coatings, *Journal of Vacuum Science & Technology a-Vacuum Surfaces and Films*, 1985. **3**(6): p. 2494-2500.
- 160 A. Vaidya, T. Streibl, L. Li, S. Sampath, O. Kovarik, and R. Greenlaw, An integrated study of thermal spray process-structure-property correlations: A case study for plasma sprayed molybdenum coatings, *Materials Science and Engineering a-Structural Materials Properties Microstructure and Processing*, 2005. **403**(1-2): p. 191-204.
- 161 H. Zhang, H. B. Xiong, L. L. Zheng, A. Vaidya, L. Li, and S. Sampath, Melting Behavior of In-flight Particles and Its Effects on Splat Morphology in Plasma Spraying, 2002 (New Orleans, LA, United States), American Society of Mechanical Engineers, New York, NY 10016-5990, United States
- 162 D. M. Gray, Y. C. Lau, C. A. Johnson, M. P. Borom, and W. A. Nelson, Thermal barrier coatings having an improved columnar microstructure, 1998, USA, Pat. No.

- 163 J. Ilavsky, A. J. Allen, G. G. Long, S. Krueger, C. C. Berndt, and H. Herman, Influence of spray angle on the pore and crack microstructure of plasma-sprayed deposits, *Journal of the American Ceramic Society*, 1997. **80**(3): p. 733-742.
- 164 G. Montavon, S. Sampath, C. C. Berndt, H. Herman, and C. Coddet, Effects of the spray angle on splat morphology during thermal spraying, *Surface & Coatings Technology*, 1997. **91**(1-2): p. 107-115.
- 165 X. Jiang, J. Matejicek, and S. Sampath, Substrate temperature effects on the splat formation, microstructure development and properties of plasma sprayed coatings Part II: case study for molybdenum, *Materials Science and Engineering a-Structural Materials Properties Microstructure and Processing*, 1999. **272**(1): p. 189-198.
- 166 L. Leblanc and C. Moreau, The long-term stability of plasma spraying, *Journal of Thermal Spray Technology*, 2002. **11**(3): p. 380-386.
- 167 J. F. Bisson, B. Gauthier, and C. Moreau, Effect of plasma fluctuations on in-flight particle parameters, *Journal of Thermal Spray Technology*, 2003. **12**(1): p. 38-43.
- 168 J. F. Bisson and C. Moreau, Effect of direct-current plasma fluctuations on in-flight particle parameters: Part II, *Journal of Thermal Spray Technology*, 2003. **12**(2): p. 258-264.
- 169 B. Dussoubs, G. Mariaux, A. Vardelle, M. Vardelle, and P. Fauchais, DC plasma spraying: Effect of arc root fluctuations on particle behavior in the plasma jet, *High Temperature Material Processes*, 1999. **3**(2-3): p. 235-254.
- 170 J. F. Coudert and P. Fauchais, Arc instabilities in a dc plasma torch, *High Temperature Material Processes*, 1997. **1**(2): p. 149-166.
- 171 V. Lago, M. De Graaf, and M. Dudeck, Arc voltage fluctuations in a nitrogen plasma torch, *High Temperature Material Processes*, 1997. **1**(2): p. 179-190.
- 172 C. Baudry, A. Vardelle, and G. Mariaux, Numerical modeling of a DC non-transferred plasma torch: Movement of the arc anode attachment and resulting anode erosion, *High Temperature Material Processes*, 2005. **9**(1): p. 1-15.
- 173 K. Ramachandran, J. L. Marques, R. Vassen, and D. Stover, Modelling of arc behaviour inside a F4 APS torch, *Journal of Physics D-Applied Physics*, 2006. **39**(15): p. 3323-3331.
- 174 Z. Duan, L. Beall, M. P. Planche, J. Heberlein, E. Pfender, and M. Stachowicz, Arc voltage fluctuations as an indication of spray torch anode condition, *Thermal Spray: a United Forum for Scientific and Technological Advances*, 1997 (Indianapolis, Indiana; USA),

- 175 J. F. Coudert and P. Fauchais, Transient phenomena in d.c. plasma-spray torches, *Heat and Mass Transfer under Plasma Conditions*, 1999. **891**: p. 382-390.
- 176 Z. Duan, L. Beall, J. Schein, J. Heberlein, and M. Stachowicz, Diagnostics and modeling of an argon/helium plasma spray process, *Journal of Thermal Spray Technology*, 2000. **9**(2): p. 225-234.
- 177 J. F. Bisson, C. Moreau, M. Dorfman, C. Dambra, and J. Mallon, Influence of hydrogen on the microstructure of plasma-sprayed yttria-stabilized zirconia coatings, *Journal of Thermal Spray Technology*, 2005. **14**(1): p. 85-90.
- 178 A. Vardelle, M. Vardelle, and P. Fauchais, Heat and Momentum-Transfer between Powder Particulates and Atmospheric Plasma-Jet, *Revue Internationale Des Hautes Temperatures Et Des Refractaires*, 1986. **23**(2): p. 69-85.
- 179 H. B. Xiong, L. L. Zheng, S. Sampath, R. L. Williamson, and J. R. Fincke, Three-dimensional simulation of plasma spray: effects of carrier gas flow and particle injection on plasma jet and entrained particle behavior, *International Journal of Heat and Mass Transfer*, 2004. **47**(24): p. 5189-5200.
- 180 M. Vardelle, A. Vardelle, P. Fauchais, K. I. Li, B. Dussoubs, and N. J. Themelis, Controlling particle injection in plasma spraying, *Journal of Thermal Spray Technology*, 2001. **10**(2): p. 267-284.
- 181 C. Moreau and L. Leblanc, Optimization and process control for high performance thermal spray coatings, *Durable Surfaces*, 2001. **197**: p. 27-57.
- 182 S. Sampath, X. Jiang, A. Kulkarni, J. Matejicek, D. L. Gilmore, and R. A. Neiser, Development of process maps for plasma spray: case study for molybdenum, *Materials Science and Engineering a-Structural Materials Properties Microstructure and Processing*, 2003. **348**(1-2): p. 54-66.
- 183 S. Sampath and R. McCune, Thermal-spray processing of materials, *Mrs Bulletin*, 2000. **25**(7): p. 12-14.
- 184 S. Sampath, V. Srinivasan, A. Vaidya, A. Gouldstone, Y. Liu, and T. Nakamura, Sensing, Control, and Insitu Extraction of Coating Properties: An Integrated Approach towards Establishing Process Maps, *ITSC 2006*, 2006 (Seattle, Washington, USA), ASM International
- 185 P. Fauchais and M. Vardelle, Understanding the formation of DC plasma sprayed coatings, *Thermec'2003, Pts 1-5*, 2003. **426-4**: p. 2459-2465.
- 186 Y. P. Wan, V. Prasad, G. X. Wang, S. Sampath, and J. R. Fincke, Model and powder particle heating, melting, resolidification, and evaporation in plasma spraying processes, *Journal of Heat Transfer-Transactions of the Asme*, 1999. **121**(3): p. 691-699.

- 187 M. Fukumoto, H. Nagai, and T. Yasui, Influence of Surface Character Change of Substrate Due to Heating on Flattening Behavior of Thermal Sprayed Particles, *Journal of Thermal Spray Technology*, 2006. **15**: p. 759-764.
- 188 C.-J. Li, C.-X. Li, G.-J. Yang, and Y.-Y. Wang, Examination of Substrate Surface Melting-Induced Splashing During Splat Formation in Plasma Spraying, *Journal of Thermal Spray Technology*, 2006. **15**: p. 717-724.
- 189 R. Mcpherson, On the Formation of Thermally Sprayed Alumina Coatings, *Journal of Materials Science*, 1980. **15**(12): p. 3141-3149.
- 190 J. Mostaghimi, Modelling droplet impact in plasma spray processes, *Pure and Applied Chemistry*, 1998. **70**(6): p. 1209-1215.
- 191 Y. P. Wan, H. Zhang, X. Y. Jiang, S. Sampath, and V. Prasad, Role of solidification, substrate temperature and Reynolds number on droplet spreading in thermal spray deposition: Measurements and modeling, *Journal of Heat Transfer-Transactions of the Asme*, 2001. **123**(2): p. 382-389.
- 192 V. Srinivasan, A. Vaidya, T. Streibl, M. Friis, and S. Sampath, On the Reproducibility of Air Plasma Spray Process and Control of Particle State, *Journal of Thermal Spray Technology*, 2006. **15**: p. 739-743.
- 193 A. Vaidya, T. Streibl, S. Sampath, and H. Zhang, A comparative diagnostic analysis of morphologically different YSZ powders, *Thermal Spray 2004: Advances in Technology and Application*, 2004 (Osaka, Japan), ASM International
- 194 L. Li, On The Deposit Formation Dynamics And Multiscale Characterization Of Thermal Sprayed Splat Structures, Ph.D. Thesis, Stony Brook University, 2004
- 195 L. B. Delcea, Plasma torch with axial injection of feedstock, 1995, USA, Pat. No. 5,420,391
- 196 P. Fauchais, A. Grimaud, A. Vardelle, and M. Vardelle, Plasma Spraying - an Overview, *Annales De Physique*, 1989. **14**(3): p. 261-310.
- 197 M. Vardelle, A. Vardelle, A. C. Leger, P. Fauchais, and D. Gobin, Influence of Particle Parameters at Impact on Splat Formation and Solidification in Plasma Spraying Processes, *Journal of Thermal Spray Technology*, 1995. **4**(1): p. 50-58.
- 198 S. Guessasma, G. Montavon, and C. Coddet, Velocity and temperature distributions of alumina-titania in-flight particles in the atmospheric plasma spray process, *Surface & Coatings Technology*, 2005. **192**(1): p. 70-76.
- 199 V. Srinivasan, M. Friis, A. Vaidya, T. Streibl, and S. Sampath, Particle Injection in Direct Current Air Plasma Spray: Salient Observations and Optimization Strategies, *Plasma Chemistry and Plasma Processing*, 2007. **In Press**.

- 200 H.-B. Xiong, L.-L. Zheng, and T. Streibl, A Critical Assessment of Particle Temperature Distributions During Plasma Spraying: Numerical Studies for YSZ, *Plasma Chemistry and Plasma Processing*, 2006. **26**(1): p. 53-72.
- 201 J. L. Smialek, Segmented thermal barrier coating, 2001, US, Pat. No. 6,316,078
- 202 T. E. Strangman, Laser segmented thick thermal barrier coatings for turbine shrouds, 2001, US, Pat. No. 6,224,963
- 203 T. E. Strangman, Columnar Grain Ceramic Thermal Barrier Coatings, 1982, USA, Pat. No.
- 204 T. A. Taylor, Thermal Barrier Coatings for Substrates and Process for Producing It, 1991, USA, Pat. No.
- 205 J. Madejski, Solidification of droplets on a cold surface, *International Journal of Heat and Mass Transfer*, 1976. **19**: p. 1009.
- 206 E. Turunen, T. Varis, T. E. Gustafsson, J. Keskinen, T. Falt, and S.-P. Hannula, Parameter optimization of HVOF sprayed nanostructured alumina and alumina-nickel composite coatings, *Surface and Coatings Technology*, 2006. **200**(16-17): p. 4987-4994.
- 207 M. Fukumoto and Y. Huang, Flattening mechanism in thermal sprayed nickel particle impinging on flat substrate surface, *Journal of Thermal Spray Technology*, 1999. **8**(3): p. 427-432.
- 208 P. Roy, G. Bertrand, and C. Coddet, Spray drying and sintering of zirconia based hollow powders, *Powder Technology*, 2005. **157**(1-3): p. 20-26.
- 209 P. Roy, G. Bertrand, and C. Coddet, Influence of spraying variables and of a new zirconia hollow powder on the microstructure of plasma sprayed Thermal Barrier Coating, *ITSC*, 2003 (Orlando , Florida, USA), ASM
- 210 P. Fauchais and A. Vardelle, Heat, mass and momentum transfer in coating formation by plasma spraying, *International Journal of Thermal Sciences*, 2000. **39**(9-11): p. 852-870.
- 211 M. Vardelle, A. Vardelle, P. Fauchais, and M. I. Boulos, Plasma - Particle Momentum and Heat-Transfer - Modeling and Measurements, *Aiche Journal*, 1983. **29**(2): p. 236-243.
- 212 M. Vardelle, A. Vardelle, P. Fauchais, and M. I. Boulos, Particle Dynamics and Heat-Transfer under Plasma Conditions, *Aiche Journal*, 1988. **34**(4): p. 567-573.
- 213 H.-B. Xiong, L.-L. Zheng, L. Li, and A. Vaidya, Melting and oxidation behavior of in-flight particles in plasma spray process, *International Journal of Heat and Mass Transfer*, 2005. **48**(25-26): p. 5121-5133.

- 214 P. Gougeon and C. Moreau, Simultaneous independent measurement of splat diameter and cooling time during impact on a substrate of plasma-sprayed molybdenum particles, *Journal of Thermal Spray Technology*, 2001. **10**(1): p. 76-82.
- 215 C. Moreau, P. Cielo, M. Lamontagne, S. Dallaire, J. C. Krapez, and M. Vardelle, Temperature Evolution of Plasma-Sprayed Niobium Particles Impacting on a Substrate, *Surface & Coatings Technology*, 1991. **46**(2): p. 173-187.
- 216 W. Zhang, V. Srinivasan, L. L. Zheng, and S. Sampath, An Investigation of Particle Injection and Resulting In-flight Particle Behavior during Air Plasma Spraying, *International Mechanical Engineering Congress & Exposition (IMECE)*, 2006 (Chicago, Illinois, USA), ASME
- 217 J. R. Fincke, C. L. Jeffery, and R. E. Spjut, Measurement of the Emissivity of Small Particles at Elevated-Temperatures, *Optical Engineering*, 1988. **27**(8): p. 684-690.
- 218 J. R. Fincke, W. D. Swank, C. L. Jeffery, and C. A. Mancuso, Simultaneous Measurement of Particle-Size, Velocity and Temperature, *Measurement Science & Technology*, 1993. **4**(5): p. 559-565.